

https://dspace.org/

A polymeric implant for application in post-surgical resection of osteosarcoma

Suleman, Ayesha

2024

https://hdl.handle.net/10539/37794

Downloaded from a DSpace repository. https://dspace.org/

A Polymeric Implant for Application in Post-Surgical Resection of Osteosarcoma

Ayesha Suleman

A dissertation submitted to the Faculty of Health Sciences, University of the Witwatersrand, in fulfilment of the requirements for the degree Master of Pharmacy.



Supervisors:

Prof. Yahya E. Choonara

University of the Witwatersrand, Department of Pharmacy and Pharmacology,

Johannesburg, South Africa

Associate Prof. Pierre P. D. Kondiah

University of the Witwatersrand, Department of Pharmacy and Pharmacology,

Johannesburg, South Africa

2023, Johannesburg, South Africa

DECLARATION

I, Ayesha Suleman, declare that this dissertation is my own, unaided work. It is being submitted for the Degree Master of Pharmacy at the University of the Witwatersrand, Johannesburg. It has not been submitted before for any degree or examination at any other University.



(Signature of candidate)

27th day of June 2023 in Pretoria

DEDICATION

For my Grandparents, Sultan Salahuddin Al Ayyubi (R.A.) and the Ottomans, especially Sultan Abdul Hamid Han Hz (Jannat Makkan).

Their life stories have inspired me to always do my best and be my best. May the Almighty grant them the Highest Stages in Paradise. Ameen.

RESEARCH OUTPUTS

Presentations:

1. Ayesha Suleman, Pierre Kondiah and Yahya E Choonara. BRICS Summit

2021: 04 November 2021. Oral presentation.

2. Suleman A, Kondiah PPD, Mabrouk M and Choonara YE (2021) The Application of 3D-Printing and Nanotechnology for the Targeted Treatment of Osteosarcoma. Front. Mater. 8:668834. doi: 10.3389/fmats.2021.668834.

3. Suleman A, Kondiah PPD, Mabrouk M and Choonara YE . The Influence of Incorporating Bioglass Within a Composite Hydrogel for Application in Osteosarcoma. To be submitted to a suitable journal.

ABSTRACT

Osteosarcoma is a malignant neoplasm of which there is osteoid formation by tumour cells. According to the American Cancer Society, osteosarcoma is prevalent in patients between the ages of 10 and 30 and those diagnosed with osteosarcoma over the age of 60, consist of 10% of the population afflicted. Surgery is a critical component in the treatment of osteosarcoma. Wide margin resections are standard in surgical treatment of osteosarcoma, therefore an osteotomy occurs, inducing a severe bone defect. Adjuvant chemotherapy is administered by IV after surgical removal of osteosarcoma to mitigate the risk of tumour micro metastases. The chemotherapeutic drugs are accompanied by severe side effects. To address the issue of a critical bone defect, the use of bone grafts and prosthetic devices (endoprosthesis or megaprosthesis), have been utilised. However, Osteosarcoma is mainly prevalent in adolescents, their growth poses a constant challenge to prosthetics and bone grafts have their own drawbacks. There is a need for customising implants for individual patients. To this end, this study focused on the development of a mouldable implants. The materials of these implants may have the ability to regenerate bone and provide localised drug delivery which may bypass the severe side effects of IV administered chemotherapeutics. Two hydrogel implants (one containing bioglass and the other without bioglass) were synthesised and compared. The polymers used were Alginate and Polyacrylamide. The hydrogel implants displayed great moulding ability when cast into different shapes and characterisation studies such as FTIR, XRD, TGA and DSC was conducted. Scaffolds containing bioglass initially possessed enough strength to match cancellous bone. Biomineralisation studies proved the formation of hydroxyapatite on the scaffold surface. Both hydrogel implants displayed ~20% of Doxorubicin released over 8 weeks. At 6 weeks, ALG-PAAM hydrogel implants degraded to 87,674% ± 5,042 of their original weight, while BG-ALG-PAAM hydrogel implants degraded to 86,528% ± 0,0987 of their original weight. Cell studies were conducted using MG-63 cells and proved that both scaffolds were non-cytotoxic and could facilitate cell adhesion. However, these hydrogel implants lacked the presence of pores from formation. Therefore, the same polymers were used to fabricate implantable scaffolds. These scaffolds were formed by lyophilisation and contained pores from formation. However, mechanical strength of these scaffold implants did not match the strength of bone and only two of the 5 criteria of the diamond concept were met in implantable scaffolds containing bioglass. Overall, it was concluded that BG-ALG-PAAM was better than the double network hydrogel without bioglass and had potential for application in Osteosarcoma as it met three of the five criteria mentioned in the diamond concept. Further research is needed to improve the scaffolds formed by lyophilization to meet at least three of the 5 criteria of the Diamond Concept.

AKNOWLEDGEMENTS

In the name of the Almighty, the most Beneficent, the most Merciful.

All Praise and Thanks is due to the Almighty alone, Who, in His Infinite Mercy has allowed me to start and complete this M. Pharm journey.

The biggest thank you goes to my Mum and brother for their never-ending support, affection and encouragement throughout my Master's.

I would like to thank my supervisors, Prof Yahya E Choonara and Prof Pierre P.D. Kondiah. Their supervision has helped me grow in leaps and bounds. A special thank you goes to Prof Thashree Marimuthu and Prof Pradeep Kumar for the encouraging words always passed to me in the hallways of 8th floor. A special mention goes to Prof Mostafa Mabrouk for his kind advice.

A special mention goes to the technical team for the never-ending, always available assistance: Dr. Hillary Mndlovu, Mr. Kleinbooi Mohlabi, Mr. Bafana Themba, Miss Tshidi Mosete, Phumzile Madondo, and Siya Maphumulo. Your help and amazing personalities will continue to inspire me forever. A special thank you to Miss Petra Dinham for her expertise in SEM.

To Yosra Sharfy, Iman Hoosen, Henna Cassimjee and Tayzuma Patel may the Almighty bless you for every little conversation and word of encouragement that you gave me. I will always treasure our friendship.

To my other friends on 8th floor, you all deserve a mention. You all have acted as my friends, counsellors, personal cheerleaders and some of you, even comedians. This is list extensive, however, each of you deserve a mention for the special part you have played in my journey. Here goes: Ranya Ibrahim, Eeman Cohen, Taskeen Sarwan, Mashudu Mphaphuli, Leon Khoza, Lindokuhle Ngema, Variksha Singh, Divesha Essa, Onyinye Jennifer Uwaezuoke, Nombeko Sikhosana, Ayesha Wadee, Shazia Mansoor, Kruti Naik, Kate Da Silva, Dalton Brouwer, Kimaya Moodley, Magdi Abobaker, Ahmed Abdelgadir, Brian Karithi, Kara de La Harpe, Kundai Mazarura, Simisola Ayodele, Abu Bakr Nana, Lara Freidus, Vanessa Chivere, Fadzai Mutingwede, Alex Adekiya, Cuthbert Kibungu, Sarjan Patel, Lusanda and Mpume.

To my fellow Texture Analyser custodians, Atang Motaung and Theresa Varughese, your friendship and work ethic deserve a special mention.

To Dr. Gillian Mahumane: Thou art bae.

I thank the following Postdocs for their very effective training and help with instruments and advice: Dr. Mershen Govender, Dr Sunaina Indermun, Dr Pavan Walvekar, Dr Sam, Dr Sifiso,

Dr Mduduzi Sithole. Dr Philemon Ubanako, I thank you for the help and training in the cell lab and cell-work techniques.

The financial assistance of the National Research Foundation (NRF) towards this research is hereby acknowledged (and thanked). Opinions expressed and conclusions arrived at, are those of the author and are not necessarily to be attributed to the NRF.

TABLE OF CONTENTS

Title: A Polymeric Implant for Application in Post-Surgical Resection of Osteosarcoma ……..i
DECLARATION ii
DEDICATION ……iii
RESEARCH OUTPUTS iv
ABSTRACT ……v
AKNOWLEDGEMENTS vi
TABLE OF CONTENTS viii
LIST OF ABBREVIATIONS xiv
LIST OF TABLES xvi
LIST OF FIGURES xvii
LIST OF EQUATIONS xxii

CHAPTER.1.INTRODUCTION AND OVERVIEW OF THE STUDY……. ……..1

1.1 Introduction and background to the study 1
1.2 Rationale and motivation 4
1.3 Aims and objectives 7
1.4 Potential benefits of undertaking this research 8
1.6 References 10

CHAPTER.2.LITERATURE REVIEW: THE APPLICATION OF 3D-PRINTING AND NANOTECHNOLOGY FOR THE TARGETED TREATMENT OF OSTEOSARCOMA 13

2.1 Introduction 13
2.2 Fabrication of 3D-Printed Scaffolds for Enhanced Bone Regeneration 14
2.2.1 Natural polymers used for 3D-printing of scaffolds in bone regeneration 18
2.2.1.1 3D-printed chitosan scaffolds 18
2.2.1.2 3D- printed alginate scaffolds 19
2.2.1.3 3D printed collagen scaffolds 20
2.2.1.4 3D printed gelatin scaffolds 21
2.2.1.5 3D printed silk fibroin scaffolds 22
2.2.2 Synthetic polymers used for 3D-printing of scaffolds in bone regeneration 23
2.2.2.1 3D printed polycaprolactone scaffolds 23
2.2.2.2 3D printed polyurethane scaffolds 24

2.2.2.3 3D printed poly (lactic acid) scaffolds 25
2.2.2.4 3D printed polyvinyl alcohol scaffolds 26
2.2.3 Bioceramics used for 3D-printing of scaffolds in bone regeneration 27
2.2.3.1 3D printed calcium phosphate scaffolds 27
2.2.3.2 3D printed calcium silicates 28
2.2.3.3 3D printed bioactive glasses in bone regeneration 29
2.2.4 Comparison Between Different Scaffold Compositions 30
2.3 Stimuli-Responsive Scaffolds in Bone Regeneration 31
2.4 3D-Printing of Bioactive-Loaded Scaffolds for Bone Regeneration 34
2.5 Nano-Enabled 3D-Printed Scaffolds for Bone Regeneration 35
2.5.1 Nano-liposomes and 3D-printed scaffolds 36
2.5.2 Polymeric nanoparticles and 3D printed scaffolds 38
2.5.3 Iron oxide nanoparticles and 3D printed scaffolds 38
2.5.4 Gold nanoparticles and 3D printed scaffolds 39
2.5.5 Silver Nanoparticles and 3D printed scaffolds 40
2.6 Nanocarriers for Potential Incorporation into 3D-Printed Scaffolds 40
2.6.1 Mesoporous silica nanoparticles as anti-osteosarcoma nanocarriers 41
2.6.2 Micelles as anti-osteosarcoma nanocarriers 42
2.6.3 Targeted nanocarriers and stimuli-responsive nanocarriers 43
2.7 Concluding Remarks 48
2.8 References 51

CHAPTER.3.DEVELOPMENT OF A COMPOSITE HYDROGEL IMPLANT FOR APPLICATION IN OSTEOSARCOMA 69
3.1 Introduction 69
3.2 Materials 70
3.3 Methods 71
3.3.1 Hydrogel Fabrication to determine the best cross linker 71
3.3.1.1 Hydrogel Fabrication 71
3.3.1.2 Assessment of mechanical strength to determine best crosslinker: 71
3.3.2 The Fabrication of hydrogel implants to establish the optimal concentration of the best crosslinker. 72
3.3.2.1 Synthesis of hydrogel implants with different crosslinker concentrations 72
3.3.2.2 Assessment of hydrogel implants synthesised with different cross-linker concentrations to establish the optimal concentration of the best crosslinker 72

3.3.2.3 Assessment of mechanical strength of the hydrogel implants to establish the optimal concentration of best crosslinker 72
3.3.2.4 Assessment of swelling of the hydrogel implants to establish the optimal concentration of best crosslinker 72
3.3.2.5 Assessment of morphology of the hydrogel implant with the best crosslinker concentration..... 73
3.3.2.6 Assessment of mouldability 73
3.3.3 Hydrogel Fabrication to induce macro-pores after determining the optimal cross-linking concentration:..... 73
3.4 Results and discussion..... 74
3.4.1 Hydrogel Fabrication to assess the best cross linker..... 74
3.4.2 Hydrogel Fabrication to establish the optimal concentration of the best crosslinker: 75
3.4.3 Hydrogel Fabrication to induce to induce macro-pores after determining the optimal cross-linking concentration:..... 78
3.5 Concluding Remarks 81
3.6 References..... 82

CHAPTER.4.THE INFLUENCE OF INCORPORATING BIOGLASS WITHIN A COMPOSITE HYDROGEL FOR APPLICATION IN OSTEOSARCOMA.. 85
4.1 Introduction 85
4.2 Materials 86
4.3 Methods 87
4.3.1 Fabrication of ALG-PAAM hydrogel implant: 87
4.3.2 Bioglass incorporation into ALG-PAAM hydrogel implants to form BG-ALG-PAAM hydrogel implants 87
4.3.3 Characterisation studies of ALG-PAAM and BG-ALG-PAAM hydrogel implants. . ……...88
4.3.3.1 Moulding capability of the ALG-PAAM and BG-ALG-PAAM hydrogel implants……..88
4.3.3.2 Physicochemical properties of ALG-PAAM and BG-ALG-PAAM hydrogel implants…. 88
4.3.3.3 Thermal properties of ALG-PAAM and BG-ALG-PAAM hydrogel implants…..88
4.3.3.4 Biomineralization ALG-PAAM and BG-ALG-PAAM hydrogel implants..... 88
4.3.3.5 Mechanical analysis of ALG-PAAM and BG-ALG-PAAM hydrogel implants……..88

4.3.3.6 Swelling and shape retention of ALG-PAAM and BG-ALG-PAAM hydrogel implants…. 89
4.3.3.7 Degradation, morphology and porosity of ALG-PAAM and BG-ALG-PAAM hydrogel implants 89
4.3.3.8 Doxorubicin Loading and release of ALG-PAAM and BG-ALG-PAAM hydrogel implants..... 90
4.3.3.9 Invitro cytotoxicity and cell proliferation of ALG-PAAM and BG-ALG-PAAM hydrogel implants 90
4.3.3.10 Statistical analysis 91
4.4 Results 92
4.4.1 Moulding capabilities of ALG-PAAM and BG-ALG-PAAM hydrogel implants.. 92
4.4.2 Physicochemical properties of ALG-PAAM and BG-ALG-PAAM hydrogel implants..... 93
4.4.3 Thermal Characteristics of ALG-PAAM and BG-ALG-PAAM hydrogel implants…. 95
4.4.4 Biomineralization of ALG-PAAM and BG-ALG-PAAM hydrogel implants 97
4.4.5 Mechanical analysis of ALG-PAAM and BG-ALG-PAAM hydrogel implants. 102
4.4.6 Swelling and shape retention of ALG-PAAM and BG-ALG-PAAM hydrogel implants..... 103
4.4.7 Degradation of ALG-PAAM and BG-ALG-PAAM hydrogel implants 106
4.4.8 Morphology, Porosity and Pore size of ALG-PAAM and BG-ALG-PAAM hydrogel implants..... 107
4.4.9 Drug Loading and Drug release of ALG-PAAM and BG-ALG-PAAM hydrogel implants……113
4.4.10 In Vitro cell compatibility of ALG-PAAM and BG-ALG-PAAM hydrogel implants…. 115
4.5 Discussion..... 120
4.5.1 Moulding Capability of ALG-PAAM and BG-ALG-PAAM hydrogel implants . 120
4.5.2 Mechanical Strength of ALG-PAAM and BG-ALG-PAAM hydrogel implants 120
4.5.3 Swelling capabilities of ALG-PAAM and BG-ALG-PAAM hydrogel implants. 121
4.5.4 Biomineralisation of ALG-PAAM and BG-ALG-PAAM hydrogel implants 122
4.5.5 Degradation of ALG-PAAM and BG-ALG-PAAM hydrogel implants 122
4.5.6 Morphology of ALG-PAAM and BG-ALG-PAAM hydrogel implants..... 122

4.5.7 Drug Loading and Drug Release of ALG-PAAM and BG-ALG-PAAM hydrogel implants..... 123
4.5.8 In vitro cytocompatibility of ALG-PAAM and BG-ALG-PAAM hydrogel implants…. 123
4.6 Concluding Remarks 123
4.7 References..... 125

CHAPTER.5.THE INFLUENCE OF INCORPORATING BIOGLASS WITHIN A COMPOSITE IMPLANT FOR APPLICATION IN OSTEOSARCOMA 131
5.1 Introduction 131
5.2 Materials: 131
5.3 Methods: 132
5.3.1 Fabrication of APDL scaffolds: 132
5.3.2 Fabrication of BGAPDL scaffolds 132
5.3.3 Characterisation studies of the implantable scaffolds. 132
5.3.3.1 Physicochemical properties of the implantable scaffolds. 132
5.3.3.2 Thermal properties of the implantable scaffolds 132
5.3.3.3 Mechanical analysis of the implantable scaffolds 133
5.3.3.4 Degradation of the implantable scaffolds 133
5.3.3.5 Swelling analysis of the implantable scaffolds 133
5.3.3.6 Morphology of the implantable scaffolds..... 133
5.3.3.7 Porosity of the implantable scaffolds 134
5.3.3.8 Biomineralisation of the implantable scaffolds 134
5.3.3.9 Doxorubicin Loading and release of the implantable scaffolds 134
5.4 Results 135
5.4.1 Physicochemical Characterisation of the implantable scaffolds:..... 135
5.4.2 Thermal Analysis of the implantable scaffolds..... 137
5.4.3 Mechanical Strength of the implantable scaffolds: 138
5.4.4 Degradation of the implantable scaffolds: 139
5.4.5 Swelling of the implantable scaffolds: 140
5.4.6 Morphology of the implantable scaffolds 141
5.4.7 Porosity of the implantable scaffolds 143
5.4.8 Biomineralisation of the implantable scaffolds..... 143

5.4.9 Doxorubicin loading and release of the implantable scaffolds 145
5.5 Discussion:..... 147
5.5.1 Mechanical Strength of the implantable scaffolds: 148
5.5.2 Swelling of the implantable scaffolds: 148
5.5.3 Biomineralisation of the implantable scaffolds:..... 148
5.5.4 Degradation of the implantable scaffolds 149
5.5.5 Morphology and Porosity of the implantable scaffolds:..... 149
5.5.6 Drug Loading and Drug Release of the implantable scaffolds: 149
5.6 Concluding Remarks..... 150
5.7 References..... 151

CHAPTER.6.: CONCLUSIONS, RECOMMENDATIONS, AND FUTURE PROSPECTS 155

6.1 Conclusions..... 155
6.2 Future prospects 156
6.3 References..... 158
Appendix A: International Published Review Paper 160
Appendix B: Research output: Oral presentation: BRICS Summit 2021: 04 November 2021… 161

LIST OF ABBREVIATIONS

3D-	Three-dimensional
3DP	Three-dimensional printing
AgNP-	Silver Nanoparticles
ALG-PAAM-	Alginate-polyacrylamide
APDL-	Alginate-polyacrylamide double lyophilised
AuNP-	Gold Nanoparticles
β-TCP-	β-Tricalcium phosphate
BG-	Bioglass
BG-ALG-PAAM-	Bioglass- Alginate-polyacrylamide
BGAPDL-	Bioglass-Alginate-polyacrylamide- double lyophilised
BMP-	Bone Morphogenic Proteins
CAD-	Computer-Aided Design
$CaCl_2$-	Calcium Chloride
DMEM-	Dulbecco's Modified Eagle Medium
DN-	Double Network Hydrogel
FBS-	Fetal bovine serum
$FeCl_3$-	Iron (III) Chloride
FTIR-	Fourier transform infrared spectroscopy
MBIS-	N,N'-Methylenebisacrylamide
Mw-	Molecular Weight
MRI-	Magnetic resonance imaging
MSN-	Mesoporous silica nanoparticles
OS-	Osteosarcoma
PBS-	Phosphate Buffer Solution
PCL	Polycaprolactone
PDLA-	Poly (D-lactic acid)
PLA-	Poly (lactic acid)
PLLA-	Poly (L-lactic acid)
P-S-	Penicillin-Streptomycin
PVA-	Polyvinyl Alcohol
SBF-	Simulated Body Fluid
SEM-	Scanning Electron Microscopy
TEMED-	Tetramethylethylenediamine
TEOS-	Tetraethyl orthosilicate

TGA-	Thermogravimetric Analysis
VEGF-	Vascular Endothelial Growth Factor
XRD-	X-ray diffraction

LIST OF TABLES

Table 1.1: The types of Osteosarcomas and their relevant treatments (Moore and Luu, 2014) (van der Spuy and Vlok, 2009) 3

Table 1.2: Chemotherapeutic regimen for osteosarcoma (OS99). D- Doxorubicin, C-Carboplatin, I- Ifosfamide. Figure from (Union for International Cancer Control, 2014) Table licenced under Creative Commons (http://creativecommons.org/licenses/by-nc-sa/2 4

Table 1.3: Chemotherapeutic regimen for osteosarcoma (6 cycle MAP). A- Doxorubicin, P-Cisplatin, M- Methotrexate. (Union for International Cancer Control, 2014).Table licenced under Creative Commons (http://creativecommons.org/licenses/by-nc-sa/2.5/deed..... 4

Table 2.1: Combinations of polymers and bioceramic composite scaffolds and their properties 17

Table 2.2: A summary of the different studies comparing different scaffold compositions and their bone regeneration outcomes 31

Table 2.3: Information on strategies to confer targeting properties to nanoparticles 45

Table 2.4: Information on strategies utilized to confer intrinsic stimuli properties to nanoparticles as well as the anti-osteosarcoma drugs and cell lines utilized... 47

Table 3.1: Different alginate concentrations used to form the double network hydrogel 75

Table 3.2: The strength capabilities of the double network hydrogel at different $FeCl_3$ concentrations. 75

Table 3.3: The different concentrations of sodium bicarbonate and its resultant effects..... 79

Table 4.1: Porosity and range of Pore sizes present in ALG-PAAM and BG-ALG-PAAM hydrogel implants 113

LIST OF FIGURES

Figure 1.1: Schematic illustration of the concept and application of the proposed polymeric implant for the regeneration of bone and treatment of residual osteosarcoma cells. 7

Figure 2.1: Illustration of the hierarchical structure of bone. Reproduced from X. Chen et al. 2018 under Creative Commons Attribution (CC BY) license (CC BY 4.0) (https://creativecommons.org/licenses/by/4.0/) 15

Figure 2.2: Schematic depicting the use of NIR laser to trigger photothermal effects in tumor **cells**. HSP- Heat shock protein. Reproduced from Andersson et al. 2014 under Creative Commons Attribution license (CC BY-NC-SA 3.0)) ((http://creativecommons.org/licenses/by/3.0/)..... 32

Figure 2.3: A depiction of how the magnetic field is generated from the coil to affect tumor cells. A generator is connected to a coil and oscilloscope. The generator provides voltage and frequency to the coil while the oscilloscope displays the frequency and amplitude on a screen. Reproduced from Vegerhof et al. 2016 under Creative Commons Attribution (CC-BY) license (CC BY 4.0) (http://creativecommons.org/licenses/by/4.0/). 34

Figure 2.4: The various types of nanocarriers that may be incorporated into a scaffold. The nanocarriers are included in a 3D printed scaffold. The scaffold is then implanted into the critical defect site present in the femur due to osteosarcoma resection. Chemotherapeutics are released from the scaffold to target residual cancer cells while the scaffold regenerates the bone. This figure was created with BioRender.com..... 36

Figure 2.5: Nanoparticles with ligands for targeted delivery bind to cell receptors to be internalized by receptor mediated endocytosis. Reproduced from G. J. Kim and Nie 2005 under Creative Commons Attribution (CC-BY) license (CC BY-NC-ND 3.0) (https://creativecommons.org/licenses/by-nc-nd/3.0/) 44

Figure 3.1: Illustration of the method used to impart pores to the double network hydrogel. Illustrated using biorender. 74

Figure 3.2: Swelling profiles of DN hydrogels crosslinked in 0,2 M, 0,3 M and 0,4 M of $FeCl_3$. 76

Figure 3.3: SEM images of the optimal implant. The first SEM picture on the left indicates a single pore with the diameter of 79.99 μm at a magnification of 50 μm. The SEM picture on the left displays the implant at a higher magnification of 10 μm and a

single pore of 19.95 μm can be seen. No interconnected pores could be identified. 77

Figure 3.4: Mouldability of hydrogel. A- the needle in the hydrogel after 24 hours. B- after the removal of the capped needle, no hydrogel is messed on the needle cap. B also displays that the hydrogel maintained the void after removal as indicated by the white arrow. C and D are pictures of the hydrogel at different angles. C and D display that the hydrogel maintained the void in the shape of the capped needle. D displays that the hydrogel even maintained the shape of the needle cap where it narrows as indicated by blue arrows. 78

Figure 3.5: SEM images of hydrogel implants with larger pores imparted by sodium bicarbonate. The images were taken at different scales (image on the right is at 100 μm while image on the left is at 400 μm). 1% w/v Sodium bicarbonate was added to the hydrogel scaffolds cross-linked in 0,3 M $FeCl_3$. 80

Figure 3.6: SEM image of hydrogel implants with larger pores imparted by sodium bicarbonate at 200 μm. % w/v Sodium bicarbonate was added to the hydrogel scaffolds cross-linked in 0,3 M $FeCl_3$. A variety of pore sizes above 100 μm in size could be observed. 80

Figure 4.1: Moulding capabilities of ALG-PAAM and BG-ALG-PAAM hydrogel implants The moulding capabilities indicate the potential for customisation per individual patient. A- The various moulds the hydrogel implants were cast in. B- ALG-PAAM hydrogel implants moulding capabilities. C- BG-ALG-PAAM hydrogel implants. 92

Figure 4.2: FTIR spectra of Pristine Alginate, ALG-PAAM before immersion in FeCl3, ALG-PAAM, BG, BG-ALG-PAAM 94

Figure 4.3: XRD spectra of Pristine Alginate, ALG-PAAM before immersion in FeCl3, ALG-PAAM, BG, BG-ALG-PAAM 95

Figure 4.4: TGA thermograms of Pristine Alginate, ALG-PAAM before immersion in FeCl3, ALG-PAAM, BG, BG-ALG-PAAM 96

Figure 4.5: Derivative TGA thermograms of Pristine ALG, ALG-PAAM before CL, ALG-PAAM, BG-ALG-PAAM and BG..... 97

Figure 4.6: XRD Spectra of ALG-PAAM Hydrogel implants after immersion in SBF (Weeks 0-4). The hydrogel implants before immersion is completely amorphous while crystalline peaks appear with a maximum at around 32° as the weeks go on after immersion in SBF. 98

Figure 4.7: XRD spectra of BG-ALG-PAAM after immersion in SBF (weeks 0-4). The hydrogel implants before immersion is completely amorphous while crystalline peaks

appear with a maximum at around 32° as the weeks go on after immersion in SBF. 99
Figure 4.8: EDS of ALG-PAAM before immersion in SBF. Only the presence of Fe and Cl could be noted. 99
Figure 4.9: EDS of ALG-PAAM hydrogel implants after immersion in SBF at week 2 (right) and week 4 (left). The presence of Ca and P was noted at both time points. 100
Figure 4.10: EDS of BG-ALG-PAAM before immersion in SBF. Only the presence of Fe, Cl, Si and P was observed. 100
Figure 4.11: EDS of BG-ALG-PAAM after immersion in SBF for 2 weeks (right) and 4 weeks (left). The presence of Ca and P was noted at both time points. 100
Figure 4.12: SEM images of ALG-PAAM hydrogel implants after immersion in SBF. Hydroxyapatite crystals can be observed on its surface..... 101
Figure 4.13: SEM of BG-ALG-PAAM after immersion in SBF. Hydroxyapatite crystals can be observed on its surface..... 101
Figure 4.14: Graph depicting the decrease in compressive strength of ALG-PAAM and BG-ALG-PAAM hydrogel implants over time when exposed to SBF. 102
Figure 4.15: Graphs depicting matrix resilience (right) and deformation energy (left) of ALG-PAAM and BG-ALG-PAAM scaffolds after 24 hours and 4 weeks of exposure to SBF. Matrix resilience increased as exposure to SBF increased while deformation energy decreased as exposure to SBF increased. 103
Figure 4.16: Swelling profiles of ALG-PAAM and BG-ALG-PAAM. ALG-PAAM displayed a slightly higher swelling capacity than BG-ALG-PAAM..... 104
Figure 4.17: ALG-PAAM shape maintenance over time. It can be seen that ALG-PAAM hydrogel implants can maintain its shape after swelling substantially. 105
Figure 4.18: BG-ALG-PAAM shape maintenance over time. It can be seen that ALG-PAAM hydrogel implants can maintain its shape after swelling substantially. 105
Figure 4.19: Degradation of ALG-PAAM hydrogel implants and BG-ALG-PAAM hydrogel implants over 6 weeks. 106
Figure 4.20: Morphology at 24 hours of degradation. A- ALG-PAAM. B- BG-ALG-PAAM. No interconnecting pores could be observed. 108
Figure 4.21: Morphology at 1 week degradation captured at different scales. A porous structure can be observed for both ALG-PAAM and BG-ALG-PAAM hydrogel implants. A- ALG-PAAM at 100 μm. B- ALG-PAAM at 30 μm. . C- BG-ALG-PAAM at 100 μm. D- BG-ALG-PAAM at 30 μm. 109
Figure 4.22: Morphology at 2 weeks degradation captured at different scales. A porous structure can be observed for both ALG-PAAM and BG-ALG-PAAM hydrogel

implants. A- ALG-PAAM at 100 μm. B- ALG-PAAM at 30 μm. . C- BG-ALG-PAAM at 100 μm. D- BG-ALG-PAAM at 30 μm. 110

Figure 4.23: Morphology at 3 weeks degradation captured at different scales. Web like structures can be observed due to degradation implants as indicated by the white arrows. A porous structure can still be observed. A- ALG-PAAM at 100 μm. B- ALG-PAAM at 30 μm. . C- BG-ALG-PAAM at 100 μm. D- BG-ALG-PAAM at 30 μm. 111

Figure 4.24: Morphology at 4 weeks degradation captured at different scales. . Web like structures can be observed due to degradation implants as indicated by the white arrows. A porous structure can still be observed A- ALG-PAAM at 100 μm. B- ALG-PAAM at 30 μm. . C- BG-ALG-PAAM at 100 μm. D- BG-ALG-PAAM at 30 μm. 112

Figure 4.25: % drug loading of ALG-PAAM and BG-ALG-PAAM hydrogel implants. ALG-PAAM hydrogel implants displayed a slightly greater drug loading capability. 114

Figure 4.26: Cumulative drug release of Doxorubicin from ALG-PAAM and BG-ALG-PAAM hydrogels..... 115

Figure 4.27: Cell viability of ALG-PAAM and BG-ALG-PAAM hydrogel implants treated with 3 days and 7 days conditioned media, conditioned media combined with the concentration of DOX released at that time point and Freed Doxorubicin drug. Data is presented as mean ± SD, n=3. * Indicates statistical difference ($p < 0.05$). 116

Figure 4.28:Cell adhesion onto ALG-PAAM hydrogel implants. Images show sparse cells. A- image of MG-63 cells on ALG-PAAM hydrogel implants at 200 μm. B,C- areas of A containing MG-63 cells at 100 μm. 118

Figure 4.29:Cell adhesion of BG-ALG-PAAM hydrogel implants. Images show cell clusters. A- image of MG-63 cells on ALG-PAAM hydrogel implants at 200 μm. B,C- areas of A containing MG-63 cells at 100 μm 119

Figure 5.1: FTIR spectra of APDL, BGAPDL, ALG-PAAM and BG-ALG-PAAM. The lines running through the spectra indicate the common bonds found throughout all four spectra. 136

Figure 5.2: XRD spectra of APDL, BGAPDL, ALG-PAAM and BG-ALG-PAAM. The spectra indicate a lack of crystalline peaks proving the amorphous nature of the scaffolds. 136

Figure 5.3: TGA thermograms of APDL, BGAPDL, ALG-PAAM and BG-ALG-PAAM..... 137

Figure 5.4: Derivatives of TGA thermograms for APDL,BGAPDL, ALG-PAAM and BG-ALG-PAAM. Derivative thermograms indicate that APDL and BGAPDL degrade at a lower temperature compared to ALG-PAAM and BG-ALG-PAAM 138

Figure 5.5: Compressive strength, matrix resilience and deformation energy of APDL scaffolds and BGAPDL scaffolds. BGAPDL scaffolds have a higher compressive strength, matrix resilience and deformation energy than APDL scaffolds..... 139

Figure 5.6: Degradation profile of APDL and BGAPDL scaffolds over 8 weeks. BGAPDL scaffolds had a higher degradation than APDL scaffolds. 140

Figure 5.7: Swelling of APDL and BGAPDL scaffolds in SBF. APDL had a greater swelling capacity than BGAPDL scaffolds. 141

Figure 5.8: Cross-section of APDL scaffold under SEM. A variety of pore sizes can be observed. 142

Figure 5.9: Cross-section of BGAPDL scaffold under SEM. Smaller pores can be seen in this image. 142

Figure 5.10: FTIR and XRD Spectra of APDL and BGAPDL scaffolds displaying biomineralisation at various time points. A- FTIR spectra of APDL scaffolds. B- FTIR spectra of BGAPDL scaffolds. C- XRD spectra of APDL scaffolds. D- XRD spectra of APDL scaffolds 143

Figure 5.11: EDX spectra of APDL and BGAPDL scaffolds before and after immersion in SBF. A- APDL scaffolds before immersion in SBF. B- BGAPDL scaffolds before immersion in SBF. C- APDL scaffolds after immersion in SBF. D- BGAPDL scaffolds after immersion in SBF. The EDX spectra display the presence of Ca and P for both APDL and BGAPDL scaffolds after immersion in SBF..... 144

Figure 5.12: Hydroxyapatite formation on APDL and BGAPDL scaffolds as seen at 500 nm. A- Hydroxyapatite crystals on the surface of APDL scaffolds that underwent exposure to SBF. B- Hydroxyapatite crystals on the surface of BGAPDL scaffolds that underwent exposure to SBF. 145

Figure 5.13: The doxorubicin loading profile of APDL and BGAPDL scaffolds. APDL scaffolds displayed a slightly higher loading capacity 146

Figure 5.14: The doxorubicin release profiles of APDL and BGAPDL scaffolds..... 147

LIST OF EQUATIONS

Equation 3.1 Swelling ratio %..... 72
Equation 4.1 Swelling ratio % 89
Equation 4.2 Degradation % 89
Equation 4.3 % Cell viability 91
Equation 5.1 Degradation % 133
Equation 5.2 Swelling % 133
Equation 5.3 % Porosity..... 134

CHAPTER.1. INTRODUCTION AND OVERVIEW OF THE STUDY

1.1 Introduction and background to the study

Osteosarcoma is a malignant neoplasm and is characterised by the production of osteoid by tumour cells (Heck and Toy, 2017). The American Cancer Society reports that people between the ages of 10 and 30 are most likely to develop osteosarcoma, and those over 60 make up 10% of those affected by the disease (American Cancer Society, 2020). Osteosarcoma can develop as a result of a number of predisposing factors, including Paget's disease, radiation exposure, chemotherapy, genetics, as well as when foreign bodies are inserted into bone such as orthopaedic implants. The majority of osteosarcomas develop in long bones, around the joint areas (proximal areas of the humerus and tibia, and the distal areas of the femur). The spine and flat bones are less likely to develop osteosarcomas (Reith, 2018).

Surgery is a critical component in the treatment of osteosarcoma (Tiwari, 2012). Wide margin resections are standard in surgical treatment of osteosarcoma. A wide margin resection involves removing the tumour along with rim of healthy tissue. Thus an osteotomy occurs, inducing a severe bone defect (Tiwari, 2012). When treating Low-grade osteosarcoma, a wide margin resection of the tumour is the only treatment. Higher grade osteosarcomas, are treated with surgery as well as chemotherapy which me be administered before surgery to mitigate the risk ask of micrometastases (neoadjuvant chemotherapy) or after surgery (adjuvant chemotherapy) (Tiwari, 2012). Table 1.1 describes in detail the types of osteosarcoma and their treatments.

Wide margin resections are limb-salvage procedures. A currently used modality to address defects caused by wide margin resections is the use of a prosthetic device (endoprosthesis or megaprosthesis). However, as Osteosarcoma is mainly prevalent in adolescents, their growth poses a constant challenge to the suitability of the fit of the prosthetic devices. Prosthetic enlargement to match the growth of affected adolescents has advanced from intermittent surgeries to non-invasive means (such as using magnetic devices). However, complications, such as loosening and wear and tear of the prosthetic device are frequent and the need for advancement is greatly needed (Tiwari, 2012; Bielack *et al.*, 2016).

The utilisation of bone grafts is another current approach to replacing bone. Bone grafts may be autogenous (from the patient’s own body) or homogenous (allografts) (from other humans). Each of these approaches have their own draw backs (autografts cause more pain and morbidity to patient and the quantity available is limited while allografts may cause an antigenic response and require processing that may cause loss of properties). Therefore research has

been focused on the use of safer, more cost effective synthetic grafts (Tiwari, 2012; Oryan *et al.*, 2014; Martin and Bettencourt, 2018).

Following the surgical resection of the osteosarcoma, adjuvant chemotherapy may be utilised to reduce the chance of tumour micrometastases. Methotrexate, doxorubicin, and cisplatin form part of the most common chemotherapeutic regimen for osteosarcoma. (Jones, 2020). The severe side effects of these chemotherapeutic include cisplatin's permanent ototoxic and nephrotoxic consequences, methotrexate's myelosuppression and mucositis, doxorubicin's cardiotoxicity, and tissue necrosis (Toy and Heck, 2017). As chemotherapeutics are systemically delivered and do not distinguish between healthy, normal cells and tumour cells, these side effects are common. While conventional chemotherapy has improved the survival rate of those patients with high-grade Osteosarcoma, no improvement has been made to the survival rate since the 1980's, despite various attempts made at better chemotherapy regimens. Therefore, research into novel drug delivery systems is needed (Luetke *et al.*, 2014).

To address bone defects induced by surgery, osteo-regenerative platforms may be utilised. Bone regeneration is a complex process as molecular, biochemical, mechanical and cellular aspects have to be accounted for. Therefore, osteo-regenerative platforms, such as scaffolds and hydrogels, should be biocompatible and should have the appropriate porosity, degradability, compositional and mechanical properties(Wang *et al.*, 2020).

This project therefore proposes the development of an implant that will utilise localised delivery of chemotherapeutics, thereby bypassing the adverse effects of traditional chemotherapy administered systemically via intravenous infusion. The implant should have mouldable properties to allow for patient customisability. In addition, the implant will be fabricated with biomaterials with an osteo-regenerative potential to address the bone defects caused by osteosarcoma resection.

Table 1.1: The types of Osteosarcomas and their relevant treatments (Moore and Luu, 2014)(van der Spuy and Vlok, 2009)

Osteosarcoma Type	Osteosarcoma subtype	Description	Treatment
Intermedullary OS	Conventional OS	High grade intermedullary tumour. Mainly affects the metaphyseal region of bone. (May be further subclassified into chondroblastic, fibroblastic or osteoblastic OS depending on the histological profiles.)	Wide margin resection and chemotherapy.
	Telangiectatic OS	Affects metaphysis of long bones. One of the most aggressive forms of OS.	Treated similarly to conventional OS.
	Small cell OS	One of the rare forms of OS. Mainly affects the metaphyseal region of long bones. And is similar to Ewing's sarcoma.	Wide margin resection, Chemotherapy.
	Low grade central OS	Has painless progression. Usually in older patients.	Wide margin resection surgery. This type of OS has a recurrence rate if it is not properly resected.
Surface OS Usually treated with surgery alone. This OS sits on the surface of the bone and is not continuous with the medullary	Parosteal OS	Slow growing surface OS. Can be found on many different bones of appendicular skeleton but most commonly found on the posterior distal femur.	Wide margin resection surgery and reconstruction.
	Periosteal OS	Can be found along the diaphysis of long bones,	Wide margin resection surgery,

canal. It is usually painless (indolent) unless it is a high-grade surface OS.		most commonly on the Tibia.	
	High grade surface OS.	Likely to erode cortical surface of the bone	Treatment is similar to conventional OS. Wide margin resection surgery and chemotherapy.

1.2 Rationale and motivation

Treatment of Osteosarcoma in the developing countries, such as South Africa, still lag behind the osteosarcoma treatments made in first world countries. Difficulties in access to healthcare facilities, the lack resources within healthcare facilities (which result in referral to another healthcare facility) as well as delays in access to diagnostic equipment and procedures delay the osteosarcoma diagnosis. This may lead to higher stage osteosarcoma and worse patient prognoses (Lisenda et al., 2017). Thus, when considering advancement in treatment, the South African context must be taken into account.

According to the Unioin for International Cancer Control's 2014 Review of the WHO's cacncer medicines on the list of Essential medicines (Union for International Cancer Control, 2014), the standard chemotherapy regimens for osteosarcoma include a 6 cycle MAP **(Table 1.3)** where chemotherapy is provided to the patient for 17 weeks after surgery or 12 cycle OS99 where chemotherapy is provided to the patient for 21 weeks after surgery. (**Table 1.2**). These chemotherapy regimens include the delivery of doxorubicin by intravenous infusion after surgery.

Table 1.2: Chemotherapeutic regimen for osteosarcoma (OS99). D- Doxorubicin, C- Carboplatin, I- Ifosfamide. Figure from (Union for International Cancer Control, 2014) Table licenced under Creative Commons (http://creativecommons.org/licenses/by-nc-sa/2

Week	0	3	6	9	SURGERY	14	17	20	23	26	29	32	35
Chemo	CI	CI	CI	D		ID	CI	CD	ID	CI	CD	ID	CD

Table 1.3: Chemotherapeutic regimen for osteosarcoma (6 cycle MAP). A- Doxorubicin, P- Cisplatin, M- Methotrexate. (Union for International Cancer Control, 2014).Table licenced under Creative Commons (http://creativecommons.org/licenses/by-nc-sa/2.5/deed

Week	1	4	5	6	9	10	SURGERY	12	15	16	17	20	21	22	24	25	26	28	29
Chemo	AP	M	M	AP	M	M		AP	M	M	AP	M	M	A	M	M	A	M	M

These chemotherapy regimens require multiple visits to the clinic to receive IV infusions of Chemotherapy.

Therefore, methods of the implant fabrication need to preferably use minimal resources and equipment. In addition, if the drug is loaded within the implant for localised therapy, it provides the advantage of bypassing IV methods of chemotherapy administration, which does not require patients to make difficult journeys to the clinic Thus, the patient receives chemotherapy, with minimal side effects and healthcare workers are not overburdened.

Therefore, a key approach in developing treatments for Osteosarcoma would be to utilise a dual therapy approach, whereby the loading of an anticancer drug into a biocompatible implant would prevent the recurrence of Osteosarcoma by mitigating the risk of residual cancer cells after surgery, while filling the resection site and providing aid to regenerate the bone (Palamà *et al.*, 2017).

The implant that fills the defect site should possess the appropriate bone regenerative properties. According to the diamond concept, there are five general therapeutic targets that bone regeneration platforms should aim for. The implant should possess a minimum of three of these five properties (Giannoudis, Einhorn and Marsh, 2007; Giannoudis *et al.*, 2008; Jahan and Tabrizian, 2016):

- Osteoconduction,
- Growth factors (osteoinduction),
- Mechanical properties,
- Vascularization (angiogenesis) and,
- Osteogenesis (synthesis of new bone).

Osteo-regenerative implants synthesised from biomaterials such as bioceramics, have the potential to address bone defects caused by surgical resection of osteosarcoma, due to their osteo-regenerative properties. Implants derived from bioceramics are structurally, compositionally and mechanistically similar to the apatite present in bone tissue (Wang *et al.*, 2020). High mechanical strength materials are important for application in bone tissue engineering applications (Sithole, 2019). Bioglass is osteoconductive and osteoproductive (stimulates growth of new bone) (Rainer *et al.*, 2008). However, despite the many applications in bone tissue engineering, bioglass tends to have weaker mechanical properties when used

alone which restricts use of these materials in certain applications (Mabrouk *et al.*, 2014). Therefore, it would be important incorporate bioglass into other polymers.

There is a need for the development of patient-customised implants for the individual patient (Howard *et al.*, 2008) This need is emphasised when approaching osteosarcoma, as the population affected are growing adolescents. A method of ensuring customisability of implants would be to ensure that the implant may be mouldable to fit the defect site perfectly.

Therefore, in brief, the development of a mouldable, polymeric implant that will utilise localised delivery of chemotherapeutics, thereby bypassing the adverse effects of traditional IV administered chemotherapy and fabricated with biomaterials that can meet the standards set by the diamond concept, is required for application in Osteosarcoma. This concept is illustrated in **Figure 1.1**.

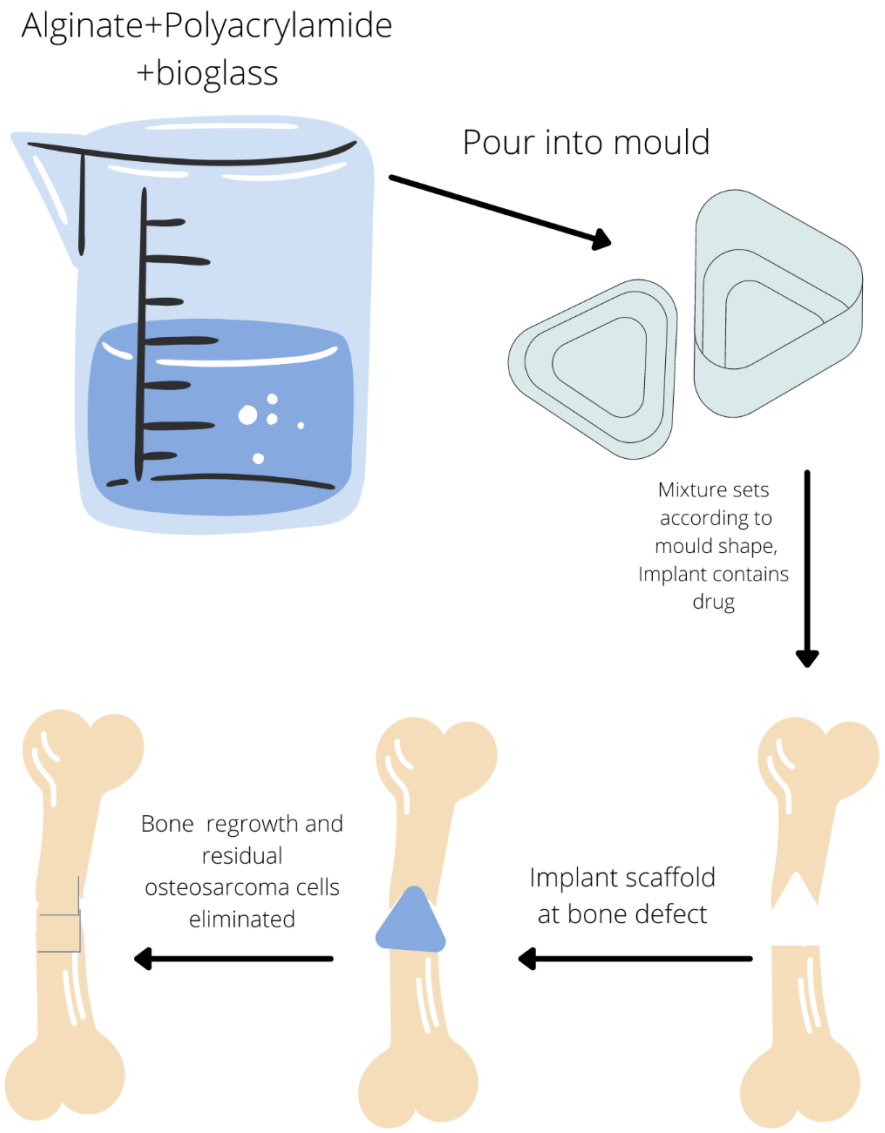


Figure 1.1: Schematic illustration of the concept and application of the proposed polymeric implant for the regeneration of bone and treatment of residual osteosarcoma cells.

1.3 Aims and objectives

The aim of this study was to fabricate a polymeric implant for the treatment of residual osteosarcoma that will also possess bone regeneration properties, once implanted at the site of resected bone.

Objectives:

1) To formulate a polymeric implant with mouldable properties that will allow for patient customisation.
2) To incorporate bioglass (a bioceramic) into the polymeric implant.
3) To undertake physicochemical, physicomechanical, morphological and thermal characterisation studies on the polymeric implant for determination of key characteristics such as mechanical strength.
4) To assess the polymeric implant's suitability for localised chemotherapeutic drug delivery.
5) To evaluate the cytocompatibility by evaluating cytotoxicity of the polymeric implant utilising MG-63 cells.

1.4 Potential benefits of undertaking this research

- Patients' quality of life may be improved due to a restoration of limb function without implants or prosthesis that possess the potential for loosening and require adjustment.
- Reduced expenditure by patient and decreased health burden due to reduced hospital visits.
- Patient specific polymeric implants may be designed by utilising X-ray or CAT scans to design the mould.
- The polymeric implant may be used for application in other morbidity types that require bone regeneration.

1.5. Overview of dissertation

Chapter One of this dissertation provides a brief background about Osteosarcoma, its current treatment approaches and subsequent disadvantages. It also details the rationale and motivation by highlighting the need for research into bone regeneration platforms in the South African context and explains the aim and objectives of the study.

Chapter Two covers the approaches taken to 3D printing scaffolds for application in Bone regeneration. It details the natural and synthetic polymers utilised as well as the bioceramics researched in 3D printing scaffolds for bone tissue engineering and criticizes how applicable the current scaffolds are for application in Osteosarcoma. The need for mouldable scaffolds is also briefly mentioned.

Chapter Three discusses the preliminary approaches that were made to establish an appropriate hydrogel implant. The use of two polymers (alginate and polyacrylamide) to form a double network hydrogel implant are explained in this chapter as well the efforts to impart

appropriate porosity. Its moulding ability is also briefly illustrated. Experiments conducted in this chapter include mechanical analysis, swelling ratio % and imaging by SEM.

Chapter Four of this dissertation covers the comparison of two double network hydrogel implant formulations, one containing bioglass and the other without bioglass. The hydrogels consist of Polyacrylamide (crosslinked with MBis) and Alginate (crosslinked with $FeCl_3$). Various properties of the hydrogel implant such as physicochemical properties, mechanical strength, morphology, mouldable capabilities and biomineralization properties will be discussed in this chapter. Analysis of these properties were undertaken by various characterisation methods such as FTIR, XRD, Texture analysis, TGA and SEM. Drug release of the chemotherapeutic, doxorubicin, from both implantable hydrogels is also covered in this chapter. Chapter four also details the cytocompatibility of the hydrogel implant with cytotoxicity and cell adhesion studies.

Chapter Five of this dissertation covers the conversion of the hydrogel implant into a scaffold implant by applying lyophilisation twice. A comparison between scaffold implants with bioglass and scaffold implants without bioglass was made. Various properties of the scaffold implant such as physicochemical properties, mechanical strength, morphology is discussed in this chapter. Analysis of these properties were undertaken by various characterisation methods such as FTIR, XRD, Texture analysis, TGA and SEM. Drug release of doxorubicin, from both implantable scaffolds is also covered in this chapter.

Chapter Six provides a summary of the previously obtained results and presents the future prospects and limitations of the hydrogel implants (ALG-PAAM and BG-ALG-PAAM) as well as the scaffold implants (APDL and BGAPDL).

1.6 References

American Cancer Society (2020) *Key Statistics for Osteosarcoma*. Available at: https://www.cancer.org/cancer/osteosarcoma/about/key-statistics.html (Accessed: 10 February 2020).

Bielack, S. S. *et al.* (2016) 'Advances in the management of osteosarcoma', *F1000Research*, 5(0), pp. 1–10. doi: 10.12688/f1000research.9465.1.

Giannoudis, P. V. *et al.* (2008) 'The diamond concept - open questions', *Injury*, 39(SUPPL.2), p. S5. doi: 10.1016/S0020-1383(08)70010-X.

Giannoudis, P. V., Einhorn, T. A. and Marsh, D. (2007) 'Fracture healing: The diamond concept', *Injury*, 38(S4), pp. S3–S6. 10.1016/s0020-1383(08)70003-2.

Heck, R. K. and Toy, P. C. (2017) 'Malignant Tumors of Bone', in *Campbell's Operative Orthopaedics*. 13th edn. Philadelphia: Elsevier, pp. 945–983. Available at: https://www.clinicalkey.com/#!/content/book/3-s2.0-B9780323374620000276?scrollTo=%23hl0000691.

Howard, D. *et al.* (2008) 'Tissue engineering: Strategies, stem cells and scaffolds', *Journal of Anatomy*, 213(1), pp. 66–72. doi: 10.1111/j.1469-7580.2008.00878.x.

Jahan, K. and Tabrizian, M. (2016) 'Composite biopolymers for bone regeneration enhancement in bony defects', *Biomaterials Science*. Royal Society of Chemistry, 4(1), pp. 25–39. doi: 10.1039/c5bm00163c.

Jones, R. L. (2020) 'Malignant Tumors of Bone, Sarcomas, and Other Soft Tissue Neoplasms', in *Goldman-Cecil Medicine*. 26th edn. Elsevier, pp. 1341–1344. Available at: https://0-www-clinicalkey-com.innopac.wits.ac.za/#!/content/book/3-s2.0-B9780323532662001922?scrollTo=%23top.

Lipson, H. and Kurman, L. (2013) *Fabricated: The new world of 3D Printing*. John Wiley & Sons, Inc,1st edition 1–5.

Lisenda, L. *et al.* (2017) 'Osteosarcoma outcomes at a South African tertiary hospital', *South African Medical Journal*, 107(9), pp. 754–757. doi: 10.7196/SAMJ.2017.v107i9.11424.

Luetke, A. *et al.* (2014) 'Osteosarcoma treatment - Where do we stand? A state of the art review', *Cancer Treatment Reviews*. Elsevier Ltd, 40(4), pp. 523–532. doi: 10.1016/j.ctrv.2013.11.006.

Mabrouk, M. *et al.* (2014) 'Effect of ciprofloxacin incorporation in PVA and PVA bioactive glass composite scaffolds', *Ceramics International*. Elsevier, 40(3), pp. 4833–4845. doi:

10.1016/j.ceramint.2013.09.033.

Martin, V. and Bettencourt, A. (2018) ‘Bone regeneration: Biomaterials as local delivery systems with improved osteoinductive properties’, *Materials Science and Engineering C*. Elsevier B.V., 82, pp. 363–371. doi: 10.1016/j.msec.2017.04.038.

Moore, D. D. and Luu, H. H. (2014) ‘Osteosarcoma’, in Peabody, T. D. and Attar, S. (eds) *Orthopaedic Oncology*. Switzerland: Springer International Publishing, pp. 65–92. doi: DOI: 10.1007/978-3-319-07323-1_4,.

Oryan, A. *et al.* (2014) ‘Bone regenerative medicine: Classic options, novel strategies, and future directions’, *Journal of Orthopaedic Surgery and Research*., 9(1), pp. 1–27. doi: 10.1186/1749-799X-9-18.

Palamà, I. E. *et al.* (2017) ‘Therapeutic PCL scaffold for reparation of resected osteosarcoma defect’, *Scientific Reports*, 7(1), pp. 1–12. doi: 10.1038/s41598-017-12824-3.

Rainer, A. *et al.* (2008) ‘Fabrication of bioactive glass-ceramic foams mimicking human bone portions for regenerative medicine’, *Acta Biomaterialia*, 4(2), pp. 362–369. doi: 10.1016/j.actbio.2007.08.007.

Reith, J. D. (2018) ‘Bone and Joints’, in *Rosai and Ackerman’s Surgical Pathology*. 11th edn. Elsevier, pp. 1740–1809. Available at: https://www.clinicalkey.com/#!/content/book/3-s2.0-B9780323263399000408?scrollTo=%23top.

Sithole, M. N. (2019) *In situ conjugation-co-fabrication of bioarchetypes employing 3D print processing*. University of the Witwatersrand, South Africa.

van der Spuy, D. and Vlok, G. (2009) ‘Osteosarcoma: Pathology, staging and management’, *SA Orthopaedic Journal*, 8(3), pp. 69–78.

Tiwari, A. (2012) ‘Current concepts in surgical treatment of osteosarcoma’, *Journal of Clinical Orthopaedics and Trauma*. Elsevier, 3(1), pp. 4–9. doi: 10.1016/j.jcot.2012.04.004.

Toy, P. C. and Heck, R. K. (2017) ‘General Principles of Tumors’, in *Campbell’s Operative Orthopaedics*. 13th edn. Philadelphia: Elsevier, pp. 829–895. Available at: https://0-www-clinicalkey-com.innopac.wits.ac.za/#!/content/book/3-s2.0-B9780323374620000240?scrollTo=%23top.

Union for International Cancer Control (2014) ‘Osteosarcoma: 2014 Review of Cancer Medicines on the WHO List of Essential Medicines’, (3), pp. 1–10. Available at: http://www.who.int/selection_medicines/committees/expert/20/applications/Osteosarcoma.pdf?ua=1.

Wang, C. *et al.* (2020) ‘3D printing of bone tissue engineering scaffolds’, 5, pp. 82–91. doi: 10.1016/j.bioactmat.2020.01.004.

CHAPTER.2. LITERATURE REVIEW: THE APPLICATION OF 3D-PRINTING AND NANOTECHNOLOGY FOR THE TARGETED TREATMENT OF OSTEOSARCOMA

2.1 Introduction

Osteosarcoma is a malignant neoplasm of which there is osteoid formation by tumor cells (Heck and Toy, 2017). According to the American Cancer Society, osteosarcoma is prevalent in patients between the ages of 10 and 30. Those diagnosed with osteosarcoma over the age of 60, consist of 10% of the population afflicted (The American Cancer Society, 2020). Osteosarcoma may arise from certain predisposing factors such as Paget's disease, exposure to radiation, chemotherapy, genetics as well as foreign bodies inserted into bone such as orthopaedic implants. The majority of osteosarcomas occur in long bones, close to the joint areas (proximal areas of the humerus and tibia, and the distal areas of the femur). Osteosarcomas are less prevalent in flat bones and the spine (Reith, 2018).

Current therapy for osteosarcoma employs the administration of neoadjuvant chemotherapy followed by surgery and adjuvant chemotherapy. Adjuvant chemotherapy is utilized after surgical removal of osteosarcoma to mitigate the risk of tumor micro metastases. The most common chemotherapeutic regimen for osteosarcoma consists of methotrexate, doxorubicin and cisplatin (Chou, Geller and Gorlick, 2008; Luetke *et al.*, 2014). These chemotherapeutic agents vary in severe adverse effects, including irreversible ototoxic and nephrotoxic complications (cisplatin), myelosuppression and mucositis (methotrexate), cardiotoxicity and tissue necrosis (doxorubicin) (Toy and Heck, 2017). These adverse effects are prevalent as chemotherapeutics do not differentiate between healthy, normal cells and tumor cells. Surgery is a critical component in the treatment of osteosarcoma. The current approach to replace bone after surgery is to employ bone grafts. Bone grafts may be autogenous (from the patient's own body), homogenous (from other humans), xenografts (from other species). Each of these approaches has its own limitations, therefore research has been focused on the use of safer, more cost-effective synthetic grafts (Martin and Bettencourt, 2018).

Synthetic osteo-regenerative scaffolds should be biocompatible and have the appropriate porosity, degradability, compositional and mechanical properties to be suitable for bone regeneration as bone regeneration is a complex process as molecular, biochemical, mechanical and cellular aspects have to be considered (C. Wang *et al.*, 2020).

3D printing is an advantageous method to fabricate implantable scaffolds for bone regeneration. 3D printed scaffolds can be precisely designed to mimic bone tissue morphologically (C. Wang *et al.*, 2020) and provides control over scaffold pore shape, size

(Ghorbani *et al.*, 2020), and facilitates the incorporation of other functional agents within the scaffold (C. Wang *et al.*, 2020).

In addition, one of the strategies to target the delivery of chemotherapeutic compounds in osteosarcoma has been to employ nanocarriers. For example, targeted nanoparticles can increase the bioavailability and stability of chemotherapeutics while reducing the risks of side effects (Raj *et al.*, 2019). Selective and precise release of chemotherapeutic compounds may also be achieved by the employment of stimuli-responsive nanoparticles. In addition, nanocarriers can be designed to release chemotherapeutic drugs according to triggers such as intrinsic stimuli (S. Y. Wang *et al.*, 2020).

This review details the 3D printing and nano-enabling of synthetic and natural polymers as well as bioceramics that have been researched as potential candidates for targeted bone regeneration in Osteosarcoma. In particular, magneto- and photo-responsive scaffolds for application in osteosarcoma are discussed as well as a concise incursion into nanoparticles that have been incorporated into scaffolds for targeted bone regeneration. Nanoparticles that have the potential to be incorporated into osteo-mimetic scaffolds for localized adjuvant therapy are also elaborated on.

2.2 Fabrication of 3D-Printed Scaffolds for Enhanced Bone Regeneration

Among the techniques used to fabricate 3D printed scaffolds, extrusion printing is most popular for bone regeneration (Martínez-Vázquez *et al.*, 2015; Bendtsen, Quinnell and Wei, 2017; Fahimipour *et al.*, 2017; Pei *et al.*, 2017; H. Kim *et al.*, 2018; Luo *et al.*, 2018; Du *et al.*, 2019; Martin *et al.*, 2019). Other techniques that have been employed include Fused Deposition Modeling (FDM) (Rajzer *et al.*, 2018; Chen, Chen and Wang, 2019; Liu *et al.*, 2020), Binder Jet Printing (Sarkar and Bose, 2019), Melt Electrohydrodynamic 3D Printing (Bai *et al.*, 2020) and Selective Laser Sintering (Feng *et al.*, 2020; Shuai *et al.*, 2020).

Bone is a dynamic and complex tissue consisting of a hard matrix. Two components contribute to the matrix of bone- mineral (majority in the form of hydroxyapatite) and matrix proteins (the main protein being collagen type I). Bone consists of two types of cells- the osteoblast family and osteoclasts. The osteoblast family includes osteoblasts (which form bone by depositing mineral). Once surrounded by bony matrix the osteoblasts are referred to as osteocytes (which maintain bone). Osteoclasts resorb (remove) bone tissue. Together, these cells continuously remodel and maintain bone (White, Black and Folkens, 2012). Structurally, human bone tissue consists of cancellous and cortical bone. Cancellous bone is spongy-like with a high porosity at 50-90% and accounts for 20% of the human skeleton. Cortical bone makes up 80% of the weight of the human skeleton with a porosity of 5-10%. Cortical bone has a greater Young's modulus and compressive strength than cancellous bone (Zhang *et al.*, 2014).

Cortical bone possesses the ultimate strength of 30- 211 MPa and an elastic modulus of 16-20 GPa. Cancellous bone on the other hand has the ultimate strength of 51-193 MPa and an elastic modulus of 4.6-15 GPa (Huang, Wang and Wang, 2014). **Figure 2.1** illustrates the hierarchical structure of bone tissue.

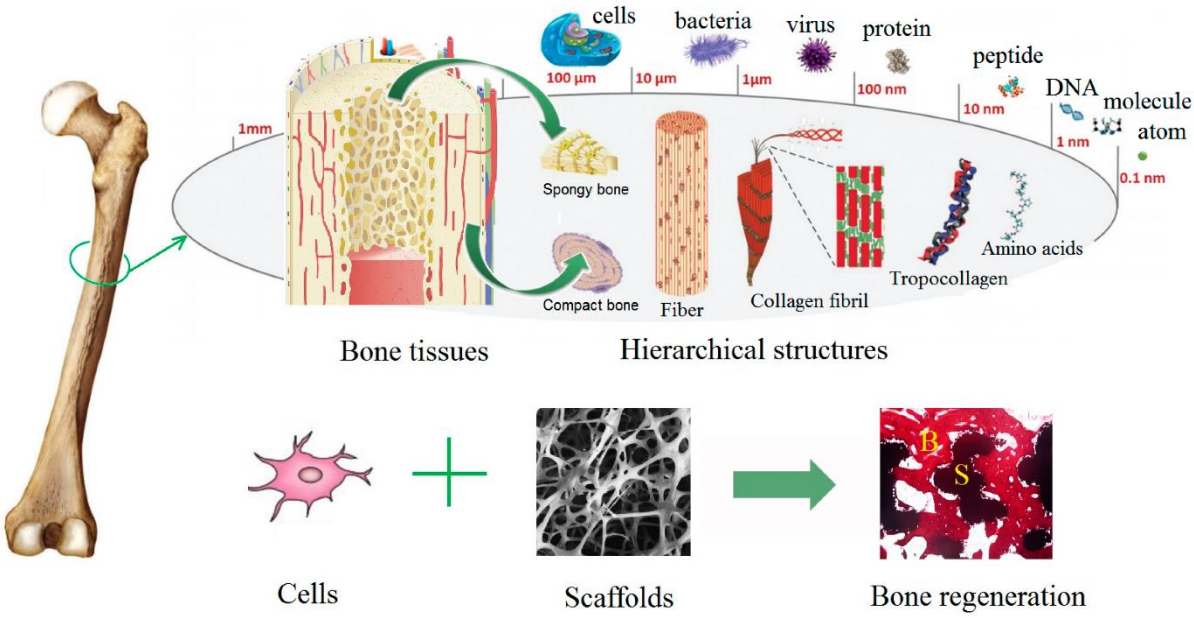


Figure 2.1: Illustration of the hierarchical structure of bone. Reproduced from X. Chen et al. 2018 under Creative Commons Attribution (CC BY) license (CC BY 4.0) (https://creativecommons.org/licenses/by/4.0/)

In general, there are five therapeutic targets that bone regeneration scaffolds aim for; 1) growth factors (osteoinduction), 2) vascularization (angiogenesis), 3) mechanical properties, 4) osteogenesis and 5) osteoconduction. These five targets form part of the “diamond concept” developed by Giannoudis et al., 2007, 2008. Scaffolds for bone regeneration should possess at least three of these five properties. (Giannoudis, Einhorn and Marsh, 2007; Giannoudis *et al.*, 2008; Jahan and Tabrizian, 2016). When a scaffold is referred to as “osteoconductive” it facilitates the ingrowth of mesenchymal stem cells (MSCs), perivascular tissue and capillaries. When a scaffold is referred to as “osteoinductive”, it facilitates the recruitment and differentiation of MSCs into osteoblasts and chondroblasts which leads to new bone formation. Osteoinduction is modulated by growth factors such as bone morphogenetic proteins (BMP) -2, -4 and -7 and vascular endothelial growth factor (VEGF). Osteogenesis is the synthesis of new bone by viable cells (Khan *et al.*, 2005; Roberts and Rosenbaum, 2012).

Several researchers have studied and reviewed the effects of porosity and pore size on angiogenesis, cell behaviour during ossification, mechanical and degradation properties and concluded that scaffold pore size and porosity may influence ossification, angiogenesis as

well as mechanical and degradation properties. Scaffolds that are microporous (100-600 μm) displayed superior vascularization and integration with the bone tissue of the host. Increased pore size increased bone ingrowth (and therefore osteoconduction). Angiogenesis was supported by triangular, rectangular and elliptic pores while mechanical strength was improved by square pores. Smaller pores, staggered orientation of pores and a gradient porosity provided greater mechanical strength (compressive modulus). Larger pore size was associated with faster degradation rates (Abbasi *et al.*, 2020). Zaharin and co-workers 3D printed titanium alloy scaffolds (Ti6Al4V) with cube and gyroid pore structures. The scaffold's pore sizes ranged between 300 to 600 μm. Interestingly, in this study, pore size was the deciding factor of whether the scaffold displayed similar properties to bone. It was concluded that scaffolds of both pore geometries showed similarity to natural bone properties at a pore size of 300 μm (Zaharin *et al.*, 2018). Pore structure and size impact the mechanical strength of scaffolds. Zhao and co-workers researched the effect of honeycomb structured pores on the mechanical strength of 3-D printed polylactic acid and photosensitive resin scaffolds. PLA scaffolds with honeycomb structure displayed a greater compressive modulus. It was also suggested that a smaller pore size be used when designing scaffolds to improve mechanical strength (Zhao *et al.*, 2018). Hence, the geometry and physical characteristics of scaffolds such as curvature, pore size and shape need to be carefully controlled to enhance mechanical strength and cellular responses for effective bone tissue regeneration.

Most polymers and bioceramics are therefore used in combination to form composite scaffolds due to individual polymers lacking the required properties for optimal bone tissue regeneration. **Table 2.1** provides a list of selected combinations of polymer-ceramic composite scaffolds that have been explored.

Table 2.1: Combinations of polymers and bioceramic composite scaffolds and their properties

Polymer/ s	Bioceramic	Drug	Properties:	Ref
Chitosan/PVA	Hydroxyapatite	BMP-2	BMP enhanced proliferation and attachment of cells Mechanical Strength- Elastic modulus of 91.14 MPa.	(Ergul *et al.*, 2019)
Alginate/Gelatin	Hydroxyapatite	-	Nanoapatite increased proliferation and osteogenic differentiation. Nanohydroxyapatite increased mechanical strength of scaffolds.	(Luo *et al.*, 2018)
Alginate	-	BFP-1	*In vitro*: Cell viability, migration, proliferation *In vivo*: accelerated bone regeneration	(Heo *et al.*, 2017)
Collagen/ decellularized extracellular matrix (dECM)/ Silk Fibroin (SF)	-	-	Collagen/dECM and Collagen/dECM/SF scaffolds displayed better cell proliferation and differentiation compared to pure collagen scaffold. Collagen/dECM/SF had better mechanical strength.	(Lee *et al.*, 2018)
Gelatin/PVA	-	-	Cell proliferation and differentiation. Mechanical Strength	(H. Kim *et al.*, 2018)
Silk Fibroin/sodium alginate	Hydroxyapatite	Bovine Serum Albumin	Cell attachment and migration. Increased SF/HA ed to increased cell proliferation.	(Huang *et al.*, 2019)

PCL	β-tricalcium phosphate	-	β-tricalcium phosphate enhanced proliferation and differentiation. Mechanical strength	(Bruyas *et al.*, 2018)
Piperazine based-polyurethane-urea	-	-	Osteoconductive Sufficient mechanical strength.	(Ma *et al.*, 2019)
PLLA/MgO/Halloysite nanotubes	-	-	Cell adhesion, proliferation, migration facilitated. Mechanical Strength	(Liu *et al.*, 2020)
PVA	Biphasic Calcium Phosphate	Platelet rich fibrin (PRF)	*In vitro*: scaffolds with PRF promoted greater cell adhesion, proliferation and differentiation. *In vivo*: scaffolds with PRF stimulated greater bone formation	(Song *et al.*, 2018)

2.2.1 Natural polymers used for 3D-printing of scaffolds in bone regeneration

2.2.1.1 3D-printed chitosan scaffolds

Chitosan is a natural biopolymer (Ahmed *et al.*, 2015; Saravanan, Leena and Selvamurugan, 2016) that can be 3D-printed with appropriate binders . Chavanne and co-workers (2013) explored various binders such as citric acid, lactic acid and acetic acid on chitosan/hydroxyapatite composites. Due to high wettability, medium viscosity and short solidification time lactic acid (40% wt.) was found to be an optimal binder (Chavanne *et al.*, 2013).

Native chitosan poses some limitations for fabricating scaffolds in bone regeneration due to its limited potential to repair bone defects. These limitations include poor antimicrobial activity, quick depolymerization that occurs *in vivo,* poor water solubility and hemo-incompatibility. Therefore, chemical modifications such as phosphorylation, carboxyalkylation, hydroxylation, quaternization, copolymerization and sulfation may be necessary (Logithkumar *et al.*, 2016) and should be considered when 3D printing chitosan scaffolds for application in bone tissue

engineering. Combining chitosan with other polymers (such as alginate and gelatin), ceramics (such as hydroxyapatite) and other materials (such as silicon dioxide) can assist with attaining the desired chemical and biological properties required for bone tissue regeneration (Saravanan, Leena and Selvamurugan, 2016).

Caballero and colleagues (2019) studied the relationship between rheology and the composition of chitosan/calcium phosphate inks. It was shown that the higher the concentration of chitosan, the greater the 3D-printability of the ink. The polymer chain entanglement was influenced by chitosan. With higher chitosan concentrations, the ink had more structure (i.e., more viscous), less Newtonian in nature and displayed increased shear thinning behavior. The calcium phosphate morphed from dicalcium phosphate dihydrate into hydroxyapatite that was mineralized in the chitosan scaffold upon printing in basic water/ethanol baths. In addition to the chitosan concentration, the properties of the inks depended on the inorganic to organic ratio. The inorganic to organic ratio influenced the ionic strength and mineral content of the inks. While chain entanglement and mineral content resulted in the ink being less Newtonian, increasing the ionic strength made the ink more Newtonian. The chitosan/calcium phosphate inks were used to fabricate 3D printed scaffolds by robocasting. (Caballero *et al.*, 2019).

In another study, chitosan and chitosan/hydroxyapatite hydrogels laden with MC3T3-E1 pre-osteoblast cells were compared with alginate and alginate/hydroxyapatite hydrogels. In terms of cell differentiation and proliferation, chitosan was regarded to be superior compared with alginate. These hydrogels were printed by an extrusion based printer. (Demirtaş, Irmak and Gümüşderelioğlu, 2017).

2.2.1.2 3D- printed alginate scaffolds

Alginate is a biopolymer derived from brown algae (Venkatesan *et al.*, 2015) and may require further purification for application in bone regeneration applications(Torres *et al.*, 2019). Alginates form hydrogels by ionic crosslinking with divalent cations and can be used as bioinks to form 3D-printed scaffolds (Hernández-González, Téllez-Jurado and Rodríguez-Lorenzo, 2020). Typically, alginate is deficient in biological properties that can precipitate bone formation (Park *et al.*, 2018), neither does it have sufficient mechanical strength (Venkatesan *et al.*, 2015). However, alginates have been still used in bone regeneration as they are suitable vehicles for the delivery of peptides such as BFP-1 (Heo *et al.*, 2017). Introducing sulfate groups to alginate in bio-inks for 3D printing has shown to prolong BMP-2 activity (Park *et al.*, 2018). To overcome the lack of mechanical properties, alginate may be used in combination with other natural or synthetic osteo-compatible biopolymers used in bone regeneration (Venkatesan *et al.*, 2015).

Bendsten and co-workers (2017) studied various concentrations of 3D printable hydrogels comprising alginate, polyvinyl alcohol (PVA) and hydroxyapatite. Two hydrogels had optimized printing quality. Among the two optimized hydrogels, the hydrogel constituting 2.5% alginate, 0.15% Na_2HPO_4, 0.20% $CaSO_4$, 2.5% hydroxyapatite and 0.72% NaCl possessed the optimal 3D-printing quality when developed with cell culture media. The presence of PVA and hydroxyapatite within the alginate hydrogel contributed significantly towards the printability, viscosity and cell viability. These hydrogels were fabricated by extrusion printing. (Bendtsen, Quinnell and Wei, 2017). In addition, Luo and colleagues (2017) fabricated 13-93 bioactive glass/alginate scaffolds composed of different mass ratios by extrusion printing. The mass ratios of 13-93 bioactive glass: alginate were 4: 4, 2: 4, 1: 4 and 0: 4. When compared to the pure alginate scaffold, the scaffolds that contained 13-93 bioactive glass had increased apatite mineralization and improved mechanical strength. The presence of bioactive glass within the scaffold also improved scaffold porosity and pore size. Optimal mechanical strength, and the highest proliferation and attachment of rat bone mesenchymal stem cells (rBMSCs) was found in the scaffold consisting of mass ratio 2: 4 (Luo *et al.*, 2017). These are classical examples of combining alginate with biomaterials having superior mechanical strength to render alginate suitable for the fabrication of 3D-printed bone regenerative scaffolds. However, based on the values provided above for cortical and cancellous bone regeneration, further improvements have to be made to enhance the mechanical strength of alginate scaffolds to facilitate implantation at load-bearing sites.

2.2.1.3 3D printed collagen scaffolds

Collagen (type I) is secreted by osteoblasts and is the most abundant type of collagen found in the extracellular matrix (ECM) of bone (Boskey, 2003; Ferreira *et al.*, 2012). Collagen is osteoconductive, has weak antigenicity (Ferreira *et al.*, 2012; Zhang *et al.*, 2018) and is the most abundant organic component of bone; therefore it serves as an excellent mineralization template. Collagen also provides a surface for cell adhesion (Zhang *et al.*, 2018). However, native collagen is deficient in mechanical strength And therefore may be combined with other biopolymers to increase the mechanical strength and achieve enhanced cellular activity (Lee *et al.*, 2018). In a study by Montalbano and co-workers (2018), 3D-printed scaffolds fabricated from collagen Type I (with bioactive components such as mesoporous bioactive glass containing strontium) were combined to form a hybrid system. Interestingly, the results of the bioactivity studies displayed that the bioactivity of the constructs may be enhanced due to the acidic groups of the collagen fibers providing increased sites for hydroxyapatite nucleation (Montalbano *et al.*, 2018).

Lin et al. (2016) fabricated chemical and solvent-free collagen/hydroxyapatite scaffolds by robocasting. The hydroxyapatite powder used measured <100nm in particle size. Optimal printing parameters were established as rods of 600 ųm in diameter for moderate mechanical strength and bone regeneration outcomes. Non-printed scaffolds were compared to 3D printed scaffolds. Non-Printed scaffolds were prepared by filling molds with ink utilized for the 3D printed scaffolds. The molds matched the dimensions and shape of the 3D printed scaffolds. The ink filled molds were then lyophilized to form non-printed scaffolds. The results displayed that when compared *in vitro*, 3D printed scaffolds improved cell proliferation and differentiation. When compared *in vivo* the 3D printed scaffolds facilitated cell migration, osteogenesis and enhanced repair. However, despite possessing moderate mechanical strength, the scaffolds were still deemed as suitable for application only in bone defects with low load-bearing capacity or cancellous bone (Lin *et al.*, 2016). This may not be suitable for application in post-surgical resection of osteosarcoma of the tibia or femur due to the load-bearing nature of the bone.

A collagen-based scaffold by use of indirect 3D printing was developed by Sachlos and co-workers (2006). Nano-sized carbonate substituted hydroxyapatite crystals with dimensions of approximately 180x80x20 nm were precipitated within collagen fibers. This was achieved by enlisting a biomimetic precipitation technique. A calcium chloride solution served as the source of calcium while potassium dihydrogen phosphate served as the phosphate source. These two solutions were separated by a collagen membrane and precipitated within the membrane as carbonate substituted hydroxyapatite crystals. The collagen membranes were air-dried after precipitation was allowed to occur, then shredded into flakes and mixed in a collagen dispersion. This mixture was then cast into 3D printed molds that were fabricated by hot-melt inkjet printing. The mold could facilitate the formation of microchannels that would permit the perfusion of the scaffold. However, appropriate mechanical testing, *in vitro* cell studies and *in vivo* experiments were not conducted (Sachlos *et al.*, 2006). Appropriate testing will have to be conducted to prove that this scaffold meets at least 3 of the 5 criteria mentioned in the diamond concept and will have to prove sufficient mechanical strength if scaffolds of this nature is to be considered for application of post-surgical resection of osteosarcoma.

2.2.1.4 3D printed gelatin scaffolds

Gelatin is a derivative of collagen synthesized by partial acid (type A) or alkaline (type B) hydrolysis from animal collagen. (Djagny, Wang and Xu, 2001; Hoque *et al.*, 2015). Type A gelatin can be employed as a vehicle for acidic proteins *in vivo*, while type B has been used for the prolonged release of basic molecules (Echave *et al.*, 2017). To improve the thermal and mechanical properties of gelatin for *in vivo* applications, crosslinking of gelatin is

necessary (Yang *et al.*, 2016). Compared to collagen, gelatin displays lower immunogenicity (Santoro, Tatara and Mikos, 2014; Echave *et al.*, 2017) and has several positive traits such as elasticity and cell-adherence due to the RGD sequences present in its primary structure (Su and Wang, 2015). When gelatin is extracted at a reduced temperature, greater mechanical strength is obtained but not sufficient for application in bone tissue engineering or regeneration (Usta *et al.*, 2003; Kuttappan, Mathew and Nair, 2016).

To overcome this, Kim H. and co-workers (2018) fabricated combined gelatin/PVA scaffolds by extrusion printing using different gelatin: PVA ratios. The pure gelatin scaffold displayed exceptional protein and water absorption capabilities and the optimal gelatin: PVA ratio for cell differentiation, cell proliferation and mechanical strength was established to be 5:5 (H. Kim *et al.*, 2018). Hydroxyapatite/gelatin scaffolds were also fabricated by extrusion printing by Martinez-Vazquez and colleagues (2015). In their study, hydroxyapatite was doped with silicone and the average size of the hydroxyapatite-silicone crystals was 35 ± 5 nm. The presence of gelatin within the scaffold resulted in an increase in cell differentiation when compared to pure ceramic scaffolds. The mechanical characteristics of the scaffolds were similar to trabecular bone tissue (Martínez-Vázquez *et al.*, 2015) and thus may not be suitable for application in post-surgical resection of osteosarcoma in load-bearing bones.

In another study by Celikkin and co-workers (2019), 3D-printed gelatin methacrylate hydrogel scaffolds containing gold nanoparticles (AuNP) were fabricated by extrusion printing. AuNPs were included to enhance Computed Tomography (CT) imaging. The study also researched the impact of different AuNP sizes and concentrations on scaffold cytocompatibility and mechanical properties. The optimal hydrogel formulation was determined to contain AuNPs of 60 nm in size and 0.16 mM concentration. This formulation was then utilized to fabricate 3D printed scaffolds to assess the behavior of Mesenchymal stem cells. Cell studies indicated that both gelatin methacrylate scaffolds with and without AuNPs successfully facilitated osteogenic differentiation. The scaffolds containing AuNPs also enhanced μCT imaging (Celikkin *et al.*, 2019). The inclusion of AuNPs to enhance CT imaging may be of advantage in monitoring the bone regeneration and healing process after scaffold implantation into the resected tumor site.

2.2.1.5 3D printed silk fibroin scaffolds

Silk is a proteinaceous biopolymer (Melke *et al.*, 2016; Bhattacharjee *et al.*, 2017; Ma, Wang and Dai, 2018) commercially available from two families of silk worms. Silk fibroin from the tropical tasar silkworm possesses the RGD peptide sequence that facilitates superior cell adhesion (Datta, Ghosh and Kundu, 2001; Bhattacharjee *et al.*, 2017). In bone regeneration silk protein is advantageous in that it possesses mechanical strength and biodegradability.

Silk fibroin systems have slow degradation while maintaining their load-bearing capacity (Ma, Wang and Dai, 2018). Mulberry silk in particular has a Young's Modulus of 12.4–17.9 GPa. (Pérez-Rigueiro *et al.*, 2001; Melke *et al.*, 2016). However, these mechanical characteristics cannot be compared to silk fibroin processed into scaffolds as their mechanical characteristics will differ depending on the process parameters used to form the scaffold (e.g. matrix stiffness, processing techniques and composition) (Melke *et al.*, 2016).

A study by Huang and co-workers (2019) researched combined 3D printed silk fibroin/hydroxyapatite scaffolds. Silk fibroin/hydroxyapatite nanocomposites of <100 nm in width were prepared by co-precipitation. The nanocomposites were combined with sodium alginate to form a bio-ink and were 3D printed by extrusion. The mechanical strength of the 3D printed silk fibroin/hydroxyapatite scaffolds demonstrated that they were suitable for trabecular bone applications. However, when compared to hydroxyapatite/sodium alginate scaffolds, scaffolds containing increased amounts of silk fibroin/hydroxyapatite nanocomposites displayed poorer mechanical strength. The scaffolds with higher silk fibroin/hydroxyapatite facilitated greater cell proliferation and osteogenic differentiation. (Huang *et al.*, 2019).

In a study employing pure collagen, collagen/decellularized ECM and collagen/dCEM/silk fibroin scaffolds, the 3D printed scaffolds with silk fibroin displayed the most potential for bone regeneration due to superior mechanical properties, increased cell viability and increased preosteoblast cell deposition of calcium (Lee *et al.*, 2018). However, the mechanical strength of these scaffolds may not be suitable for application in post-surgical resection of osteosarcoma at load-bearing sites.

2.2.2 Synthetic polymers used for 3D-printing of scaffolds in bone regeneration

2.2.2.1 3D printed polycaprolactone scaffolds

Polycaprolactone (PCL) is a semi-crystalline polymer that is suitable in bone tissue engineering due to its prolonged biodegradation rate (2-3years)(Dwivedi *et al.*, 2020). Although not osteoconductive, PCL may be modified to obtain osteoconductivity and osteoinductivity, for example, by incorporation of growth factors (Mantila Roosa *et al.*, 2010). 3D printed PCL scaffolds are available as bioresorbable implants used in craniofacial surgery(Prasadh and Wong 2018). The mechanical properties and osteoinductivity of PCL can be improved by the addition of β-tricalcium phosphate. Bruyas et al. (2018) observed that the concentration of β-tricalcium phosphate influenced the mechanical properties of the scaffolds fabricated by FDM. PCL scaffolds containing 0, 20, 40, and 60 wt.% β-tricalcium phosphate displayed a Young's Modulus of 264, 355, 495, and 1140 MPa, respectively. Furthermore, by adjusting the β-tricalcium phosphate concentration, the biodegradation ratio can be optimized

(Bruyas *et al.*, 2018). The mechanical strength and osteoconductivity of these scaffolds make it a potential candidate for application in post-surgical resection of osteosarcoma, however, at least one other criteria of the diamond concept has to first be observed.

Heo and co-workers (2019) developed 3D printed PCL scaffolds coated in fish bone extract. The scaffolds were first fabricated by extrusion of melted PCL pellets then soaked in 1 wt% and 3 wt% fish bone extract solutions. Native PCL scaffolds, as well as scaffolds coated with fish bone extract, exhibited similar mechanical properties suitable for bone regeneration. Scaffolds coated in fishbone extract had increased cell proliferation, calcium and phosphorous deposition and osteoblast differentiation (Heo *et al.*, 2019).

Kim J-Y and colleagues (2018) researched the fabrication of 3D printed PCL scaffolds incorporated with β-tricalcium phosphate and bone-derived decellularized ECM (bone dECM) derived from porcine. The PCL and PCL-β-tricalcium phosphate scaffolds were first fabricated by extrusion printing at 120°C and then immersed in bone dECM solution followed by incubation and lyophilization. *In vitro* studies conducted with the 3D printed scaffolds coated in bone dECM demonstrated excellent cell seeding, proliferation and differentiation. *In vivo* studies demonstrated that scaffolds decorated with bone dECM displayed bone tissue growth within the scaffold. 3D printed scaffolds without bone dECM only had bone tissue growth on the edges of the scaffolds whereas those with bone dECM displayed greater mineralization and osteoid formation. The scaffolds also mimicked the mechanical properties of human cancellous bone (J. Y. Kim *et al.*, 2018).

In another study, 3D printed PCL scaffolds were fabricated by FDM into different geometries namely, honeycomb, gyroid and mesh structures. These 3D printed scaffolds were then loaded with hydrogels formulated from alginate and gelatin and the hydrogel retention capabilities of the different scaffold structures were researched. The gyroid structured 3D printed PCL scaffold retained the most hydrogel and was selected for further research. Apatite formation increased within the hydrogel, whereas smaller apatite formation was noted on PCL surfaces, which reduced over time due to dissolution. The PCL-gel scaffold displayed cytocompatibility, adhesion and viability of cells (Hernandez, Kumar and Joddar, 2017).

2.2.2.2 3D printed polyurethane scaffolds

Polyurethanes are biopolymers that comprise hard segments formed by the reaction between a chain extender and a diisocyanate; and the soft segments are formed from olygodiols and diisocyanates (Marzec *et al.*, 2017). The properties of polyurethanes are influenced by its hard-soft segment ratio. One study indicated that as the ratio of hard segments increased, the hydrophilicity of the polyurethane surface increased as well as cell proliferation of human

bone-derived cells. However, an increase in hard segments of polyurethane decreased the osteogenic potential (Bil *et al.*, 2009). The properties of polyurethanes can be tailored by manipulation of chemical composition and synthesis technology and parameters. Polyurethanes are non-toxic, promote calcification *in vivo*, possess mechanical and physicochemical flexibility and are biocompatible. Their properties can range from thermoplastic to thermosetting and can be hydrophilic or hydrophobic. Polyurethanes implanted *in vivo* have supported bone regeneration. Polyurethanes can serve as bone void fillers, shape memory scaffolds and drug carriers (Marzec *et al.*, 2017).

Ma et al. (2019) showed that piperazine can regulate the osteogenesis of osteoblasts in a dose-dependent manner, and may enhance the osteoconductivity of 3D printed piperazine-based polyurethane-urea scaffolds. These scaffolds were 3D printed by extrusion printing. The optimal concentration of piperazine was determined to be ~0.5 mM (Ma *et al.*, 2019).

Wang and co-workers (2018) fabricated biodegradable shape memory polyurethane 3D printed scaffolds by low temperature fused deposition modeling. The soft segments of the polyurethane were formed by PCL diol and PLLA diol. The hard segments were formed from 2,2-bis(hydroxymethyl)propionic acid and ethylenediamine as chain extenders and isophorone diisocyanate. Superparamagnetic iron oxide nanoparticles were incorporated into the polyurethane ink to facilitate shape fixity and osteoinduction. To impart printability, the bio-inks were combined with either gelatin or polyethylene oxide (PEO). They concluded that the presence of superparamagnetic iron oxide nanoparticles promoted osteogenesis and enhanced shape fixity by promoting crystallinity of the PCL and PLLA. Scaffolds containing gelatin had superior cell viability while scaffolds containing PEO had enhanced shape memory capabilities (Wang, Jeng and Hsu, 2018).

2.2.2.3 3D printed poly (lactic acid) scaffolds

Poly (lactic acid) (PLA) is a thermoplastic biopolymer with properties affected by its stereochemistry. Poly (L-lactic acid) (PLLA) and poly (D- lactic acid) (PDLA) are both semi-crystalline in nature, however, when combined to form poly (D, L-lactic acid), an amorphous polymer is produced. Both PLLA and PDLA have desirable mechanical strength (Narayanan *et al.*, 2016). Due to its hydrophobicity, PLA has slow biodegradation rates but also decreased cell adhesion. It may stimulate inflammatory reactions due to lactic acid build-up upon biodegradation. These limitations may be mitigated by including buffers in the scaffold matrix to counter lactic acid formation and inclusion of other bioactive material to increase cell adhesion and osteoconductivity (Tajbakhsh and Hajiali, 2017). To improve the mechanical strength of PLA, buffering of the lactic acid biodegradation products to improve the osteogenic activity of PLLA, the incorporation of MgO and halloysite nanotubes have been explored.

Halloysite nanotubes increased scaffold strength while MgO promoted cell adhesion, proliferation and differentiation. (Liu *et al.*, 2020).

In another study by Mondal and co-workers (2020), PLA scaffolds were 3D printed by FDM and modified with hydroxyapatite nanoparticles post-fabrication. The 3D printed scaffolds were immersed in a hydroxyapatite mixture and sonicated followed by drying. The average size of the hydroxyapatite nanoparticles was 36 ±4 nm. The scaffolds were printed at varying orientations of 0°, 45° and 90°. Scaffolds printed at 90° displayed the highest compressive strength. 3D printed scaffolds modified with hydroxyapatite nanoparticles displayed greater mechanical strength as compared to scaffolds without hydroxyapatite nanoparticles, regardless of printing orientations. In addition, the scaffolds modified with hydroxyapatite nanoparticles displayed greater cell adhesion and proliferation (Mondal *et al.*, 2020).

An interesting combination of scaffold fabrication techniques was used to fabricate gelatin/PLLA hybrid layered scaffolds for application in subchondral bone and nasal cartilage reconstruction. FDM was utilized to 3D print a porous PLLA layer of the scaffold, while electrospinning was utilized to develop a gelatin nanofibrous top layer. A bioactive powder (Osteogenon) was incorporated into the gelatin solutions. The layered scaffolds were formed by electrospinning the gelatin solutions directly onto the 3D printed PLLA scaffolds (Rajzer *et al.*, 2018). These scaffolds may have been designed for application in subchondral bone and nasal cartilage reconstruction, however, the combination of scaffold fabrication techniques may be useful in fabricating scaffolds for application in osteosarcoma. Perhaps due to technology constraints, if only certain biomaterials can be 3D printed, other biomaterials can be added to the 3D printed scaffold by other scaffold fabrication techniques.

In one study, 3D printed PLA scaffolds with different pore sizes of 0.50 mm, 1.00 mm and 1.25 mm were fabricated. Increased cell proliferation was noticed on scaffolds with pore size of 1.25 mm when compared to scaffolds with pore size of 1 mm. Mechanical testing was conducted on bovine bones and compared to mechanical characteristics of the scaffolds. Although the scaffolds displayed lower modulus values compared to bovine bone, it was concluded that the scaffolds could still have the potential to be utilized for bone repair. The reason provided was that during *in vivo* implantation, cells that infiltrate the scaffold would be able to produce extracellular matrix which would aid in mechanical strength (Velioglu *et al.*, 2019).

2.2.2.4 3D printed polyvinyl alcohol scaffolds

Polyvinyl alcohol (PVA) is a water-soluble polymer that imbues scaffolds with strength and flexibility (H. Kim *et al.*, 2018; Song *et al.*, 2018). PVA has also been used in 3D printed

scaffolds to enhance the viscosity of hydrogels, increase biocompatibility and osteoconductivity (Bendtsen, Quinnell and Wei, 2017). In a study by Kim and co-workers (2018), PVA was utilized to impart mechanical properties to the scaffold. Native PVA scaffolds displayed the greatest mechanical strength as compared to the other scaffolds (H. Kim *et al.*, 2018).

Chen et al. (2019) developed 3D printed PVA/β-tricalcium phosphate scaffolds by FDM. PVA/β-tricalcium phosphate composites were first synthesized with β-tricalcium phosphate concentrations ranging from 5-20%. These composites were then mixed with co-plasticizers and extruded into filaments. It was noted that an increase in β-tricalcium phosphate concentration led to an increase in mechanical strength and cell proliferation (Chen, Chen and Wang, 2019).

In a study conducted by Feng and colleagues (2020), polyetheretherketone (PEEK) was combined with PVA to form composite scaffolds by selective laser sintering. Graphene oxide (GO) was added to the combination to enhance interfacial bonding between polar PVA and non-polar PEEK. Different ratios of GO 0, 0.5, 1, 1.5 and 2 wt% loaded within the PEEK/PVA composites were researched. The scaffolds with 1 wt% of GO possessed optimal mechanical properties and was selected for further study. 3D printed PEEK/PVA scaffolds with 1 wt% GO displayed greater cell proliferation and differentiation *in vitro* compared to PEEK/PVA scaffolds. *In vivo* research demonstrated that PEEK/PVA scaffolds with 1 wt% GO did not just promote new bone formation but could accelerate it (Feng *et al.*, 2020).

The mechanical strength in these scaffolds may not be suitable for application in post-surgical resection of osteosarcoma at load-bearing sites. More research is required to impart sufficient mechanical strength to PVA scaffolds for it to be considered for application in osteosarcoma.

2.2.3 Bioceramics used for 3D-printing of scaffolds in bone regeneration

2.2.3.1 3D printed calcium phosphate scaffolds

Calcium phosphates are a group of bioceramics that includes hydroxyapatite, biphasic calcium phosphate and tricalcium phosphate. Calcium phosphate ceramics are not osteoinductive in solid and non-porous forms but may be rendered osteoinductive by employing surface modification strategies such as forming macroscopic and microscopic pores, ensuring appropriate scaffold roughness and surface morphology (Samavedi, Whittington and Goldstein, 2013). The osteoinductivity of calcium phosphates is also dependent on surface charge and chemistry of calcium phosphates (Samavedi, Whittington and Goldstein, 2013; Xiao *et al.*, 2020). Phosphate bioceramics are also bioresorbable (Wei *et al.*, 2009; Venkatraman and Swamiappan, 2020).

3D printed β-Tricalcium phosphate (β-TCP) scaffolds lack mechanical strength. To enhance mechanical strength, microwave sintering of these scaffolds has been explored. Microwave sintering increased densification of the 3D printed scaffolds thereby increasing the strength of the 3D printed β-TCP scaffolds (Tarafder *et al.*, 2013).

The weight % of bioceramics present in a scaffold may also need to be optimized. Ergul et al. (2019) researched various ratios of hydroxyapatite (2.5, 5, 10, and 15 wt%) in 3D printed chitosan/PVA scaffolds. Chitosan and PVA mixtures were first blended followed by the addition of hydroxyapatite solution to obtain the hydrogel. The chitosan/PVA scaffold containing 15% weight of hydroxyapatite displayed superior results in printing quality (Ergul *et al.*, 2019).

Coating a scaffold with nanohydroxyapatite may also lead to an increase in scaffold mechanical strength. Luo et al. fabricated alginate/gelatin scaffolds with nanohydroxyapatite. It was determined that the scaffolds coted in nanohydroxyapatite displayed Young's modulus that was twice that of the scaffolds without the coating. In addition, the presence of the nanohydroxyapatite coating contributed to greater cell proliferation, protein adsorption and osteogenic differentiation (Luo *et al.*, 2018). However, despite the increase in Young's modulus of the scaffold, the mechanical strength of the scaffold may not be suitable for application in post-surgical resection of osteosarcoma at load-bearing sites.

2.2.3.2 3D printed calcium silicates

Calcium silicate bioceramics have superior mechanical properties compared with calcium phosphate bioceramics. Apatite deposition is induced by the silicon-rich layer present on the bioceramic surface. Silicate bioceramics are bioactive- they have excellent interfacial bonding with natural tissue (Wei *et al.*, 2009; Venkatraman and Swamiappan, 2020). Examples of calcium silicates include: α'_L-dicalcium silicate (Ca_2SiO_4), wollastonite ($CaSiO_3$) and larnite (β-Ca_2SiO_4), diopside ($CaMgSi_2O_6$) and hatrurite (Ca_3SiO_5) (Ribas *et al.*, 2019; Venkatraman and Swamiappan, 2020). The biological and physicochemical properties of 3D printed calcium silicate scaffolds may be improved by the addition of compounds such as CeO_2. When compared to ordinary 3D printed mesoporous calcium silicate scaffolds, 3D printed calcium silicate scaffolds incorporated with CeO_2 displayed enhanced osteoinduction markers as well as enhanced vascularization markers (Zhu *et al.*, 2016).

To improve the mechanical strength of calcium silicate scaffolds, calcium sulfate was incorporated into mesoporous calcium silicate scaffolds. Calcium sulfate hemi-hydrate was incorporated into mesoporous calcium silicate powder by being ground followed by passing through a mesh sieve. The powders were then incorporated into a PCL solution for 3D printing

by extrusion followed by hydration process. Calcium silicate scaffolds incorporated with calcium sulfate displayed greater mechanical strength. Despite pure mesoporous calcium silicate scaffolds displaying slightly higher cell viability, there were no significant differences between cell adhesion and proliferation between scaffolds with and without calcium sulfate. The composite scaffolds also facilitated the sustained drug release of dexamethasone (Pei *et al.*, 2017).

In another study, 3D printed calcium silicate scaffolds incorporated with strontium were developed. Calcium silicate powder and strontium doped calcium silicate powders were mixed with ethanol and added to melted PCL for 3D printing by extrusion. 3D printed calcium silicate scaffolds containing strontium displayed a 2-fold increase in mechanical strength. *In vitro* studies demonstrated the osteoinductive ability of calcium silicate scaffolds containing strontium. In vivo studies demonstrated the capability of the scaffolds containing strontium to promote angiogenesis and osteogenesis (Chiu *et al.*, 2019).

2.2.3.3 3D printed bioactive glasses in bone regeneration

Bioactive glasses may be grouped into silicate-based bioactive glasses, phosphate-based bioactive glasses, borate based bioactive glasses and black glass (Baino, 2018). The most recent generation of bioactive glasses to be developed has been mesoporous bioactive glasses (MBG) by Yan et al. (Yan *et al.*, 2004). Bioglasses are osteoconductive and osteoproductive (Rainer *et al.*, 2008).

In a study by Wu and co-workers (2011), MBG was combined with PVA as a binder for 3D printing. By combining MBG with PVA, the 3D printed scaffolds' toughness was improved and was less brittle. The scaffolds displayed increased mechanical strength as compared to other inorganic scaffolds fabricated by traditional methods and had 200 times the strength of MBG scaffolds prepared by polyurethane foam templating. The MBG scaffolds also displayed the potential to be utilized for sustained drug release. It was noted that cell proliferation was lower on MGB scaffolds but Alkaline phosphatase activity was higher when compared to control scaffolds (Wu *et al.*, 2011).

In another study, MBG scaffolds were 3D printed by extrusion and also utilized PVA as a binder. However, research was conducted on the removal of PVA post scaffold fabrication to prevent the reduction of MBG's osteogenic potential due to the presence of PVA. The removal of PVA was accomplished by immersion of MBG scaffolds in phosphate-buffered saline solution. This resulted in a biomimetic mineralized layer forming on the surface of the scaffolds as well as throughout the scaffolds. 3D printed scaffolds that underwent immersion displayed

an increase in osteogenic related genes and have the potential to accelerate new bone formation (Gómez-Cerezo *et al.*, 2020).

2.2.4 Comparison Between Different Scaffold Compositions

Different bioceramics possess different bone regeneration mechanisms. Therefore, it becomes necessary to develop and compare scaffolds with different bioceramic compositions. Alksne et al. 3D printed PLA/hydroxyapatite and PLA/bioglass composite scaffolds using the FDM technique for comparison of bone regeneration *in vitro*. It was concluded that the PLA/bioglass composite possessed superior osteoinductivity than the PLA/hydroxyapatite scaffolds (Alksne *et al.*, 2020). Feng et al. 3D printed (by extrusion) and compared mesoporous calcium silicate/PCL and mesoporous bioactive glass/PCL scaffolds *in vitro*. The mesoporous bioactive glass/PCL scaffold proved to be superior. By employing 3D printing, an advantage was provided. The comparison of osteogenic properties between the scaffolds were eliminated as highly similar inter-structural and mechanical characteristics were ensured by 3D printing (X. Feng *et al.*, 2019). These studies prompt further research on comparison between scaffolds *in vivo.*

Anbu et al. compared the bone regeneration ability between grafts formed from powdered PLA, 3D printed PLA and commercially available hydroxyapatite–β-tricalcium phosphate. There was bone formation with all three polymers. In the fourth week, the PLA based grafts induced shallow bone formation as compared to the commercially available product. Interestingly, the 3D printed PLA graft was not rejected by healthy living bone- new bone surrounding the graft was observed (Anbu *et al.*, 2019).

These studies prompt more research comparing various composite scaffolds *in vitro* and *in vivo* to determine the superior and optimal 3D printed composite scaffold combinations. Research on scaffolds for application in osteosarcoma should not just focus on osteogenic properties of the scaffolds but rather should strive to incorporate angiogenesis, mechanical strength, osteoconductivity, osteoinductivity and osteogenesis.

Du et al. fabricated and compared 3D printed MBG/SF scaffolds and 3D printed MBG/ PCL scaffolds. It was determined that when compared to MBG/PCL scaffolds, the MBG/SF scaffolds had lower degradation ratios, greater mechanical strength, greater *in vitro and in vivo* osteogenic capabilities (Du *et al.*, 2019). **Table 2.2** summarizes the scaffold composition comparisons and their outcomes.

Table 2.2: A summary of the different studies comparing different scaffold compositions and their bone regeneration outcomes

Scaffold Compositions that were compared	Study conducted *in vitro*/ *in vivo*	Outcome	Reference
PLA/hydroxyapatite vs PLA/bioglass	In vitro	PLA/bioglass scaffolds displayed superior osteoinductive properties.	(Alksne *et al.*, 2020)
Mesoporous calcium silicate/PCL Vs Mesoporous bioglass/PCL	In vitro	Mesoporous bioglass/PCL scaffolds displayed superior osteogenic-related gene expressions.	(X. Feng *et al.*, 2019)
commercially available hydroxyapatite–β-tricalcium phosphate vs powdered PLA vs 3D printed PLA	In vivo	Bone formation was noted with all 3 groups. However, a significant difference was noted between 3D printed PLA scaffolds and the powdered formulations.	(Anbu *et al.*, 2019)
Mesoporous bioactive glass/SF Vs Mesoporous bioactive glass/PCL	In vitro and in vivo	MBG/SF scaffolds had lower degradation ratios, greater mechanical strength, greater *in vitro and in vivo* osteogenic capabilities	(Du *et al.*, 2019)

2.3 Stimuli-Responsive Scaffolds in Bone Regeneration

Addressing bone defects induced by surgical resection in osteosarcoma may not be sufficient. There is still a risk of residual tumor cells remaining that may result in the recurrences of osteosarcoma. To address this, Fu et al. 3D printed a bioceramic free carbon-embedding larnite (larnite/C). This was achieved by mixing and 3D printing siliesquioxane silicone and a $CaCO_3$ filler then placing the printed scaffolds under argon atmosphere to undergo ceramic transformation to form larnite/C. The purpose of the free carbon was to facilitate a photothermal effect when stimulated by a NIR laser. The scaffold could successfully destroy human osteosarcoma cells, hindered tumor growth in nude mice and promoted new bone

formation *in vivo*. The scaffolds could facilitate the expression of rat bone mesenchymal stem cells *in vitro* (Fu *et al.*, 2020). **Figure 2.2** depicts the concept of NIR laser used to produce photothermal effects in tumor cells.

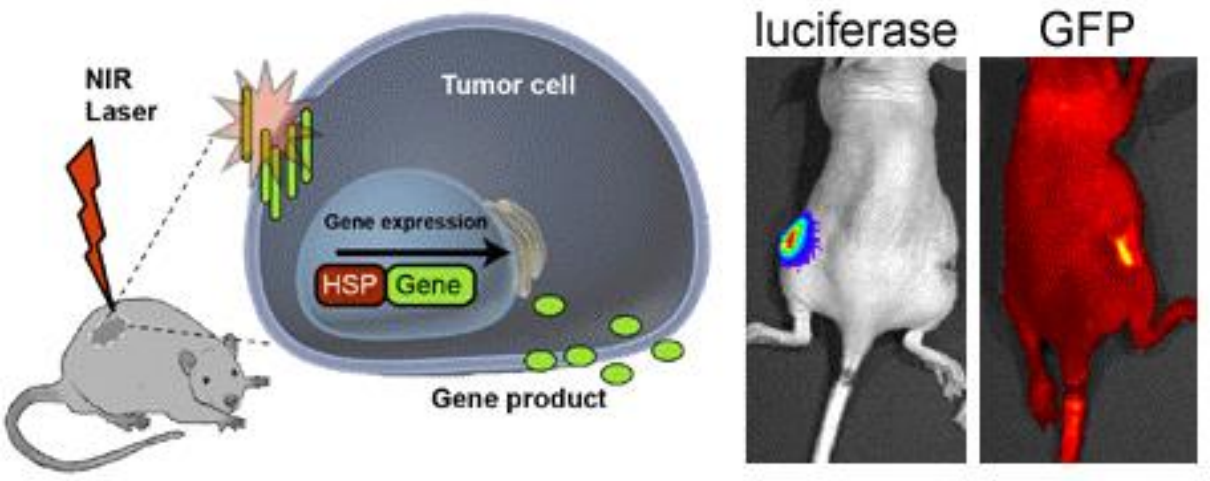


Figure 2.2: Schematic depicting the use of NIR laser to trigger photothermal effects in tumor cells. HSP- Heat shock protein. Reproduced from Andersson et al. 2014 under Creative Commons Attribution license (CC BY-NC-SA 3.0)) ((http://creativecommons.org/licenses/by/3.0/)

Other carbon sources such as graphene oxide may also imbue scaffolds with photothermal conversion properties. Ma et al. developed graphene oxide (GO)-modified β-tricalcium phosphate (GO-TCP) composite scaffolds that displayed photothermal effects even at a low power density of 0.36 W cm^{-2}. The photothermal effects induces significant MG-63 osteosarcoma cell death *in vitro* and inhibited mice tumor growth. The photothermal temperature of the scaffolds could be modulated by adjusting the concentrations of GO, NIR power densities and surface modification times. Furthermore, the GO-TCP scaffolds displayed better osteogenic differentiation and new bone formation than the plain β-TCP scaffolds (Ma *et al.*, 2016).

Other compounds that have been used in bioceramic scaffolds to imbue scaffolds with photothermal conversion capabilities led to scaffolds with successful photothermal effects and bone regenerating potential. These include, MoS_2 (H. Wang *et al.*, 2020); Fe and Mn (Liu *et al.*, 2018) and $CuFeSe_2$ nanocrystals (Dang *et al.*, 2018). 3D printed Fe-$CaSiO_3$ composite scaffolds were developed and not only displayed anticancer properties due to photothermal ablation but also due to the generation of ROS. The photothermal effect, as well as ROS, had synergistic effects *in vivo* and *in vitro*. The scaffolds also displayed high compressive strength

that is suitable for mechanical support in cortical bone defect and displayed bone regeneration potential *in vivo* and *in vitro* (Ma *et al.*, 2018).

NIR may have promising results *in vitro* and *in vivo* with small animals such as rats, however, it is uncertain if it can be translated to be effective when applied to humans. Henderson and Morries (2015) endeavored to determine if enough photonic energy from NIR can be delivered to the human brain to precipitate beneficial effects for application in traumatic brain injury and stroke. Their study also included NIR penetration tests using *in vivo* human tissue, through structures such as the hand, ear with cartilage, cheek, subcutaneous flesh and the web of the hand. An 810 nm laser was employed with output setting of 13.5 W for the human tissue *in vivo* study. Several interesting facts were gleaned from their study: i) NIR penetrated better in living tissue due to the lack of post-mortem protein crosslinking; ii) Light may be scattered between the interfaces of different tissue (e.g., fascia and muscle); iii) Pulsed NIR seems to have greater penetration in living tissue as compared to continuous wave NIR. Most importantly, despite the fact that NIR penetration proved to be greater in tissues that contained bone, only over 0.8% of the pulsed NIR energy passed through 2.5 to 3.0 cm of a living human hand (Henderson and Morries, 2015). Based on this, NIR may not be able to penetrate deep enough with energy for application in osteosarcoma if applied from outside the skin, thus posing a barrier to the use of NIR.

Thus, to facilitate NIR reaching the scaffolds, other routes needed to be explored. Researchers have inserted optical fiber diffusers. A recently published clinical trial employed the use of AuroLase® therapy to treat 16 low-to intermediate risk prostate cancer patients. The treatment occurred over two consecutive days. AuroShells® (Gold-silica nano shells) were administered intravenously on day one and mediated the laser ablation. On the second day, catheters containing optical fiber diffuses were inserted into the tumors, guided by MRI and ultrasound. The optical fiber diffusers facilitated the delivery of NIR to the AuroShells® which resulted in focal photothermal ablation of prostate tumors. After undergoing the procedure, the patients were discharged on the same day. There was minimal damage to the surrounding tissue. Due gastric pain, only one patient did complete the two-day treatment protocol. Of the 15 men that did complete the treatment, 13 men had negative follow-up targeted biopsy results from the targeted ablation zone 12 months after treatment (Rastinehad *et al.*, 2019). In the context of osteosarcoma, the use of optical fibers to facilitate NIR reaching the scaffolds will be accompanied by a major disadvantage in that this would become a very invasive treatment procedure.

Tumor cells may also be destroyed by magneto-thermal therapy. Zhang et al. developed a magnetic scaffold composed of β-TCP–Fe–GO. Nano Fe_3O_4 particles were sandwiched by

GO sheets. The sandwich strategy displayed superior magnetothermal efficacy compared to lone Fe_3O_4 nanoparticles on the scaffold surface. The temperature of the scaffolds could be controlled by magnetic intensity and Fe_3O_4 content. GO provided a synergistic effect due its thermal conductivity (Zhang *et al.*, 2016).

The application of a magnetic field to scaffolds may not only be used for magnetothermal purposes. Shuai et al. fabricated polyglycolic acid (PGA)/Fe_3O_4 composite scaffolds. Upon applying a self-developed external static magnetic field (SMF), the Fe_3O_4 nanoparticles rearranged according to the SMF resulting in a magnetic field that was locally enhanced. As a result, cell adhesion, differentiation and proliferation were promoted and bone regeneration accelerated (Shuai *et al.*, 2020). **Figure 2.3** depicts how a magnetic field generated from a coil will interact with a tumor.

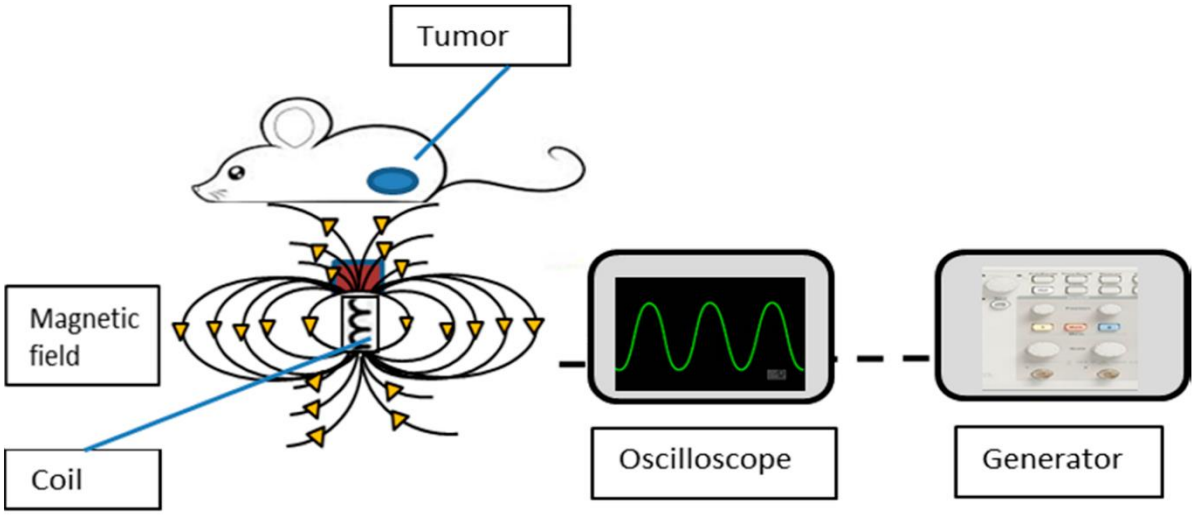


Figure 2.3: A depiction of how the magnetic field is generated from the coil to affect tumor cells. A generator is connected to a coil and oscilloscope. The generator provides voltage and frequency to the coil while the oscilloscope displays the frequency and amplitude on a screen. Reproduced from Vegerhof et al. 2016 under Creative Commons Attribution (CC-BY) license (CC BY 4.0) (http://creativecommons.org/licenses/by/4.0/).

2.4 3D-Printing of Bioactive-Loaded Scaffolds for Bone Regeneration

To increase the formation of bone, bone regenerative scaffolds may be loaded with bioactives such as drugs, proteins or other compounds. Examples of proteins that have been added to scaffolds include growth factors such as Bone Morphogenic Protein-2 (BMP-2) and Vascular Endothelial Growth Factor (VEGF). Ergul et al. employed BMP-2 to facilitate natural growth of bone cells and to provide easy attachment of cells to the 3D printed chitosan/PVA scaffolds (Ergul *et al.*, 2019). Angiogenesis is crucial in skeletal development and VEGF plays an important role in this regard (Zelzer *et al.*, 2002). VEGF has also been included in a scaffold

to enhance angiogenesis, bone repair and growth (Fahimipour *et al.*, 2017). In another study, BMP-2 and VEGF were dual loaded into a 3D printed hydroxyapatite composite scaffold for the combined effects and sustained release of VEGF and BMP-2 (Chen *et al.*, 2020). However, BMP-2 and VEGF have *in vivo* limitations including the potential to elicit immune reactions during prolonged use. Therefore, to overcome these limitations, Yan et al. explored the use of deferoxamine, an iron chelator, loaded into 3D printed PCL based scaffolds. In vivo testing displayed that deferoxamine enhances the regeneration of bone and promotes vascular invasion (Yan *et al.*, 2019). The bone regeneration capability of an amino acid peptide derived from BMP-7, called, bone formation peptide-1 (BFP1), was explored in a 3D printed alginate scaffold. BFP-1 enhancement of bone regeneration increases as BFP-1 increases and accelerated bone regeneration was displayed *in vivo* (Heo *et al.*, 2017).

To increase the formation of bone, Zhang et al. incorporated small molecule drugs resveratrol and strontium ranelate into PCL/ β-tricalcium phosphate scaffolds. The scaffolds had methacrylated hyaluronic acid and methacrylated gelatin-based hydrogels deposited between the PCL/ β-tricalcium phosphate frames. The dual-loaded scaffolds had synergistic effects in enhancing MSC osteogenic differentiation and a combined advantage of promoting angiogenesis and inhibiting osteoclasts. The scaffolds were tested *in vivo* and promoted bone formation. Reservatrol displayed a sustained release profile while Strontium ranelate displayed an initial burst release followed by sustained release. A limitation noted was the erratic release of Strontium Ranelate due to its water solubility (Zhang *et al.*, 2020).

While many studies focus on bone tissue engineering, not many address the need of a scaffold functionalized with antibacterial properties to mitigate the risk of post-surgical infection at the site of scaffold implantation. Therefore, Bai et al. developed a PCL/PEG scaffold, loaded with the antibacterial roxithromycin (Bai *et al.*, 2020). Martínez-Vázquez et al. developed hydroxyapatite/gelatin scaffolds utilising extrusion printing. The hydroxyapatite was doped with silicon. Vancomycin was incorporated within the ink before 3D printing (Martínez-Vázquez *et al.*, 2015). Martin et al. 3D printed a PLA/Collagen/citrate-hydroxyapatite (cHA) scaffold loaded with the antibacterial drug minocycline (Martin *et al.*, 2019). The loading of antibacterial drugs may not be the only approach to fabricating a scaffold with antibacterial properties. The use of silver as an antibacterial compound may also be beneficial (Zhang *et al.*, 2017). However, caution should be exercised that the concentration of silver nanoparticles should not toxic to cells responsible for bone regeneration.

2.5 Nano-Enabled 3D-Printed Scaffolds for Bone Regeneration

Zhang et al. proposed a solution to overcome the undesirable release rate of strontium ranelate by encapsulating the compound into microspheres and to load the microspheres in

to a bio-ink used for scaffold fabrication (Zhang *et al.*, 2020). . To this end, nanocarrier-loaded scaffolds were explored as the limitations that many bioactive have such as low solubility and high side effects profile (precipitated by long term use) may be overcome. Furthermore, loading anti-cancer drug-loaded nanoparticles within scaffolds may have application in addressing the problem of residual osteosarcoma cells. **Figure 2.4** illustrates the different types of nanocarriers that may be incorporated into a 3D printed scaffold. The interaction between the bone and the scaffold is also illustrated.

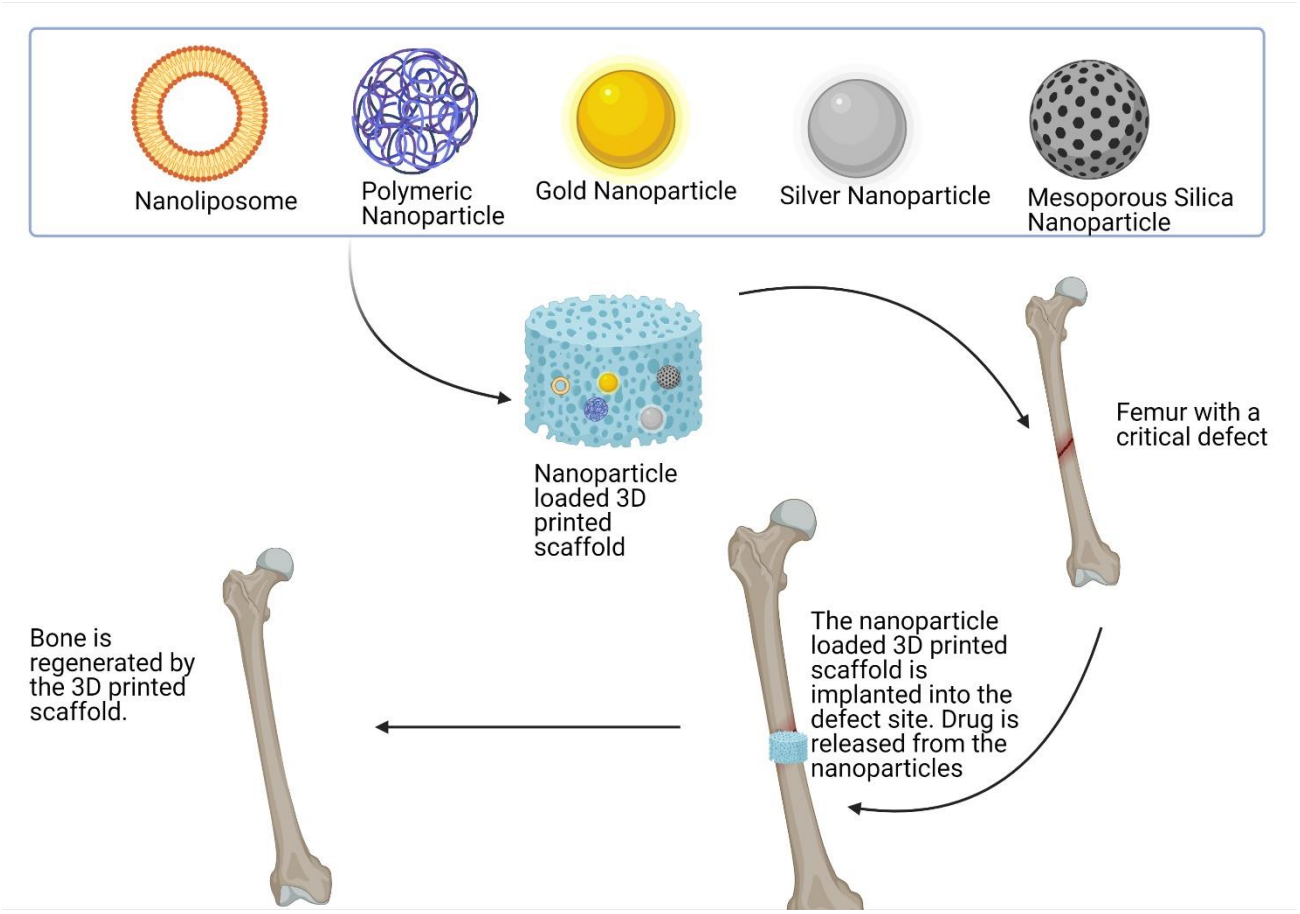


Figure 2.4: The various types of nanocarriers that may be incorporated into a scaffold. The nanocarriers are included in a 3D printed scaffold. The scaffold is then implanted into the critical defect site present in the femur due to osteosarcoma resection. Chemotherapeutics are released from the scaffold to target residual cancer cells while the scaffold regenerates the bone. This figure was created with BioRender.com

2.5.1 Nano-liposomes and 3D-printed scaffolds

Liposomes are lipid bilayer spherical nanoparticles with hydrophilic cores (Alavi and Hamidi, 2019). Liposomal carriers are advantageous in many ways. They are highly biocompatible, possess low immunogenicity and prolong the half-life of the drugs they contain (M. Li *et al.*, 2019). They facilitate the delivery of drugs of various sizes, shapes and solubilities. Hydrophilic

drugs can be encapsulated inside the hydrophilic core of liposomes while hydrophobic drugs may be trapped within the lipid bilayer (Alavi and Hamidi, 2019).

Aspirin has displayed positive aspects with regards to bone formation, however, its side effects limit its application for long-term use. Therefore, Li et al. formulated liposomes that had aspirin adsorbed to its surface. These liposomes were loaded into a 3D printed PCL scaffold. Osteoblast differentiation was promoted *in vivo* and *in vitro.* The liposomes were under 200nm in size and the loading of aspirin had little effect on size and morphology of the liposomes (Y. Li *et al.*, 2019). Sarkar and Bose et al. loaded curcumin-encapsulated nanoliposomes into a calcium phosphate 3D printed scaffold. The nanoliposomes were between 40 and 50 nm in size. This bifunctional scaffold not only promoted the formation of healthy bone cells, but also displayed anti-cancer properties (Sarkar and Bose, 2019).

Liposomes that are loaded with anticancer drugs that are standard for adjuvant therapy may also be incorporated into scaffolds for a localized anticancer effect. Below are the anti-osteosarcoma advancements made in liposomes.

Liposomal formulations have been synthesized and studied to address the resistance of osteosarcoma cells to treatment. Caliskan et al. developed dual-loaded Gemcitabine and Clofazimine liposomes. Gemcitabine was encapsulated within the hydrophilic core of the liposomes whereas Clofazamine was trapped within the lipid bilayer of the liposomes. The dual-loaded liposomes displayed a greater cytotoxicity in Saos-2 cells than the individually loaded Gemcitabine and Clofazimine liposomes (Caliskan *et al.*, 2019). In an effort to overcome the resistance of osteosarcoma cells to Doxorubicin, Giansanti et al. demonstrated that vocamine (a plant alkaloid) displays greater efficiency when loaded into cationic liposomes than the free alkaloid in increasing the accumulation of doxorubicin in osteosarcoma cells. The U-2 OS/DX cell line (human multidrug resistant (MDR) osteosarcoma cell line) was employed for this study (Giansanti *et al.*, 2019). Hyaluronic conjugated liposomes containing Hydrogen Sulfide releasing doxorubicin displayed promising results in overcoming doxorubicin-resistant osteosarcoma cells (Gazzano *et al.*, 2019).

There are various FDA approved liposome formulations on the market with indications for various cancers namely; Doxil®, DaunoXome®, Depocyt®, Myocet®, Mepact®, Marqibo® and Onivyde™. In addition, there are various liposomal formulations available for antifungal therapy, photodynamic therapy and antiviral therapy. Mepact® (approved in 2004) has a specific indication, among other indications, for non-metastatic osteosarcoma (Bulbake *et al.*, 2017).

2.5.2 Polymeric nanoparticles and 3D printed scaffolds

Polymeric nanoparticles are nanoscale, polymer derived drug delivery vehicles. They may be synthesized using one of two methods: i) the “bottom-up” method wherein monomers are polymerized to form the nanoparticles or; ii) the “top down” method whereby polymers are used to synthesize the nanoparticles. Drug loading my occur through absorption, adsorption and entrapment (Choudhury *et al.*, 2019).

Fahimipour et al. developed a gelatin/alginate/ β-TCP scaffold 3D printed composite. The scaffold was then loaded with PLGA microcarriers loaded with VEGF. VEGF was encapsulated in PLGA microspheres to facilitate its sustained release (Fahimipour *et al.*, 2017).

Other polymeric nanoparticles loaded with anticancer agents have the potential to be incorporated into scaffolds for bone regeneration. These are the advancements made in polymeric nanoparticles researched for use in osteosarcoma:

Zhao et al developed polymeric nanoparticles using the top-down method. Paclitaxel was entrapped within the nanoparticles. Pluronic F68 was used as a stabilizer and the nanoparticles were coated with polydopamine. Alendronate was used as a targeting molecule. These nanoparticles were researched on K7M2 wt osteosarcoma cells (Zhao *et al.*, 2019).

To combine the advantages of liposomes and polymeric nanoparticles, lipid-polymer hybrid nanoparticles have also been developed for use in osteosarcoma (F. Chen *et al.*, 2018). To target cancer stem cells and cancer cells in osteosarcoma, nanoparticles tagged with CD 133 aptamers and CL4 were developed to confer CD-133 and Epidermal Growth Factor Receptor targeting. These nanoparticles entrapped the drug salinomycin. (F. Chen *et al.*, 2018). To treat osteosarcoma initiating cells, all trans-retinoic acid was loaded into hybrid polymer nanoparticles and tagged with CD-133 aptamers to confer CD-133 gene targeting (Gui *et al.*, 2019). Lipid-polymer nanoparticles can be used as a dual-drug loaded vehicle. Lipid-polymer nanoparticles were dually loaded with paclitaxel and etoposide and displayed an efficacy that was two times greater than the free drugs. The dual-loaded lipid-polymer nanoparticles induced greater apoptosis in cells. Decrease cell proliferation was noted in cell groups treated with etoposide and paclitaxel dual-loaded lipid-polymer nanoparticles (Duan *et al.*, 2017).

2.5.3 Iron oxide nanoparticles and 3D printed scaffolds

Under the section of stimuli-responsive scaffolds, the use of iron to impart magnetic abilities to scaffolds was discussed. However, in addition to magnetic properties iron oxide may exert an anti-cancer effect. Iron oxide nanoparticles induce ROS-mediated toxicity in osteosarcoma cells (Du *et al.*, 2017) and could be used as drug carriers. Popescu et al. conjugated

Gemcitabine onto the iron nanoparticles surface. However, the Gemcitabine conjugated iron oxide nanoparticles displayed low cytotoxicity due to decreased cell uptake in MG-63 cells (Popescu *et al.*, 2017). Raghubir et al. loaded riluzole (a glutamate release inhibitor) into iron oxide nanocages and iron oxide nanospheres. The riluzole-loaded nanocages displayed better efficacy as compared to the riluzole-loaded nanospheres in reducing the osteosarcoma tumor size *in vivo* (Raghubir *et al.*, 2020). More research regarding drug loading of Iron oxide nanoparticles with osteosarcoma first line drugs is required.

Due to the potential of iron oxide nanoparticles to agglomerate, strategies need to be developed to modify the surface of the iron oxide nanoparticles. One such strategy, that has been explored, was to coat the iron oxide nanoparticles with Hydroxyapatite (Mondal *et al.*, 2017). Coating iron oxide nanoparticles with a combination of compounds such as tartaric acid and ascorbic acid could be another strategy to overcome the agglomeration of iron oxide nanoparticles. However, due to low cytotoxicity displayed by such nanoparticles in Saos-2 cells, drug-loading of these nanoparticles should be considered for applications in osteosarcoma (Özel *et al.*, 2019).

2.5.4 Gold nanoparticles and 3D printed scaffolds

Gold Nanoparticles (AuNP) were incorporated into 3D printed gelatin methacrylate nanoparticles to enhance CT imaging (Celikkin *et al.*, 2019). However, AuNPs have long been explored as anticancer tools. This is due to the outstanding properties of AuNPs such as multi-functionalization capabilities, high surface area to volume ratio, increased permeability, increased retention, stability, facile synthesis and surface chemistry (Singh *et al.*, 2018). AuNPs are exogenous inducers of Reactive Oxygen Species (ROS). Cancer cells undergo apoptosis after exposure to AuNPS due to their inability to withstand the oxidative stress due to excess ROS generation (Dayem *et al.*, 2017). It is important to note that cellular response to AuNPs differs across cell lines (Ju *et al.*, 2015). The shape of AuNPs influences its cytotoxicity and anticancer potential. In one study, AuNP stars were proven to have greater cytotoxicity and anticancer potential than AuNP rods, while AuNP rods have greater cytotoxicity than AuNP spheres. This study was conducted employing a variety of cell lines including osteosarcoma cell lines (143-B, MG-63) (Steckiewicz *et al.*, 2019). The size of AuNPs also influences its cytotoxicity. The larger the size of the AuNPs, the greater the cytotoxicity the AuNPs display. In one study, it was observed that 60 nm and 46 nm AuNPs displayed greater cytotoxicity than 38 nm AuNPs in MG-63 cells (Chakraborty *et al.*, 2020).

AuNPs enhance the potency of drugs in osteosarcoma. Studies conducted have concluded that the effects of chemotherapeutics such as Doxorubicin (Iram *et al.*, 2017; Steckiewicz *et al.*, 2020) , Cisplatin (Iram *et al.*, 2017), bile acid cisplatin derivatives (Sánchez-Paradinas *et*

al., 2014), Gemcitabine and Cytarabine (Steckiewicz *et al.*, 2020) are enhanced in osteosarcoma cell lines when conjugated to AuNPs. Glycogenic AuNPs have also proven to have anticancer potential (Rahim *et al.*, 2014).

2.5.5 Silver Nanoparticles and 3D printed scaffolds

Silver nanoparticles (AgNP) are under intense investigation due to their remarkable physical, chemical and biological properties (Lee and Jun, 2019). AgNPs have been incorporated into 3D printed β-TCP scaffolds in the form of Ag-GO nanocomposites. First β-TCP scaffolds were fabricated followed by immersion in an Ag-GO suspension. The scaffolds displayed osteogenic and antibacterial activity (Zhang *et al.*, 2017). However, AgNPs may also be incorporated into 3D scaffolds for anti-osteosarcoma applications. The ability of AgNP to induce apoptosis in cancer cells may be due to its ability to generate ROS which in turn leads to mitochondrial dysfunction (Dayem *et al.*, 2017). Dávid Kovács et al. demonstrated that AgNP can induce apoptosis in osteosarcoma cells with and without the P53 tumor suppressor gene. Their results also proved that, unlike AuNPs, smaller AgNPs (5 nm) exhibited greater cytotoxicity than larger AgNPs (35 nm) (Kovács *et al.*, 2016). The shape of AgNPs, unlike AuNPs, may not have an impact on cytotoxicity. In one study, no cell viability differences were noted between synthesized protein capped prism and spherical shaped AgNPs. By capping the AgNPs with proteins, the influence of AgNP shape on AgNP cytotoxicity could be analyzed without the complication of toxicity due to the surface chemistry of AgNP (Chakraborty *et al.*, 2018). However, this study was conducted with Human cervical adenocarcinoma cells (HeLa cells) thus leaving a gap for exploration on the effects of different AgNP geometries in osteosarcoma cells.

The cytotoxicity of AgNPs may be enhanced in osteosarcoma cells by capping AgNPs with various agents such as adenosine 5′-triphosphate (ATP) (Rajabnia and Meshkini, 2018) and bovine serum albumin (Majeed *et al.*, 2019). This was not the case, however, when AgNPs etched onto silica nanoparticles were functionalized with lipoic acid. Greater cytotoxicity in MG-63 osteosarcoma cells were found with plain AgNPs etched onto silica nanoparticles than those that were functionalized with lipoic acid (Tudose *et al.*, 2017).

2.6 Nanocarriers for Potential Incorporation into 3D-Printed Scaffolds

To the Author’s knowledge, these nanoparticles have not yet been incorporated into scaffolds employed for bone regeneration. However, these nanoparticles are worth being mentioned, as their advancements in anti-osteosarcoma treatment may have the potential to be incorporated into scaffolds for localized adjuvant therapy.

2.6.1 Mesoporous silica nanoparticles as anti-osteosarcoma nanocarriers

Mesoporous silica nanoparticles (MSNs) are inorganic nanoparticles that possess desirable attributes such as high surface area, tunable pore size, increased chemical, colloidal and thermal stability. In addition, their surfaces are easily modified (Murugan and Krishnan, 2018). MSNs are often capped with a gate-keeper that prevents premature release of loaded drug and can provide for controlled release of the contained drug (Murugan and Krishnan, 2018; Sábio *et al.*, 2019).

MSNs have been widely explored as potential drug delivery vehicles. In the context of osteosarcoma, Martinez-Carmona et al. developed doxorubicin loaded MSNs by assembly of two different building blocks. The first building bock was a polyacrylic acid cap that was anchored to the MSNs by means of an acid cleavable acetal linker. This conferred a pH-responsive property. The second building block was the plant lectin concanavalin A which conferred a targeting property. These building blocks had a synergistic effect and potentiated the antitumor efficacy (Martínez-carmona, Lozano and Vallet-regí, 2018). Paris et al. developed ultrasound responsive MSNs capped with polyethylene glycol (PEG). On exposure to ultrasound, the PEG capping was shed, resulting in the exposure of a cationic surface that enhanced osteosarcoma cell uptake of the MSNs that contained topotecan. The use of ultrasound increased the toxicity of the topotecan loaded MSNs (Paris *et al.*, 2018). Lu et al synthesized multifunctional mesoporous silica–coated bismuth sulfide nanoparticles that could treat osteosarcoma and facilitate Computed Tomography (CT) imaging. These nanoparticles were conjugated with the targeting peptide RGD and encapsulated doxorubicin. In addition, these nanoparticles have displayed potential for applications in photothermal therapy (Lu *et al.*, 2018).

MSNs have also been explored as vectors for gene delivery in osteosarcoma. Xiong et al. synthesized magnetic core-shell MSNs with large radial mesopores. The MSNs were loaded with siRNA and were capped with tannic acid that served as a pH responsive gatekeeper (Xiong *et al.*, 2016).

Dual drug delivery systems for application in osteosarcoma may prove to be advantageous, as they provide an opportunity to address the need for delivery of an antibacterial drug and an anticancer drug. Cheng et al. developed asymmetric, lollipop-shaped, dual compartment MSNs for co-delivery of hydrophobic and hydrophilic drugs. The MSN nanosphere head included iron oxide (Fe_3O_4) and enclosed the hydrophilic drug gentamicin. The “stick” of the lollipop was a nanorod of ethane bridged periodic mesoporous organosilica, and contained the hydrophobic drug curcumin. The asymmetrical MSNs displayed high antibacterial and high anticancer performance and can be used to load increased amounts of hydrophilic drugs

(Cheng *et al.*, 2020). This study was conducted using MCF-7 cells (human breast cancer cells).

One of the drawbacks of MSNs is its low biodegradability. A suggested strategy to tune the biodegradability of MSNs, is to dope MSNs with metal cations, such as zirconium, calcium, iron, and manganese. This has yet to be properly researched in the context of osteosarcoma (Croissant, Fatieiev and Khashab, 2017).

2.6.2 Micelles as anti-osteosarcoma nanocarriers

Micelles are polymeric drug delivery vehicles assembled into a hydrophobic core/ hydrophilic shell structure. As micellar shape and size are controllable, the drug loading capacity of micelles can be increased. The hydrophobic core of micelles allows the encapsulation of poorly soluble drugs, while the hydrophilic shell provides an opportunity for surface modification of the micelles to improve targeting (Melim *et al.*, 2020).

In osteosarcoma, there exists several studies employing micelles as drug delivery systems to improve the therapeutic efficacy of hydrophobic drugs. Xi et al. loaded the compound curcumin into hyaluronic acid-octadecanoic acid micelles. These micelles were modified with alendronate to improve bone targeting. These micelles displayed high drug loading, high affinity to hydroxyapatite and sustained release (Xi *et al.*, 2019). PEG-sheddable reduction-sensitive polyurethane micelles loaded with Doxorubicin were researched and was found to achieve triggered release. These micelles can also improve the antitumor efficacy of doxorubicin (Yang *et al.*, 2020). Fang et al. developed micelles formed from poly (ethylene glycol)-block-poly (trimethylene carbonate) terminated with the cell affinitive peptide RGD. These RGD terminate micelles displayed increased cell uptake as compared to micelles not terminated with RGD (Fang *et al.*, 2017).

Micelles could also be used to deliver hydrophilic drugs in osteosarcoma. Noy et al. reported the incorporation of PENAO (an arsenic drug-(4-(N-(S-penicillaminylacetyl) amino)) into the micelle polymer matrix. This prevents drug leakage and premature release of PENAO (Noy *et al.*, 2018). Noy et al. also noted that due to the minimal availability of hydrophilic drugs, there is little information on the effect of hydrophilic drugs on the micelle surfaces (Noy *et al.*, 2018). More research should be conducted on such effects.

Micelles may be stable in aqueous solutions, however when immersed in blood, dissociation occurs, leading to accelerated drug release (Li *et al.*, 2014). Therefore, strategies such as cross-linking the micelle core has been developed to improve micelle stability in the blood (Cajot *et al.*, 2011). However, cross-linking the core of the micelle may decrease the drug

loading capacity, therefore, other methods such as interface crosslinking may be more suitable (Lu *et al.*, 2020).

2.6.3 Targeted nanocarriers and stimuli-responsive nanocarriers

Should a nanocarrier-loaded scaffold be employed for bone regeneration and adjuvant therapy after osteosarcoma resection, targeting strategies and intrinsic stimuli-responsive nanocarriers (such as pH and redox responsive nanocarriers) should be considered, to provide chemotherapeutic delivery that is specific to cancer cells.

Drug delivery may be controlled by utilising the pH gradients present between normal physiological compartment and tumor tissue. The normal physiological pH of blood is 7.4, while the pH of the extracellular tumor tissue is more acidic at 6.0- 7.2. The pH of subcellular compartments have a lower pH compared to the extracellular environment- the lysosome has pH of between 4.0-5.0 while endosomes have a pH of 5.0-6.0 (Bertrand *et al.*, 2014; Ruttala *et al.*, 2018). pH-responsive nanocarriers may developed by use of two means: i) the nanocarrier is formed from, capped or layered with a pH-responsive polymer (e.g. chitosan) or ii) there are pH-sensitive moieties employed to link either a drug or polymer to the nanocarrier (e.g. hydrazone and acetal bonds) (Lavrador, Gaspar and Mano, 2018; Ruttala *et al.*, 2018).

Glutathione is a tripeptide (cysteine, glycine, and glutamic acid) and is found abundantly in the mammalian cell with an abundance of important functions. Glutathione in its reduced state exists as GSH (Pizzorno, 2014). GSH is present in intracellular environments in concentrations that are approximately 100 times greater than the GSH concentrations present in the extracellular environment (Lavrador, Gaspar and Mano, 2018; Ruttala *et al.*, 2018). A study revealed that intrinsic GSH concentrations correlated to cisplatin resistance in osteosarcoma cells and that a depletion of GSH increased the sensitivity of osteosarcoma cells to cisplatin (Komiya *et al.*, 1998). The redox potential created by the difference of glutathione levels between the intracellular and extracellular environments provides an opportunity for a stimuli-responsive mechanism. By adding a disulfide linkage to the nanocarrier, drugs may be released in the intracellular environment where GSH concentrations are increased (Lavrador, Gaspar and Mano, 2018; Ruttala *et al.*, 2018).

Targeting may be classified into active and passive targeting. To enhance active targeting, functionalizing nanoparticles with ligands that lead to surface interaction with overexpressed surface molecule and proteins on cancer cells, thereby facilitating cellular uptake via receptor-mediated endocytosis (Huang *et al.*, 2020). Figure 5 illustrates the internalization of nanocarriers by the cell through receptor-mediated endocytosis by use of a targeting ligand. **Figure 2.5:** Nanoparticles with ligands for targeted delivery bind to cell receptors to be

internalized by receptor mediated endocytosis. Reproduced from G. J. Kim and Nie 2005 under Creative Commons Attribution (CC-BY) license (CC BY-NC-ND 3.0) (https://creativecommons.org/licenses/by-nc-nd/3.0/)

Table 2.3 discusses the targeting strategies that have been employed in nanoparticles for osteosarcoma treatment. **Table 2.4** describes the strategies that have been researched in imbuing nanocarriers with intrinsic stimuli-responsive properties.

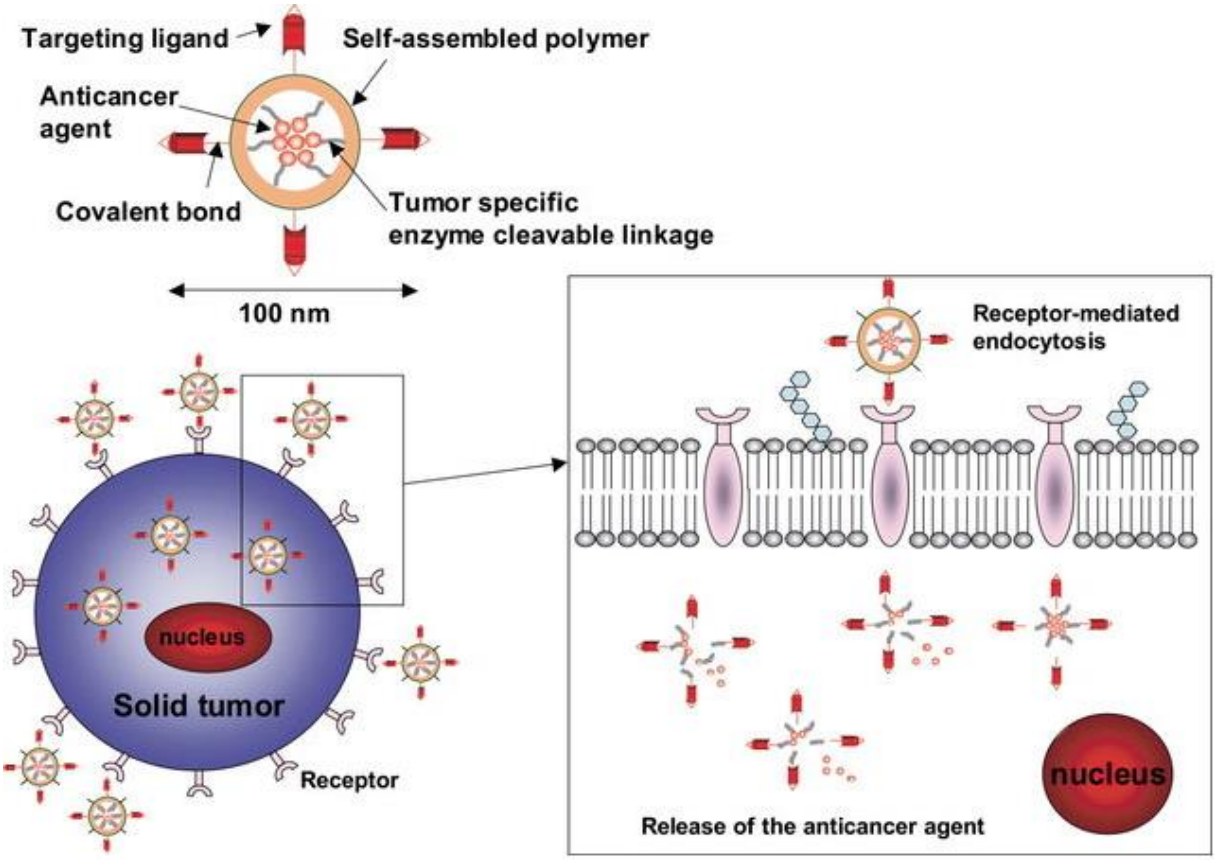


Figure 2.5: Nanoparticles with ligands for targeted delivery bind to cell receptors to be internalized by receptor mediated endocytosis. Reproduced from G. J. Kim and Nie 2005 under Creative Commons Attribution (CC-BY) license (CC BY-NC-ND 3.0) (https://creativecommons.org/licenses/by-nc-nd/3.0/)

Table 2.3: Information on strategies to confer targeting properties to nanoparticles

Target	Nanoparticle	Drug	Compound that conferred targeting properties	Reference
Bone targeting	Polymeric nanoparticle	Paclitaxel	Alendronate (Bisphosphonate)	(Zhao *et al.*, 2019)
Bone (Hydroxyapatite) and CD44	Liposome	Doxorubicin	Alendronate and hyaluronic acid	(S. Feng *et al.*, 2019)
Bone targeting (Hydroxyapatite)	Micelle	Doxorubicin	D-aspartic acid octapeptide	(Low, Yang and Kopeček, 2014)
CD44	Liposome	Doxorubicin conjugated with a H2S-releasing moiety	Hyaluronic acid	(Gazzano *et al.*, 2019)
CD44	Liposome	Doxorubicin	Hyaluronic acid	(Chi *et al.*, 2017)
CD44 Hydroxyapatite	Micelle	Curcumin	Hyaluronic acid Alendronate	(Xi *et al.*, 2019)
CD133	Lipid-polymeric nanoparticle	All-trans retinoic acid	CD133 aptamers	(Gui *et al.*, 2019)
EphA2 receptor	Liposome	Doxorubicin and siRNA	YSA peptide	(Haghiralsadat *et al.*, 2018)
Epidermal Growth Factor CD133	Lipid-polymeric nanoparticle	Salinomycin	EGFR and CD133 aptamers	(F. Chen *et al.*, 2018)
Epidermal Growth Factor	Lipid-polymer nanoparticle	Salinomycin	EGFR aptamer	(Yu *et al.*, 2018)
Estrogen Receptors	Liposome	Doxorubicin	Estrogen	(Yin *et al.*, 2018)

Integrin Receptors- αvβ3 and αvβ5	MSN	Doxorubicin	Targeting peptide RGD	(Lu *et al.*, 2018)
Integrin Receptors- αvβ3 and αvβ5	Micelle	Doxorubicin	RGD	(Fang *et al.*, 2017)
Over expressed cell surface glycans	MSN	Doxorubicin	Lectin concanavalin A	(Martínez-carmona, Lozano and Vallet-regí, 2018)
Overexpressed folate receptors	Mesoporous zinc-substituted hydroxyapatite	Methotrexate	Methotrexate	(Meshkini and Oveisi, 2017)

Table 2.4: Information on strategies utilized to confer intrinsic stimuli properties to nanoparticles as well as the anti-osteosarcoma drugs and cell lines utilized.

Intrinsic Stimuli	Nanoparticle	Anti-osteosarcoma drug/ compound	Compound that conferred stimuli responsive property	OS Cell line	Reference
pH	MSN	Doxorubicin	Poly acrylic acid cap linked by acetal cleavable linker	HOS cells-CRL-1543 Mouse preosteoblastic cell line - MC3T3-E1	(Martínez-carmona, Lozano and Vallet-regí, 2018)
	MSN	siRNA	Tannic acid	KHOS	(Xiong *et al.*, 2016)
	Calcium carbonate ($CaCO_3$)-based therapeutic modulator with a layer of Collagen type I	CeO_2 and doxorubicin	$CaCO_3$	Saos-2	(Tapeinos *et al.*, 2018)
	Liposome	Doxorubicin	Cationic nitrogen of the ammonium moiety	mouse osteosarcoma cells (K7M2)	(Rayamajhi *et al.*, 2020)
	Micelle	Doxorubicin	Hydrazone bond that bound Doxorubicin	Saos-2	(Low, Yang and Kopeček, 2014)
	Cationic cyclodextrin	Methotrexate	ionic interaction between carboxylate anions of	Saos-2	(Ahmadi *et al.*, 2020)

	coated magnetic nanoparticles		methotrexate and the nanocarrier		
	Mesoporous ZSM-5 zeolites	Doxorubicin	Chitosan layer	MG-63	(Yang *et al.*, 2018)
Redox	Liposome (estrogen functionalized)	Doxorubicin	The disulfate bond that tethered the chitooligosaccharides to the liposome	MG-63	(Yin *et al.*, 2018)
	Liposome	Doxorubicin	The disulfide linker that attached the chitooligosaccharide to cholesterol	MG-63	(Yin *et al.*, 2017)
	Liposome	Doxorubicin	Disulfide bonds that linked PEG with cholesterol	MG-63	(Chi *et al.*, 2017)
	Liposome (Dual Targeting-Bone and CD44)	Doxorubicin	Disulfide bond that links Alendronate-Hyaluronic acid to PEG_{2000}−DSPE	MG-63	(S. Feng *et al.*, 2019)
	Micelle	Doxorubicin	Disulfide bonds attached to PEG. Disulfide bonds attached to polyurethane	Saos-2	(Yang *et al.*, 2020)

2.7 Concluding Remarks

In this literature review, the various polymers and bioceramics utilized for 3D printed scaffolds as well as the nanocarriers that may be incorporated into these scaffolds that may be employed for bone tissue engineering has been discussed. For these scaffolds to be utilized for application in post-surgical resection of osteosarcoma however, certain factors have to be taken into account. Scaffolds that have mechanical strength only suitable for non-load bearing joints may not be utilized for application in post-surgical resections of osteosarcoma of load-bearing bones. Based on the data presented, there is much research to be done on 3D printing

polymeric scaffolds for bone regeneration at loadbearing sites. The ideal combination of polymers to fabricate 3D printed scaffolds for bone regeneration has yet to be established.

Other 3D printed scaffolds that require further research as potential scaffolds for bone regeneration are 3D printed nanoclay composite scaffolds. Coppola et al. (2018) investigated the influence of temperature on PLA/clay nanocomposites. The nanoclay used was Cloisite 30B modified by methyl, tallow, bis-2-hydroxyethyl, and quaternary ammonium chloride. The samples were printed by FDM and two PLA grades were used. It was concluded that PLA nanocomposite samples had a higher elastic modulus that plain PLA samples. PLA nanocomposite with with D-isomer at 4 displayed an increase in elastic modulus as the printing temperature increased. Other noteworthy observations include that nanoclay acted as a nucleating agent and increased thermal stability (Coppola *et al.*, 2018). However, cell studies should be conducted on these scaffolds to determine their suitability for bone regeneration. Cidonio et al. also used Laponite (a type of nanoclay) for its physiochemical and osteogenic differentiation inducing properties in a bioink that also consisted of alginate and methyl cellulose. These scaffolds were fabricated with their own in-house 3D printer. Based on *in vitro, ex vivo and in vitro* studies it was concluded that scaffolds produced from the nanoclay-based bioink had the potential to be clinically relevant bone regenerative constructs (Cidonio *et al.*, 2020). Further investigation and research should include the formulation of polymer/bioceramic/nanoclay as well as various other polymer/nanoclay 3D printed scaffolds for the suitability of bone regeneration in the context of osteosarcoma.

One of the drawbacks to 3D printing is that the materials used in the direct printing of scaffolds may be limited due to the printing technology available. Indirect 3D printing approaches may be undertaken to overcome drawbacks of 3D printing such as 3D printing a dissolvable negative mold to cast the solutions required for the scaffolds. The 3D printed mold can then be dissolved once the scaffold has set by methods such as lyophilization (Sachlos *et al.*, 2006; Hassanajili *et al.*, 2019).

The bone regeneration abilities of polymers in bone tissue engineering may be enhanced by incorporating other compounds, molecules and drugs such as BMP and VEGF. Photo-responsive and magneto-responsive 3D printed scaffolds may be utilized for applications in post-surgical-resection of osteosarcoma. However, due to poor penetration of NIR through tissue, other routes to facilitate NIR reaching the scaffolds must be considered.

Recent studies indicate that bone regeneration abilities of polymers may also be enhanced by the inclusion of Magnesium (Mg). Golafshan et al. (2020) prepared Magnesium Phosphate scaffolds modified with Strontium ions (MPSr) by including it in a polymer phase. The polymer selected was polycaprolactone. Scaffolds with 30 wt% of PCL could print the desired shape

by extrusion-based printing. It was concluded that when compared to pristine PCL scaffolds, MPSr/PCL scaffolds were superior in terms of biological and mechanical qualities (Golafshan *et al.*, 2020). Lai et al. (2019) developed 3D printed poly (lactide-co-glycolide) (PLGA)/β-TCP/ Mg scaffolds by utilising low-temperature rapid prototyping. PLGA/β-TCP/Mg scaffolds displayed osteogenic and angiogenic properties. *In vivo* studies further demonstrated that subjects with PLGA/β-TCP/Mg scaffolds had greater mean bone volume than those with just PLGA/β-TCP scaffolds (Lai *et al.*, 2019).Thus, incorporating Mg into other 3D printed polymeric/bioceramic scaffolds should be considered for future studies that research 3D printed scaffolds for application in osteosarcoma.

In conclusion, 3D printed scaffolds pose an opportunity with untapped potential. They may be used as sustained release platforms for drugs not just to enhance bone regeneration, but to target residual osteosarcoma cells after surgical resection and to mitigate infections after surgical implantation of the scaffold. This may be achieved by two means so far; to directly load the drug within the scaffold (if the drug is suitable) or to load the scaffolds with drug encapsulated nanoparticles which can overcome limitations such as poor solubility and toxicity that are inherent to many drugs. Strategies such as tagging the nanocarriers with targeting compounds and refining nanocarriers to respond to certain stimuli may allow for precision in targeting cancer cells in adjuvant therapy.

2.8 References

Abbasi, N. *et al.* (2020) 'Porous scaffolds for bone regeneration', *Journal of Science: Advanced Materials and Devices*. Elsevier Ltd, 5(1), pp. 1–9. doi: 10.1016/j.jsamd.2020.01.007.

Ahmadi, D. *et al.* (2020) 'Preparation and in-vitro evaluation of pH-responsive cationic cyclodextrin coated magnetic nanoparticles for delivery of methotrexate to the Saos-2 bone cancer cells', *Journal of Drug Delivery Science and Technology*, 57. doi: 10.1016/j.jddst.2020.101584.

Ahmed, S. *et al.* (2015) 'Chitosan Based Dressings for Wound Care', *Immunochemistry & Immunopathology: Open Access*, 1(2), pp. 1–6. doi: 10.4172/icoa.1000106.

Alavi, M. and Hamidi, M. (2019) 'Passive and active targeting in cancer therapy by liposomes and lipid nanoparticles', *Drug Metabolism and Personalized Therapy*, 34(1), pp. 1–8. doi: https://0-doi-org.innopac.wits.ac.za/10.1515/dmpt-2018-0032.

Alksne, M. *et al.* (2020) 'In vitro comparison of 3D printed polylactic acid/hydroxyapatite and polylactic acid/bioglass composite scaffolds: Insights into materials for bone regeneration', *Journal of the Mechanical Behavior of Biomedical Materials*. Elsevier Ltd, 10, p. 103641. doi: 10.1016/j.jmbbm.2020.103641.

American Cancer Society (2020) *Key Statistics for Osteosarcoma*. Available at: https://www.cancer.org/cancer/osteosarcoma/about/key-statistics.html (Accessed: 10 February 2020).

Anbu, R. T. *et al.* (2019) 'Comparison of the Efficacy of Three Different Bone Regeneration Materials: An Animal Study', *European Journal of Dentistry*, 13(1), pp. 22–28. doi: 10.1055/s-0039-1688735.

Andersson, H. A. *et al.* (2014) 'HSP70 promoter-driven activation of gene expression for immunotherapy using gold nanorods and near infrared light', *Vaccines*, 2(2), pp. 216–227. doi: 10.3390/vaccines2020216.

Bai, J. *et al.* (2020) 'Melt electrohydrodynamic 3D printed poly (ε-caprolactone)/polyethylene glycol/roxithromycin scaffold as a potential anti-infective implant in bone repair', *International Journal of Pharmaceutics*. Elsevier, 576, p. 118941. doi: 10.1016/j.ijpharm.2019.118941.

Baino, F. (2018) 'Bioactive glasses – When glass science and technology meet regenerative medicine', *Ceramics International*. Elsevier Ltd and Techna Group S.r.l., 44(13), pp. 14953–14966. doi: 10.1016/j.ceramint.2018.05.180.

Bendtsen, S. T., Quinnell, S. P. and Wei, M. (2017) 'Development of a novel alginate-polyvinyl alcohol-hydroxyapatite hydrogel for 3D bioprinting bone tissue engineered scaffolds', *Journal of Biomedical Materials Research - Part A*, 105(5), pp. 1457–1468. doi: 10.1002/jbm.a.36036.

Bertrand, N. *et al.* (2014) 'Cancer nanotechnology: The impact of passive and active targeting in the era of modern cancer biology', *Advanced Drug Delivery Reviews*. Elsevier B.V., 66, pp. 2–25. doi: 10.1016/j.addr.2013.11.009.

Bhattacharjee, P. *et al.* (2017) 'Silk scaffolds in bone tissue engineering: An overview', *Acta Biomaterialia*. Acta Materialia Inc., 63, pp. 1–17. doi: 10.1016/j.actbio.2017.09.027.

Bil, M. *et al.* (2009) 'Optimization of the structure of polyurethanes for bone tissue engineering applications, in: *Acta Biomaterialia*. Elsevier BV,pp. 2501-2510. doi: 10.1016/j.actbio.2009.08.037.

Boskey, A. L. (2003) 'Biomineralization: An Overview', *Connective Tissue Research*, 44, pp. 5–9. doi: 10.1080/03008200390152007.

Bruyas, A. *et al.* (2018) 'Systematic characterization of 3D-printed PCL/β-TCP scaffolds for biomedical devices and bone tissue engineering: Influence of composition and porosity', *Journal of Materials Research*, 33(14), pp. 1948–1959. doi: 10.1557/jmr.2018.112.

Bulbake, U. *et al.* (2017) 'Liposomal Formulations in Clinical Use : An Updated Review', *Pharmaceutics,* pp. 1–33. doi: 10.3390/pharmaceutics9020012.

Caballero, S. S. R. *et al.* (2019) '3-D printing of chitosan-calcium phosphate inks: rheology, interactions and characterization', *Journal of Materials Science: Materials in Medicine*. Springer US, 30(1). doi: 10.1007/s10856-018-6201-y.

Cajot, S. *et al.* (2011) 'Design of reversibly core cross-linked micelles sensitive to reductive environment', *Journal of Controlled Release*. Elsevier B.V., 152(1), pp. 30–36. doi: 10.1016/j.jconrel.2011.03.026.

Caliskan, Y. *et al.* (2019) 'A new therapeutic combination for osteosarcoma : Gemcitabine and Clofazimine co-loaded liposomal formulation', *International Journal of Pharmaceutics*. Elsevier, 557(May 2018), pp. 97–104. doi: 10.1016/j.ijpharm.2018.12.041.

Celikkin, N. *et al.* (2019) 'Enhancing X-ray attenuation of 3D Printed Gelatin Methacrylate (GelMA) hydrogels utilizing gold nanoparticles for bone tissue engineering applications', *Polymers*, 11(2), pp. 1–13. doi: 10.3390/POLYM11020367.

Chakraborty, A. *et al.* (2020) 'Size-dependent apoptotic activity of gold nanoparticles on osteosarcoma cells correlated with SERS signal', *Journal of Photochemistry and Photobiology*

B: Biology. Elsevier, 203(January 2019), p. 111778. doi: 10.1016/j.jphotobiol.2020.111778.

Chakraborty, I. *et al.* (2018) 'Protein-Mediated Shape Control of Silver Nanoparticles'. doi: 10.1021/acs.bioconjchem.8b00034.

Chavanne, P. *et al.* (2013) '3D printed chitosan / hydroxyapatite scaffolds for potential use in regenerative medicine', *Biomedizinische Technik*, 58(1), pp. 2–3. doi: 10.1515/bmt-2013-40.

Chen, F. *et al.* (2018) 'Targeted salinomycin delivery with EGFR and CD133 aptamers based dual-ligand lipid-polymer nanoparticles to both osteosarcoma cells and cancer stem cells', *Nanomedicine: Nanotechnology, Biology, and Medicine*. Elsevier Inc., 14(7), pp. 2115–2127. doi: 10.1016/j.nano.2018.05.015.

Chen, G., Chen, N. and Wang, Q. (2019) 'Fabrication and properties of poly(vinyl alcohol)/β-tricalcium phosphate composite scaffolds via fused deposition modeling for bone tissue engineering', *Composites Science and Technology*. Elsevier, 172(November 2018), pp. 17–28. doi: 10.1016/j.compscitech.2019.01.004.

Chen, S. *et al.* (2020) 'Evaluation of BMP-2 and VEGF loaded 3D printed hydroxyapatite composite scaffolds with enhanced osteogenic capacity in vitro and in vivo', *Materials Science and Engineering C*. Elsevier, 112, p. 110893. doi: 10.1016/j.msec.2020.110893.

Chen, X. *et al.* (2018) 'Scaffold structural microenvironmental cues to guide tissue regeneration in bone tissue applications', *Nanomaterials*, 8(11), pp. 1–15. doi: 10.3390/nano8110960.

Cheng, Y. *et al.* (2020) 'Antibacterial and anticancer activities of asymmetric lollipop-like mesoporous silica nanoparticles loaded with curcumin and gentamicin sulfate', *Colloids and Surfaces B: Biointerfaces*. Elsevier, 186, p. 110744. doi: 10.1016/j.colsurfb.2019.110744.

Chi, Y. *et al.* (2017) 'Redox-sensitive and hyaluronic acid functionalized liposomes for cytoplasmic drug delivery to osteosarcoma in animal models', *Journal of Controlled Release*. Elsevier, 261, pp. 113–125. doi: 10.1016/j.jconrel.2017.06.027.

Chiu, Y. C. *et al.* (2019) 'Effect of strontium substitution on the physicochemical properties and bone regeneration potential of 3D printed calcium silicate scaffolds', *International Journal of Molecular Sciences*, 20(11). doi: 10.3390/ijms20112729.

Chou, A. . ., Geller, D. S. and Gorlick, R. (2008) 'Therapy for Osteosarcoma Where Do We Go From Here?', *Pediatric Drugs*, 10(5), pp. 315–327. doi: https://0-doi-org.innopac.wits.ac.za/10.2165/00148581-200810050-00005.

Choudhury, H. *et al.* (2019) 'Strategizing biodegradable polymeric nanoparticles to cross the

biological barriers for cancer targeting', *International Journal of Pharmaceutics*. Elsevier, 565, pp. 509–522. doi: 10.1016/j.ijpharm.2019.05.042.

Cidonio, G. *et al.* (2020) 'Nanoclay-based 3D printed scaffolds promote vascular ingrowth ex vivo and generate bone mineral tissue in vitro and in vivo', *Biofabrication*, 12(3). doi: 10.1088/1758-5090/ab8753.

Coppola, B. *et al.* (2018) '3D printing of PLA/clay nanocomposites: Influence of printing temperature on printed samples properties', *Materials*, 11(10), pp. 1–17. doi: 10.3390/ma11101947.

Croissant, J. G., Fatieiev, Y. and Khashab, N. M. (2017) 'Degradability and Clearance of Silicon , Organosilica , Silsesquioxane , Silica Mixed Oxide , and Mesoporous Silica Nanoparticles'. doi: 10.1002/adma.201604634.

Dang, W. *et al.* (2018) 'A bifunctional scaffold with CuFeSe 2 nanocrystals for tumor therapy and bone reconstruction', *Biomaterials*, 160, pp. 92–106. doi: 10.1016/j.biomaterials.2017.11.020.

Datta, A., Ghosh, A. K. and Kundu, S. C. (2001) 'Differential expression of the fibroin gene in developmental stages of silkworm, Antheraea mylitta (Saturniidae)', *Comparative Biochemistry and Physiology - B Biochemistry and Molecular Biology*, 129(1), pp. 197–204. doi: 10.1016/S1096-4959(01)00377-3.

Dayem, A. A. *et al.* (2017) 'The Role of Reactive Oxygen Species (ROS) in the Biological Activities of Metallic Nanoparticles', pp. 1–21. doi: 10.3390/ijms18010120.

Demirtaş, T. T., Irmak, G. and Gümüşderelioğlu, M. (2017) 'A bioprintable form of chitosan hydrogel for bone tissue engineering', *Biofabrication*, 9(3). doi: 10.1088/1758-5090/aa7b1d.

Djagny, K. B., Wang, Z. and Xu, S. (2001) 'Gelatin: A valuable protein for food and pharmaceutical industries: Review', *Critical Reviews in Food Science and Nutrition*, 41(6), pp. 481–492. doi: 10.1080/20014091091904.

Du, S. *et al.* (2017) 'Overendocytosis of superparamagnetic iron oxide particles increases apoptosis and triggers autophagic cell death in human osteosarcoma cell under a spinning magnetic field', *Oncotarget*, 8(6), pp. 9410–9424. doi: 10.18632/oncotarget.14114.

Du, X. *et al.* (2019) '3D printing of mesoporous bioactive glass/silk fibroin composite scaffolds for bone tissue engineering', *Materials Science and Engineering C*. Elsevier, 103, p. 109731. doi: 10.1016/j.msec.2019.05.016.

Duan, R. *et al.* (2017) 'Polymer–lipid hybrid nanoparticles-based paclitaxel and etoposide

combinations for the synergistic anticancer efficacy in osteosarcoma', *Colloids and Surfaces B: Biointerfaces*. Elsevier B.V., 159, pp. 880–887. doi: 10.1016/j.colsurfb.2017.08.042.

Dwivedi, R. *et al.* (2020) 'Polycaprolactone as biomaterial for bone scaffolds: Review of literature', *Journal of Oral Biology and Craniofacial Research*. Elsevier, 10(1), pp. 381–388. doi: 10.1016/j.jobcr.2019.10.003.

Echave, M. C. *et al.* (2017) 'Progress of gelatin-based 3D approaches for bone regeneration', *Journal of Drug Delivery Science and Technology*, 42, pp. 63–74. doi: 10.1016/j.jddst.2017.04.012.

Ergul, N. M. *et al.* (2019) '3D printing of chitosan/ poly(vinyl alcohol) hydrogel containing synthesized hydroxyapatite scaffolds for hard-tissue engineering', *Polymer Testing*. Elsevier, 79(July), p. 106006. doi: 10.1016/j.polymertesting.2019.106006.

Fahimipour, F. *et al.* (2017) '3D printed TCP-based scaffold incorporating VEGF-loaded PLGA microspheres for craniofacial tissue engineering', *Dental Materials*. The Academy of Dental Materials, 33(11), pp. 1205–1216. doi: 10.1016/j.dental.2017.06.016.

Fang, Z. *et al.* (2017) 'Targeted osteosarcoma chemotherapy using RGD peptide-installed doxorubicin-loaded biodegradable polymeric micelle', *Biomedicine and Pharmacotherapy*. Elsevier Masson SAS, 85, pp. 160–168. doi: 10.1016/j.biopha.2016.11.132.

Feng, P. *et al.* (2020) 'Graphene oxide-driven interfacial coupling in laser 3D printed PEEK/PVA scaffolds for bone regeneration', *Virtual and Physical Prototyping*. Taylor & Francis, 15(2), pp. 211–226. doi: 10.1080/17452759.2020.1719457.

Feng, S. *et al.* (2019) 'Engineering of Bone- and CD44-Dual-Targeting Redox-Sensitive Liposomes for the Treatment of Orthotopic Osteosarcoma', *ACS Applied Materials and Interfaces*, 11(7), pp. 7357–7368. doi: 10.1021/acsami.8b18820.

Feng, X. *et al.* (2019) 'Comparison of 3D-printed mesoporous calcium silicate/polycaprolactone and mesoporous Bioacive glass/polycaprolactone scaffolds for bone regeneration', *Microporous and Mesoporous Materials*. Elsevier, 278(December 2018), pp. 348–353. doi: 10.1016/j.micromeso.2019.01.007.

Ferreira, A. M. *et al.* (2012) 'Collagen for bone tissue regeneration', *Acta Biomaterialia*. Acta Materialia Inc., 8(9), pp. 3191–3200. doi: 10.1016/j.actbio.2012.06.014.

Fu, S. *et al.* (2020) 'Silicone resin derived larnite / C sca ff olds via 3D printing for potential tumor therapy and bone regeneration', *Chemical Engineering Journal*. Elsevier, 382, p. 122928. doi: 10.1016/j.cej.2019.122928.

Gazzano, E. *et al.* (2019) 'Hyaluronated liposomes containing H2S-releasing doxorubicin are effective against P-glycoprotein-positive / doxorubicin-resistant osteosarcoma cells and xenografts', *Cancer Letters*. Elsevier, 456(April), pp. 29–39. doi: 10.1016/j.canlet.2019.04.029.

Ghorbani, F. *et al.* (2020) '3D printing of acellular scaffolds for bone defect regeneration : A review', *Materials Today Communications*, 22. doi: 10.1016/j.mtcomm.2020.100979.

Giannoudis, P. V. *et al.* (2008) 'The diamond concept - open questions', *Injury*, 39(SUPPL.2), p. S5. doi: 10.1016/S0020-1383(08)70010-X.

Giannoudis, P. V., Einhorn, T. A. and Marsh, D. (2007) 'Fracture healing: The diamond concept', *Injury*, 38(S4), pp. S3–S6.

Giansanti, L. *et al.* (2019) 'Influence of lipid composition on the ability of liposome loaded voacamine to improve the reversion of doxorubicin resistant osteosarcoma cells', *Chemistry and Physics of Lipids*. Elsevier, 223, p. 104781. doi: 10.1016/j.chemphyslip.2019.05.006.

Golafshan, N. *et al.* (2020) 'Tough magnesium phosphate-based 3D-printed implants induce bone regeneration in an equine defect model', *Biomaterials*, 261. doi: 10.1016/j.biomaterials.2020.120302.

Gómez-Cerezo, M. N. *et al.* (2020) 'The effect of biomimetic mineralization of 3D-printed mesoporous bioglass scaffolds on physical properties and in vitro osteogenicity', *Materials Science and Engineering C*. Elsevier, 109, p. 110572. doi: 10.1016/j.msec.2019.110572.

Gui, K. *et al.* (2019) 'Lipid-polymer nanoparticles with CD133 aptamers for targeted delivery of all-trans retinoic acid to osteosarcoma initiating cells', *Biomedicine and Pharmacotherapy*. Elsevier, 111, pp. 751–764. doi: 10.1016/j.biopha.2018.11.118.

Haghiralsadat, F. *et al.* (2018) 'Codelivery of doxorubicin and JIP1 siRNA with novel EphA2-targeted pegylated cationic nanoliposomes to overcome osteosarcoma multidrug resistance', *International Journal of Nanomedicine*, 13, pp. 3853–3866. doi: 10.2147/IJN.S150017.

Hassanajili, S. *et al.* (2019) 'Preparation and characterization of PLA/PCL/HA composite scaffolds using indirect 3D printing for bone tissue engineering', *Materials Science and Engineering C*. Elsevier, 104, p. 109960. doi: 10.1016/j.msec.2019.109960.

Heck, R. K. and Toy, P. C. (2017) 'Malignant Tumors of Bone', in *Campbell's Operative Orthopaedics*. 13th edn. Philadelphia: Elsevier, pp. 945–983. Available at: https://www.clinicalkey.com/#!/content/book/3-s2.0-B9780323374620000276?scrollTo=%23hl0000691.

Henderson, T. A. and Morries, L. D. (2015) ‘Near-infrared photonic energy penetration: Can infrared phototherapy effectively reach the human brain?’, *Neuropsychiatric Disease and Treatment*, 11, pp. 2191–2208. doi: 10.2147/NDT.S78182.

Heo, E. Y. *et al.* (2017) ‘Novel 3D printed alginate–BFP1 hybrid scaffolds for enhanced bone regeneration’, *Journal of Industrial and Engineering Chemistry*, 45, pp. 61–67. doi: 10.1016/j.jiec.2016.09.003.

Heo, S. Y. *et al.* (2019) ‘Fabrication and characterization of the 3D-printed polycaprolactone/fish bone extract scaffolds for bone tissue regeneration’, *Journal of Biomedical Materials Research - Part B Applied Biomaterials*, 107(6), pp. 1937–1944. doi: 10.1002/jbm.b.34286.

Hernández-González, A. C., Téllez-Jurado, L. and Rodríguez-Lorenzo, L. M. (2020) ‘Alginate hydrogels for bone tissue engineering, from injectables to bioprinting: A review’, *Carbohydrate Polymers*. Elsevier, 229, p. 115514. doi: 10.1016/j.carbpol.2019.115514.

Hernandez, I., Kumar, A. and Joddar, B. (2017) ‘A Bioactive Hydrogel and 3D Printed Polycaprolactone System for Bone Tissue Engineering’, *Gels*, 3(3), p. 26. doi: 10.3390/gels3030026.

Hoque, M. *et al.* (2015) ‘Gelatin Based Scaffolds for Tissue Engineering-a Review’, *Polymers Research Journal*, 9(1), pp. 15-32.

Huang, Q. wei, Wang, L. ping and Wang, J. ye (2014) ‘Mechanical properties of artificial materials for bone repair’, *Journal of Shanghai Jiaotong University (Science)*, 19(6), pp. 675–680. doi: 10.1007/s12204-014-1565-8.

Huang, T. *et al.* (2019) ‘3D-printed scaffolds of biomineralized hydroxyapatite nanocomposite on silk fibroin for improving bone regeneration’, *Applied Surface Science*, 467–468, pp. 345–353. doi: 10.1016/j.apsusc.2018.10.166.

Huang, X. *et al.* (2020) ‘Surface engineering of nanoparticles with ligands for targeted delivery to osteosarcoma’, *Colloids and Surfaces B: Biointerfaces*. Elsevier, 190, p. 110891. doi: 10.1016/j.colsurfb.2020.110891.

Iram, S. *et al.* (2017) ‘Gold nanoconjugates reinforce the potency of conjugated cisplatin and doxorubicin’, *Colloids and Surfaces B: Biointerfaces*. Elsevier B.V., 160, pp. 254–264. doi: 10.1016/j.colsurfb.2017.09.017.

Jahan, K. and Tabrizian, M. (2016) ‘Composite biopolymers for bone regeneration enhancement in bony defects’, *Biomaterials Science*. Royal Society of Chemistry, 4(1), pp.

25–39. doi: 10.1039/c5bm00163c.

Ju, P. *et al.* (2015) 'Differential cytotoxic effects of gold nanoparticles in different mammalian cell lines', *Journal of Hazardous Materials*. Elsevier B.V., 264(2014), pp. 303–312. doi: 10.1016/j.jhazmat.2013.11.031.

Khan, S. N. *et al.* (2005) 'The biology of bone grafting.', *The Journal of the American Academy of Orthopaedic Surgeons*, 13(1), pp. 77–86. doi: 10.5435/00124635-200501000-00010.

Kim, G. J. and Nie, S. (2005) 'Targeted cancer nanotherapy', *Materials Today*, 8(8 SUPPL.), pp. 28–33. doi: 10.1016/S1369-7021(05)71034-8.

Kim, H. *et al.* (2018) 'Gelatin/PVA scaffolds fabricated using a 3D-printing process employed with a low-temperature plate for hard tissue regeneration: Fabrication and characterizations', *International Journal of Biological Macromolecules*. Elsevier B.V., 120, pp. 119–127. doi: 10.1016/j.ijbiomac.2018.07.159.

Kim, J. Y. *et al.* (2018) 'Synergistic Effects of Beta Tri-Calcium Phosphate and Porcine-Derived Decellularized Bone Extracellular Matrix in 3D-Printed Polycaprolactone Scaffold on Bone Regeneration', *Macromolecular Bioscience*, 18(6), pp. 1–10. doi: 10.1002/mabi.201800025.

Komiya, S. *et al.* (1998) 'Role of Glutathione in Cisplatin Resistance in Osteosarcorna Cell Lines', *Jourimal of Orthopaedic Research*, 16(1), pp. 15–22. doi: 10.1002/jor.1100160104.

Kovács, D. *et al.* (2016) 'Silver nanoparticles defeat p53-positive and p53-negative osteosarcoma cells by triggering mitochondrial stress and apoptosis', pp. 1–13. doi: 10.1038/srep27902.

Kuttappan, S., Mathew, D. and Nair, M. B. (2016) 'Biomimetic composite scaffolds containing bioceramics and collagen/gelatin for bone tissue engineering - A mini review', *International Journal of Biological Macromolecules*. Elsevier B.V., 93, pp. 1390–1401. doi: 10.1016/j.ijbiomac.2016.06.043.

Lai, Y. *et al.* (2019) 'Osteogenic magnesium incorporated into PLGA/TCP porous scaffold by 3D printing for repairing challenging bone defect', *Biomaterials*, 197, pp. 207–219. doi: 10.1016/j.biomaterials.2019.01.013.

Lavrador, P., Gaspar, V. M. and Mano, J. F. (2018) 'Stimuli-responsive nanocarriers for delivery of bone therapeutics – Barriers and progresses', *Journal of Controlled Release*. Elsevier, 273, pp. 51–67. doi: 10.1016/j.jconrel.2018.01.021.

Lee, H. *et al.* (2018) 'Fabrication of micro/nanoporous collagen/dECM/silk-fibroin biocomposite scaffolds using a low temperature 3D printing process for bone tissue

regeneration', *Materials Science and Engineering C*. Elsevier, 84, pp. 140–147. doi: 10.1016/j.msec.2017.11.013.

Lee, S. H. and Jun, B. (2019) 'Silver Nanoparticles : Synthesis and Application for Nanomedicine'. *International Journal of Molecular Sciences*. doi: 10.3390/ijms20040865.

Li, M. *et al.* (2019) 'Composition design and medical application of liposomes', 164, pp. 640–653. doi: 10.1016/j.ejmech.2019.01.007.

Li, Y. *et al.* (2014) 'Stimuli-responsive cross-linked micelles for on-demand drug delivery against cancers ☆', *Advanced Drug Delivery Reviews*. Elsevier B.V., 66, pp. 58–73. doi: 10.1016/j.addr.2013.09.008.

Li, Y. *et al.* (2019) 'A hybrid 3D-printed aspirin-laden liposome composite scaffold for bone tissue engineering', *Journal of Materials Chemistry B*. Royal Society of Chemistry, 7(4), pp. 619–629. doi: 10.1039/C8TB02756K.

Lin, K. F. *et al.* (2016) 'Low-Temperature Additive Manufacturing of Biomimic Three-Dimensional Hydroxyapatite/Collagen Scaffolds for Bone Regeneration', *ACS Applied Materials and Interfaces*, 8(11), pp. 6905–6916. doi: 10.1021/acsami.6b00815.

Liu, K. *et al.* (2020) 'The design, fabrication and evaluation of 3D printed gHNTs/gMgO whiskers/PLLA composite scaffold with honeycomb microstructure for bone tissue engineering', *Composites Part B: Engineering*, 192. doi: 10.1016/j.compositesb.2020.108001.

Liu, Y. *et al.* (2018) '3D-printed scaffolds with bioactive elements-induced photothermal effect for bone tumor therapy', *Acta Biomaterialia*. Acta Materialia Inc., 73, pp. 531–546. doi: 10.1016/j.actbio.2018.04.014.

Logithkumar, R. *et al.* (2016) 'A review of chitosan and its derivatives in bone tissue engineering', *Carbohydrate Polymers*. Elsevier Ltd., 151, pp. 172–188. doi: 10.1016/j.carbpol.2016.05.049.

Low, S. A., Yang, J. and Kopeček, J. (2014) 'Bone-targeted acid-sensitive doxorubicin conjugate micelles as potential osteosarcoma therapeutics', *Bioconjugate Chemistry*, 25(11), pp. 2012–2020. doi: 10.1021/bc500392x.

Lu, Y. *et al.* (2018) 'Enhancing Osteosarcoma Killing and CT Imaging Using Ultrahigh Drug Loading and NIR-Responsive Bismuth Sulfide @ Mesoporous Silica Nanoparticles', *Advanced Healthcare Materials*, 1800602, pp. 1–12. doi: 10.1002/adhm.201800602.

Lu, Y. *et al.* (2020) 'Interface crosslinked mPEG- b -PAGE- b -PCL triblock copolymer micelles with high stability for anticancer drug delivery', *Colloids and Surfaces B: Biointerfaces*.

Elsevier, 189(January), p. 110830. doi: 10.1016/j.colsurfb.2020.110830.

Luetke, A. *et al.* (2014) 'Osteosarcoma treatment - Where do we stand? A state of the art review', *Cancer Treatment Reviews*. Elsevier Ltd, 40(4), pp. 523–532. doi: 10.1016/j.ctrv.2013.11.006.

Luo, G. *et al.* (2017) '13-93 bioactive glass/alginate composite scaffolds 3D printed under mild conditions for bone regeneration', *RSC Advances*. Royal Society of Chemistry, 7(20), pp. 11880–11889. doi: 10.1039/c6ra27669e.

Luo, Y. *et al.* (2018) '3D printing of concentrated alginate/gelatin scaffolds with homogeneous nano apatite coating for bone tissue engineering', *Materials and Design*. Elsevier Ltd, 146, pp. 12–19. doi: 10.1016/j.matdes.2018.03.002.

Ma, D., Wang, Y. and Dai, W. (2018) 'Silk fibroin-based biomaterials for musculoskeletal tissue engineering', *Materials Science and Engineering C*. Elsevier, 89(23), pp. 456–469. doi: 10.1016/j.msec.2018.04.062.

Ma, H. *et al.* (2016) 'A Bifunctional Biomaterial with Photothermal Effect for Tumor Therapy and Bone Regeneration', *Advanced Functional Materials*, 26(8), pp. 1197–1208. doi: https://doi.org/10.1002/adfm.201504142.

Ma, H. *et al.* (2018) '3D printing of high-strength bioscaffolds for the synergistic treatment of bone cancer', *NPG Asia Materials*. Springer US, 10(4), pp. 31–44. doi: 10.1038/s41427-018-0015-8.

Ma, Y. *et al.* (2019) 'Three-Dimensional Printing of Biodegradable Piperazine-Based Polyurethane-Urea Scaffolds with Enhanced Osteogenesis for Bone Regeneration', *ACS Applied Materials and Interfaces*, 11(9), pp. 9415–9424. doi: 10.1021/acsami.8b20323.

Majeed, S. *et al.* (2019) 'Bioengineered silver nanoparticles capped with bovine serum albumin and its anticancer and apoptotic activity against breast , bone and intestinal colon cancer cell lines', *Materials Science & Engineering C*. Elsevier, 102(March), pp. 254–263. doi: 10.1016/j.msec.2019.04.041.

Mantila Roosa, S. M. *et al.* (2010) 'The pore size of polycaprolactone scaffolds has limited influence on bone regeneration in an in vivo model', *Journal of Biomedical Materials Research - Part A*, 92(1), pp. 359–368. doi: 10.1002/jbm.a.32381.

Martin, V. *et al.* (2019) 'Engineering a multifunctional 3D-printed PLA-collagen-minocycline-nanoHydroxyapatite scaffold with combined antimicrobial and osteogenic effects for bone regeneration', *Materials Science and Engineering C*. Elsevier, 101, pp. 15–26. doi:

10.1016/j.msec.2019.03.056.

Martin, V. and Bettencourt, A. (2018) 'Bone regeneration: Biomaterials as local delivery systems with improved osteoinductive properties', *Materials Science and Engineering C*. Elsevier B.V., 82, pp. 363–371. doi: 10.1016/j.msec.2017.04.038.

Martínez-carmona, M., Lozano, D. and Vallet-regí, M. (2018) 'Lectin-conjugated pH-responsive mesoporous silica nanoparticles for targeted bone cancer treatment', *Acta Biomaterialia*, 65, pp. 393–404. doi: 10.1016/j.actbio.2017.11.007.

Martínez-Vázquez, F. J. *et al.* (2015) 'Fabrication of novel Si-doped hydroxyapatite/gelatine scaffolds by rapid prototyping for drug delivery and bone regeneration', *Acta Biomaterialia*, 15, pp. 200–209. doi: 10.1016/j.actbio.2014.12.021.

Marzec, M. *et al.* (2017) 'Development of polyurethanes for bone repair', *Materials Science & Engineering C*, 80(July), pp. 736–747. doi: 10.1016/j.msec.2017.07.047.

Melim, C. *et al.* (2020) 'The potential of micelleplexes as a therapeutic strategy for osteosarcoma disease', *3 Biotech*. Springer International Publishing, 10(4), pp. 1–15. doi: 10.1007/s13205-020-2142-5.

Melke, J. *et al.* (2016) 'Silk fibroin as biomaterial for bone tissue engineering', *Acta Biomaterialia*. Acta Materialia Inc., 31, pp. 1–16. doi: 10.1016/j.actbio.2015.09.005.

Meshkini, A. and Oveisi, H. (2017) 'Methotrexate-F127 conjugated mesoporous zinc hydroxyapatite as an efficient drug delivery system for overcoming chemotherapy resistance in osteosarcoma cells', *Colloids and Surfaces B: Biointerfaces*. Elsevier B.V., 158, pp. 319–330. doi: 10.1016/j.colsurfb.2017.07.006.

Mondal, S. *et al.* (2017) 'Hydroxyapatite coated iron oxide nanoparticles: A promising nanomaterial for magnetic hyperthermia cancer treatment', *Nanomaterials*, 7(12), pp. 1–15. doi: 10.3390/nano7120426.

Mondal, S. *et al.* (2020) 'Hydroxyapatite nano bioceramics optimized 3D printed poly lactic acid scaffold for bone tissue engineering application', *Ceramics International*. Elsevier Ltd and Techna Group S.r.l., 46(3), pp. 3443–3455. doi: 10.1016/j.ceramint.2019.10.057.

Montalbano, G. *et al.* (2018) 'Type I collagen and strontium-containing mesoporous glass particles as hybrid material for 3D printing of bone-like materials', *Materials*, 11(5). doi: 10.3390/ma11050700.

Murugan, B. and Krishnan, U. M. (2018) 'Chemoresponsive smart mesoporous silica systems – An emerging paradigm for cancer therapy', *International Journal of Pharmaceutics*. Elsevier,

553(1–2), pp. 310–326. doi: 10.1016/j.ijpharm.2018.10.026.

Narayanan, G. *et al.* (2016) 'Poly (lactic acid)-based biomaterials for orthopaedic regenerative engineering', *Advanced Drug Delivery Reviews*. Elsevier B.V., 107, pp. 247–276. doi: 10.1016/j.addr.2016.04.015.

Noy, J. M. *et al.* (2018) 'Direct Polymerization of the Arsenic Drug PENAO to Obtain Nanoparticles with High Thiol-Reactivity and Anti-Cancer Efficiency', *Bioconjugate Chemistry*, 29(2), pp. 546–558. doi: 10.1021/acs.bioconjchem.8b00032.

Osteopore™ (2019). Available at: https://osteopore.com (Accessed: 11 May 2020).

Özel, F. *et al.* (2019) 'A simple way to synthesize tartaric acid, ascorbic acid and their mixture coated superparamagnetic iron oxide nanoparticles with high saturation magnetisation and high stability against oxidation: Characterizations and their biocompatibility studies', *Journal of Magnetism and Magnetic Materials*. Elsevier B.V., 474(September 2018), pp. 654–660. doi: 10.1016/j.jmmm.2018.11.025.

Paris, J. L. *et al.* (2018) 'Mesoporous silica nanoparticles engineered for ultrasound-induced uptake by cancer cells', *Nanoscale*. Royal Society of Chemistry, pp. 6402–6408. doi: 10.1039/c8nr00693h.

Park, J. *et al.* (2018) 'Three dimensional cell printing with sulfated alginate for improved bone morphogenetic protein-2 delivery and osteogenesis in bone tissue engineering', *Carbohydrate Polymers*. Elsevier, 196, pp. 217–224. doi: 10.1016/j.carbpol.2018.05.048.

Pei, P. *et al.* (2017) 'The effect of calcium sulfate incorporation on physiochemical and biological properties of 3D-printed mesoporous calcium silicate cement scaffolds', *Microporous and Mesoporous Materials*. Elsevier Ltd, 241, pp. 11–20. doi: 10.1016/j.micromeso.2016.11.031.

Pérez-Rigueiro, J. *et al.* (2001) 'Tensile properties of silkworm silk obtained by forced silking', *Applied Polymer Science*, 82(8), pp. 1928–1935. doi: 10.1002/app.2038.

Pizzorno, J. (2014) 'Glutathione!', *Integrative Medicine: A Clinician's Journal*, 13(1), pp. 8–12.

Popescu, R. C. *et al.* (2017) 'Fabrication and cytotoxicity of gemcitabine-functionalized magnetite nanoparticles', *Molecules*, 22(7). doi: 10.3390/molecules22071080.

Prasadh, S. and Wong, R. C. W. (2018) 'Unraveling the mechanical strength of biomaterials used as a bone scaffold in oral and maxillofacial defects', *Oral Science International*. Japanese Stomatological Society, 15(2), pp. 48–55. doi: 10.1016/S1348-8643(18)30005-3.

Raghubir, M. *et al.* (2020) 'Osteosarcoma growth suppression by riluzole delivery via iron

oxide nanocage in nude mice', *Oncology Reports*, 43(1), pp. 169–176. doi: 10.3892/or.2019.7420.

Rahim, M. *et al.* (2014) 'Glycation-assisted synthesized gold nanoparticles inhibit growth of bone cancer cells', *Colloids and Surfaces B: Biointerfaces*. Elsevier B.V., 117, pp. 473–479. doi: 10.1016/j.colsurfb.2013.12.008.

Rainer, A. *et al.* (2008) 'Fabrication of bioactive glass-ceramic foams mimicking human bone portions for regenerative medicine', *Acta Biomaterialia*, 4(2), pp. 362–369. doi: 10.1016/j.actbio.2007.08.007.

Raj, S. *et al.* (2019) 'Specific targeting cancer cells with nanoparticles and drug delivery in cancer therapy', *Seminars in Cancer Biology*. Elsevier, pp. 0–1. doi: 10.1016/j.semcancer.2019.11.002.

Rajabnia, T. and Meshkini, A. (2018) 'Fabrication of adenosine 5 ′ -triphosphate-capped silver nanoparticles : Enhanced cytotoxicity e ffi cacy and targeting e ff ect against tumor cells', 65(June 2017), pp. 186–196. doi: 10.1016/j.procbio.2017.11.003.

Rajzer, I. *et al.* (2018) 'Layered gelatin/PLLA scaffolds fabricated by electrospinning and 3D printing- for nasal cartilages and subchondral bone reconstruction', *Materials and Design*, 155, pp. 297–306. doi: 10.1016/j.matdes.2018.06.012.

Rastinehad, A. R. *et al.* (2019) 'Gold nanoshell-localized photothermal ablation of prostate tumors in a clinical pilot device study', *Proceedings of the National Academy of Sciences of the United States of America*, 116(37), pp. 18590–18596. doi: 10.1073/pnas.1906929116.

Rayamajhi, S. *et al.* (2020) 'pH-responsive cationic liposome for endosomal escape mediated drug delivery', *Colloids and Surfaces B: Biointerfaces*. Elsevier, 188, p. 110804. doi: 10.1016/j.colsurfb.2020.110804.

Reith, J. D. (2018) 'Bone and Joints', in *Rosai and Ackerman's Surgical Pathology*. 11th edn. Elsevier, pp. 1740–1809. Available at: https://www.clinicalkey.com/#!/content/book/3-s2.0-B9780323263399000408?scrollTo=%23top.

Ribas, R. G. *et al.* (2019) 'Current advances in bone tissue engineering concerning ceramic and bioglass scaffolds: A review', *Ceramics International*. Elsevier Ltd and Techna Group S.r.l., 45(17), pp. 21051–21061. doi: 10.1016/j.ceramint.2019.07.096.

Roberts, T. T. and Rosenbaum, A. J. (2012) 'Bone grafts, bone substitutes and orthobiologics the bridge between basic science and clinical advancements in fracture healing', *Organogenesis*, 8(4), pp. 114–124. doi: 10.4161/org.23306.

Ruttala, H. B. *et al.* (2018) ‘Emerging potential of stimulus-responsive nanosized anticancer drug delivery systems for systemic applications’, *Archives of Pharmacal Research*. Pharmaceutical Society of Korea, 41(2), pp. 111–129. doi: 10.1007/s12272-017-0995-x.

Sábio, R. M. *et al.* (2019) ‘New insights towards mesoporous silica nanoparticles as a technological platform for chemotherapeutic drugs delivery’, *International Journal of Pharmaceutics*. Elsevier, 564(April), pp. 379–409. doi: 10.1016/j.ijpharm.2019.04.067.

Sachlos, E. *et al.* (2006) ‘Collagen Scaffolds Reinforced with Biomimetic Composite Nano-Sized Carbonate-Substituted Hydroxyapatite Crystals and Shaped by Rapid Prototyping to Contain Internal Microchannels’, *Tissue Engineering*, 12(9). doi:10.1089/ten.2006.12.2479

Samavedi, S., Whittington, A. R. and Goldstein, A. S. (2013) ‘Calcium phosphate ceramics in bone tissue engineering: A review of properties and their influence on cell behavior’, *Acta Biomaterialia*. Acta Materialia Inc., 9(9), pp. 8037–8045. doi: 10.1016/j.actbio.2013.06.014.

Sánchez-Paradinas, S. *et al.* (2014) ‘Enhanced cytotoxic activity of bile acid cisplatin derivatives by conjugation with gold nanoparticles’, *Journal of Inorganic Biochemistry*. Elsevier B.V., 131, pp. 8–11. doi: 10.1016/j.jinorgbio.2013.10.021.

Santoro, M., Tatara, A. M. and Mikos, A. G. (2014) ‘Gelatin carriers for drug and cell delivery in tissue engineering’, *Journal of Controlled Release*. Elsevier B.V., 190, pp. 210–218. doi: 10.1016/j.jconrel.2014.04.014.

Saravanan, S., Leena, R. S. and Selvamurugan, N. (2016) ‘Chitosan based biocomposite scaffolds for bone tissue engineering’, *International Journal of Biological Macromolecules*. Elsevier B.V., 93, pp. 1354–1365. doi: 10.1016/j.ijbiomac.2016.01.112.

Sarkar, N. and Bose, S. (2019) ‘Liposome-Encapsulated Curcumin-Loaded 3D Printed Scaffold for Bone Tissue Engineering’, *ACS Applied Materials and Interfaces*, 11(19), pp. 17184–17192. doi: 10.1021/acsami.9b01218.

Shuai, C. *et al.* (2020) ‘Magnetically actuated bone scaffold: Microstructure, cell response and osteogenesis’, *Composites Part B: Engineering*. Elsevier Ltd, 192(January), p. 107986. doi: 10.1016/j.compositesb.2020.107986.

Singh, P. *et al.* (2018) ‘Gold nanoparticles in diagnostics and therapeutics for human cancer’, *International Journal of Molecular Sciences*, 19(7). doi: 10.3390/ijms19071979.

Song, Y. *et al.* (2018) ‘Nano-biphasic calcium phosphate/polyvinyl alcohol composites with enhanced bioactivity for bone repair via low-temperature three-dimensional printing and loading with platelet-rich fibrin’, *International Journal of Nanomedicine*, 13, pp. 505–523. doi:

10.2147/IJN.S152105.

Steckiewicz, K. P. *et al.* (2019) 'Impact of gold nanoparticles shape on their cytotoxicity against human osteoblast and osteosarcoma in in vitro model. Evaluation of the safety of use and anti-cancer potential', *Journal of Materials Science: Materials in Medicine*. Springer US, 30(2), pp. 1–15. doi: 10.1007/s10856-019-6221-2.

Steckiewicz, K. P. *et al.* (2020) 'Assessment of anti-tumor potential and safety of application of glutathione stabilized gold nanoparticles conjugated with chemotherapeutic', *Int. J. Med. Sci.*, 17. doi: doi:10.7150/ijms.40159.

Su, K. and Wang, C. (2015) 'Recent advances in the use of gelatin in biomedical research', *Biotechnology Letters*. Springer Netherlands, 37(11), pp. 2139–2145. doi: 10.1007/s10529-015-1907-0.

Tajbakhsh, S. and Hajiali, F. (2017) 'A comprehensive study on the fabrication and properties of biocomposites of poly(lactic acid)/ceramics for bone tissue engineering', *Materials Science and Engineering C*. Elsevier B.V., 70, pp. 897–912. doi: 10.1016/j.msec.2016.09.008.

Tapeinos, C. *et al.* (2018) 'CeO2 Nanoparticles-Loaded pH-Responsive Microparticles with Antitumoral Properties as Therapeutic Modulators for Osteosarcoma', *ACS Omega*, 3(8), pp. 8952–8962. doi: 10.1021/acsomega.8b01060.

Tarafder, S. *et al.* (2013) 'Microwave-sintered 3D printed tricalcium phosphate scaffolds for bone tissue engineering', *JOURNAL OF TISSUE ENGINEERING AND REGENERATIVE MEDICINE*, 7, pp. 631–641. doi: 10.1002/term.555.

Torres, M. L. *et al.* (2019) 'Purification of alginate improves its biocompatibility and eliminates cytotoxicity in matrix for bone tissue engineering', *Algal Research*. Elsevier, 40(October 2018), p. 101499. doi: 10.1016/j.algal.2019.101499.

Toy, P. C. and Heck, R. K. (2017) 'General Principles of Tumors', in *Campbell's Operative Orthopaedics*. 13th edn. Philadelphia: Elsevier, pp. 829–895. Available at: https://0-www-clinicalkey-com.innopac.wits.ac.za/#!/content/book/3-s2.0-B9780323374620000240?scrollTo=%23top.

Tudose, M. *et al.* (2017) 'Lipoic acid functionalized SiO 2 @ Ag nanoparticles . Synthesis , characterization and evaluation of biological activity', 79, pp. 499–506. doi: 10.1016/j.msec.2017.05.083.

Usta, M. *et al.* (2003) 'Behavior and properties of neat and filled gelatins', *Biomaterials*, 24(1), pp. 165–172. doi: 10.1016/S0142-9612(02)00274-0.

Vegerhof, A. *et al.* (2016) ‘Targeted magnetic nanoparticles for mechanical lysis of tumor cells by low-amplitude alternating magnetic field’, *Materials*, 9(11). doi: 10.3390/ma9110943.

Velioglu, Z. B. *et al.* (2019) ‘3D-printed poly(lactic acid) scaffolds for trabecular bone repair and regeneration: scaffold and native bone characterization’, *Connective Tissue Research*. Taylor & Francis, 60(3), pp. 274–282. doi: 10.1080/03008207.2018.1499732.

Venkatesan, J. *et al.* (2015) ‘Alginate composites for bone tissue engineering: A review’, *International Journal of Biological Macromolecules*. Elsevier B.V., 72, pp. 269–281. doi: 10.1016/j.ijbiomac.2014.07.008.

Venkatraman, S. K. and Swamiappan, S. (2020) ‘Review on calcium- and magnesium-based silicates for bone tissue engineering applications’, *Journal of Biomedical Materials Research - Part A*, (February), pp. 1546–1562. doi: 10.1002/jbm.a.36925.

Wang, C. *et al.* (2020) ‘3D printing of bone tissue engineering scaffolds’, 5, pp. 82–91. doi: 10.1016/j.bioactmat.2020.01.004.

Wang, H. *et al.* (2020) ‘Integrative treatment of anti-tumor/bone repairing by combination of MoS2 nanosheets with 3D printed bioactive borosilicate glass scaffolds’, *Chemical Engineering Journal*. Elsevier, 396(December 2019), p. 125081. doi: 10.1016/j.cej.2020.125081.

Wang, S. Y. *et al.* (2020) ‘Recent advances of drug delivery nanocarriers in osteosarcoma treatment’, *Journal of Cancer*, 11(1), pp. 69–82. doi: 10.7150/jca.36588.

Wang, Y. J., Jeng, U. S. and Hsu, S. H. (2018) ‘Biodegradable Water-Based Polyurethane Shape Memory Elastomers for Bone Tissue Engineering’, *ACS Biomaterials Science and Engineering*, 4(4), pp. 1397–1406. doi: 10.1021/acsbiomaterials.8b00091.

Wei, J. *et al.* (2009) ‘Preparation and characterization of bioactive mesoporous wollastonite - Polycaprolactone composite scaffold’, *Biomaterials*. Elsevier Ltd, 30(6), pp. 1080–1088. doi: 10.1016/j.biomaterials.2008.10.046.

White, T. D., Black, M. T. and Folkens, P. A. (2012) ‘Bone Biology and Variation’, *Human Osteology*, (Chapter 21), pp. 25–42. doi: 10.1016/b978-0-12-374134-9.50003-9.

Wu, C. *et al.* (2011) ‘Three-dimensional printing of hierarchical and tough mesoporous bioactive glass scaffolds with a controllable pore architecture, excellent mechanical strength and mineralization ability’, *Acta Biomaterialia*. Acta Materialia Inc., 7(6), pp. 2644–2650. doi: 10.1016/j.actbio.2011.03.009.

Xi, Y. *et al.* (2019) ‘Dual targeting curcumin loaded alendronate-hyaluronan- octadecanoic

acid micelles for improving osteosarcoma therapy', *International Journal of Nanomedicine*, 14, pp. 6425–6437. doi: 10.2147/IJN.S211981.

Xiao, D. *et al.* (2020) 'The role of calcium phosphate surface structure in osteogenesis and the mechanisms involved', *Acta Biomaterialia*. Elsevier Ltd, 106, pp. 22–33. doi: 10.1016/j.actbio.2019.12.034.

Xiong, L. *et al.* (2016) 'Magnetic Core-Shell Silica Nanoparticles with Large Radial Mesopores for siRNA Delivery', *Small (Weinheim an der Bergstrasse, Germany)*, 12(34), pp. 4735–4742. doi: 10.1002/smll.201600531.

Yan, X. *et al.* (2004) 'Highly ordered mesoporous bioactive glasses with superior in vitro bone-forming bioactivities', *Angewandte Chemie - International Edition*, 43(44), pp. 5980–5984. doi: 10.1002/anie.200460598.

Yan, Y. *et al.* (2019) 'Vascularized 3D printed scaffolds for promoting bone regeneration', *Biomaterials*. Elsevier, 190–191, pp. 97–110. doi: 10.1016/j.biomaterials.2018.10.033.

Yang, F. *et al.* (2018) 'pH-responsive mesoporous ZSM-5 zeolites/chitosan core-shell nanodisks loaded with doxorubicin against osteosarcoma', *Materials Science and Engineering C*. Elsevier, 85(December 2017), pp. 142–153. doi: 10.1016/j.msec.2017.12.024.

Yang, Z. *et al.* (2016) 'Nonlinear Behavior of Gelatin Networks Reveals a Hierarchical Structure', *Biomacromolecules*, 17(2), pp. 590–600. doi: 10.1021/acs.biomac.5b01538.

Yang, Z. *et al.* (2020) 'Poly(ethylene glycol)-sheddable reduction-sensitive polyurethane micelles for triggered intracellular drug delivery for osteosarcoma treatment', *Journal of Orthopaedic Translation*. Elsevier Ltd, 21(xxxx), pp. 57–65. doi: 10.1016/j.jot.2019.11.001.

Yin, X. *et al.* (2017) 'Chitooligosaccharides Modified Reduction-Sensitive Liposomes: Enhanced Cytoplasmic Drug Delivery and Osteosarcomas-Tumor Inhibition in Animal Models', *Pharmaceutical Research*. Pharmaceutical Research, 34(10), pp. 2172–2184. doi: 10.1007/s11095-017-2225-0.

Yin, X. *et al.* (2018) 'Estrogen-functionalized liposomes grafted with glutathione-responsive sheddable chotooligosaccharides for the therapy of osteosarcoma', *Drug Delivery*. Informa Healthcare USA, Inc, 25(1), pp. 900–908. doi: 10.1080/10717544.2018.1458920.

Yu, Z. *et al.* (2018) 'Epidermal growth factor receptor aptamer-conjugated polymer-lipid hybrid nanoparticles enhance salinomycin delivery to osteosarcoma and cancer stem cells', *Experimental and Therapeutic Medicine*, 15(2), pp. 1247–1256. doi: 10.3892/etm.2017.5578.

Zaharin, H. A. *et al.* (2018) 'Effect of unit cell type and pore size on porosity and mechanical

behavior of additively manufactured Ti6Al4V scaffolds', *Materials*, 11(12). doi: 10.3390/ma11122402.

Zelzer, E. *et al.* (2002) 'Skeletal defects in VEGF120/120 mice reveal multiple roles for VEGF in skeletogenesis', *Development*, 129(8), pp. 1893–1904.

Zhang, D. *et al.* (2018) 'The development of collagen based composite scaffolds for bone regeneration', *Bioactive Materials*. Elsevier Ltd, 3(1), pp. 129–138. doi: 10.1016/j.bioactmat.2017.08.004.

Zhang, J. *et al.* (2014) 'Calcium phosphate cements for bone substitution: Chemistry, handling and mechanical properties', *Acta Biomaterialia*. Acta Materialia Inc., 10(3), pp. 1035–1049. doi: 10.1016/j.actbio.2013.11.001.

Zhang, W. *et al.* (2020) '3D printed composite scaffolds with dual small molecule delivery for mandibular bone regeneration', *Biofabrication*, In Press(May), pp. 0–14. Available at: https://doi.org/10.1088/1758-5090/ab906e.

Zhang, Y. *et al.* (2016) '3D-printed bioceramic scaffolds with a Fe3O4/graphene oxide nanocomposite interface for hyperthermia therapy of bone tumor cells', *Journal of Materials Chemistry B*. Royal Society of Chemistry, 4(17), pp. 2874–2886. doi: 10.1039/c6tb00390g.

Zhang, Y. *et al.* (2017) '3D-printed bioceramic scaffolds with antibacterial and osteogenic activity', *Biofabrication*, 9(2). doi: https://doi.org/10.1088/1758-5090/aa6ed6.

Zhao, H. *et al.* (2018) 'Effect of porous structure and pore size on mechanical strength of 3D-printed comby scaffolds', *Materials Letters*. Elsevier B.V., 223, pp. 21–24. doi: 10.1016/j.matlet.2018.03.205.

Zhao, L. *et al.* (2019) 'Polydopamine-based surface modification of paclitaxel nanoparticles for osteosarcoma targeted therapy', *Nanotechnology*. IOP Publishing, 30(25). doi: 10.1088/1361-6528/ab055f.

Zhu, M. *et al.* (2016) 'Three-dimensional printing of cerium-incorporated mesoporous calcium-silicate scaffolds for bone repair', *Journal of Materials Science*. Springer US, 51(2), pp. 836–844. doi: 10.1007/s10853-015-9406-1.

CHAPTER.3. DEVELOPMENT OF A COMPOSITE HYDROGEL IMPLANT FOR APPLICATION IN OSTEOSARCOMA

3.1 Introduction

There is a need for the development of patient-customised implants for the individual patient (Howard *et al.*, 2008) A method of ensuring customisability of implants would be to ensure that the implant may be mouldable to fit the defect site perfectly. Researchers have previously demonstrated the possibility of this by using lyophilisation to allow implantable scaffolds to take the shape of the mould (Sachlos *et al.*, 2006; Hassanajili *et al.*, 2019). However, lyophilisation requires adequate freezing time and a lyophilising machine which may not be available in certain areas. Therefore, implants need to possess an inherent moulding ability.

Hydrogels are polymeric networks with a hydrophilic nature that possess the capacity to absorb up to thousands of times their dry weight in water (Hoffman, 2012). The high-water content of hydrogels allows them to exhibit biocompatibility and can be applied in tissue regeneration. Hydrogels have been used for a variety of biomedical applications including the drug delivery of small molecules proteins (Mandal *et al.*, 2020). Hydrogels possess the ability to integrate with surrounding tissue and this advantageous as it bypasses the need for surgical removal. Furthermore, hydrogel raw materials are easy to obtain (Silva, Fabry and Boccaccini, 2014; Bai *et al.*, 2018).

Alginate is a natural polymer originating from brown algae (Venkatesan *et al.*, 2015) and can form hydrogels by ionic crosslinking with multivalent cations (Hernández-González, Téllez-Jurado and Rodríguez-Lorenzo, 2020). Alginate is deficient in the required biological properties that can induce bone formation (Park *et al.*, 2018), and also lacks the required mechanical strength (Venkatesan *et al.*, 2015) for application in bone regeneration. However, alginates have been still used in bone regeneration as they biocompatible, can fill irregularly shape defects and are suitable vehicles for the delivery of drugs and may be combined with other polymers and molecules to attain the required biological properties for bone regeneration. To overcome the lack of mechanical properties, alginate may be used in combination with other natural or synthetic osteo-compatible biopolymers used in bone regeneration. Alginate is also widely available and cost-effective (Lee and Mooney, 2012; Venkatesan *et al.*, 2015).

Polyacrylamide (PAAM) is a synthetic polymer that has been widely used as it is hydrophilic and non-toxic (Fang *et al.*, 2019). Polyacrylamide is also biocompatible, stable *in vivo*, non-immunogenic and has been used in contact lenses and drug treatment and has great potential

for biomedical applications (Guo, Yuan and Chi, 2014; Saber-Samandari *et al.*, 2016). However, PAAM- based hydrogels are usually brittle (Fang *et al.*, 2019) and its monomer, acrylamide is toxic (Saber-Samandari *et al.*, 2016). Previous studies concerning bone tissue engineering has seen PAAM has been combined with Dextran (Fang *et al.*, 2019) and cellulose and hydroxyapatite (Saber-Samandari *et al.*, 2016).

Double Network (DN) hydrogels are tough hydrogels with high mechanical strength that have the potential for a variety of applications including tissue engineering (Gu *et al.*, 2018). Among them, Alginate-Polyacrylamide (ALG-PAAM) have gained considerable interest as biomaterials for biomedical applications (Darnell *et al.*, 2013; Zheng *et al.*, 2017; Wang, Lou and Qiu, 2019), whereby ionically crosslinked alginate is one network and covalently crosslinked polyacrylamide is the other network. Previously, Zheng et al. researched ALG-PAAM hydrogels with the addition of demineralised bone matrix and concluded that the system had potential for bone regeneration (Zheng *et al.*, 2017). However, to the best of our knowledge, no ALG-PAAM hydrogel was incorporated with bioglass and tested for application in bone regeneration.

As discussed in Chapter 1 and ideal bone implant should possess at least three of the of the five characteristics described by the diamond concept (Giannoudis *et al.*, 2008) namely; Osteoconduction, growth factors (osteoinduction), mechanical properties, vascularization (angiogenesis) and, osteogenesis as well as possess the appropriate pore size and porosity. Implants derived from bioceramics (such a bioglass) are structurally, compositionally and mechanistically similar to the apatite present in bone tissue (Wang *et al.*, 2020).

Bioglass is osteoconductive and osteoproductive (Rainer *et al.*, 2008) and thus already possesses two of the three required criteria set out by the diamond concept. However, bioglass tends to have weaker mechanical properties when used alone which restricts its use (Mabrouk *et al.*, 2014). Therefore, it would be important incorporate and combine bioglass with other polymers. In this chapter, the best ALG-PAAM implantable hydrogel formulation is determined so that bioglass may be incorporated into it in the next chapter.

3.2 Materials

Alginic acid, sodium salt (viscosity of 20.000-40.000 cps) (SA), N,N'-Methylenebisacrylamide (MBIS), tetramethylethylenediamine (TEMED), Acrylamide, Ammonium persulfate (APS) Tetraethyl orthosilicate (TEOS) was obtained from Sigma Aldrich (Darmstadt, Germany).
Ferric chloride hexahydrate ($FeCl_3$), Calcium Nitrate was obtained from ACE pharmaceuticals. The water used in this study was Mille-Q water from a Millipore Water Purification System (Merck Chemicals GmbH, Darmstadt, Germany).

3.3 Methods

3.3.1 Hydrogel Fabrication to determine the best cross linker

3.3.1.1 Hydrogel Fabrication

Tough implantable hydrogels were synthesised according to a briefly modified method reported by (Wang, Lou and Qiu, 2019) was followed. Briefly, a two-step method was followed. Alginate was dissolved to form a 2% w/v, 4% w/v and 6% w/v solution. Thereafter, Acrylamide monomer (1200 mg) was added to 10 mL of each solution alginate solution. 3 mg of N,N'-Methylenebisacrylamide (MBIS) was then added to each solution. This solution was subsequently put in an ice-bath. Following this, 1mL of Ammonium persulfate (APS) solution 26 mg/mL was added to each solution, followed by 5 µL of Tetramethylethylenediamine (TEMED).

The solution was mixed in ice bath for 15 minutes to ensure homogeneity then transferred to glass tubes and allowed to polymerise for 24 hours at ambient temperature.

After removal from glass tubes, the Alginate-Polyacrylamide (ALG-PAAM) hydrogels were thoroughly washed with deionised water to remove any unreacted reagents. Subsequently the hydrogels were immersed in 0,3 M $FeCl_3$ and 0,3 M $CaCl_3$ cross linker solution overnight (Li *et al.*, 2017; Wang, Lou and Qiu, 2019). 0,3 M of each crosslinker was used as a standard comparator concentration it established in previously published studies (Li *et al.*, 2017; Wang, Lou and Qiu, 2019). The hydrogels were then washed to remove any residual crosslinker.

3.3.1.2 Assessment of mechanical strength to determine best crosslinker:

As prepared hydrogel implants were used to test mechanical strength. Tests were conducted using a 50 kg load cell on cylindrical hydrogels of diameter 25 mm and height of 12,64 mm. The method used to conduct the test was adapted from (Cuadros, Erices and Aguilera, 2015). The compressive strength was measured using a compression platen with a test speed of 1,2 mm/min, at 80% strain so as to prevent harm to the instrument. Human bones are more often undergo compression stress and the usage of compression tests as a method to assess biomaterials bone regeneration potential has been widely accepted. Therefore mechanical behaviour of the hydrogel implants were assessed by compression (Mabrouk *et al.*, 2014).

3.3.2 The Fabrication of hydrogel implants to establish the optimal concentration of the best crosslinker.

3.3.2.1 Synthesis of hydrogel implants with different crosslinker concentrations

The same two-step method of fabricating the hydrogel was followed as above. After removal from glass tubes, the ALG-PAAM hydrogels were thoroughly washed with deionised water to remove any unreacted reagents and were immersed in different concentrations of $FeCl_3$ (0,2 M, 0,3 M and 0,4 M) to establish the best concentration of $FeCl_3$ to use. Hereafter the hydrogel implants were denoted as 0,2DN hydrogel, 0,3DN hydrogel and 0,4DN hydrogel.

3.3.2.2 Assessment of hydrogel implants synthesised with different cross-linker concentrations to establish the optimal concentration of the best crosslinker

To assess the capabilities of these hydrogels, swelling, mechanical tests and imaging were conducted in order to establish the optimal concentration.

3.3.2.3 Assessment of mechanical strength of the hydrogel implants to establish the optimal concentration of best crosslinker

As prepared hydrogels were used to test mechanical strength. Tests were conducted on cylindrical hydrogel implants of diameter 25 mm and height of 12,64 mm. The compressive strength was measured using a compression platen with a test speed of 1,2 mm/min, at 80% strain so as to prevent harm to the instrument. The method used to conduct the test was adapted from (Cuadros, Erices and Aguilera, 2015).

3.3.2.4 Assessment of swelling of the hydrogel implants to establish the optimal concentration of best crosslinker

Hydrogel implants immersed in the various concentrations of $FeCl_3$ crosslinking solutions were air dried. Dry weights of the hydrogels were recorded then immersed in 0,9% of saline solution. At each time point, hydrogel implants were removed from the saline solution, blotted dry then weighed. The following equation was used to determine the swelling ratio percentage:

$$\text{Swelling ratio \%} = \frac{(Wf - Wi)}{Wi} x100 \qquad \text{Equation 3.1}$$

Where Wi is the initial dry weight of the hydrogel implants and Wf is the weight of the hydrogel implants at each time point.

Swelling ratio % was conducted in triplicate and data was recorded as a mean ± SD (n=3)

3.3.2.5 Assessment of morphology of the hydrogel implant with the best crosslinker concentration

The hydrogel with from the best $FeCl_3$ crosslinking solution was then determined from the above assessments of mechanical and swelling. This hydrogel implant was then selected and imaged under SEM. Scanning Electron Microscopy (SEM) was utilised to determine the morphology of the sample using a SIGMA 03-39 field emission scanning electron microscope (Zeiss, Jena, Germany). Cross-section samples were cut from the middle of the hydrogel implants and sputter coated with 30 nm of carbon and subsequently analysed at different magnifications.

3.3.2.6 Assessment of mouldability

To assess initial mouldability of the hydrogel implants, a capped needle was inserted into mixture after it was transferred to glass tubes. After 24 hours, the capped needle was removed and pictures were taken to assess whether the hydrogel implants could maintain the shape of the void left after the capped needle was removed. The assessment was done before immersion into $FeCl_3$ to form the double network.

3.3.3 Hydrogel Fabrication to induce macro-pores after determining the optimal cross-linking concentration:

After determining the best concentration of $FeCl_3$ and Alginate to use, the same two-step method as described above was used with one minor addition.

After the solution was mixed in ice bath for 15 min to ensure homogeneity then transferred to glass tubes containing varying sodium bicarbonate percentages (1-5% w/v). The solution was mixed with the sodium bicarbonate and allowed to polymerise for 24 hours at ambient temperature (Huh, Baek and Park, 2005). After removal from glass tubes, the ALG-PAAM hydrogels were thoroughly washed with deionised water to remove any unreacted reagents. Subsequently the hydrogels were immersed in 0,3 M $FeCl_3$ cross linker solution overnight (Li *et al.*, 2017; Wang, Lou and Qiu, 2019). The hydrogels were then thoroughly washed to remove any residual crosslinker before they were airdried for further characterisation under SEM, using a SIGMA 03-39 field emission scanning electron microscope (Zeiss, Jena, Germany). Cross-section samples were cut from the middle of the hydrogel implants and sputter coated with 30 nm of carbon and subsequently analysed. **Figure 3.1** illustrates the method of synthesis with sodium bicarbonate.

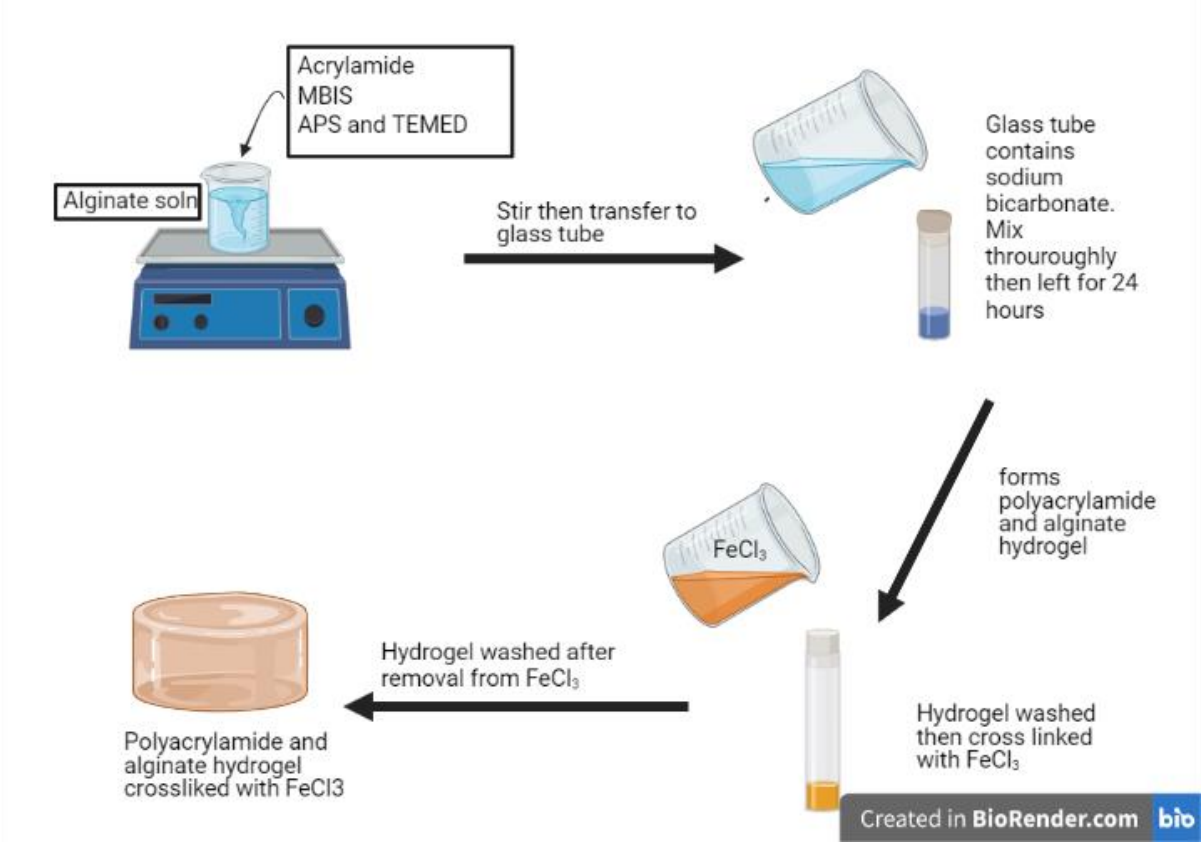


Figure 3.1: Illustration of the method used to impart pores to the double network hydrogel. Illustrated using biorender.

3.4 Results and discussion

3.4.1 Hydrogel Fabrication to assess the best cross linker

As the alginate concentration of the double network hydrogel increased, so did the strength of the double network hydrogel. The mechanical strength of $FeCl_3$ as the alginate crosslinker proved to have greater strength than $CaCl_2$ as a crosslinker. At 8% w/v, the alginate viscosity was extremely thick. This viscosity was therefore excluded as ensuring even mixing of reagents would not be guaranteed. 6% w/v alginate crosslinked with $FeCl_3$ displayed the best mechanical strengths and was selected for further characterisation. **Table 3.1** displays the different strengths that the double network hydrogels possessed as the concentration of alginate increased.

Table 3.1: Different alginate concentrations used to form the double network hydrogel

Alginate concentration	$CaCl_2$ Strength (MPa)	$FeCl_3$ Strength (MPa)
2% w/v	0,020745 ± 0,000469597	0,03967 ± 0,000891885
4% w/v	0,04183 ± 0,000986717	1,155633 ± 0,089547548
6% w/v	0,122033 ± 0,003198691	1,377033 ± 0,031926374
8% w/v	Alginate viscosity very thick. Mixing reagents became difficult at this viscosity.	

3.4.2 Hydrogel Fabrication to establish the optimal concentration of the best crosslinker:

After $FeCL_3$ was identified as the ideal crosslinker, three concentrations of $FeCL_3$ (0,2 M, 0,3 M and 0,4 M) were used to test out swelling and strength capacities of the double network hydrogel to identify the best concentration of $FeCL_3$. **Table 3.2** details the strength capacities of the double network hydrogel at the different concentrations while **Figure 3.2** displays the swelling profiles of the double network hydrogels at different concentrations.

Table 3.2: The strength capabilities of the double network hydrogel at different $FeCl_3$ concentrations.

$FeCl_3$ Concentration	Compressive strength (MPa)
0,2 M	1,301167 ± 0,049611
0,3 M	1,377933 ± 0,033112
0,4 M	1,4542 ± 0,13087

The 0,4 M DN hydrogels displayed the lowest swelling capacity at 28 days at only 294,050% ± 4,37081. However, this DN hydrogel had the best mechanical strength at 1,454 ± 0,131 MPa. 0,2DN hydrogels displayed the lowest mechanical strength of 1,301 ± 0,0496 MPa but had the highest swelling capacity at 360,407% ± 2,47909. The intermediate concentration, 0,3DN hydrogels, possessed a swelling capacity of over 300%- 331,467% ± 6,56201 and a mechanical strength of 1,378 ± 0,0331 MPa. The swelling profile graph display that even from 24 hours, 0,4DN hydrogels had lesser swelling at 211,838% ± 2,0619 compared to 0,3DN hydrogels and 0,2DN hydrogels which were at 229,120% ± 7,170 and 235, 597 % ± 4,366% respectively.

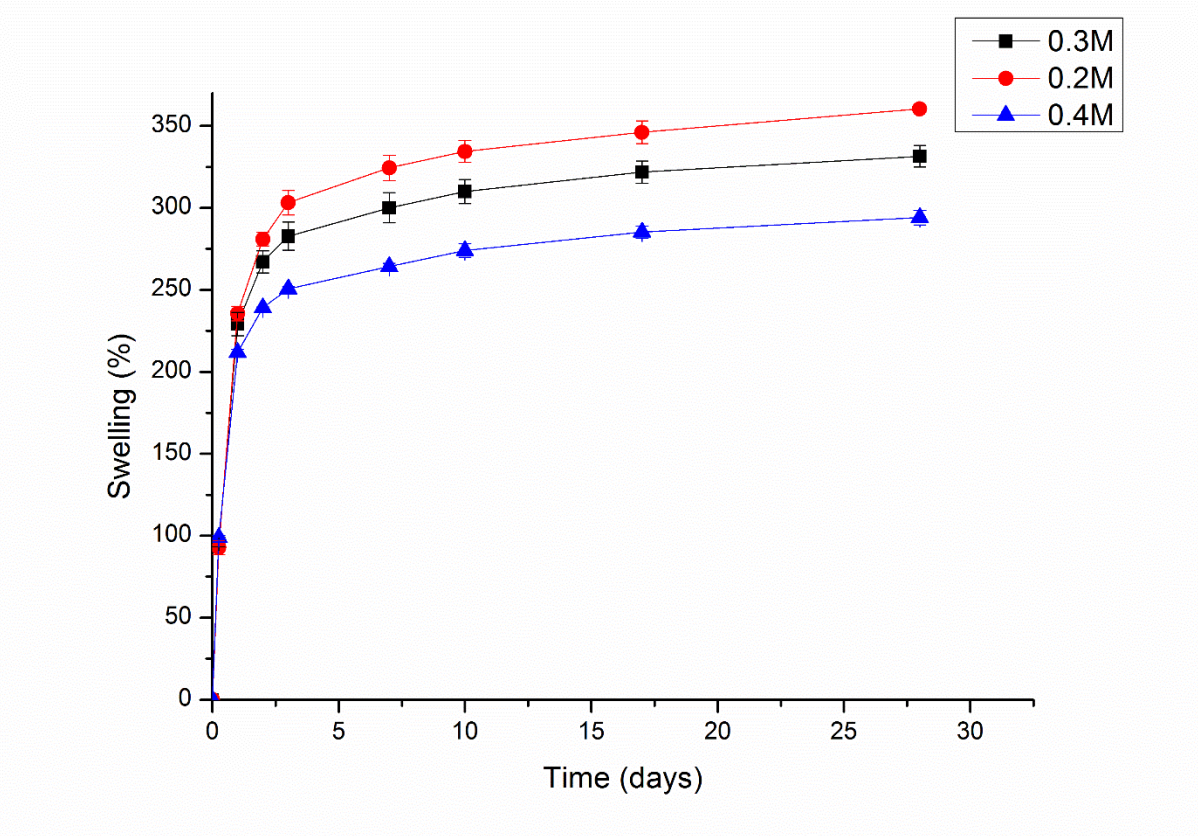


Figure 3.2: Swelling profiles of DN hydrogels crosslinked in 0,2 M, 0,3 M and 0,4 M of $FeCl_3$. Data is presented as a line chart and the experiment was conducted in triplicate and data points were recorded as a mean ± SD (n=3). The 0,4 M DN hydrogels displayed the lowest swelling capacity at 28 days at only 294,050% ± 4,37081., while 0,3 M DN hydrogels possessed a swelling capacity of 331,467% ± 6,56201. 0,2 M DN hydrogels displayed the greatest swelling at 360,407% ± 2,47909.

While mechanical strength is important, the swelling profile of the hydrogels also play an important role in hydrogel properties. Swelling is important for the hydrogel implants to absorb body fluid and for the uptake of cell nutrients (Li *et al.*, 2011; Azhar, Olad and Salehi, 2014) Swelling in this case is also important in drug loading and release. Due to the washing steps involved in the fabrication of these hydrogel implants, drug may be lost or degraded if it is light sensitive. Therefore, a method of loading would be to immerse the dried hydrogel implants into the drug solution and allow the implant to swell and uptake drug in this method. As the implant swells, drug may be released. Therefore, while 0,4 M had the best strength, its swelling ability was cause for its elimination. While 0,2 M had the best swelling ability, it proved to be the least robust of the three hydrogels in mechanical strength and this was the cause for its elimination. Therefore, the optimal of the three DN hydrogels was the 6% alginate with 0,3M $FeCL_3$ crosslinker. This formulation was then imaged under SEM.

When imaged under SEM (**Figure 3.3**), no macropores were displayed under SEM. A mostly smooth surface was seen in the SEM micrographs with sparse and small craters that can be reasoned out to have been pores. These were under 100 μm and not at all interconnected. The ideal pore size for implants bone regeneration should be between 100 and 500 μm to facilitate implant-cell interaction. Interconnected pores are vital for the facilitation of cell migration and tissue ingrowth into the implant and are key for vascular regeneration (Yu *et al.*, 2010). Therefore, efforts were made to impart increased porosity to this hydrogel implant and was done so by the addition of sodium bicarbonate.

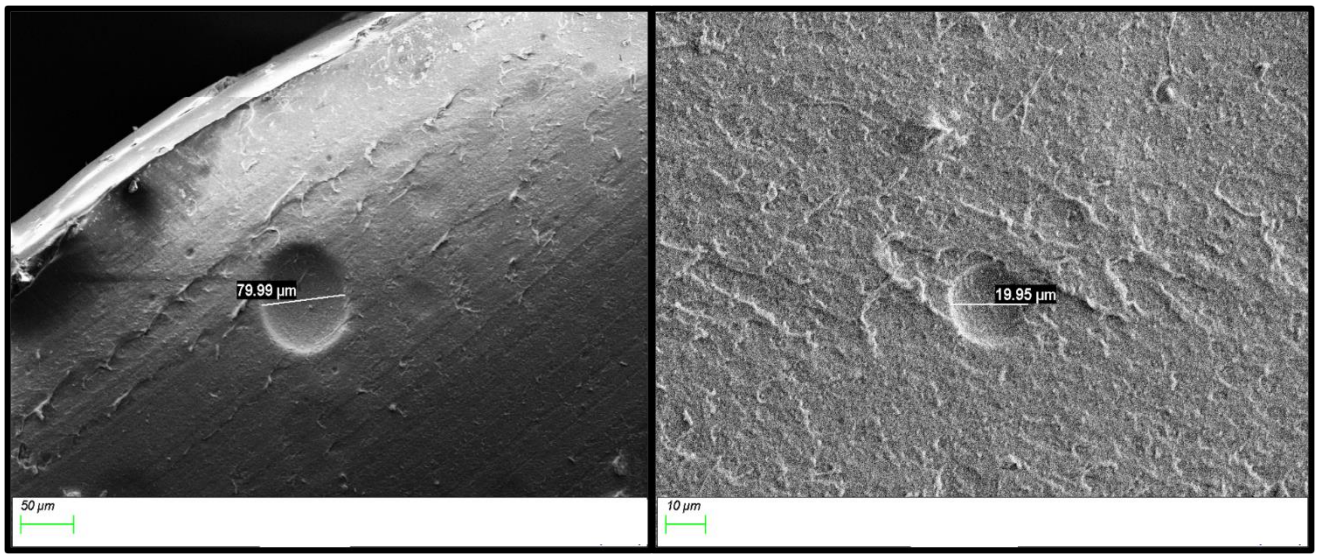


Figure 3.3: SEM images of the optimal implant. The first SEM picture on the left indicates a single pore with the diameter of 79.99 μm at a magnification of 50 μm. The SEM picture on the left displays the implant at a higher magnification of 10 μm and a single pore of 19.95 μm can be seen. No interconnected pores could be identified.

Mouldability was assessed on the hydrogel before it was immersed in $FeCl_3$ to form a double network hydrogel. For proof of concept, the pictures had to be taken before immersion in $FeCl_3$ to assess the shape of the void while the hydrogel is translucent- as after immersion in $FeCl_3$ the hydrogel cannot be seen through. It was reasoned that if it can hold its shape before its immersed in $FeCl_3$, it would hold its shape after immersion in $FeCl_3$. **Figure 3.4** below displays that the hydrogel indeed has moulding capability. The hydrogel formed around the capped needle and when the capped needle was removed, the hydrogel maintained the void in the shape of the capped needle. This indicates that that the hydrogel can take on the shape of a mould without the need of techniques such as lyophilisation that was previously used by other researchers to set the implant shape according to the mould (Sachlos *et al.*, 2006; Hassanajili *et al.*, 2019)..

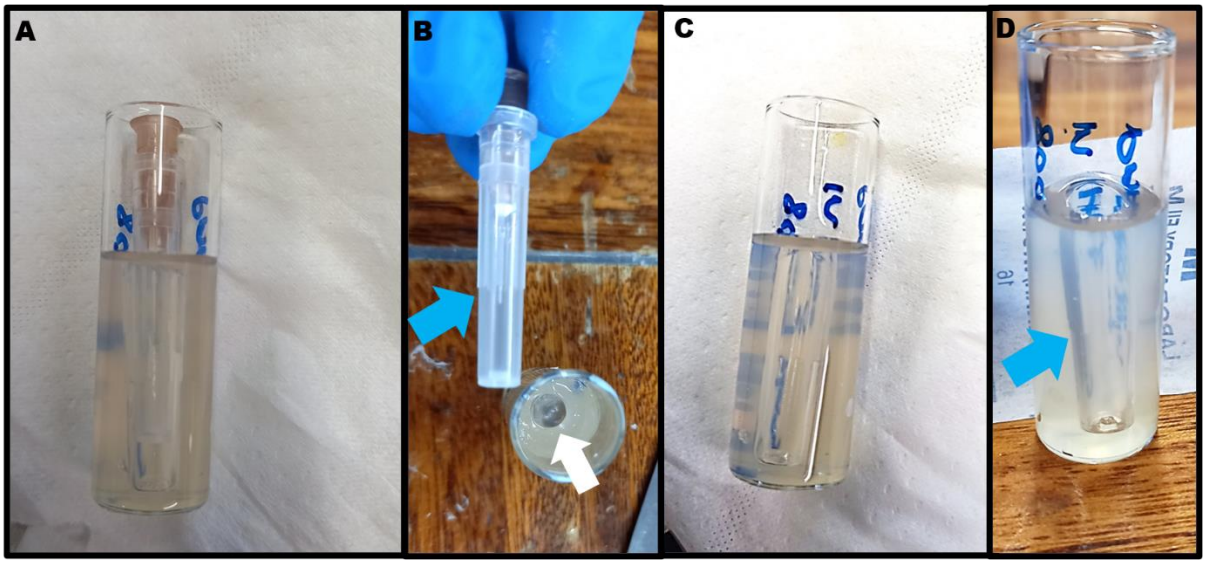


Figure 3.4: Mouldability of hydrogel. A- the needle in the hydrogel after 24 hours. B- after the removal of the capped needle, no hydrogel is messed on the needle cap. B also displays that the hydrogel maintained the void after removal as indicated by the white arrow. C and D are pictures of the hydrogel at different angles. C and D display that the hydrogel maintained the void in the shape of the capped needle. D displays that the hydrogel even maintained the shape of the needle cap where it narrows as indicated by blue arrows.

3.4.3 Hydrogel Fabrication to induce to induce macro-pores after determining the optimal cross-linking concentration:

In an effort to obtain macropores, Sodium bicarbonate was added to the glass vials. The following table represents the different concentrations of sodium bicarbonate and its effect. A high amount of Sodium Bicarbonate prevented the implant from forming a double network throughout the implant, while 1% w/v of sodium bicarbonate facilitated even crosslinking throughout the DN hydrogel implant. This implant was then chosen for further SEM imaging. **Table 3.3** details the different concentrations of sodium bicarbonate added and its resultant effects.

Table 3.3: The different concentrations of sodium bicarbonate and its resultant effects.

Sodium Bicarbonate concentration	Result:
5% w/v	After immersion in $FeCl_3$ solution, a red skin formed on the outside of the implant. However, the implant remained white on the inside. This is indicative of no crosslinking inside the implant.
3% w/v	Uneven red colouring. Indicates uneven crosslinking within the implant. Middle of implant had a lighter inside.
2% w/v	Uneven red colouring present throughout the implant, but darker colour present than when compared to 3%.
1% w/v	Even red colouring throughout.

Hydrogel implants with 1% w/v Sodium Bicarbonate were analysed under SEM. These hydrogel implants displayed not only an increase in the number of pores but also in the size of the pores (pore size was between the ranges of 100 μm and 700 μm). However, the pores were not interconnected as is desirable with implants for bone regeneration. Interconnected pores facilitate cell migration and tissue ingrowth into the implants (Yu *et al.*, 2010). This is a common issue with Gas Foaming. However, it can be reasoned that during enzymatic degradation, further pores may form and may be interconnected. However, the size of the pores may not be as large as required (between 100 and 500 μm). Therefore, the addition of 1% sodium bicarbonate to the hydrogel implants should be kept to ensure that pores greater than 100 μm are present within the hydrogel implants. **Figure 3.5** and **Figure 3.6** shows the SEM images of the hydrogel implants with 1% w/v sodium bicarbonate.

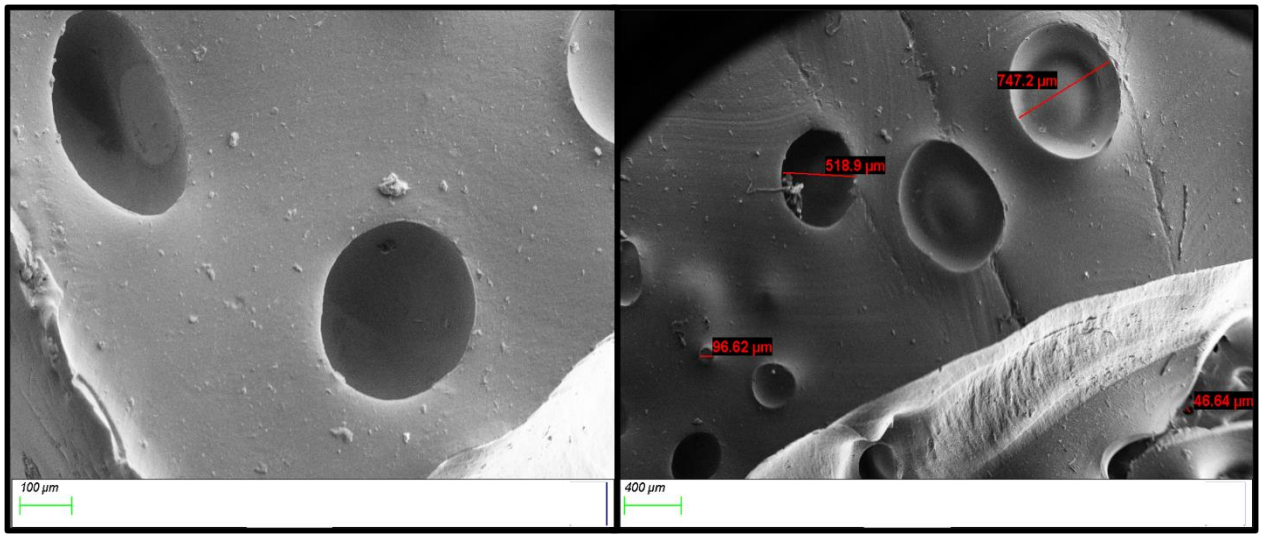


Figure 3.5: SEM images of hydrogel implants with larger pores imparted by sodium bicarbonate. The images were taken at different scales (image on the right is at 100 µm while image on the left is at 400 µm). 1% w/v Sodium bicarbonate was added to the hydrogel scaffolds cross-linked in 0,3 M $FeCl_3$.

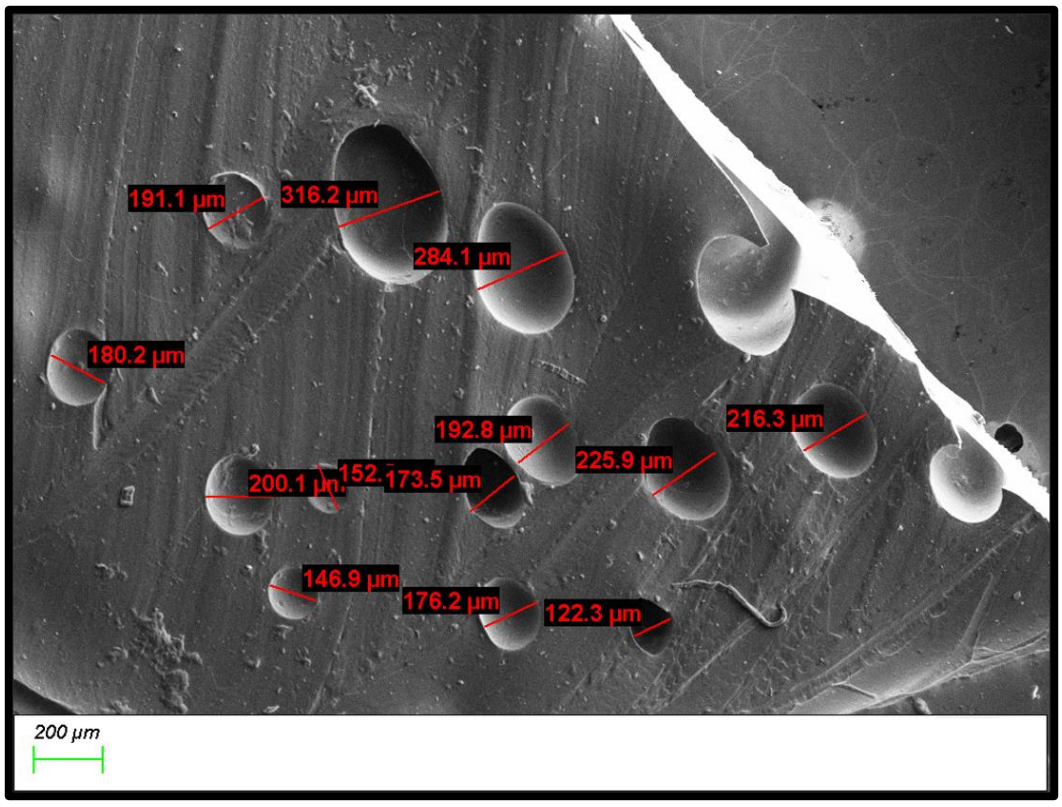


Figure 3.6: SEM image of hydrogel implants with larger pores imparted by sodium bicarbonate at 200 µm. % w/v Sodium bicarbonate was added to the hydrogel scaffolds cross-linked in 0,3 M $FeCl_3$. A variety of pore sizes above 100 µm in size could be observed.

3.5 Concluding Remarks

In this chapter, the ideal hydrogel Alg-PAAM hydrogel implants was identified by experimenting with different crosslinkers and alginate concentrations. The best formulation was identified by mechanical strength and swelling properties. The moulding ability of the hydrogel was also confirmed; however, the moulding ability of the entire double network hydrogel needs to be better confirmed by using differently shaped moulds and will be completed in the next chapter. This double network hydrogel displayed appropriately sized pores after the addition of a gas foaming step- the addition of sodium bicarbonate. However, interconnected pores were not seen and need to be better assessed during degradation. In the next chapter, the addition of bioglass to this system will be elaborated on as well as further material characterisation methods for this double network hydrogel and the bioglass incorporated double network hydrogel.

3.6 References

Azhar, F. F., Olad, A. and Salehi, R. (2014) 'Fabrication and characterization of chitosan-gelatin/nanohydroxyapatite- polyaniline composite with potential application in tissue engineering scaffolds', *Designed Monomers and Polymers*. Taylor & Francis, 17(7), pp. 654–667. doi: 10.1080/15685551.2014.907621.

Bai, X. *et al.* (2018) 'Bioactive hydrogels for bone regeneration', *Bioactive Materials*. Elsevier Ltd, 3(4), pp. 401–417. doi: 10.1016/j.bioactmat.2018.05.006.

Cuadros, T. R., Erices, A. A. and Aguilera, J. M. (2015) 'Porous matrix of calcium alginate/gelatin with enhanced properties as scaffold for cell culture', *Journal of the Mechanical Behavior of Biomedical Materials*, 46, pp. 331–342. doi: 10.1016/j.jmbbm.2014.08.026.

Darnell, M. C. *et al.* (2013) 'Performance and biocompatibility of extremely tough alginate/polyacrylamide hydrogels', *Biomaterials*. Elsevier Ltd, 34(33), pp. 8042–8048. doi: 10.1016/j.biomaterials.2013.06.061.

Fang, J. *et al.* (2019) 'A strong, tough, and osteoconductive hydroxyapatite mineralized polyacrylamide/dextran hydrogel for bone tissue regeneration', *Acta Biomaterialia*. Acta Materialia Inc., 88, pp. 503–513. doi: 10.1016/j.actbio.2019.02.019.

Giannoudis, P. V. *et al.* (2008) 'The diamond concept - open questions', *Injury*, 39(SUPPL.2), p. S5. doi: 10.1016/S0020-1383(08)70010-X.

Gu, Z. *et al.* (2018) 'Double network hydrogel for tissue engineering', *Wiley Interdisciplinary Reviews: Nanomedicine and Nanobiotechnology*, 10(6), pp. 1–15. doi: 10.1002/wnan.1520.

Guo, P., Yuan, Y. and Chi, F. (2014) 'Biomimetic alginate/polyacrylamide porous scaffold supports human mesenchymal stem cell proliferation and chondrogenesis', *Materials Science and Engineering C*. Elsevier B.V., 42, pp. 622–628. doi: 10.1016/j.msec.2014.06.013.

Hassanajili, S. *et al.* (2019) 'Preparation and characterization of PLA/PCL/HA composite scaffolds using indirect 3D printing for bone tissue engineering', *Materials Science and Engineering C*. Elsevier, 104, p. 109960. doi: 10.1016/j.msec.2019.109960.

Hernández-González, A. C., Téllez-Jurado, L. and Rodríguez-Lorenzo, L. M. (2020) 'Alginate hydrogels for bone tissue engineering, from injectables to bioprinting: A review', *Carbohydrate Polymers*. Elsevier, 229, p. 115514. doi: 10.1016/j.carbpol.2019.115514.

Hoffman, A. S. (2012) ‘Hydrogels for biomedical applications’, *Advanced Drug Delivery Reviews*. Elsevier B.V., 64(SUPPL.), pp. 18–23. doi: 10.1016/j.addr.2012.09.010.

Huh, K. M., Baek, N. and Park, K. (2005) ‘Enhanced swelling rate of poly(ethylene glycol)-grafted superporous hydrogels’, *Journal of Bioactive and Compatible Polymers*, 20(3), pp. 231–243. doi: 10.1177/0883911505053378.

Lee, K. Y. and Mooney, D. J. (2012) ‘Alginate: Properties and biomedical applications’, *Progress in Polymer Science (Oxford)*. Elsevier Ltd, 37(1), pp. 106–126. doi: 10.1016/j.progpolymsci.2011.06.003.

Li, G. *et al.* (2017) ‘Mechanical strengthened alginate/polyacrylamide hydrogel crosslinked by barium and ferric dual ions’, *Journal of Materials Science*. Springer US, 52(14), pp. 8538–8545. doi: 10.1007/s10853-017-1066-x.

Li, J. *et al.* (2011) ‘Biomimetic multicomponent polysaccharide/nano-hydroxyapatite composites for bone tissue engineering’, *Carbohydrate Polymers*. Elsevier Ltd., 85(4), pp. 885–894. doi: 10.1016/j.carbpol.2011.04.015.

Mabrouk, M. *et al.* (2014) ‘Effect of ciprofloxacin incorporation in PVA and PVA bioactive glass composite scaffolds’, *Ceramics International*. Elsevier, 40(3), pp. 4833–4845. doi: 10.1016/j.ceramint.2013.09.033.

Mandal, A. *et al.* (2020) ‘Hydrogels in the clinic’, *Bioengineering and Translational Medicine*, 5(2), pp. 1–12. doi: 10.1002/btm2.10158.

Park, J. *et al.* (2018) ‘Three dimensional cell printing with sulfated alginate for improved bone morphogenetic protein-2 delivery and osteogenesis in bone tissue engineering’, *Carbohydrate Polymers*. Elsevier, 196(May), pp. 217–224. doi: 10.1016/j.carbpol.2018.05.048.

Rainer, A. *et al.* (2008) ‘Fabrication of bioactive glass-ceramic foams mimicking human bone portions for regenerative medicine’, *Acta Biomaterialia*, 4(2), pp. 362–369. doi: 10.1016/j.actbio.2007.08.007.

Saber-Samandari, Samaneh *et al.* (2016) ‘Bioactivity evaluation of novel nanocomposite scaffolds for bone tissue engineering: The impact of hydroxyapatite’, *Ceramics International*. Elsevier, 42(9), pp. 11055–11062. doi: 10.1016/j.ceramint.2016.04.002.

Sachlos, E. *et al.* (2006) ‘Collagen Scaffolds Reinforced with Biomimetic Composite Nano-Sized Carbonate-Substituted Hydroxyapatite Crystals and Shaped by Rapid Prototyping to

Contain Internal Microchannels', *Tissue Engineering*, 12(9).

Silva, R., Fabry, B. and Boccaccini, A. R. (2014) 'Fibrous protein-based hydrogels for cell encapsulation', *Biomaterials*. Elsevier Ltd, 35(25), pp. 6727–6738. doi: 10.1016/j.biomaterials.2014.04.078.

Suleman, A. *et al.* (2021) 'The Application of 3D-Printing and Nanotechnology for the Targeted Treatment of Osteosarcoma', *Frontiers in Materials*, 8, pp. 1–23. doi: 10.3389/fmats.2021.668834.

Venkatesan, J. *et al.* (2015) 'Alginate composites for bone tissue engineering: A review', *International Journal of Biological Macromolecules*. Elsevier B.V., 72, pp. 269–281. doi: 10.1016/j.ijbiomac.2014.07.008.

Wang, C. *et al.* (2020) '3D printing of bone tissue engineering scaffolds', 5, pp. 82–91. doi: 10.1016/j.bioactmat.2020.01.004.

Wang, J., Lou, L. and Qiu, J. (2019) 'Super-tough hydrogels using ionically crosslinked networks', *Journal of Applied Polymer Science*, 136(44), pp. 1–9. doi: 10.1002/app.48182.

Yu, N. Y. C. *et al.* (2010) 'Biodegradable poly(α-hydroxy acid) polymer scaffolds for bone tissue engineering', *Journal of Biomedical Materials Research - Part B Applied Biomaterials*, 93(1), pp. 285–295. doi: 10.1002/jbm.b.31588.

Zheng, Y. *et al.* (2017) 'Hybrid hydrogels with high strength and biocompatibility for bone regeneration', *International Journal of Biological Macromolecules*. Elsevier B.V., 104, pp. 1143–1149. doi: 10.1016/j.ijbiomac.2017.07.017.

CHAPTER.4. THE INFLUENCE OF INCORPORATING BIOGLASS WITHIN A COMPOSITE HYDROGEL FOR APPLICATION IN OSTEOSARCOMA

4.1 Introduction

Osteosarcoma is a malignant neoplasm characterised by the production of osteoid from tumour cells (Heck and Toy, 2017). Most people affected by osteosarcoma are between the ages of 10 and 20. 10% of patients with osteosarcoma over the age of 60 had this disease, according to statistics. (American Cancer Society, 2020).

A crucial component of the treatment for osteosarcoma is surgery (Tiwari, 2012). Wide margin resections are standard in surgical treatment of osteosarcoma. A wide margin resection involves removing the tumour along with rim of healthy tissue. Thus an osteotomy occurs, inducing a severe bone defect (Tiwari, 2012).

There are two types of Osteosarcomas (intermedullary Osteosarcoma and surface osteosarcoma) with various subtypes of OS. Certain types of Osteosarcoma such as Low grade central OS (subtype of intermedullary OS), and certain subtypes of surface osteosarcomas only require wide surgical resection as the only treatment (Tiwari, 2012). Conventional Osteosarcomas require not only surgery, but additional chemotherapy as well, to mitigate the risk of Osteosarcoma recurrence (Tiwari, 2012).

Conventional chemotherapy treatment utilised after surgical resection includes doxorubicin (Jones, 2020), and its side effects include tissue necrosis and cardiotoxicity (Toy and Heck, 2017). Chemotherapeutic agents do not distinguish between healthy, normal cells and tumour cells especially when administered intravenously, therefore these adverse effects are prevalent.

Thus, a need arises to address the bone defect left behind after surgical resection as well to prevent local recurrence of the tumour whilst bypassing severe side effects caused by IV chemotherapeutic treatments. There is a need for the development of patient-customised implants for the individual patient (Howard *et al.*, 2008) This need is emphasised when approaching osteosarcoma, as the population affected are growing adolescents.

Bioactive glasses were first synthesized by Prof L. Hench in 1969 at the University of Florida (Hench, 2006). Bioglass is osteoconductive and osteoproductive (Rainer *et al.*, 2008). However, despite the many applications in bone tissue engineering, bioglass tends to have weaker mechanical properties when used alone which restricts use of these materials in certain applications (Mabrouk *et al.*, 2014).

Double Network (DN) hydrogels are tough hydrogels with substantial mechanical strength that possess the potential for a plethora of applications, including tissue engineering (Gu *et al.*, 2018). Among them, Alginate-Polyacrylamide (ALG-PAAM) have gained considerable interest ((Darnell *et al.*, 2013; Zheng *et al.*, 2017; Wang, Lou and Qiu, 2019), whereby ionically crosslinked alginate is one network and covalently crosslinked polyacrylamide is the other network. Alginate is a natural, biocompatible polymer that is abundantly available and cost-effective and may be used in combination with other polymers in bone regeneration (Lee and Mooney, 2012; Venkatesan *et al.*, 2015). Polyacrylamide is a synthetic biocompatible and non-toxic polymer that has proven to be stable *in-vivo,* has previously been used in contact lenses and has great potential for biomedical applications (Guo, Yuan and Chi, 2014; Saber-Samandari *et al.*, 2016; Fang *et al.*, 2019). Previously, Zheng et al. researched ALG-PAAM hydrogels with the addition of demineralised bone matrix and concluded that the system had potential for bone regeneration.

This chapter aimed to assess the suitability of an implantable ALG-PAAM Double Network hydrogel (ALG-PAAM) for suitability in addressing the defect caused by osteosarcoma resection surgery as well as its mouldable properties for patient customisation. In addition, this implantable double network hydrogel was assessed for its ability to serve as a local drug delivery platform for doxorubicin for osteosarcoma cases that require adjuvant chemotherapy. This paper also intended to assess the incorporation of bioglass into the ALG-PAAM hydrogel (BG-ALG-PAAM) and its resulting impact. To the best of our knowledge, no other study has incorporated bioglass into an ALG-PAAM Double network hydrogel before.

4.2 Materials

Alginic acid, sodium salt (viscosity of 20.000-40.000 cps) (SA), N,N'-Methylenebisacrylamide (MBIS), tetramethylethylenediamine (TEMED), Acrylamide (AAm), Tetraethyl orthosilicate (TEOS), Ammonium persulphate (APS), Sodium hydroxide, PEG (Mw = 6000) . Lysozyme from chicken egg whites and Phosphate buffered saline (PBS) tablets was obtained from Sigma Aldrich (Darmstadt, Germany). Ferric chloride hexahydrate ($FeCl_3$), Ammonium dihydrogen phosphate, Calcium Nitrate was obtained from ACE pharmaceuticals. The water used in this study was Mille-Q water from a Millipore Water Purification System (Merck Chemicals GmbH, Darmstadt, Germany).

Dulbecco's Modified Eagle Medium (DMEM) was obtained from PAN biotech and Foetal Bovine Serum (FBS) and Penicillin-Streptomycin (P-S) was obtained from Sigma Aldrich (USA), MTT Cell Proliferation Kit I was used (Roche, Basel, Switzerland).

4.3 Methods

4.3.1 Fabrication of ALG-PAAM hydrogel implant:

Tough implantable hydrogels were synthesised according to a briefly modified method reported by (Wang, Lou and Qiu, 2019). Briefly, a two-step method was followed. Alginate was dissolved to form a 6% w/v solution. Thereafter, Acrylamide monomer (1200 mg) was added to 10 mL of 6% alginate solution. 3 mg of MBIS was then added to the solution. This solution was subsequently put in an ice-bath. Following this, 1mL of APS solution 26 mg/mL was added, followed by 5 µL of TEMED.

The solution was mixed in ice bath for 15 min to ensure homogeneity then transferred to glass tubes containing sodium bicarbonate (1% w/v). The solution was mixed with the sodium bicarbonate and allowed to polymerise for 24 hours at ambient temperature (Huh, Baek and Park, 2005). After removal from glass tubes, the ALG-PAAM hydrogels were thoroughly washed with deionised water to remove any unreacted reagents. Subsequently the hydrogels were immersed overnight in 0,3M $FeCl_3$ cross linker solution (Li *et al.*, 2017; Wang, Lou and Qiu, 2019). The hydrogels were then thoroughly washed to remove any residual crosslinker before they were airdried for further characterisation unless stated otherwise.

4.3.2 Bioglass incorporation into ALG-PAAM hydrogel implants to form BG-ALG-PAAM hydrogel implants

Bioglass was synthesised using the sol-gel method according to Mabrouk et al. (Mabrouk *et al.*, 2014). Briefly, 56 ml TEOS was added to 700 mL of a mixture of water and ethanol (water:ethanol= 1:1). Nitric acid was used to adjust the pH of the solution to 2 and the solution was allowed to stir for an hour. Calcium nitrate tetrahydrate (24,5 g) was then to the above solution followed by the addition of 21,07 g of sodium hydroxide. This was labelled as Mixture A. In another beaker, 10 g of PEG was dissolved in 400 ml water followed by the addition of 3,43 g of ammonium dihydrogen phosphate. This mixture was denoted as Mixture B. Mixture B was gradually to Mixture A and this was left to stir overnight. A centrifuge was used to filter and rinse the resulting mixture at 1650 rpm for 10 min with water (3 times) and ethanol (once). The collected gel was dried at 70 °C overnight and calcined at 600 °C for 2 h. Bioglass was added to the alginate solution under stirring, allowed to mix for 15 min to ensure homogenous dispersion then the above method of hydrogel fabrication was followed. 2% w/v bioglass was chosen as the desired concentration as it was the maximum concentration the hydrogel implant could hold without any bioglass washing out during the rinsing. Thus, this concentration was chosen to further experiment on as previous studies have indicated that the highest concentration of bioglass lead to better outcomes for bone regeneration (Kwon *et al.*, 2018) ,(Sadiasa *et al.*, 2014), (Tadjoedin *et al.*, 2002).

4.3.3 Characterisation studies of ALG-PAAM and BG-ALG-PAAM hydrogel implants.

4.3.3.1 Moulding capability of the ALG-PAAM and BG-ALG-PAAM hydrogel implants

To ascertain the moulding capabilities of the implantable hydrogel implants, hydrogel solutions were cast into silicon moulds of minute detail and allowed polymerise before immersion in crosslinking solution. Samples were then removed, washed and photographed as is to display moulding capabilities for patient customisation.

4.3.3.2 Physicochemical properties of ALG-PAAM and BG-ALG-PAAM hydrogel implants

Fourier Transform Infrared Spectroscopy (FTIR; PerkinElmer Spectrum 100, FT-IR Spectrometer) was used to determine the molecular vibrations that are indicative of chemical changes within the implantable hydrogel samples. FTIR was run between wavenumbers of 4000-650 $cm^{-1.}$ X-Ray diffraction (XRD) was undertaken using a Rigaku 600 x-ray diffractometer (RIGAKU, Inc., Tokyo, Japan) to assess the types of phases present (crystalline and or amorphous) in the prepared hydrogel implants. The XRD spectra was collected from 10° to 90°.

4.3.3.3 Thermal properties of ALG-PAAM and BG-ALG-PAAM hydrogel implants

Thermogravimetric analysis (TGA) was undertaken to ascertain the thermal decomposition profile of the hydrogel implants and bioglass. Samples of weights between 10 and 20mg were placed in a ceramic pan under inert conditions (nitrogen gas) in the thermogravimetric analyser (TGA 400, PerkinElmer Inc., MA). Thermograms were obtained between 30°C and 900°C.

4.3.3.4 Biomineralization ALG-PAAM and BG-ALG-PAAM hydrogel implants

Biomineralization was conducted by immersion of hydrogel implants in Simulated Body Fluid (SBF) (pH 7.4, 37 °C). SBF was made according to Kokubo et al. (Kokubo and Takadama, 2006). Hydrogel implants were immersed in SBF for 4 weeks and media was changed every week. Hydrogel implants were then removed every week, rinsed thoroughly with deionised water and analysed by XRD, SEM and EDS.

4.3.3.5 Mechanical analysis of ALG-PAAM and BG-ALG-PAAM hydrogel implants

In the human body, bones are often subjugated to compression stress. It has been widely accepted by the research community to utilise compression tests as a method to assess biomaterials that have potential in bone regeneration. Therefore mechanical behaviour of the hydrogel implants were assessed by compression. (Mabrouk *et al.*, 2014)

Mechanical tests were conducted after the hydrogel implants were immersed in SBF (pH 7.4, 37 °C) for 24 hours. Mechanical analysis was conducted at ambient lab temperature using a Texture Analyzer (TA.XT plus Stable Microsystems, Surrey, UK) equipped with a 50 kg load cell. The method used to conduct the test was adapted from (Cuadros, Erices and Aguilera, 2015).

The compressive strength, matrix resilience and deformation energy were measured using a compression platen with a test speed of 1,2 mm/min, at 80% strain so as to prevent harm to the instrument. To assess the impact of SBF exposure on mechanical strength, hydrogel implants were also immersed in SBF for a period of 4 weeks and the experiment conditions were run as per the biomineralization experimental conditions.

Mechanical strength was conducted in triplicate and data was recorded as a mean ± SD (n=3)

4.3.3.6 Swelling and shape retention of ALG-PAAM and BG-ALG-PAAM hydrogel implants

Swelling behaviour of the synthesised ALG-PAAM and ALG-PAAM-BG hydrogel implants were assessed by were immersion of hydrogel implants in PBS at pH 7.4 at 37 °C. At predetermined time points, hydrogel implants were removed, blotted dry and weighed. The initial dry weights were recorded as Wi and the wet weight of the hydrogel implants at each time point were recorded as Wf. The following equation was used to determine the swelling ratio percentage:

$$\text{Swelling ratio \%} = \frac{(Wf - Wi)}{Wi} x100 \qquad \text{Equation 4.1}$$

Swelling ratio % was conducted in triplicate and data was recorded as a mean ± SD (n=3).

Shape retention was assessed by measuring the dimensions of the hydrogel implants to assess the ability of the hydrogel implants to maintain its shape after being dehydrated.

4.3.3.7 Degradation, morphology and porosity of ALG-PAAM and BG-ALG-PAAM hydrogel implants

Degradation studies were of implantable hydrogel implants were assessed by immersing hydrogel implants in PBS containing lysozyme (10 000 IU/mL) at 37 °C (Cassimjee *et al.*, 2022). To mimic perfect sink conditions, the w/v ratio of hydrogel implants to degradation media was at least 1:70 and media was changed every week (Khan *et al.*, 2007). At days 7, 14, 21 and 28 hydrogel implants were removed from media, washed, flash frozen and lyophilised. Hydrogel implants were weighed before immersion and after lyophilisation and the difference in weights was used to calculate degradation as per the equation below.

$$\text{Degradation \%} = \frac{(Wi - Wt)}{Wi} x100 \qquad \text{Equation 4.2}$$

Scanning Electron Microscopy (SEM) was utilised to determine the morphology of the samples at each time point using a SIGMA 03-39 field emission scanning electron microscope (Zeiss, Jena, Germany). Cross-section samples were cut from the middle of the hydrogel implants and sputter coated with 30 nm of carbon and subsequently analysed. Hydrogel implants pore size was also analysed by Image J software (Image J version 1.4.3.67) and is reported as a range. Overall porosity of the hydrogel implants at each time point was determined using Image J software (Image J version 1.4.3.67 National Institutes of Health, Bethesda, MD, USA) (Bhaskar *et al.*, 2018). Three SEM images were used and average porosity is reported ± SD. A comparator sample immersed for 24 hours in media then flash frozen and lyophilised was also used for assessment of morphology.

4.3.3.8 Doxorubicin Loading and release of ALG-PAAM and BG-ALG-PAAM hydrogel implants

Hydrogel implants were immersed in doxorubicin solution of 0,5 mg/mL for 24 hours in the dark. The hydrogel implants were then thoroughly rinsed to remove any unloaded drug then dried in an oven at 25° C (Javanbakht and Namazi, 2018). Drug loading was determined indirectly by analysing the remaining solution at 490 nm on the Nanophotometer UV/Vis spectrophotometer NP80 (Implen, Munchen, Germany).

To ascertain the release profile, hydrogel implants were immersed in 2 mL PBS at 37 °C. At predetermined time points, 0,5 mL of release media was removed for analysis and immediately replaced with fresh PBS buffer. Samples were analysed at 490 nm on the Nanophotometer UV/Vis spectrophotometer NP80 (Implen, Munchen, Germany).

Drug loading and release studies were conducted in triplicate and data was recorded as a mean ± SD (n=3).

4.3.3.9 Invitro cytotoxicity and cell proliferation of ALG-PAAM and BG-ALG-PAAM hydrogel implants

MG-63 cells were obtained from Cellonex (Johannesburg, Gauteng, South Africa). MG-63 cells were subcultured in DMEM supplemented with 1% P-S and 20% FBS. Cells were cultured until 80% confluency then utilised. Media was changed every 2-3 days as per the supplier's instructions.

Cell viability was assessed by an using MTT assay on cells incubated in conditioned media. Hydrogel implants were first sterilised by UV light for 5 minutes then incubated in DMEM supplemented with 20% FBS and 1% Penicillin-Streptomycin for 3 and 7 days. The conditioned media was then aspirated and frozen until ready to use. MG-63 cells were seeded at a density of 5000 cells/well in 96-well plates (Darnell *et al.*, 2013). After 24 hours, media

was aspirated and completely replaced with conditioned cell culture media and the cells were further incubated for 72 hours. Thereafter, the MTT assay was run using MTT Cell Proliferation Kit I (Roche, Basel, Switzerland). Absorbance measurements were carried out in triplicates using the Victor™ X3 microplate reader. Absorbances were read at 570 nm and the background was run at 690 nm and the following equation (Da Silva *et al.*, 2021; Ngema *et al.*, 2022) was used to determine % cell viability:

$$\% \text{ Cell viability} = \frac{(Asample - Ablank)}{(A\ control - A\ blank)} x100 \qquad \text{Equation 4.3}$$

Where A_{sample} is the absorbance if the treated cells and $A_{control}$ is the absorbance of the control which is the absence of treatment.

To assess the cytotoxicity of doxorubicin release from the hydrogel implants, the concentrations of doxorubuicin released at 3 and 7 days were calculated from the cumulative release graph. Doxorubicin equal to the calculated amount was added to 3 days and 7 days conditioned media as well as to plain media as a control. The total amount of drug loading was also calculated an added to plain media as a control. 10% DMSO served as a positive control. The cytotoxicity was then calculated utilising equation 4.3.

Cell adhesion studies were conducted qualitatively using briefly adapted methods from (Wang, Lou and Qiu, 2019) and (Bax *et al.*, 2018). Hydrogel implants were incubated in DMEM supplemented with 20% FBS and P-S for 2 hours. Hydrogel implants were then removed from media and placed in a 12-well plate. MG-63 cells at a density of 50 000 cells/mL were seeded on top of the hydrogel implants. Hydrogel implants were then incubated at 37 °C at 5% humidity for 24 hours. Adherent cells were then fixed with 5% formalin for 20 minutes then rinsed with PBS three times. Cells were then stained with a 0,1% crystal violet solution for 6 minutes followed by rinsing in PBS until the colour of the PBS remained clear. Hydrogel implants were then stained in Trypan blue for 5 minutes followed by another round of PBS rinsing. Hydrogel implants were transferred into unused wells then imaged under a light inverted microscope using a briefly adapted methods from (Bax *et al.*, 2018; Wang, Lou and Qiu, 2019).

4.3.3.10 Statistical analysis

Cell viability results were analysed using an unpaired student's T-test on GraphPad Software. Data was analysed at a 95% confidence interval ($p < 0.05$). All data are expressed as mean ± standard deviation of analyses in triplicate ($n = 3$).

4.4 Results

4.4.1 Moulding capabilities of ALG-PAAM and BG-ALG-PAAM hydrogel implants

The hydrogel implants were able to form according to the shape of the mould. The shape was maintained even after removal from mould and crosslinking in $FeCl_3$ occurred. **Figure 4.1** below shows this. Not only did the hydrogel implants take on the shape of the mould, but it took on the finer details of the mould. This proves not only moulding capabilities, but also moulding capability of high definition.

BG-ALG-PAAM hydrogel implants displayed similar moulding capabilities (**Figure 4.1**).

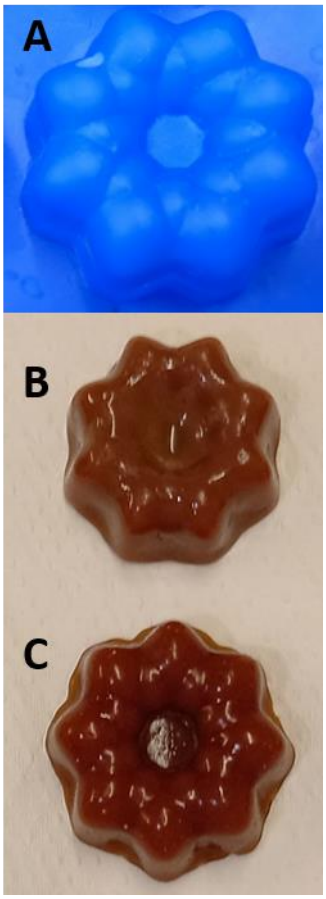


Figure 4.1: Moulding capabilities of ALG-PAAM and BG-ALG-PAAM hydrogel implants. The moulding capabilities indicate the potential for customisation per individual patient. A- The moulds the hydrogel implants were cast in. B- ALG-PAAM hydrogel implants moulding capabilities. C- BG-ALG-PAAM hydrogel implants. The hydrogels took on the finer details of the mould, indicating moulding capabilities of high definition.

4.4.2 Physicochemical properties of ALG-PAAM and BG-ALG-PAAM hydrogel implants

In the spectrum of pure SA, a broad band was noted between 3500 and 3100 cm^{-1} indicating the presence of an -OH group (Sithole *et al.*, 2018). Presence of a peak at 2925 cm^{-1} indicated the -CH_2 group. Peaks that were present at 1601 cm^{-1} and 1410 cm^{-1} corresponded to symmetric and asymmetric stretching wavenumbers of the -COO^- group. The peak at 1030 cm^{-1} corresponded with the polysaccharide glycoside -COC- bonds.(Sundarrajan *et al.*, 2012; Kuzmanović *et al.*, 2017).

In the FTIR spectra of ALG-PAAM before immersion in $FeCl_3$ crosslinker, the following characteristic peaks of PAAM were noted: A peak at 3328 cm^{-1} due to the presence of -NH group which may be attributed to the crosslinking of PAAM with MBIS (Richhariya *et al.*, 2020). A peak at 3190 cm^{-1} indicated band of NH_2 symmetric stretching. A peak at 2934 cm^{-1} indicated a symmetric stretch of CH_2, A peak at 1650 cm^{-1} indicated stretching vibrations of C=O group. 1452 cm^{-1} indicated CH_2 deformation, a peak at 1316 cm^{-1} indicated a weak C-H deformation (Kolek *et al.*, 2007).

Crosslinking of ALG-PAAM in $FeCl_3$, was confirmed by a shift in peak from 1601 cm^{-1} of the -COO^- group that's present in the spectrum before crosslinking to 1587 cm^{-1} that's in the spectrum after crosslinking (Dong *et al.*, 2011). A minute peak at 817 cm^{-1} also appeared in the ALG-PAAM spectrum which is indicative metal-O band of Fe (Tirkistani and Hassan, 2012; Demianenko and Minisini, 2016).

The FTIR spectrum of the bioglass indicated peaks at 1003 cm^{-1} which is indicative of stretching mode of Si-O-Si and PO_4^{3-} (Aguiar *et al.*, 2009; Mabrouk *et al.*, 2014) while a band at 927 cm^{-1} is indicative of Si-O (Mabrouk *et al.*, 2014; Soleymani Eil Bakhtiyari, Karbasi and Monshi, 2015). A band at 766 cm^{-1} also indicated the bending of Si-O-Si and a band at 1455 cm^{-1} displayed the presence of carbonate (CO_3^{2-}) (Aguiar *et al.*, 2009).

The FTIR spectrum for BG-ALG-PAAM displayed as shift in peak to 1080 cm^{-1} from 1092 cm^{-1} from the spectrum of ALG-PAAM. This could be indicative of an Si-OC bond that formed, confirmed the presence of bioglass within the ALG-PAAM hydrogel (Ahn *et al.*, 2020). FTIR spectra is displayed in **Figure 4.2.**

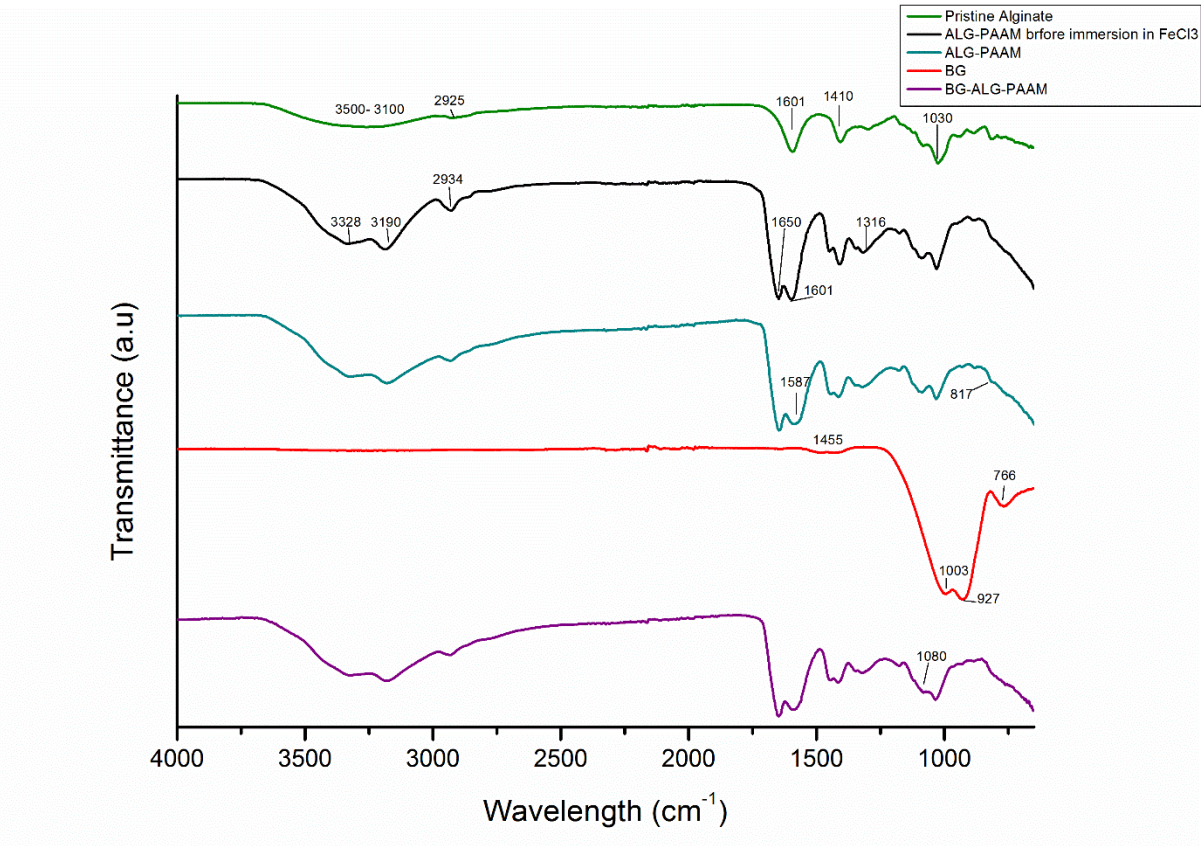


Figure 4.2: FTIR spectra of Pristine Alginate, ALG-PAAM before immersion in $FeCl_3$, ALG-PAAM, BG, BG-ALG-PAAM. FTIR spectra confirms the formation of double network hydrogel (ALG-PAAM) and the incorporation of bioglass within that double network (BG-ALG-PAAM).

The XRD spectra (**Figure 4.3**) showed that alginate displayed a semi-crystalline nature with peaks at 14° and 22° (Sithole *et al.*, 2018; Bhagyaraj and Krupa, 2020). The synthesised bioglass possessed an absence of crystalline peaks- it was amorphous (Mabrouk *et al.*, 2014). ALG-PAAM before immersion in $FeCl_3$, ALG-PAAM hydrogel implants as well as BG-ALG-PAAM hydrogel implants also displayed no noticeable crystalline peaks and were completely amorphous while displaying a broad amorphous peak at around 22 ° (Bahrami, Akbari and Eftekhari-Sis, 2019).

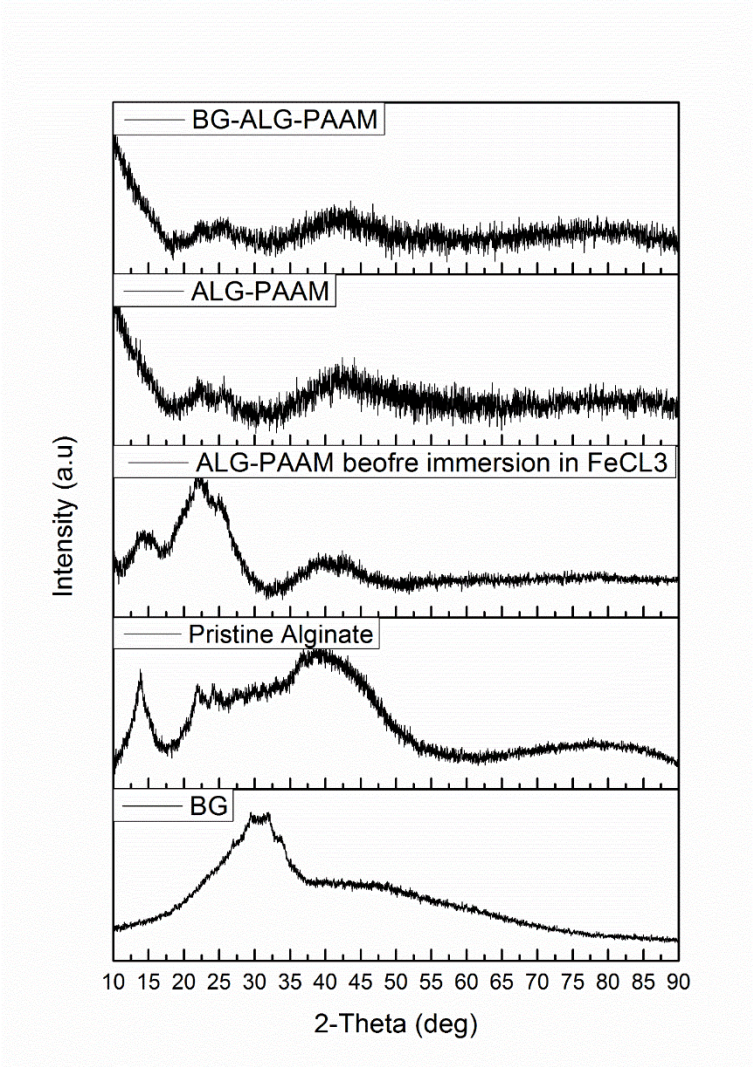


Figure 4.3: XRD spectra of Pristine Alginate, ALG-PAAM before immersion in $FeCl_3$, ALG-PAAM, BG, BG-ALG-PAAM. The spectrum of Alginate displayed a semi-crystalline nature. The spectra of ALG-PAAM, ALG-PAAM before immersion in $FeCl_3$, BG-ALG-PAAM, BG and displays an amorphous nature.

4.4.3 Thermal Characteristics of ALG-PAAM and BG-ALG-PAAM hydrogel implants

TGA thermograms **(Figure 4.4**) show that the Thermal stability of ALG-PAAM improved with the incorporation of bioglass into the double network hydrogel. The first weight loss up to 100 °C can be related to loss of adsorbed water for all samples. The thermogram of Alginate displayed rapid weight loss between 220- 270 °C. This is consistent with the degradation temperature of alginate (Zohuriaan and Shokrolahi, 2004). In the derivative thermogram of alginate, degradation of Alginate can be pinpointed to be at 242 °C (**Figure 4.5).** The thermogram of BG displays a slight overall mass loss which can be explained by densification of the sample (Mukundan *et al.*, 2013). Thermograms of ALG-PAAM before immersion in $FeCl_3$, ALG-PAAM and BG-ALG-PAAM displayed weight loss in the temperature range of 240–

350 °C and can be related to decomposition of ALG-PAAM (Bahrami, Akbari and Eftekhari-Sis, 2019). Although, it can be noted that ALG-PAAM and BG-ALG-PAAM displayed less steeper loss of weight and this can be attributed towards the increased stability of a double network hydrogel that was formed after immersion in $FeCl_3$. The derivative TGA thermograms (**Figure 4.5)** confirm this. Derivative thermograms of ALG-PAAM before immersion in $FeCl_3$ pinpointed the degradation temperature to be at 259,5 °C while ALG-PAAM and BG-ALG-PAAM display weight loss at 262,67 °C and 264,5 °C. The shift to a higher degradation temperature seen when comparing ALG-PAAM before immersion in $FeCl_3$ and ALG-PAAM can be attributed to the increased stability imparted due to the crosslinking with $FeCl_3$. The shift to slightly higher degradation temperature when comparing ALG-PAAM and BG-ALG-PAAM can be attributed to the presence of bioglass. At 900 °C, synthesised bioglass displayed the least weight loss of only 1,911% while Pristine Alginate displayed a weight loss of 84,094%. ALG-PAAM before crosslinking in $FeCL_3$ displayed a total weight loss of 84,6456 %. After cross linking, ALG-PAAM showed an increase in stability by displaying a lesser weight loss of 72,518% while BG-ALG-PAAM displayed a slightly higher stability by displaying a 70,213% reduction in weight. Therefore, order of sample stability can be stated as: ALG-PAAM before immersion in $FeCl_3$ ≤ Pristine Alginate < ALG-PAAM < BG-ALG-PAAM < BG.

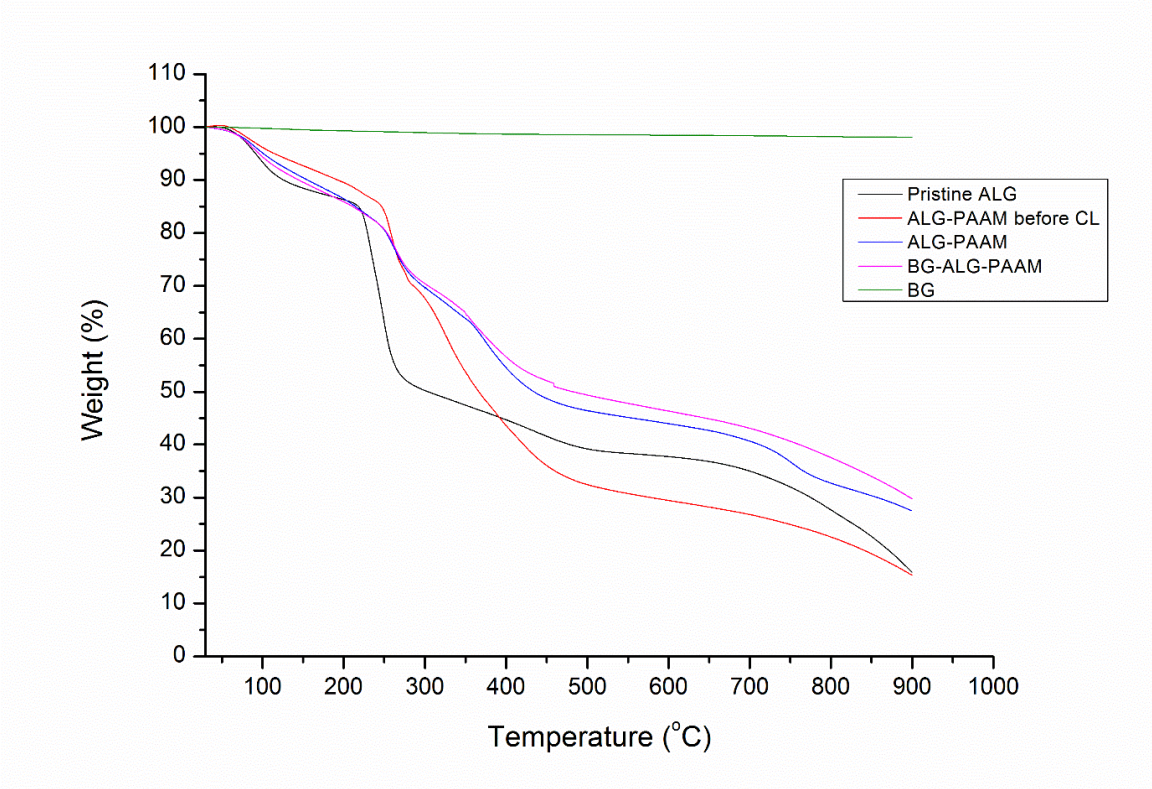


Figure 4.4: TGA thermograms of Pristine Alginate, ALG-PAAM before immersion in FeCl3, ALG-PAAM, BG, BG-ALG-PAAM. The order of stability can be stated as: ALG-PAAM before immersion in $FeCl_3$ ≤ Pristine Alginate < ALG-PAAM < BG-ALG-PAAM < BG.

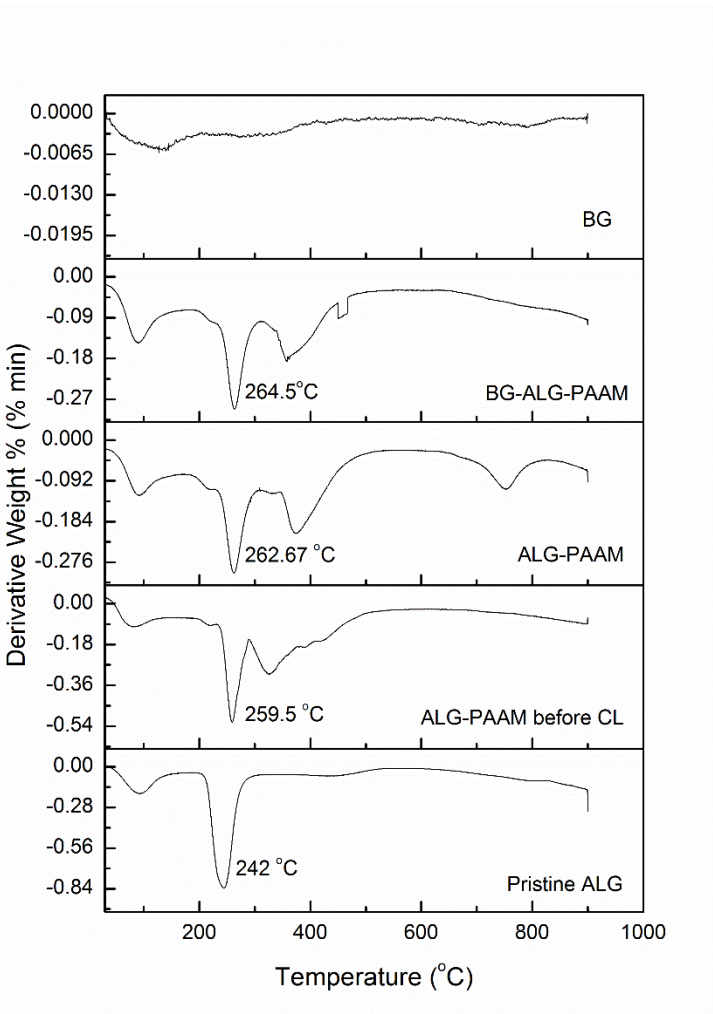


Figure 4.5: Derivative TGA thermograms of Pristine ALG, ALG-PAAM before CL, ALG-PAAM, BG-ALG-PAAM and BG. Derivative thermograms confirm the order of stability seen in the original thermograms by pinpointing the exact degradation temperatures and displaying the increase in degradation temperature of each sample.

4.4.4 Biomineralization of ALG-PAAM and BG-ALG-PAAM hydrogel implants

XRD spectra obtained for ALG-PAAM (**Figure 4.6)** and BG-ALG-PAAM (**Figure 4.7)** hydrogel implants both displayed peaks with a maximum at around 32 °. This can be attributed to the 211 plane of hydroxyapatite. (Peter *et al.*, 2009; Mabrouk *et al.*, 2014). However, it should be noted that BG-ALG-PAAM hydrogel implants displayed greater crystalline peaks after the first week of immersion as compared to ALG-PAAM hydrogel implants which displayed smaller peaks. Both hydrogel implants had the highest peak intensity after 4 weeks of immersion in SBF indicating increased crystallinity.

EDS of ALG-PAAM before immersion in SBF (**Figure 4.8)** displays the presence only of Fe and Cl which can be attributed to the crosslinker used to form these hydrogel implants. EDS

of BG-ALG-PAAM before immersion in SBF **(Figure 4.10**) indicates the presence of Si and P as well as Fe and Cl. The presence of these ions can be explained due to the presence of bioglass in the hydrogel implants.

EDS for ALG-PAAM (**Figure 4.9)** and BG-ALG-PAAM **(Figure 4.11)** after immersion in SBF for 4 weeks both display Ca and P after immersion in SBF which can be attributed to the formation of Hydroxyapatite on the surface of the hydrogel implants. The presence of Fe and Cl can be attributed to the crosslinker used in formation of the tough implantable hydrogel implants. SEM images (**Figure 4.12**, **Figure 4.13)** display the formation of hydroxyapatite for both implantable hydrogel implants.

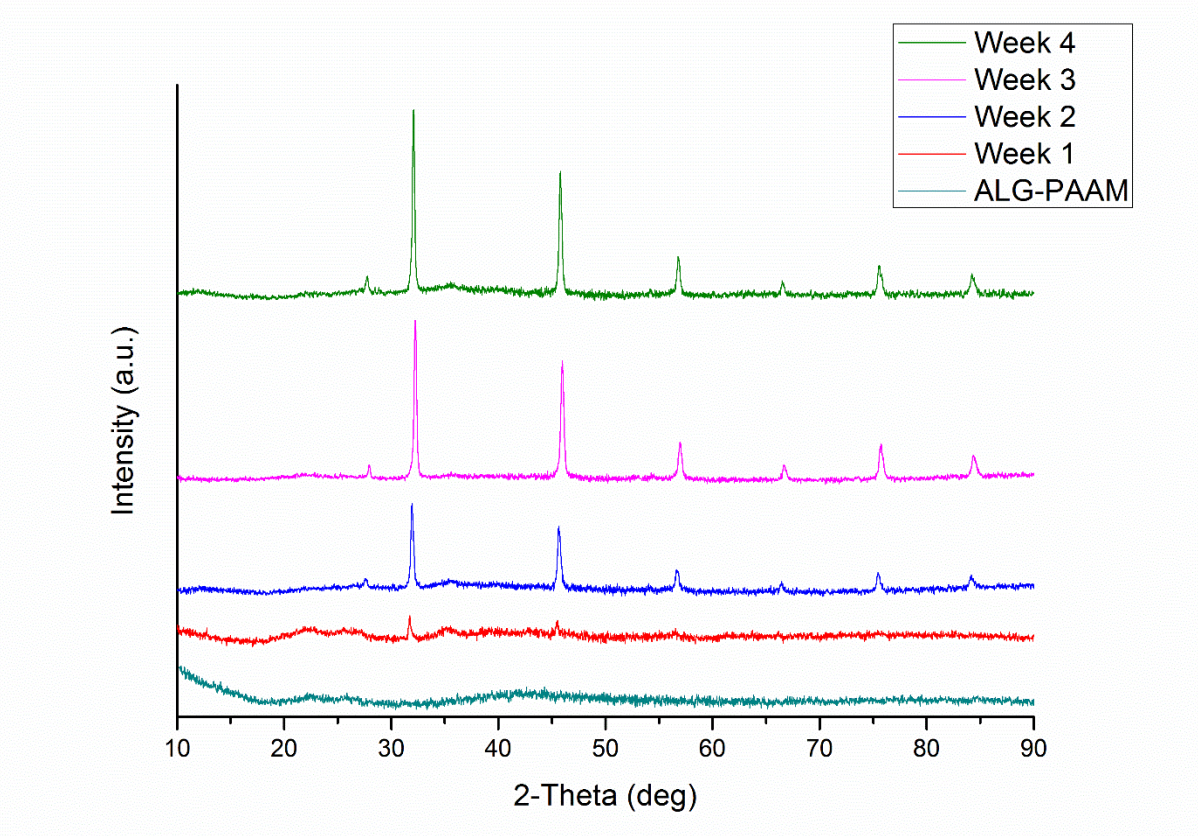


Figure 4.6: XRD Spectra of ALG-PAAM Hydrogel implants after immersion in SBF (Weeks 0-4). The hydrogel implants before immersion are completely amorphous while crystalline peaks appear with a maximum at around 32 ° as the weeks go on after immersion in SBF. These crystalline peaks are indicative of hydroxyapatite formation.

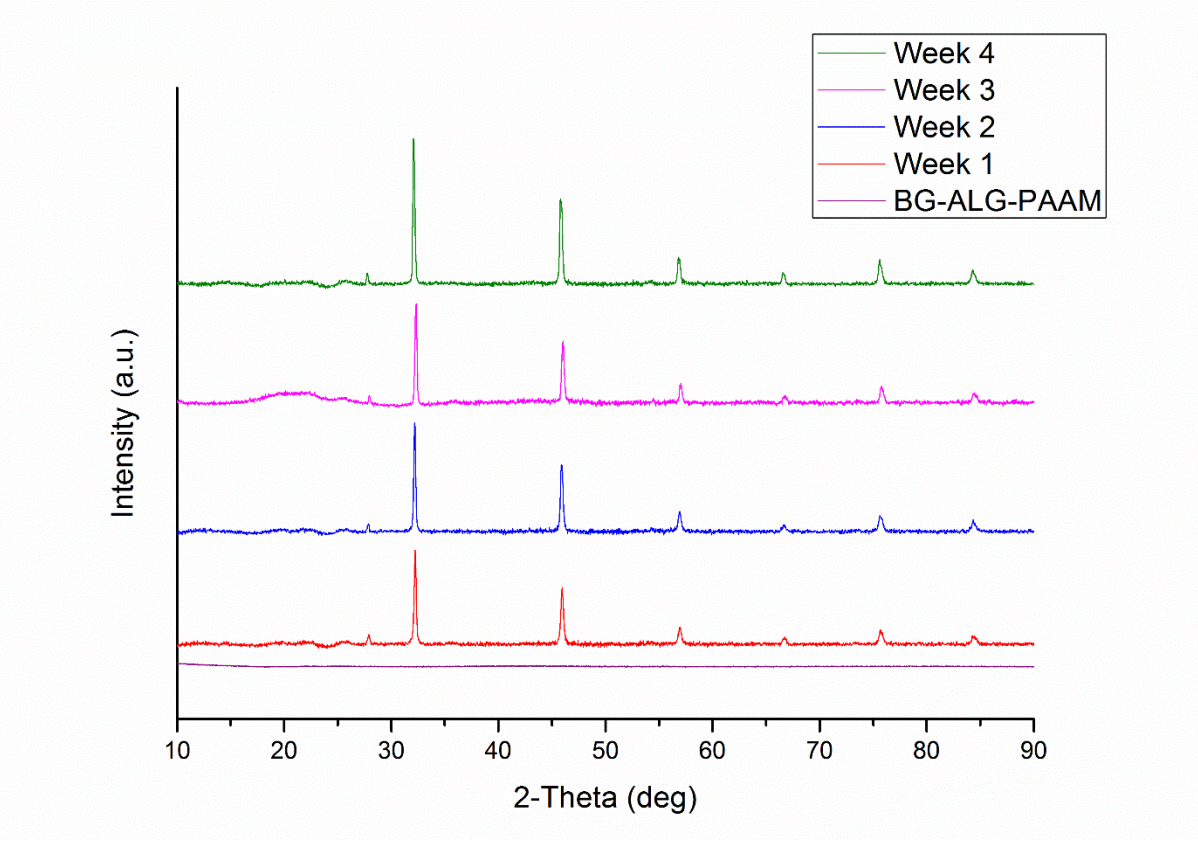


Figure 4.7: XRD spectra of BG-ALG-PAAM after immersion in SBF (weeks 0-4). The hydrogel implants before immersion were completely amorphous while crystalline peaks appear with a maximum at around 32 ° as the weeks went on after immersion in SBF. BG-ALG-PAAM implants displayed greater crystalline peaks after the first week of immersion as compared to ALG-PAAM. These crystalline peaks at 32 ° are indicative of hydroxyapatite formation.

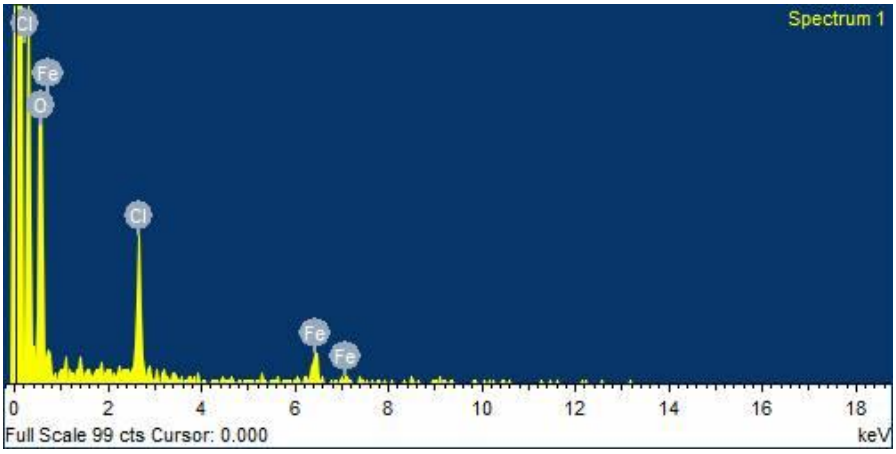


Figure 4.8: EDS of ALG-PAAM before immersion in SBF. Only the presence of Fe and Cl could be noted and this is attributed to the crosslinker used ($FeCl_3$) in the formation of the hydrogel. No Ca or P is noted which indicates the absence of hydroxyapatite (a calcium phosphate).

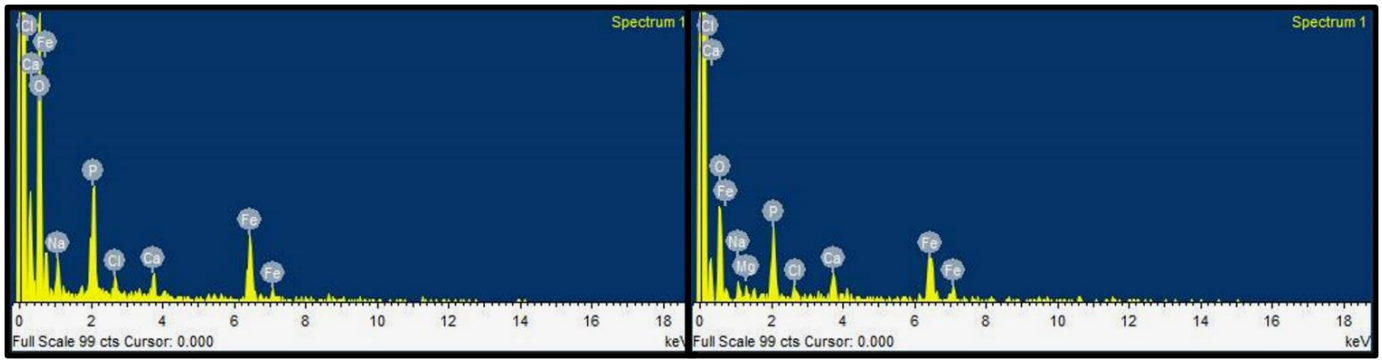


Figure 4.9: EDS of ALG-PAAM hydrogel implants after immersion in SBF at week 2 (right) and week 4 (left). The presence of Ca and P was noted at both time points and can be attributed to the formation of hydroxyapatite on the hydrogels' surfaces.

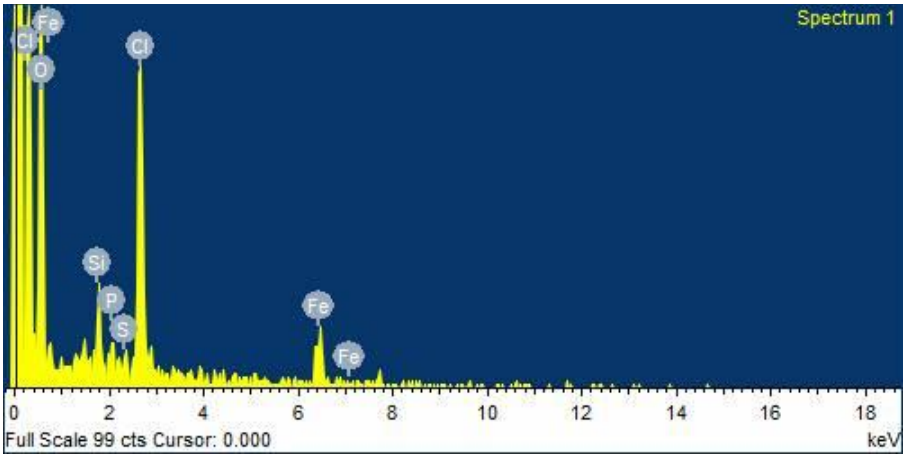


Figure 4.10: EDS of BG-ALG-PAAM before immersion in SBF. Only the presence of Fe, Cl, Si and P was observed. The presence of Fe and Cl can be attributed to the crosslinker used ($FeCl_3$) in the formation of the hydrogel, while Si and P can be attributed to the presence of bioglass. No Ca is noted which indicates the absence of hydroxyapatite.

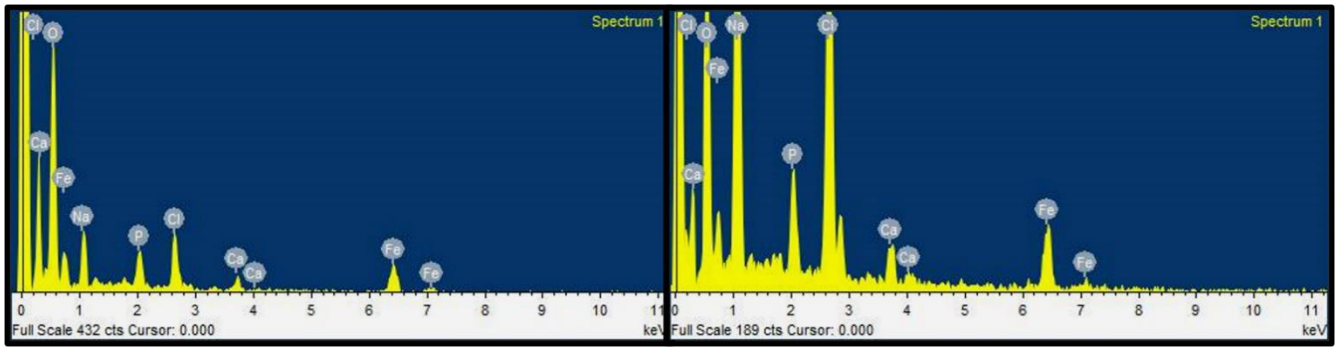


Figure 4.11: EDS of BG-ALG-PAAM after immersion in SBF for 2 weeks (right) and 4 weeks (left). The presence of Ca and P was noted at both time points and can be attributed to the formation of hydroxyapatite on the hydrogels' surfaces.

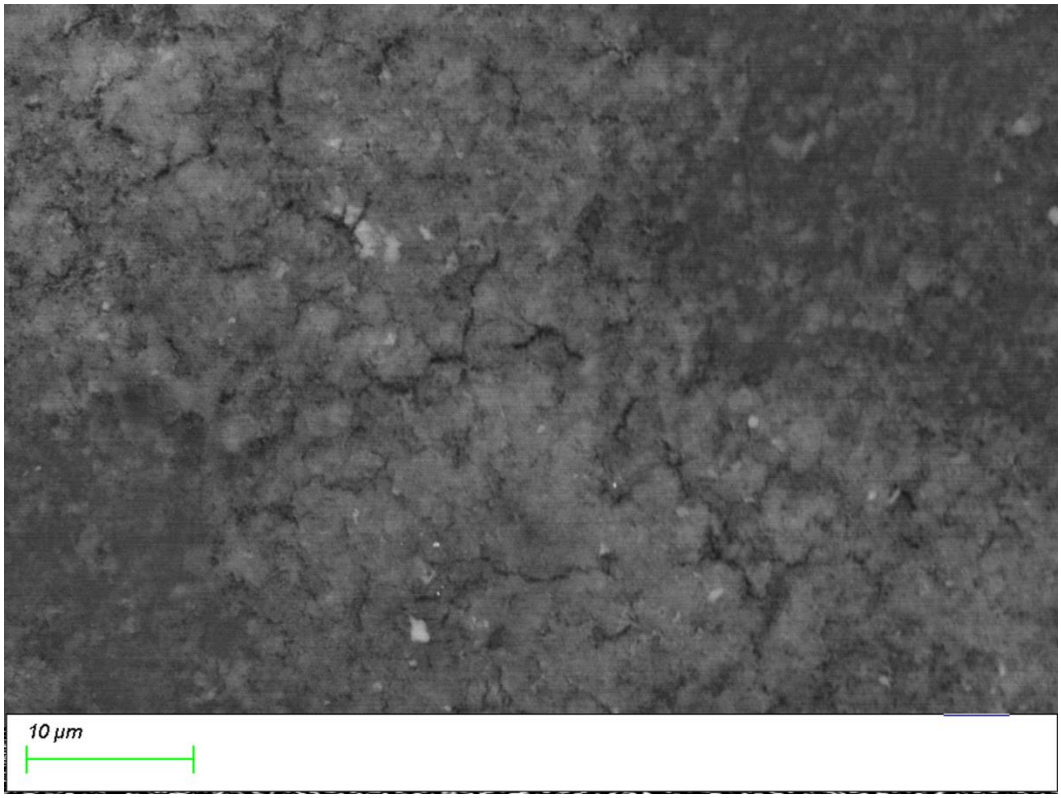


Figure 4.12: SEM images of ALG-PAAM hydrogel implants after immersion in SBF. Hydroxyapatite crystals can be observed on its surface.

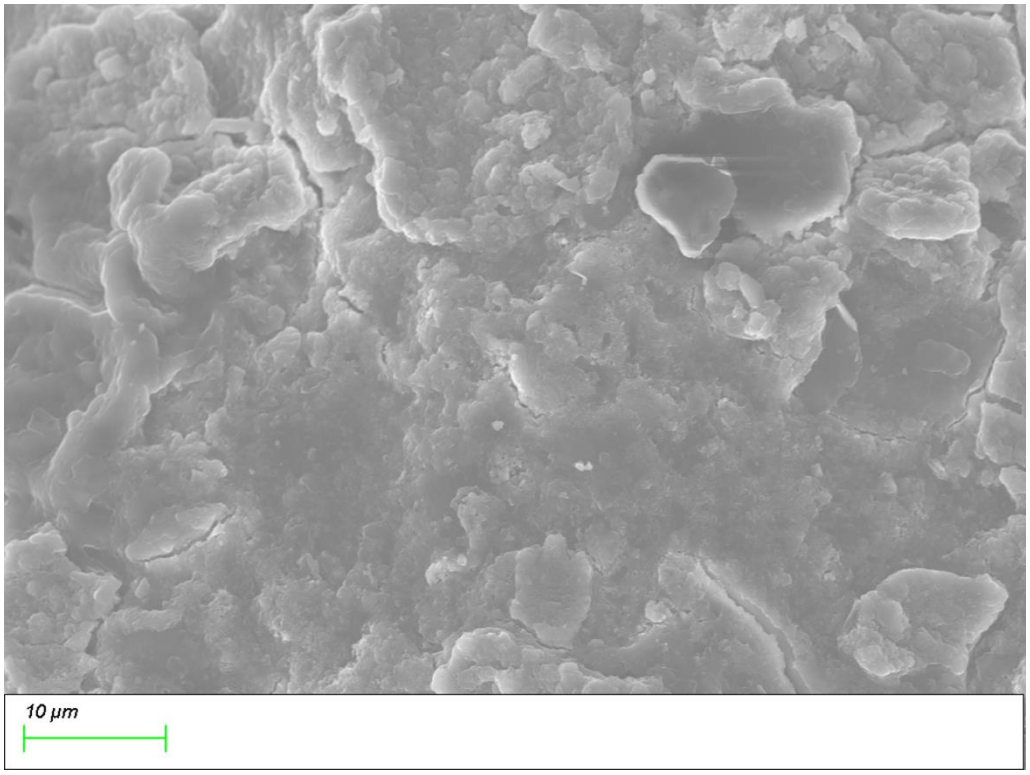


Figure 4.13: SEM of BG-ALG-PAAM after immersion in SBF. Hydroxyapatite crystals can be observed on its surface.

4.4.5 Mechanical analysis of ALG-PAAM and BG-ALG-PAAM hydrogel implants

A hydrogel implants used to reconstruct load-bearing tissues should maintain its mechanical property after implantation into the body (Prasadh and Wong, 2018). Exposure to body fluids have an impact on the strength of the hydrogel implants. Therefore, the strength of the hydrogel implants exposed to SBF over time was investigated to assess its impact on the mechanical properties of the hydrogel implants.

As shown in **Figure 4.14,** ALG-PAAM hydrogel implants itself display a lower compressive strength (1,045367 MPa ± 0,024271) after 24-hour immersion in SBF compared to BG-ALG-PAAM hydrogel implants (3,51627 MPa ± 0,06504). However, when mechanical strength was again assessed after exposure to SBF for 2 and 4 weeks, the compressive strength drastically reduced to 0,018567 MPa ± 0,000306 and 0,017598 MPa ± 0,000792 respectively. BG-ALG-PAAM hydrogel implants strength also decreased after prolonged exposure to SBF. After 2 weeks, BG-ALG-PAAM hydrogel implants displayed a compressive strength of 0,16491 MPa ± 0,001386 while after 4 weeks of exposure, it displayed a compressive strength of 0,159167 MPa ± 0,007596. However, despite a decrease in strength over time, it retained greater strength at 2 and 4 weeks as compared to ALG-PAAM hydrogel implants.

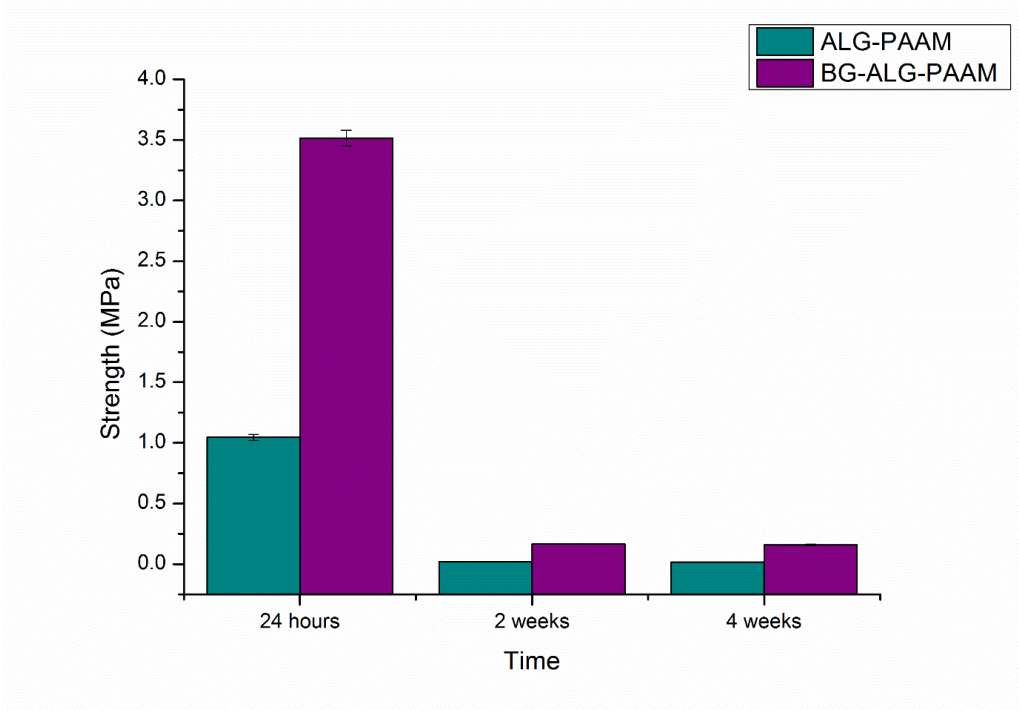


Figure 4.14: Bar graph depicting the decrease in compressive strength of ALG-PAAM and BG-ALG-PAAM hydrogel implants over time when exposed to SBF. BG-ALG-PAAM hydrogel implants displayed greater mechanical strength throughout the experiment as compared to ALG-PAAM hydrogel implants. The experiment was conducted in triplicate and data points were recorded as a mean ± SD (n=3).

Matrix resilience of BG-ALG-PAAM hydrogels were indicated to be 0,086804473% ± 0,014015811 and 0,112022256% ± 0,015229698 at 24 hours and 4 weeks respectively. ALG-PAAM scaffolds displayed an increase in matrix resilience as well when exposed to SBF. At 24 hours, MR proved to be 0,10406985% ±0,012482723 while at 4 weeks MR proved to be 0,139995834% ±0,00539164 for ALG-PAAM hydrogels (**Figure 4.15**).

The deformation energy decreased as exposure to SBF continued. It was noted for LAG-PAAM hydrogels were considerably less than that required for BG-ALG-PAAM. ALg-PAAM hydrogels required a deformation energy of 266,513 N.mm (0,26651 J) at 24 hours while at 4 weeks, ALG scaffolds Deformation energy was recorded at 18,733 N.mm (0,01873 J). Deformation energy for BG-ALG-PAAM scaffolds were at 706,094 N.mm (0,706 J) in the first 24 hours and decreased to 57,143 N.mm (0,05714 J) at 4 weeks of exposure to SBF (**Figure 4.15**).

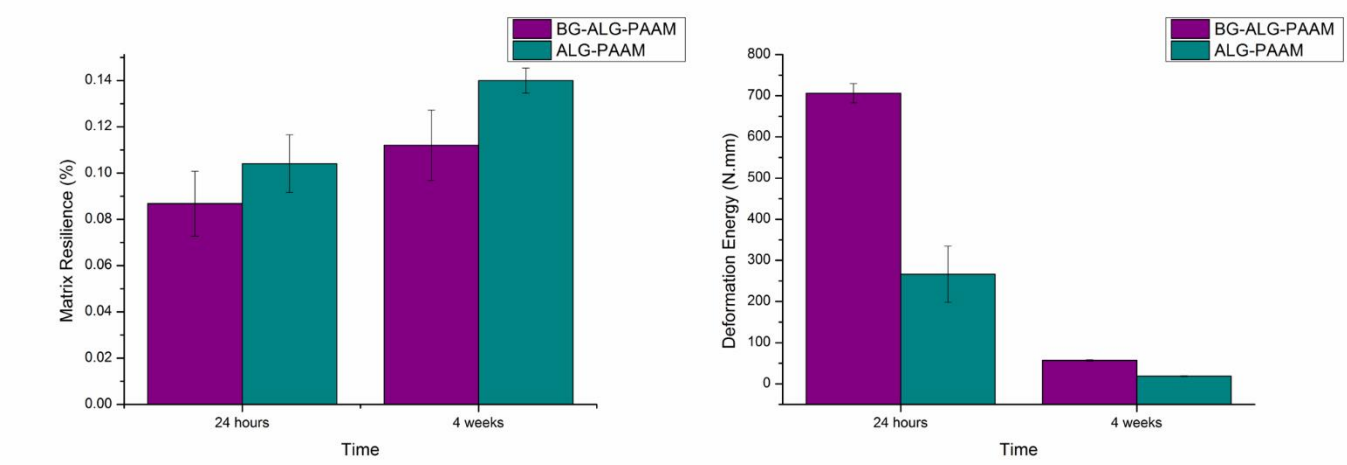


Figure 4.15: Bar graphs depicting matrix resilience (right) and deformation energy (left) of ALG-PAAM and BG-ALG-PAAM hydrogel implants after 24 hours and 4 weeks of exposure to SBF. Matrix resilience increased as exposure to SBF increased while deformation energy decreased as exposure to SBF increased. The experiment was conducted in triplicate and data points were recorded as a mean ± SD (n=3).

4.4.6 Swelling and shape retention of ALG-PAAM and BG-ALG-PAAM hydrogel implants

ALG-PAAM hydrogel implants displayed a higher swelling ratio (*ca*. 826%) compared to the hydrogel implants loaded with bioglass (*ca.* 731%). The swelling profiles can be seen in **Figure 4.16**.

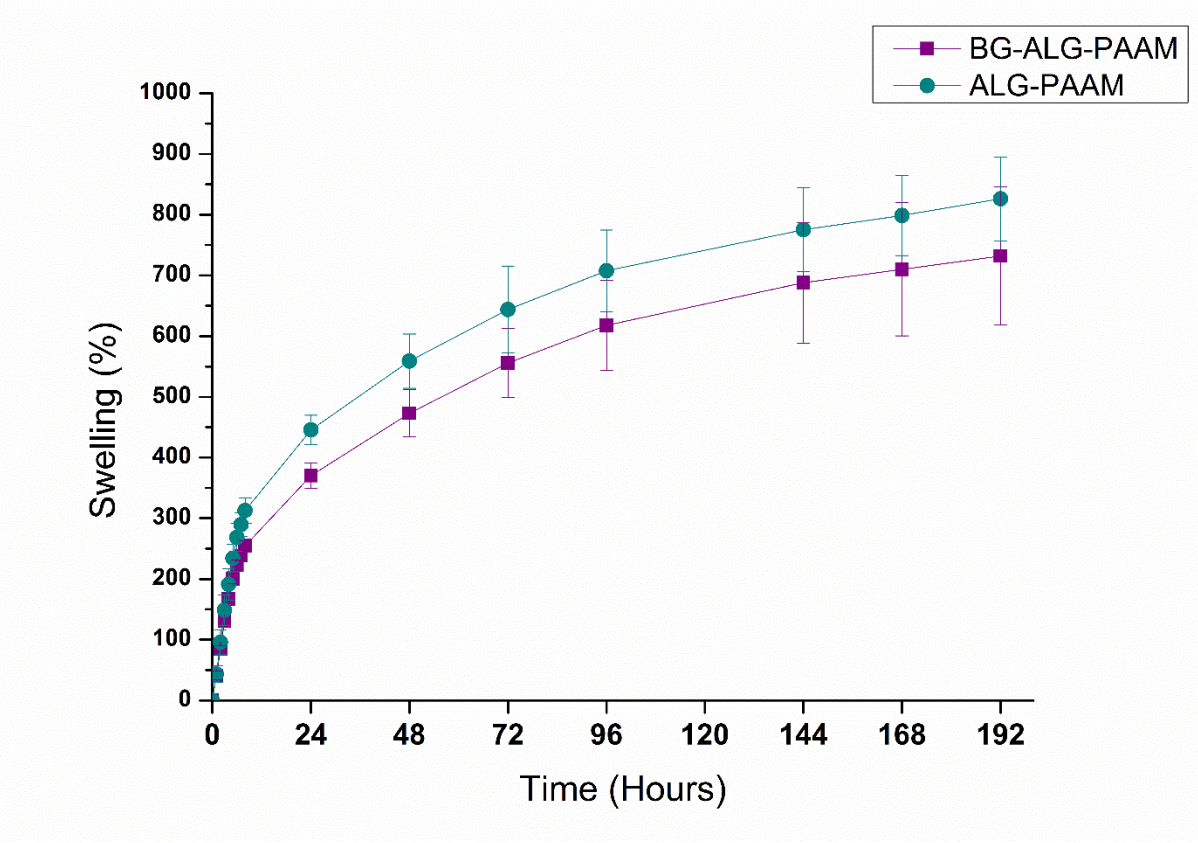


Figure 4.16: Line graphs depict the swelling profiles of ALG-PAAM and BG-ALG-PAAM. ALG-PAAM displayed a slightly higher swelling capacity than BG-ALG-PAAM. The experiment was conducted in triplicate and data points were recorded as a mean ± SD (n=3)

Both hydrogel implants (**Figure 4.17** and **Figure 4.18**) displayed the ability to maintain shape over a long period of time despite swelling substantially. This shows that it has the potential to fit in the resection site without deformation which can prevent implant loosening.

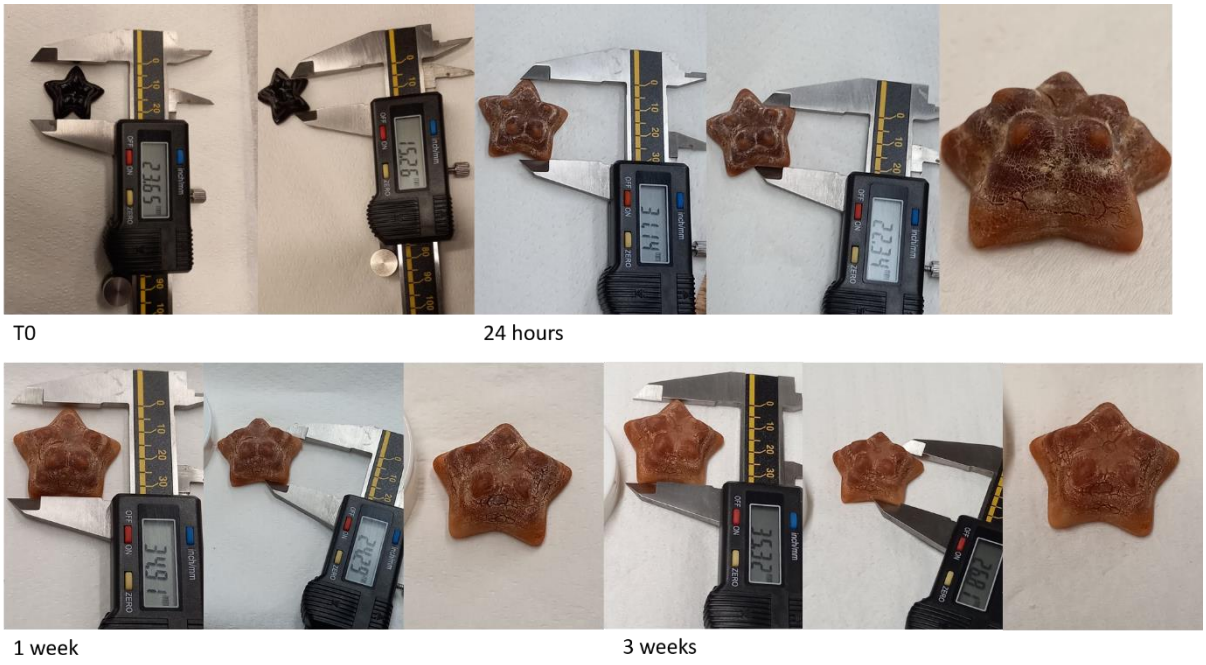


Figure 4.17: ALG-PAAM shape maintenance over time. It can be seen that ALG-PAAM hydrogel implants can maintain its shape after swelling substantially.

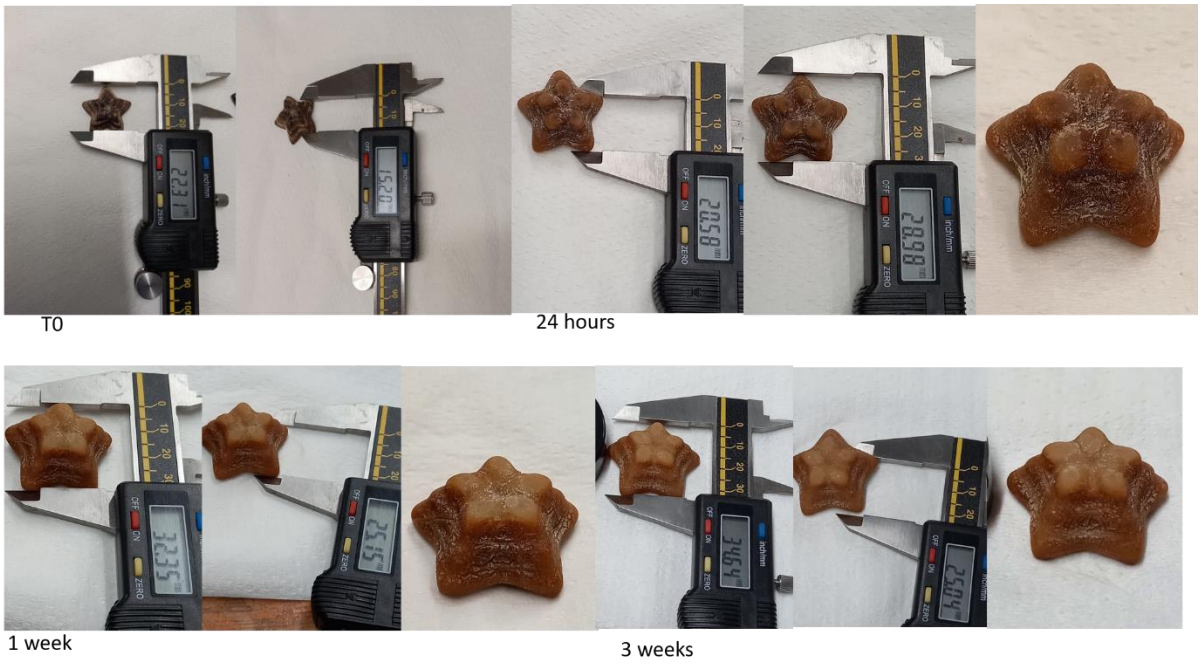


Figure 4.18: BG-ALG-PAAM shape maintenance over time. It can be seen that ALG-PAAM hydrogel implants can maintain its shape after swelling substantially.

4.4.7 Degradation of ALG-PAAM and BG-ALG-PAAM hydrogel implants

Degradation of ALG-PAAM hydrogel implants and BG-ALG-PAAM hydrogel implants were assessed over 6 weeks (**Figure 4.19**). ALG-PAAM hydrogel implants initially displayed a similar degradation profile compared to BG-ALG-PAAM hydrogel implants for the first 2 weeks. However, at the third and fourth week, BG-ALG-PAAM hydrogel implants displayed a greater degradation. ALG-PAAM hydrogel implants displayed degradation of 6,459972825% ± 1,004415844, 7,860207769% ± 4,696023197, 8,946395169% ± 3,038705096 and 8,967228098% ± 1,915695346 at 1, 2, 3, and 4 weeks respectively. BG-ALG-PAAM hydrogel implants displayed a 7,159114472% ± 1,908934873, 8,468176915% ± 1,489019185, 11,97028726% ± 2,709211293 and 13,4040672% ± 1,946145569 at the same intervals respectively. At the end of 4 weeks, ALG-PAAM hydrogel implants were at 91,0327719% ± 1,915695346 of their initial weight while BG-ALG-PAAM hydrogel implants weighed 86,5959328% ± 1,946145569 of their original weight. At 6 weeks, ALG-PAAM hydrogel implants degraded to 87,674% ± 5,042 of their original weight, while BG-ALG-PAAM hydrogel implants degraded to 86,528% ± 0,0987 of their original weight.

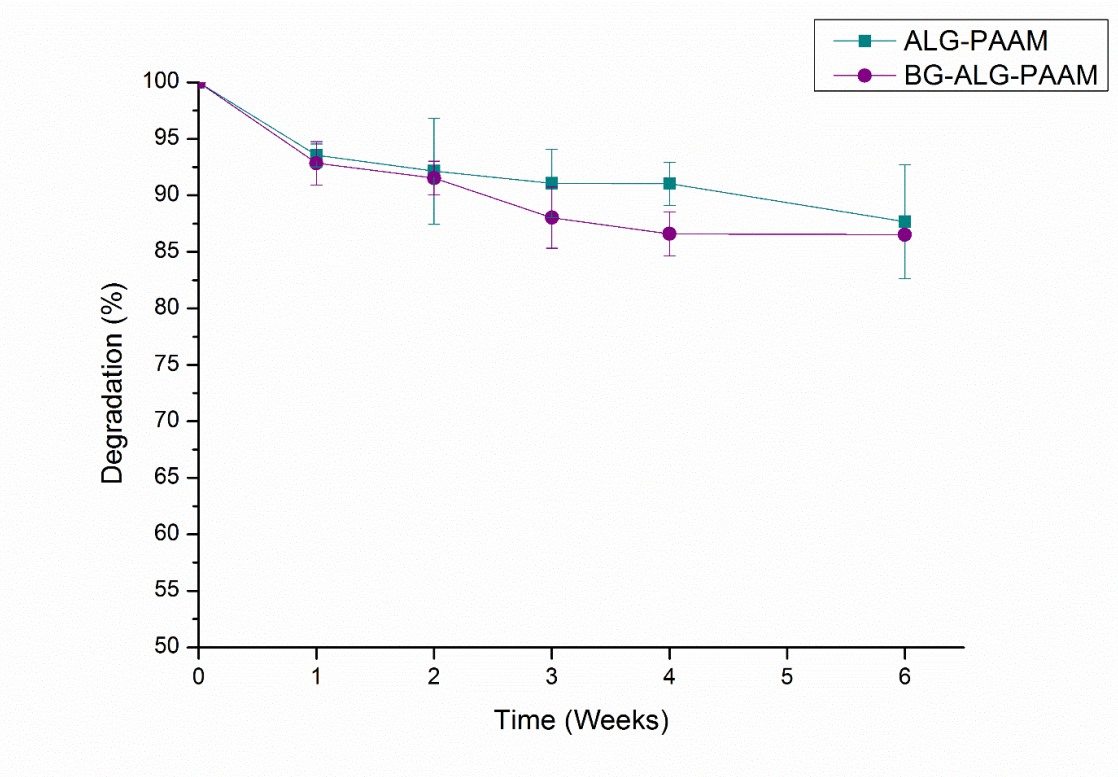


Figure 4.19: Degradation of ALG-PAAM hydrogel implants and BG-ALG-PAAM hydrogel implants over 6 weeks. BG-ALG-PAAM and ALG-PAAM displayed similar degradation profiles over the first 2 weeks, while at the third and fourth weeks BG-ALG-PAAM displayed greater degradation. The experiment was conducted in triplicate and data points were recorded as a mean ± SD (n=3).

4.4.8 Morphology, Porosity and Pore size of ALG-PAAM and BG-ALG-PAAM hydrogel implants

At 24 hours, the morphology of the hydrogel implants showed that the hydrogel implants had pores (**Figure 4.20**), however, these were not interconnected. The presence of the pores at this stage were attributed to the addition of sodium bicarbonate. BG-ALG-PAAM had an inherently rougher surface which can be attributed to the presence of bioglass. From week 1 of degradation (**Figure 4.21**) the presence of interconnected pores was noted. This morphology was maintained in week 2 (**Figure 4.22**). However, from week 3 (**Figure 4.23**) of degradation the formation of web like structures (indicated by arrows) were seen in both hydrogel implants. At week four of degradation these web-like structures were more prevalent in ALG-PAAM hydrogel implants compared to BG-ALG-PAAM hydrogel implants (**Figure 4.24**). The web like structures were attributed to the weakening structure of the hydrogel implants due to enzymatic degradation over time.

ALG-PAAM hydrogel implants displayed an initial porosity of ~30,558% which continually decreased to ~21,848 % after 4 weeks. BG-ALG_PAAM displayed a porosity of 31,902% after 1 week of degradation. Porosity then increased to ~35,236% then decreased after the third and fourth week with a final porosity of ~20,019%. The slightly greater porosity displayed by BG-ALG-PAAM can perhaps be attributed to the dissolution of bioglass which left pores behind.

Both hydrogel implants displayed a minimum pore size of under 10 μm throughout the 4 week experiment. During the first 3 weeks of the experiment both hydrogel implants also displayed a pore size of greater than 100 μm, with ALG-PAAM hydrogel implants mostly displaying a greater maximum pore size then BG-ALG-PAAM hydrogel implants. However, during the final week of the experiment, both hydrogel implants decreased in maximum pore size to under 100 μm with ALG-PAAM hydrogel implants displaying a maximum pore size of ~62 μm while BG-ALG-PAAM displayed a maximum pore size of ~89 μm.

Table 4.1 details the porosity and pore size range of the hydrogel implants over 4 weeks of exposure to degradation media.

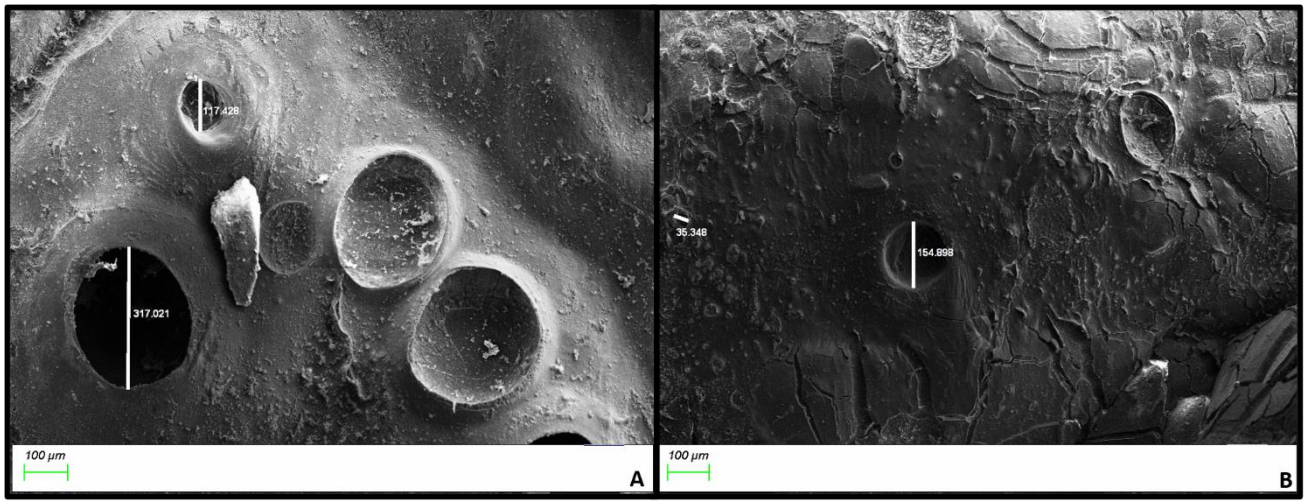


Figure 4.20: Morphology at 24 hours of degradation. A- ALG-PAAM. B- BG-ALG-PAAM. No interconnecting pores could be observed.

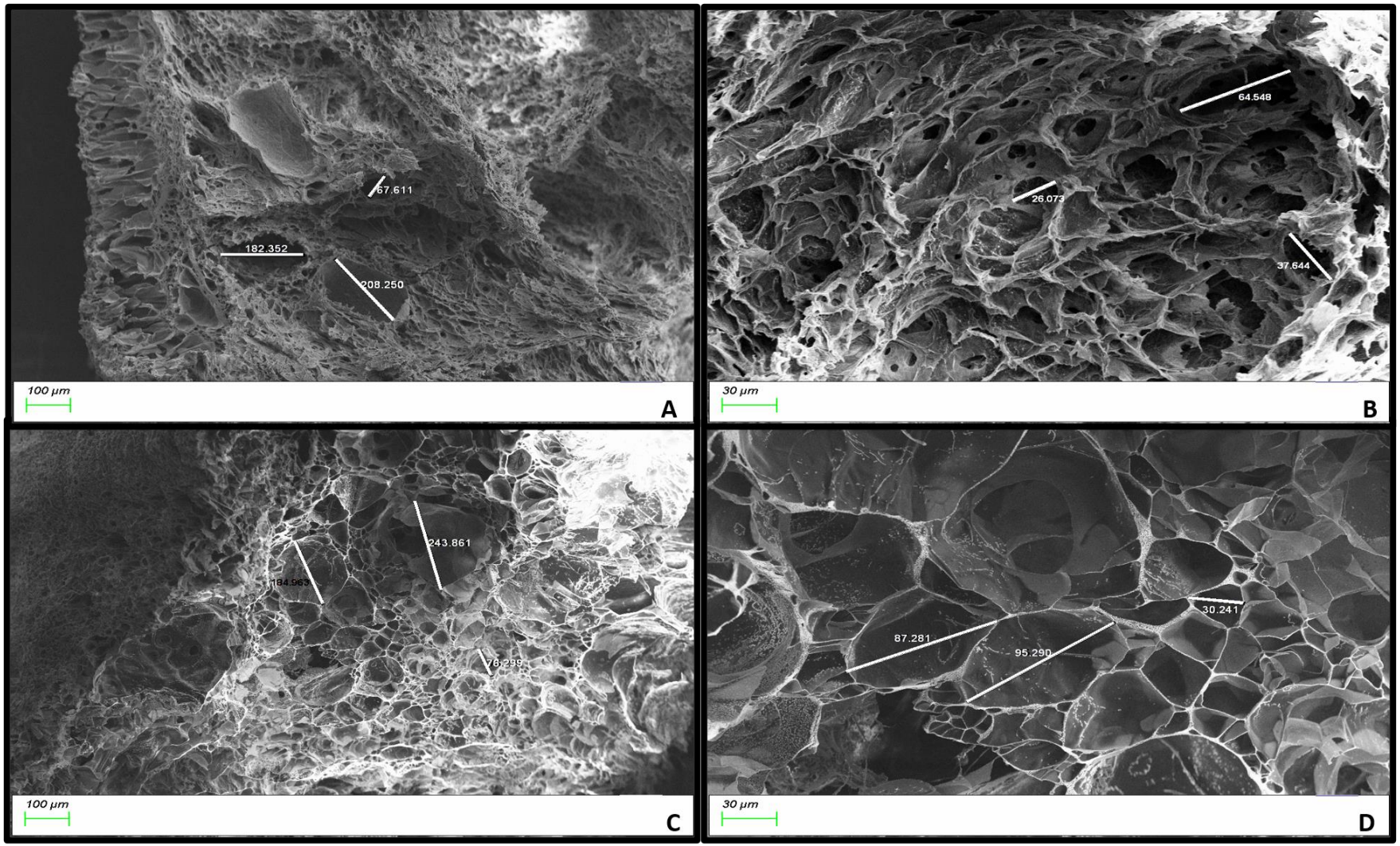


Figure 4.21: Morphology at 1 week degradation captured at different scales. A porous structure can be observed for both ALG-PAAM and BG-ALG-PAAM hydrogel implants. A- ALG-PAAM at 100 µm. B- ALG-PAAM at 30 µm. C- BG-ALG-PAAM at 100 µm. D- BG-ALG-PAAM at 30 µm.

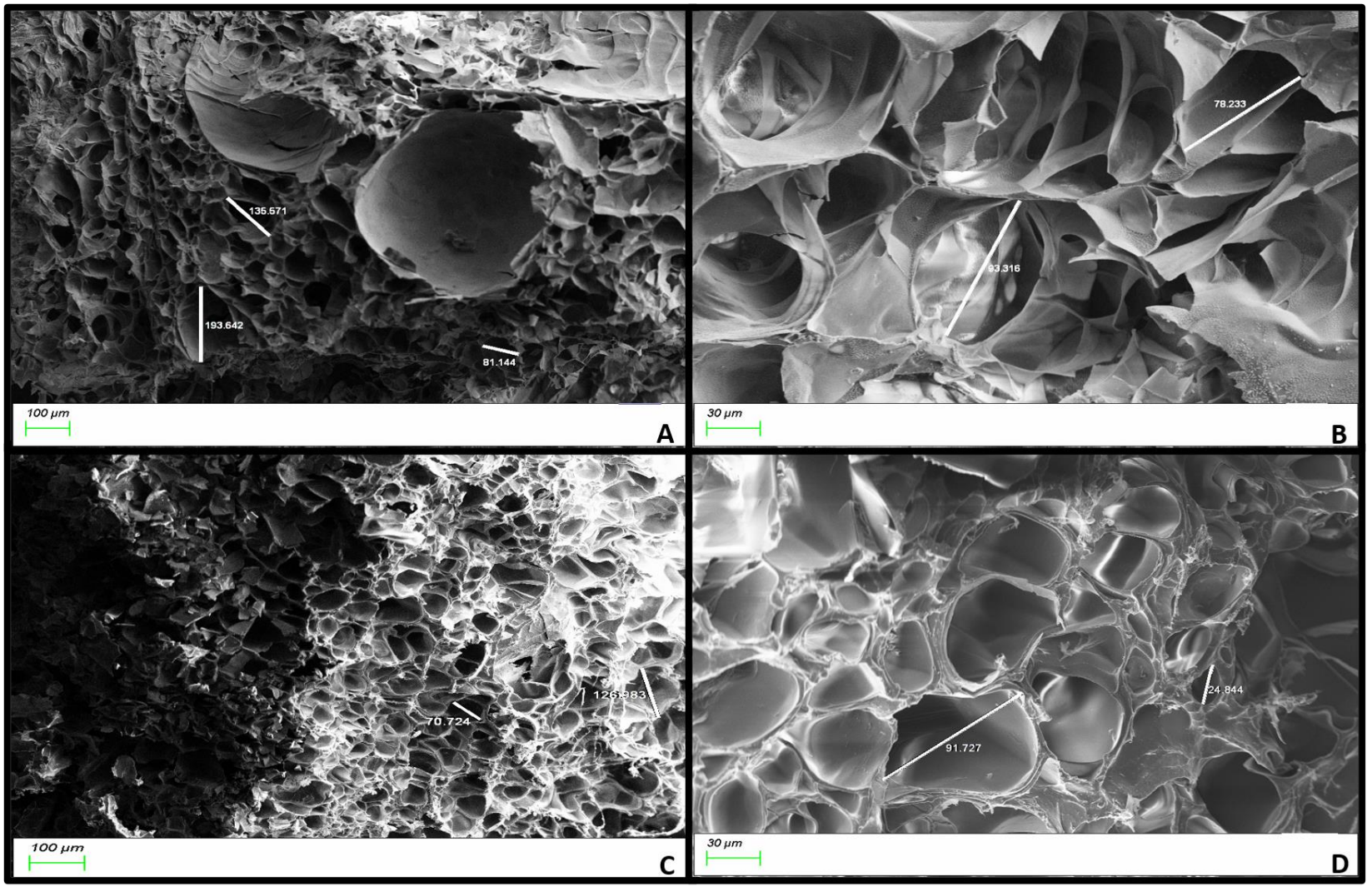


Figure 4.22: Morphology at 2 weeks degradation captured at different scales. A porous structure can be observed for both ALG-PAAM and BG-ALG-PAAM hydrogel implants. A- ALG-PAAM at 100 µm. B- ALG-PAAM at 30 µm. C- BG-ALG-PAAM at 100 µm. D- BG-ALG-PAAM at 30 µm.

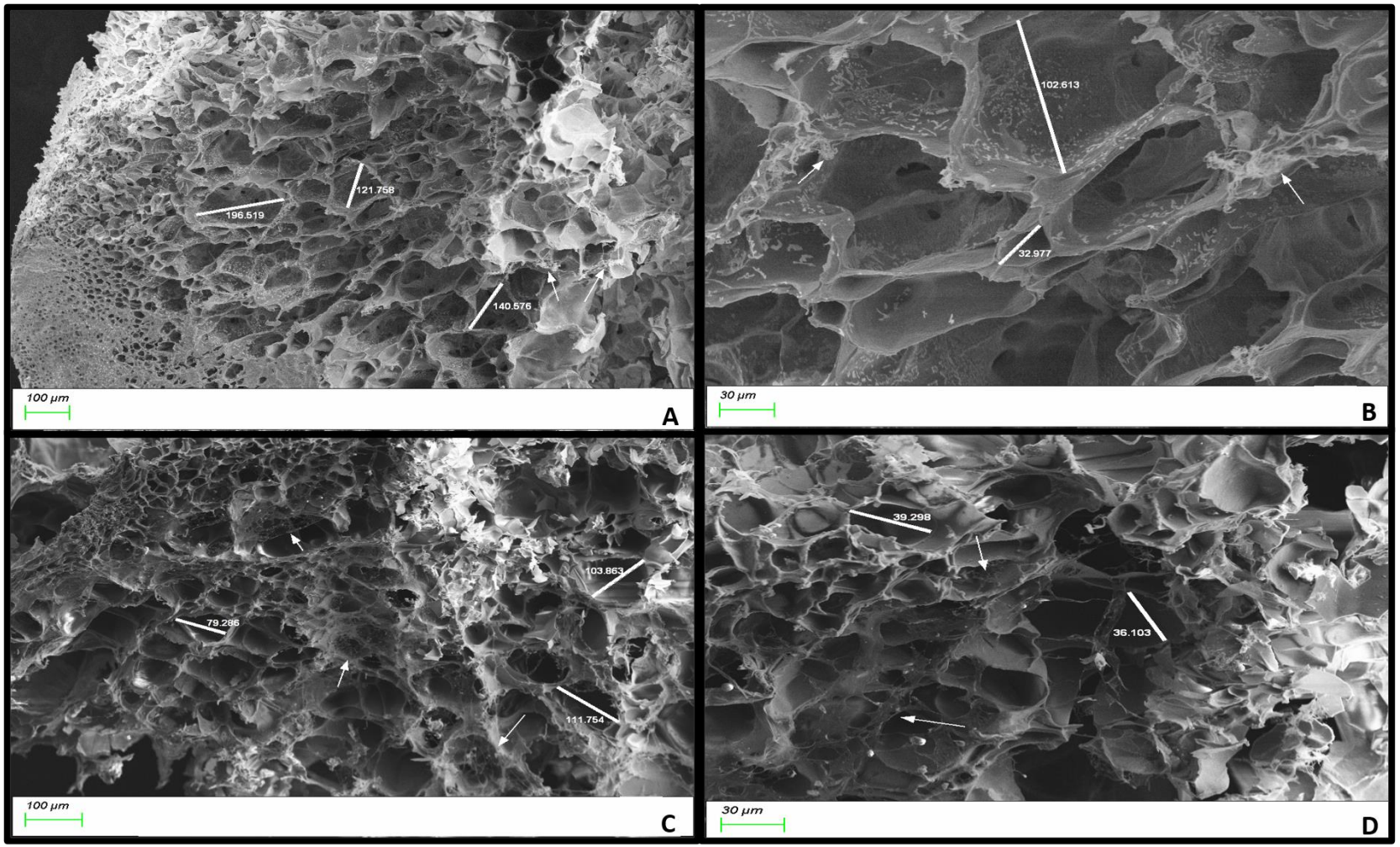


Figure 4.23: Morphology at 3 weeks degradation captured at different scales. Web like structures can be observed due to degradation implants as indicated by the white arrows. A porous structure can still be observed. A- ALG-PAAM at 100 µm. B- ALG-PAAM at 30 µm. C- BG-ALG-PAAM at 100 µm. D- BG-ALG-PAAM at 30 µm.

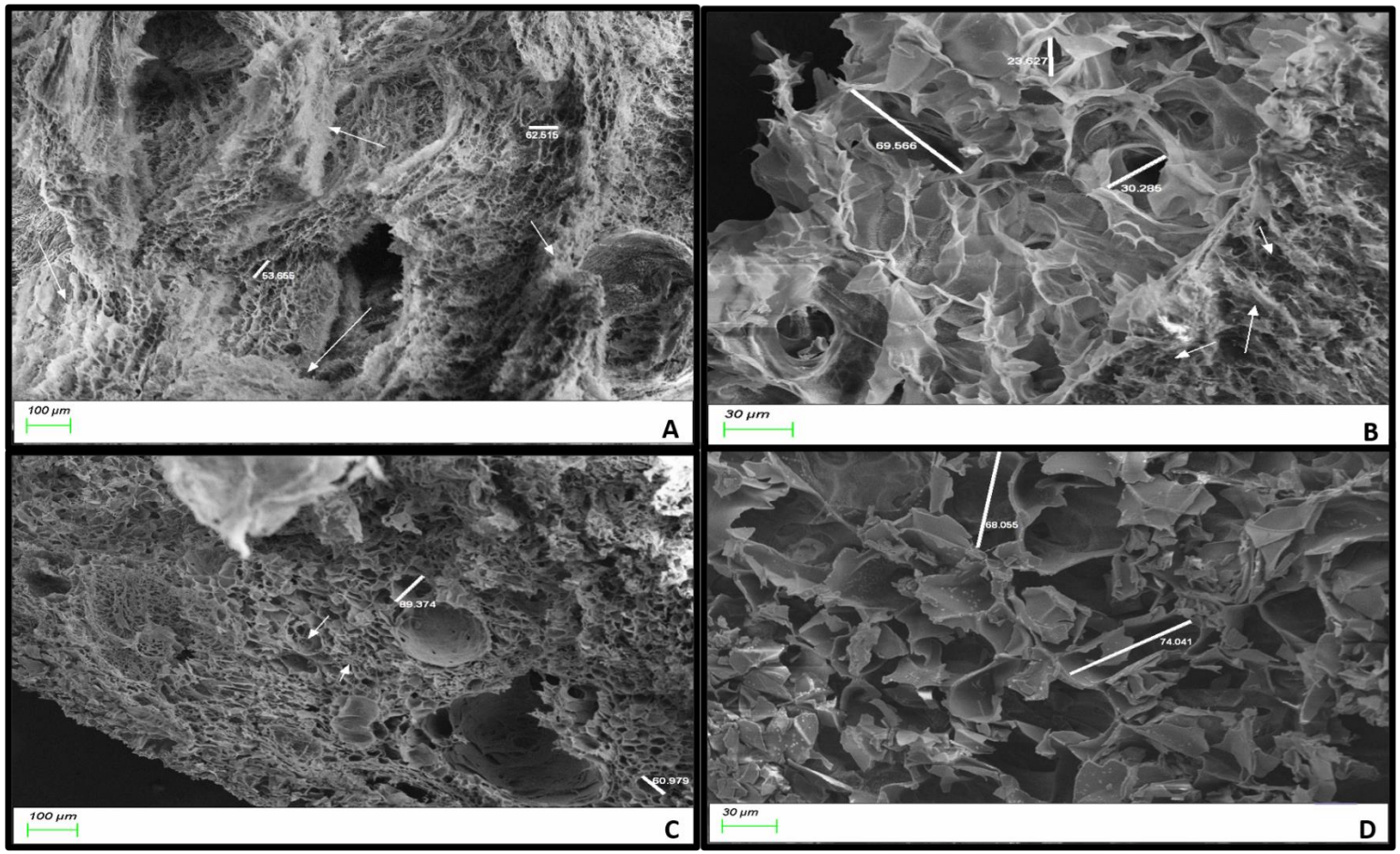


Figure 4.24: Morphology at 4 weeks degradation captured at different scales. Web like structures can be observed due to degradation implants as indicated by the white arrows. A porous structure can still be observed A- ALG-PAAM at 100 µm. B- ALG-PAAM at 30 µm. C- BG-ALG-PAAM at 100 µm. D- BG-ALG-PAAM at 30 µm.

Table 4.1: Porosity and range of Pore sizes present in ALG-PAAM and BG-ALG-PAAM hydrogel implants

	ALG-PAAM		BG-ALG-PAAM	
Week	Porosity (%)	Pore size range (μm)	Porosity (%)	Pore size range (μm)
1	30,558 ± 0,154	3,204-208,258	31,902 ± 1,203	7,963- 243,861
2	29,173 ± 1,153	7,438- 193,642	35, 236 ± 3,427	3,33 – 126,983
3	26, 272 ± 1,021	7,070 – 196,519	33,493 ± 1,604	1,969- 111,754
4	21,848 ± 1,313	6,160 – 62,515	20,019 ± 1,856	8,554- 89,374

4.4.9 Drug Loading and Drug release of ALG-PAAM and BG-ALG-PAAM hydrogel implants

ALG-PAAM hydrogel implants displayed a drug loading of 74,180% ± 0,515 while BG-ALG-PAAM hydrogel implants displayed a drug loading of 72,176% ± 0,279 (**Figure 4.25**).

Doxorubicin release from ALG-PAAM and BG-ALG-PAAM DN hydrogel implants displayed a sustained release profile. Withing the first 72 hours, BG-ALG-PAAM hydrogel implants displayed a release of 13,337 % ± 0,77285 while ALG-PAAM DN hydrogel implants displayed 12,04336 % ± 4,20521. However, at 8 weeks, ALG-PAAM hydrogel implants displayed a drug release at 20,125% ± 4,9773 while BG-ALG-PAAM displayed a drug release of 20,823% ± 1,237 (**Figure 4.26**).

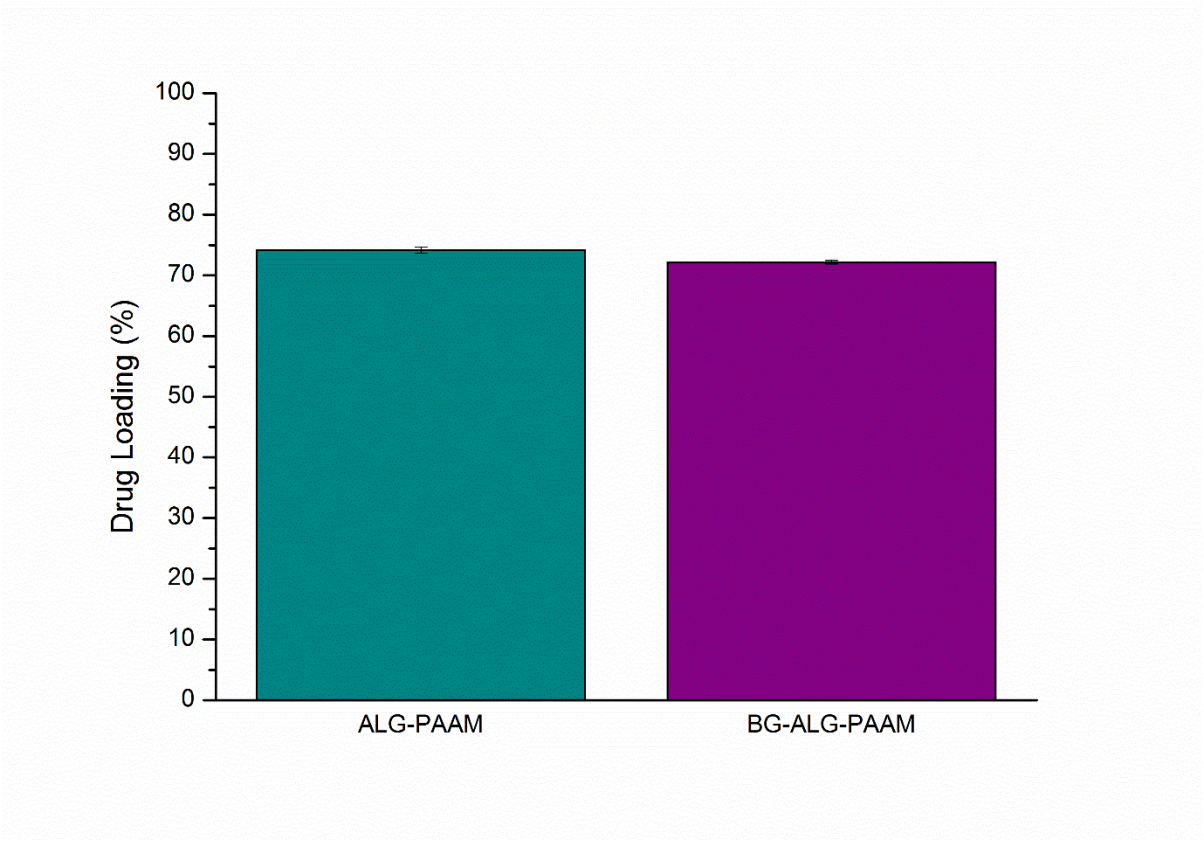


Figure 4.25: Percentage drug loading of ALG-PAAM and BG-ALG-PAAM hydrogel implants depicted as bar graphs. ALG-PAAM hydrogel implants displayed a slightly greater drug loading capability. The experiment was conducted in triplicate and data points were recorded as a mean ± SD (n=3).

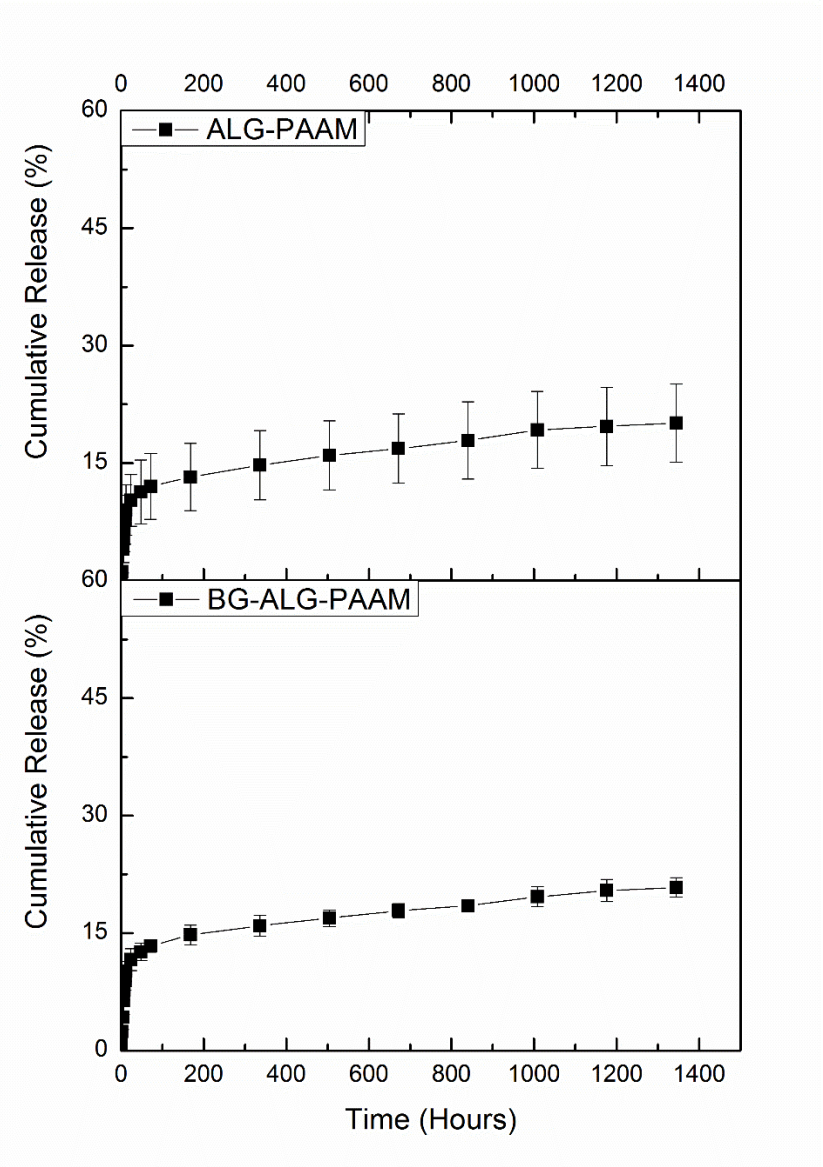


Figure 4.26: Cumulative drug release of doxorubicin from ALG-PAAM and BG-ALG-PAAM hydrogels. At 72 hours, BG-ALG-PAAM initially displayed a slightly larger drug release of 13,337 % ± 0,77285 while ALG-PAAM displayed a release of 12,04336 % ± 4,20521. At 8 weeks, drug release was noted at 20,125% ± 4,9773 and 20,823% ± 1,237 for ALG-PAAM and BG-ALG-PAAM respectively. The experiment was conducted in triplicate and data points were recorded as a mean ± SD (n=3)

4.4.10 In Vitro cell compatibility of ALG-PAAM and BG-ALG-PAAM hydrogel implants

At 72 hours cells with media conditioned with hydrogel implants at 3 days, PAAM-ALG displayed a viability of 112,6923 % ± 5,89988 while BG-ALG-PAAM showed a viability of 103,25329% ± 2,913799. BG-ALG-PAAM 7 days conditioned media displayed a cell viability of 87,21345% ± 5,84135, while PAAM-ALG 7-day conditioned media displayed a lower

viability of 94, 19111% ± 7,38252. However, no statistical differences were noted when compared to the control (**Figure 4.27**).

When extracts were incubated with the calculated drug release at the respective time points, the following was noted- 3- and 7-days extracts from ALG-PAAM hydrogel implants incubated with doxorubicin displayed a viability of 20,79593% ± 0,624503 and 19,01173% ± 1,17598 while the free drug displayed a viability of 18,10924% ± 1,418827 and 20,16808% ± 0,616214 at the respective 3- and 7-day time points. 3- and 7-days extracts from BG-ALG-PAAM hydrogel implants incubated with doxorubicin displayed a viability of 19,57567% ± 1,509053 and 18,73654% ± 0,616214, while the free drug displayed a cytotoxicity of 18,12513% ± 4,059009 and 19,8307% ± 0,863351. Statistical differences ($p < 0.05$). were noted indicating that whether alone or in combination with hydrogel implants extracts, doxorubicin elicited a cytotoxic effect (**Figure 4.27**).

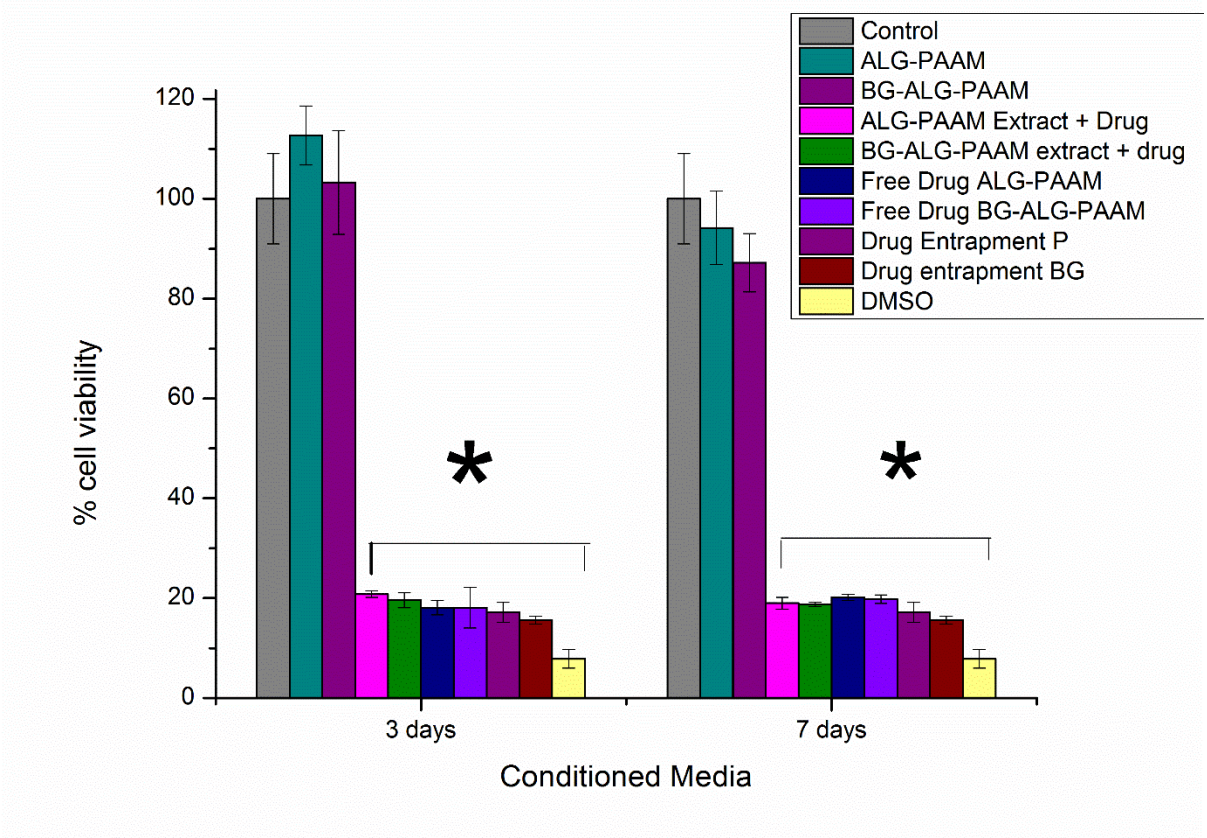


Figure 4.27: Cell viability of ALG-PAAM and BG-ALG-PAAM hydrogel implants treated with 3 days and 7 days conditioned media, conditioned media combined with the concentration of

DOX released at that time point and Freed Doxorubicin drug. Data is presented as mean ± SD, n=3. * Indicates statistical difference ($p < 0.05$).

Cell adhesion was noted on both hydrogel implants with cell clusters forming, however ALG-PAAM hydrogel implants displayed cell clusters that were noticeably sparser (**Figure 4.28**) than when compared to BG-ALG-PAAM hydrogel implants (**Figure 4.29**). Cells displayed normal morphology on both ALG-PAAM and BG-ALG-PAAM hydrogel implants. If the implants were cytotoxic, the cell would have displayed abnormal morphology.

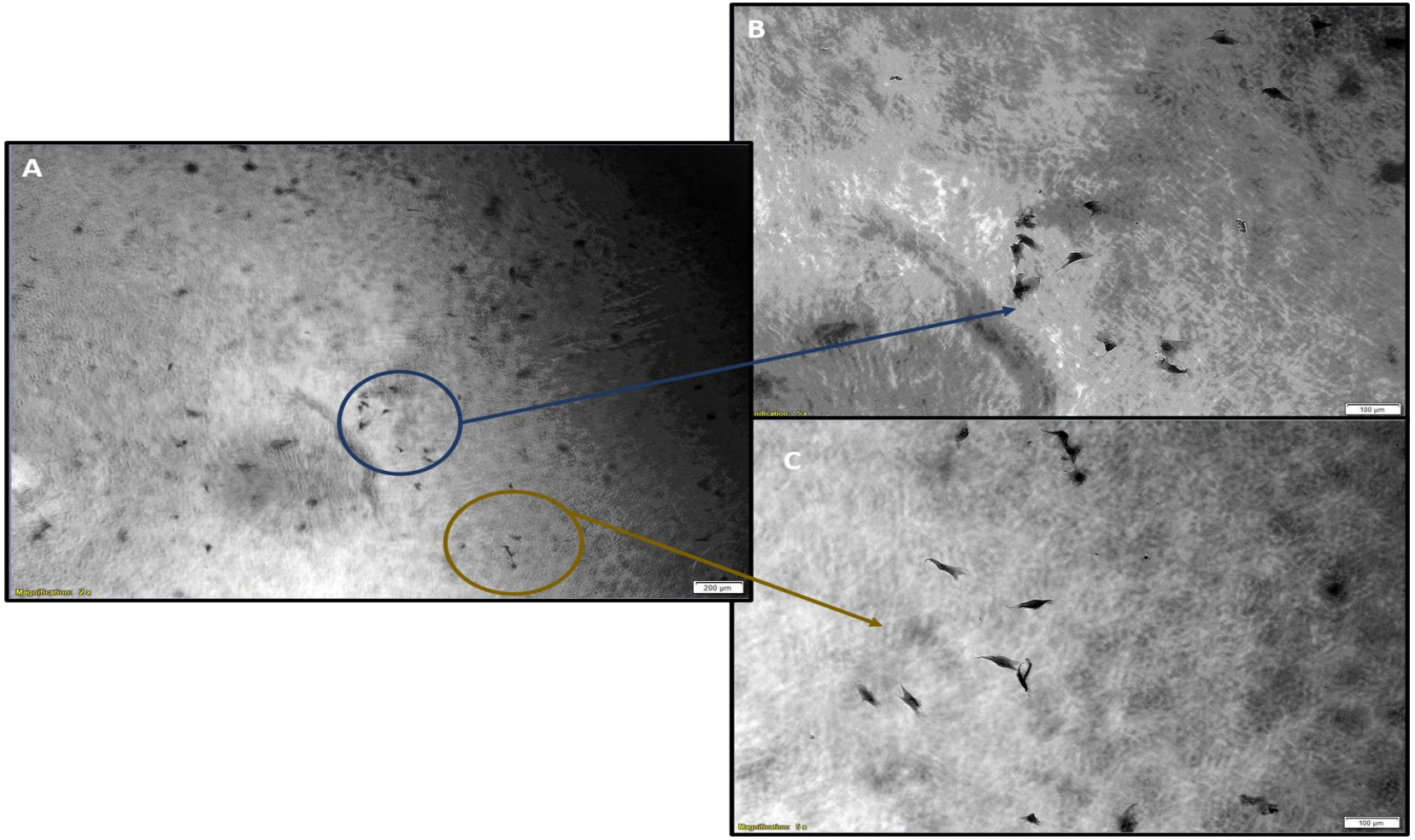


Figure 4.28:Cell adhesion onto ALG-PAAM hydrogel implants. Images show sparse cells. A- image of MG-63 cells on ALG-PAAM hydrogel implants at 200 ųm. B,C- areas of A containing MG-63 cells at 100 ųm. Cells display normal morphology.

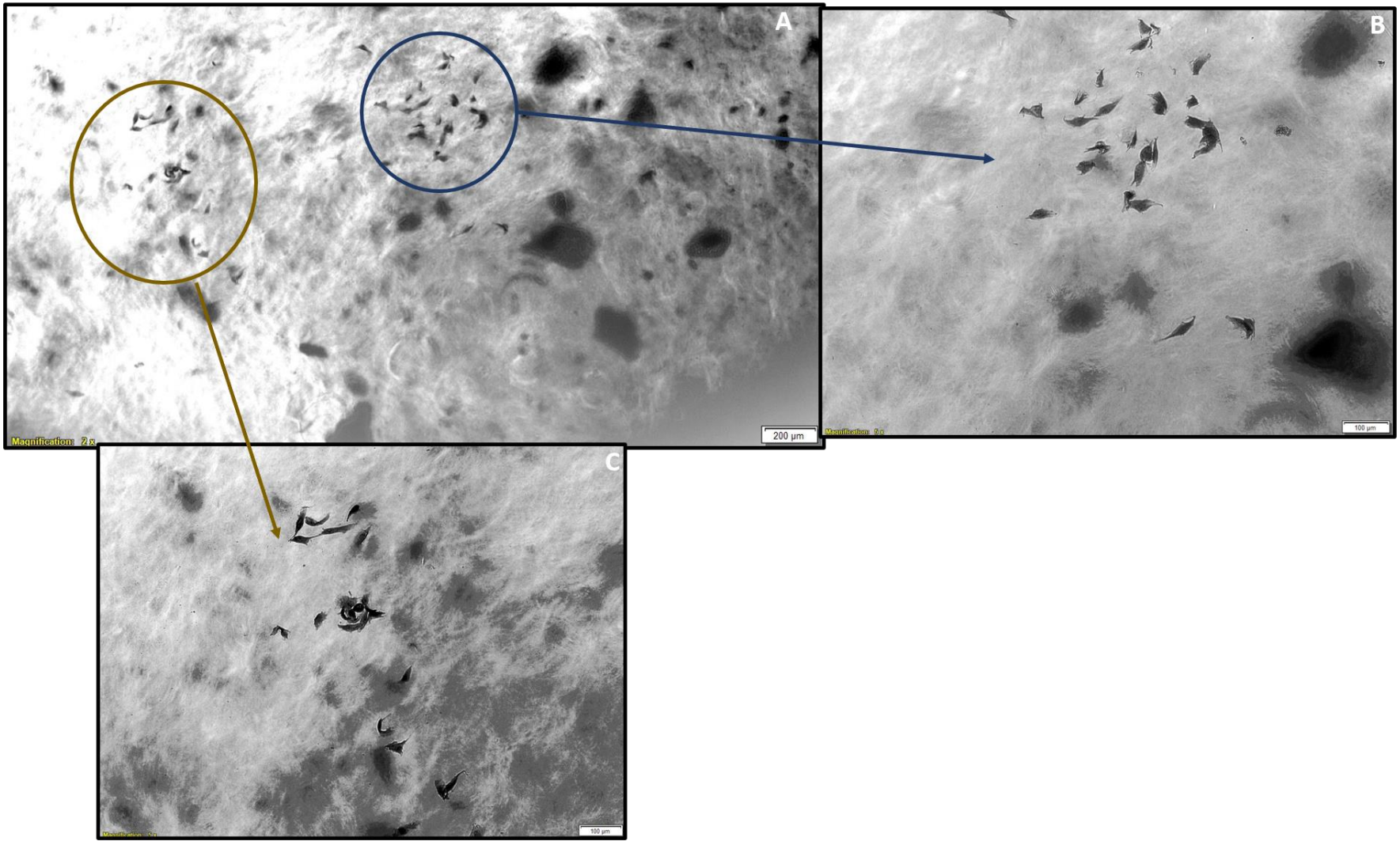


Figure 4.29:Cell adhesion of BG-ALG-PAAM hydrogel implants. Images show cell clusters. A- image of MG-63 cells on ALG-PAAM hydrogel implants at 200 µm. B,C- areas of A containing MG-63 cells at 100 µm. Cells display normal morphology.

4.5 Discussion

In this paper, ALG-PAAM implantable double network hydrogels were synthesised by a two-step method and bioglass was incorporated therein. Physicochemical analysis shows the successful synthesis of double network hydrogels while thermal characterisation and morphology over time shows the increased stability that bioglass has imparted to the hydrogel implants. According to the diamond concept, there are five general therapeutic targets that bone regeneration platforms should aim for; growth factors (osteoinduction), vascularization (angiogenesis), mechanical properties, osteogenesis (synthesis of new bone) and osteoconduction. Hydrogel implants should possess at least three of these five properties (Giannoudis, Einhorn and Marsh, 2007; Giannoudis *et al.*, 2008; Jahan and Tabrizian, 2016). By incorporating bioglass (which is osteoconductive and osteoproductive (stimulates growth of new bone) (Rainer *et al.*, 2008)) into the hydrogel implants, already two of these criteria were met.

4.5.1 Moulding Capability of ALG-PAAM and BG-ALG-PAAM hydrogel implants

The hydrogel implants ability to maintain the shape of the mould even after crosslinking proves that it is suitable for patient customisation. A mould can be made in the shape of the estimated bone defect that will be caused by osteosarcoma resection and the hydrogel implants can then be shaped according to the mould, thus displaying the advantageous property of customisation.

4.5.2 Mechanical Strength of ALG-PAAM and BG-ALG-PAAM hydrogel implants

The mechanical properties of a hydrogel implants for application in bone regeneration should be almost the same as the mechanical properties of the surrounding bone and it should maintain the same mechanical properties after implantation (Prasadh and Wong, 2018). Human cortical bone has a compressive strength of between 90 and 230 MPa and the compressive strength of cancellous bone lies between 2 and 45 MPa (Hannink and Arts, 2011). After 24 hours of immersion in SBF, ALG-PAAM hydrogel implants displayed a lower compressive strength (1,045367 MPa ± 0,024271) compared to BG-ALG-PAAM hydrogel implants (3,51627 MPa ± 0,06504). While BG-ALG-PAAM hydrogel implants match the compressive strength of cancellous bone at by being over 2 MPa in the first 24 hours, over time both hydrogels displayed drastic reduction in mechanical strength. Despite this, BG-ALG-PAAM hydrogel implants maintained higher strength compared to ALG-PAAM hydrogel implants. While osteosarcoma affects the cortical part of the bone as well, it can be reasoned that adolescents have a lower bone strength than adults (Öhman *et al.*, 2011), therefore BG-

ALG-PAAM hydrogel implants could still meet the mechanical strength criteria in osteosarcoma affecting young adolescents. Therefore, it can be said that BG-ALG-PAAM hydrogel implants meets three of the diamond concepts qualification criteria namely, mechanical strength (initially), osteoconduction and osteoproduction. However, as BG-ALG-PAAM hydrogel implants are exposed to body fluids, it loses one qualification- mechanical strength. However, if the hydrogel is not of appropriate strength, it can still be used for bone regeneration but needs to be fixed with plates, screws, wires or pins (Prasadh and Wong, 2018).

Both hydrogels possessed low matrix resilience values which are indicative of the hydrogels absorbing little impacting energy. As the hydrogels continued to be submerged in SBF, the matrix resilience values increased. Therefore it can be said that as exposure to SBF increases, the hydrogels absorbed less impacting energy and are less resistant to applied stress (Indermun *et al.*, 2014). However, BG-ALG-PAAM had lower matrix resilience values compared to ALG-PAAM hydrogels. Thus, it can be said that BG-ALG-PAAM hydrogel implants can better absorb impacting energy than ALG-PAAM hydrogel implants.

Deformation energy is the energy absorbed that causes deformation to the hydrogel (Mabrouk *et al.*, 2016). As exposure to SBF increases, less energy is required to cause scaffold deformation, however, it can be noted that BG-ALG-PAAM scaffolds require more energy to be deformed than ALG-PAAM scaffolds. This data supports the premise that Bioglass imparts better mechanical strength to hydrogel.

4.5.3 Swelling capabilities of ALG-PAAM and BG-ALG-PAAM hydrogel implants

The good swelling ability and expansion of hydrogel implants volume is advantageous as it promotes contact between implant and host tissue which can therefore promote healing Increased contact between host bone tissue and the hydrogel implants would also mean less shear forces at implant-bone interface and thus improves bone healing (Podporska-Carroll, Ip and Gogolewski, 2014). Swelling is also important for the hydrogel implants to absorb body fluid and for the uptake of cell nutrients (Li *et al.*, 2011; Azhar, Olad and Salehi, 2014). The hydrogel implants displayed a substantial swelling capacity (ALG-PAAM *ca*. 826% and BG-ALG-PAAM *ca.* 731%). ALG-PAAM and BG-ALG-PAAM hydrogel implants displayed the ability to maintain shape over a long period of time. This shows that it can fit in the resection site without deformation over time which will can prevent implant loosening. Due to the implants substantial swelling capacity and ability to maintain its shape after swelling, a very small quantity of the hydrogel implant in the shape of the defect could be inserted at the site of injury and can swell to fit the resection site.

4.5.4 Biomineralisation of ALG-PAAM and BG-ALG-PAAM hydrogel implants

Biomineralisation studies confirmed that hydroxyapatite was formed on surfaces of both DN hydrogels. XRD shows that BG-ALG-PAAM hydrogel implants had better biomineralization capabilities from week one. SEM and EDS also confirmed the presence of hydroxyapatite. As the Hydrogel implants exposure to SBF increased over time, the height of the crystalline peaks seen on XRD spectra also increased. BG-ALG-PAAM implantable hydrogels had greater crystalline peaks from week one as compared to ALG-PAAM implantable hydrogels.

4.5.5 Degradation of ALG-PAAM and BG-ALG-PAAM hydrogel implants

At the end of 6 weeks, ALG-PAAM scaffolds degraded to 87,674% ± 5,042 of their original weight, while BG-ALG-PAAM scaffolds degraded to 86,528% ± 0,0987 of their original weight. Previous research into bioglass composite scaffolds showed that bioglass containing composites do degrade faster than the scaffolds without bioglass. Furthermore, it could be seen that larger bioglass concentrations within the composite can be linked to faster degradation rates (Maquet *et al.*, 2003; Ryszkowska *et al.*, 2010). This can be attributed to the loss of bioglass particles from the composite into the degradation media (Maquet *et al.*, 2003). The degradation rate may also be linked to the porosity of the hydrogels. BG-ALG-PAAM hydrogels displayed a slightly higher porosity than ALG-PAAM hydrogels. The increase in porosity means a greater surface area was exposed to degradation media which in turn can be linked to a faster degradation time (Mabrouk *et al.*, 2014). This indicates a slow degradation rate for both scaffolds which proves that it will remain in the bone for an extended period of time. This indicated a slow degradation rate for both hydrogel implants which proves that it will remain in the bone for a while. This is advantageous as bone may take several months to completely heal (Mayo Clininc, 2022) if the biology of fracture repair is followed for critical defect healing (Cameron *et al.*, 2012). A low degradation rate may prove to be advantageous for cell attachment and differentiation (Mabrouk *et al.*, 2014).

4.5.6 Morphology of ALG-PAAM and BG-ALG-PAAM hydrogel implants

Pore size of 100 μm to 500 μm is optimal when considering hydrogel implants for bone regeneration (Yu *et al.*, 2010) as the size of osteoblasts are 50-80 μm. SEM imaging for both ALG-PAAM and BG-ALG-PAAM both displayed pore sizes of greater than 100 μm for weeks one to three of degradation. While these pores were not interconnected initially at 24 hours of swelling, degradation facilitated these pores to become interconnected as well facilitated the formation of other pores as seen in SEM images. This is advantageous as it will facilitate the migration and proliferation of osteoblasts into the hydrogel implants interior.

4.5.7 Drug Loading and Drug Release of ALG-PAAM and BG-ALG-PAAM hydrogel implants

The slightly decreased drug loading of BG-ALG-PAAM at can be attributed to its slightly lower swelling capacity.

According to the Union for International Cancer Control's 2014 Review of the WHO's cancer medicines on the list of Essential medicines (Union for International Cancer Control, 2014), the standard chemotherapy regimens for osteosarcoma include a 6 cycle MAP or 12 cycle OS99. These chemotherapy regimens include the delivery of doxorubicin by intravenous infusion after surgery. The OS99 Chemotherapeutic regimen for osteosarcoma details the administration of doxorubicin, carboplatin and ifosfamide. Chemotherapy is provided to the patient for 21 weeks after surgery for this regimen. The 6 cycle MAP regimen details the administration of doxorubicin, cisplatin and methotrexate. Chemotherapy is provided to the patient for 17 weeks after surgery for this regimen (Union for International Cancer Control, 2014).

The sustained release shown by both ALG-PAAM and BG-ALG-PAAM hydrogel implants may be advantageous as it has the potential to suit both regimens' duration as it displays a sustained release profile with ~20% of DOX released over 8 weeks. These regimens advise that chemotherapy be administered to the patient for 21 or 17 weeks after surgery. However, a disadvantage to the sustained release could be that bone growth will not be viable until complete release of doxorubicin has been achieved. (The presence of Doxorubicin may kill new bone as it grows onto the hydrogel implants).

4.5.8 In vitro cytocompatibility of ALG-PAAM and BG-ALG-PAAM hydrogel implants

Cell viability for both ALG-PAAM and BG-ALG-PAAM were above 85% for the 3 day and 7-day extract incubations. According to ISO 10993-5:2009(E), a substance has cytotoxic potential if the cell viability is reduced to below 70% (International Standards Organisation, 2009). Therefore, it can be concluded that the degradation components released from the hydrogel implants is not cytotoxic. Cell attachment studies proved that both the hydrogel implants facilitated cell attachment, with BG-ALG-PAAM hydrogel implants having facilitated better cell attachment than ALG-PAAM hydrogel implants.

4.6 Concluding Remarks

Results of this paper indicate that only BG-ALG-PAAM hydrogel implants met the criteria of the Diamond concept with the following qualifications; Osteoconductivity, osteoproductivity and mechanical strength. However, mechanical strength of BG-ALG-PAAM implants decreased over time when exposed to body fluid. Moulding abilities show that the composite

hydrogel implants are suitable for customising the implant to patient needs. Drug release profiles display a sustained release; however, while the release may suit standard treatment regimen times, it can be said that bone will not grow until DOX is released entirely from the hydrogel implants. Therefore, modification to the system for faster release of doxorubicin must be considered. BG-ALG-PAAM has the potential to be applied to certain osteosarcomas without the presence of drug, such as low-grade central OS and certain subtypes of surface osteosarcomas that only require surgery as treatment. It can also be concluded that BG-ALG-PAAM is the better double network hydrogel implant when compared to ALG-PAAM hydrogel implants.

4.7 References

Aguiar, H. *et al.* (2009) 'Structural study of sol-gel silicate glasses by IR and Raman spectroscopies', *Journal of Non-Crystalline Solids*. Elsevier B.V., 355(8), pp. 475–480. doi: 10.1016/j.jnoncrysol.2009.01.010.

Ahn, J. H. *et al.* (2020) 'The effect of mesoporous bioactive glass nanoparticles/graphene oxide composites on the differentiation and mineralization of human dental pulp stem cells', *Nanomaterials*, 10(4), pp. 1–18. doi: 10.3390/nano10040620.

American Cancer Society (2020) *Key Statistics for Osteosarcoma*. Available at: https://www.cancer.org/cancer/osteosarcoma/about/key-statistics.html (Accessed: 10 February 2020).

Azhar, F. F., Olad, A. and Salehi, R. (2014) 'Fabrication and characterization of chitosan-gelatin/nanohydroxyapatite- polyaniline composite with potential application in tissue engineering scaffolds', *Designed Monomers and Polymers*. Taylor & Francis, 17(7), pp. 654–667. doi: 10.1080/15685551.2014.907621.

Bahrami, Z., Akbari, A. and Eftekhari-Sis, B. (2019) 'Double network hydrogel of sodium alginate/polyacrylamide cross-linked with POSS: Swelling, dye removal and mechanical properties', *International Journal of Biological Macromolecules*. Elsevier B.V., 129, pp. 187–197. doi: 10.1016/j.ijbiomac.2019.02.046.

Bax, D. V. *et al.* (2018) 'Plasma processing of PDMS based spinal implants for covalent protein immobilization, cell attachment and spreading', *Journal of Materials Science: Materials in Medicine*. Springer US, 29(12). doi: 10.1007/s10856-018-6181-y.

Bhagyaraj, S. and Krupa, I. (2020) 'Alginate-mediated synthesis of hetero-shaped silver', *Molecules*, 25(435). doi:10.3390/molecules25030435

Bhaskar, B. *et al.* (2018) 'Composite porous scaffold of PEG/PLA support improved bone matrix deposition in vitro compared to PLA-only scaffolds', *Journal of Biomedical Materials Research - Part A*, 106(5), pp. 1334–1340. doi: 10.1002/jbm.a.36336.

Cameron, J. A. *et al.* (2012) 'Employing the Biology of Successful Fracture Repair to Heal Critical Size Bone Defects', *Current Topics in Microbiology and Immunology*, 367, pp. 113–132. doi: 10.1007/82_2012_291.

Cassimjee, H. *et al.* (2022) 'Genipin-Crosslinked, Proteosaccharide Scaffolds for Potential Neural Tissue Engineering Applications', *Pharmaceutics*, 14(2). doi: 10.3390/pharmaceutics14020441.

Cuadros, T. R., Erices, A. A. and Aguilera, J. M. (2015) 'Porous matrix of calcium alginate/gelatin with enhanced properties as scaffold for cell culture', *Journal of the Mechanical Behavior of Biomedical Materials*, 46, pp. 331–342. doi: 10.1016/j.jmbbm.2014.08.026.

Darnell, M. C. *et al.* (2013) 'Performance and biocompatibility of extremely tough alginate/polyacrylamide hydrogels', *Biomaterials*. Elsevier Ltd, 34(33), pp. 8042–8048. doi: 10.1016/j.biomaterials.2013.06.061.

Demianenko, P. and Minisini, B. (2016) 'Stiff IPN Hydrogels of Poly(Acrylamide) and Alginate: Influence of the Crosslinking Ion's Valence on Hydrogel's Final Properties', *Journal of Chemical Engineering & Process Technology*, 07(04). doi: 10.4172/2157-7048.1000304.

Dong, Y. *et al.* (2011) 'Preparation and catalytic activity of Fe alginate gel beads for oxidative degradation of azo dyes under visible light irradiation', *Catalysis Today*. Elsevier B.V., 175(1), pp. 346–355. doi: 10.1016/j.cattod.2011.03.035.

Fang, J. *et al.* (2019) 'A strong, tough, and osteoconductive hydroxyapatite mineralized polyacrylamide/dextran hydrogel for bone tissue regeneration', *Acta Biomaterialia*. Acta Materialia Inc., 88, pp. 503–513. doi: 10.1016/j.actbio.2019.02.019.

Giannoudis, P. V. *et al.* (2008) 'The diamond concept - open questions', *Injury*, 39(SUPPL.2), p. S5. doi: 10.1016/S0020-1383(08)70010-X.

Giannoudis, P. V., Einhorn, T. A. and Marsh, D. (2007) 'Fracture healing: The diamond concept', *Injury*, 38(S4), pp. S3–S6. doi: 10.1016/s0020-1383(08)70003-2

Gu, Z. *et al.* (2018) 'Double network hydrogel for tissue engineering', *Wiley Interdisciplinary Reviews: Nanomedicine and Nanobiotechnology*, 10(6), pp. 1–15. doi: 10.1002/wnan.1520.

Guo, P., Yuan, Y. and Chi, F. (2014) 'Biomimetic alginate/polyacrylamide porous scaffold supports human mesenchymal stem cell proliferation and chondrogenesis', *Materials Science and Engineering C*. Elsevier B.V., 42, pp. 622–628. doi: 10.1016/j.msec.2014.06.013.

Hannink, G. and Arts, J. J. C. (2011) 'Bioresorbability, porosity and mechanical strength of bone substitutes: What is optimal for bone regeneration?', *Injury*. Elsevier Ltd, 42(SUPPL. 2), pp. S22–S25. doi: 10.1016/j.injury.2011.06.008.

Heck, R. K. and Toy, P. C. (2017) 'Malignant Tumors of Bone', in *Campbell's Operative Orthopaedics*. 13th edn. Philadelphia: Elsevier, pp. 945–983. Available at: https://www.clinicalkey.com/#!/content/book/3-s2.0-B9780323374620000276?scrollTo=%23hl0000691.

Hench, L. L. (2006) ‘The story of Bioglass®’, *Journal of Materials Science: Materials in Medicine*, 17(11), pp. 967–978. doi: 10.1007/s10856-006-0432-z.

Howard, D. *et al.* (2008) ‘Tissue engineering: Strategies, stem cells and scaffolds’, *Journal of Anatomy*, 213(1), pp. 66–72. doi: 10.1111/j.1469-7580.2008.00878.x.

Huh, K. M., Baek, N. and Park, K. (2005) ‘Enhanced swelling rate of poly(ethylene glycol)-grafted superporous hydrogels’, *Journal of Bioactive and Compatible Polymers*, 20(3), pp. 231–243. doi: 10.1177/0883911505053378.

International Standards Organisation (2009) ‘Biological evaluation of medical devices — Part 5: Tests for in vitro cytotoxicity’, *ISO 10993-5:2009(E)*, (Third edition).

Jahan, K. and Tabrizian, M. (2016) ‘Composite biopolymers for bone regeneration enhancement in bony defects’, *Biomaterials Science*. Royal Society of Chemistry, 4(1), pp. 25–39. doi: 10.1039/c5bm00163c.

Javanbakht, S. and Namazi, H. (2018) ‘Doxorubicin loaded carboxymethyl cellulose/graphene quantum dot nanocomposite hydrogel films as a potential anticancer drug delivery system’, *Materials Science and Engineering C*. Elsevier, 87, pp. 50–59. doi: 10.1016/j.msec.2018.02.010.

Jones, R. L. (2020) ‘Malignant Tumors of Bone, Sarcomas, and Other Soft Tissue Neoplasms’, in *Goldman-Cecil Medicine*. 26th edn. Elsevier, pp. 1341–1344. Available at: https://0-www-clinicalkey-com.innopac.wits.ac.za/#!/content/book/3-s2.0-B9780323532662001922?scrollTo=%23top.

Khan, Y. M. *et al.* (2007) ‘In situ synthesized ceramic-polymer composites for bone tissue engineering: Bioactivity and degradation studies’, *Journal of Materials Science*, 42(12), pp. 4183–4190. doi: 10.1007/s10853-006-0636-0.

Kokubo, T. and Takadama, H. (2006) ‘How useful is SBF in predicting in vivo bone bioactivity?’, *Biomaterials*, 27(15), pp. 2907–2915. doi: 10.1016/j.biomaterials.2006.01.017.

Kolek, E. *et al.* (2007) ‘Confirmation of polymerisation effects of sodium chloride and its additives on acrylamide by infrared spectrometry’, *Journal of Food and Nutrition Research*, 46(1), pp. 39–44.

Kuzmanović, M. *et al.* (2017) ‘Sodium-alginate biopolymer as a template for the synthesis of nontoxic red emitting Mn2+-doped CdS nanoparticles’, *RSC Advances*, 7(84), pp. 53422–53432. doi: 10.1039/c7ra11011a.

Kwon, S. *et al.* (2018) ‘Bioglass-incorporated methacrylated gelatin cryogel for regeneration

of bone defects', *Polymers*, 10(8). doi: 10.3390/polym10080914.

Lee, K. Y. and Mooney, D. J. (2012) 'Alginate: Properties and biomedical applications', *Progress in Polymer Science (Oxford)*. Elsevier Ltd, 37(1), pp. 106–126. doi: 10.1016/j.progpolymsci.2011.06.003.

Li, G. *et al.* (2017) 'Mechanical strengthened alginate/polyacrylamide hydrogel crosslinked by barium and ferric dual ions', *Journal of Materials Science*. Springer US, 52(14), pp. 8538–8545. doi: 10.1007/s10853-017-1066-x.

Li, J. *et al.* (2011) 'Biomimetic multicomponent polysaccharide/nano-hydroxyapatite composites for bone tissue engineering', *Carbohydrate Polymers*. Elsevier Ltd., 85(4), pp. 885–894. doi: 10.1016/j.carbpol.2011.04.015.

Mabrouk, M. *et al.* (2014) 'Effect of ciprofloxacin incorporation in PVA and PVA bioactive glass composite scaffolds', *Ceramics International*. Elsevier, 40(3), pp. 4833–4845. doi: 10.1016/j.ceramint.2013.09.033.

Mayo Clininc (2022) *Broken leg*. Available at: https://www.mayoclinic.org/diseases-conditions/broken-leg/diagnosis-treatment/drc-20370416 (Accessed: 30 June 2022).

Mukundan, L. M. *et al.* (2013) 'A new synthesis route to high surface area sol gel bioactive glass through alcohol washing: a preliminary study', *Biomatter*, 3(2), pp. 1–10. doi: 10.4161/biom.24288.

Ngema, L. M. *et al.* (2022) 'Synthesis of Novel Conjugated Linoleic Acid (CLA) -Coated Superparamagnetic Iron Oxide Nanoparticles (SPIONs) for the Delivery of Paclitaxel with Enhanced In Vitro Anti-Proliferative Activity on A549 Lung Cancer Cells', *Pharmaceutics*, 14. doi:10.3390/pharmaceutics14040829

Öhman, C. *et al.* (2011) 'Compressive behaviour of child and adult cortical bone', *Bone*. Elsevier Inc., 49(4), pp. 769–776. doi: 10.1016/j.bone.2011.06.035.

Peter, M. *et al.* (2009) 'Development of novel α-chitin/nanobioactive glass ceramic composite scaffolds for tissue engineering applications', *Carbohydrate Polymers*. Elsevier Ltd, 78(4), pp. 926–931. doi: 10.1016/j.carbpol.2009.07.016.

Podporska-Carroll, J., Ip, J. W. Y. and Gogolewski, S. (2014) 'Biodegradable poly(ester urethane) urea scaffolds for tissue engineering: Interaction with osteoblast-like MG-63 cells', *Acta Biomaterialia*. Acta Materialia Inc., 10(6), pp. 2781–2791. doi: 10.1016/j.actbio.2014.02.016.

Prasadh, S. and Wong, R. C. W. (2018) 'Unraveling the mechanical strength of biomaterials

used as a bone scaffold in oral and maxillofacial defects', *Oral Science International*. Japanese Stomatological Society, 15(2), pp. 48–55. doi: 10.1016/S1348-8643(18)30005-3.

Rainer, A. *et al.* (2008) 'Fabrication of bioactive glass-ceramic foams mimicking human bone portions for regenerative medicine', *Acta Biomaterialia*, 4(2), pp. 362–369. doi: 10.1016/j.actbio.2007.08.007.

Richhariya, G. *et al.* (2020) 'Development of self-healing cement slurry through the incorporation of dual-encapsulated polyacrylamide for the prevention ofwater ingress in oil well', *Materials*, 13(13), pp. 1–22. doi: 10.3390/ma13132921.

Saber-Samandari, Samaneh *et al.* (2016) 'Bioactivity evaluation of novel nanocomposite scaffolds for bone tissue engineering: The impact of hydroxyapatite', *Ceramics International*. Elsevier, 42(9), pp. 11055–11062. doi: 10.1016/j.ceramint.2016.04.002.

Sadiasa, A. *et al.* (2014) 'Bioactive glass incorporation in calcium phosphate cement-based injectable bone substitute for improved in vitro biocompatibility and in vivo bone regeneration', *Journal of Biomaterials Applications*, 28(5), pp. 739–756. doi: 10.1177/0885328213478256.

Da Silva, K. *et al.* (2021) 'Three-Dimensional Printability of an ECM-Based Gelatin Methacryloyl (GelMA) Biomaterial for Potential Neuroregeneration', *ACS Omega*, 6(33), pp. 21368–21383. doi: 10.1021/acsomega.1c01903.

Sithole, M. N. *et al.* (2018) 'A 3D bioprinted in situ conjugated-co-fabricated scaffold for potential bone tissue engineering applications', *Journal of Biomedical Materials Research - Part A*, 106(5), pp. 1311–1321. doi: 10.1002/jbm.a.36333.

Soleymani Eil Bakhtiyari, S., Karbasi, S. and Monshi, A. (2015) 'Evaluation of the effects of nano-TiO2 on physical and mechanical properties of nano-bioglass 45S5 scaffold for bone tissue engineering', *Scientia Iranica*, 22(3), pp. 1337–1345.

Sundarrajan, P. *et al.* (2012) 'One pot synthesis and characterization of alginate stabilized semiconductor nanoparticles', *Bulletin of the Korean Chemical Society*, 33(10), pp. 3218–3224. doi: 10.5012/bkcs.2012.33.10.3218.

Tadjoedin, E. S. *et al.* (2002) 'High concentrations of bioactive glass material (BioGran®) vs. autogenous bone for sinus floor elevation: Histomorphometrical observations on three split mouth clinical cases', *Clinical Oral Implants Research*, 13(4), pp. 428–436. doi: 10.1034/j.1600-0501.2002.130412.x.

Tirkistani, F. A. A. and Hassan, R. M. (2012) 'Kinetics and mechanism of non-isothermal decomposition of some cross-linked metal-alginate complexes especially trivalent metal -

alginate complexes', *Oriental Journal of Chemistry*, 28(2), pp. 913–920. doi: 10.13005/ojc/280235.

Tiwari, A. (2012) 'Current concepts in surgical treatment of osteosarcoma', *Journal of Clinical Orthopaedics and Trauma*. Elsevier, 3(1), pp. 4–9. doi: 10.1016/j.jcot.2012.04.004.

Toy, P. C. and Heck, R. K. (2017) 'General Principles of Tumors', in *Campbell's Operative Orthopaedics*. 13th edn. Philadelphia: Elsevier, pp. 829–895. Available at: https://0-www-clinicalkey-com.innopac.wits.ac.za/#!/content/book/3-s2.0-B9780323374620000240?scrollTo=%23top.

Union for International Cancer Control (2014) 'Osteosarcoma: 2014 Review of Cancer Medicines on the WHO List of Essential Medicines', (3), pp. 1–10. Available at: http://www.who.int/selection_medicines/committees/expert/20/applications/Osteosarcoma.pdf?ua=1.

Venkatesan, J. *et al.* (2015) 'Alginate composites for bone tissue engineering: A review', *International Journal of Biological Macromolecules*. Elsevier B.V., 72, pp. 269–281. doi: 10.1016/j.ijbiomac.2014.07.008.

Wang, J., Lou, L. and Qiu, J. (2019) 'Super-tough hydrogels using ionically crosslinked networks', *Journal of Applied Polymer Science*, 136(44), pp. 1–9. doi: 10.1002/app.48182.

Yu, N. Y. C. *et al.* (2010) 'Biodegradable poly(α-hydroxy acid) polymer scaffolds for bone tissue engineering', *Journal of Biomedical Materials Research - Part B Applied Biomaterials*, 93(1), pp. 285–295. doi: 10.1002/jbm.b.31588.

Zheng, Y. *et al.* (2017) 'Hybrid hydrogels with high strength and biocompatibility for bone regeneration', *International Journal of Biological Macromolecules*. Elsevier B.V., 104, pp. 1143–1149. doi: 10.1016/j.ijbiomac.2017.07.017.

Zohuriaan, M. J. and Shokrolahi, F. (2004) 'Thermal studies on natural and modified gums', *Polymer Testing*, 23(5), pp. 575–579. doi: 10.1016/j.polymertesting.2003.11.001.

CHAPTER.5. THE INFLUENCE OF INCORPORATING BIOGLASS WITHIN A COMPOSITE IMPLANT FOR APPLICATION IN OSTEOSARCOMA

5.1 Introduction

The porosity of an implant is an important characteristic to assess. Previous research has demonstrated that implants with pore sizes of 100-600 μm displayed superior vascularization and integration with the bone tissue of the host. Increased pore size increased bone ingrowth (and therefore osteoconduction) (Abbasi *et al.*, 2020) In the previous chapter, double network hydrogel implants were assessed for application in Osteosarcoma. These hydrogels lacked the presence of pores initially and only developed pores during degradation.

As stated in chapter 3, There is a need for the development of patient-customised implants for the individual patient (Howard *et al.*, 2008) A method of ensuring customisability of implants would be to ensure that the implant may be mouldable to fit the defect site perfectly.
Some have demonstrated the possibility of this by using lyophilisation to allow the implantable scaffolds to take the shape of the mould (Sachlos *et al.*, 2006; Hassanajili *et al.*, 2019). Lyophilisation also provides the advantage of imparting porosity.

Therefore, this chapter aims to investigate the formation of Alginate-Polyacrylamide (APDL) and Alginate-Polyacrylamide scaffolds combined with bioglass (BGAPDL) by lyophilisation. These scaffolds will be assessed for suitability in addressing the defect caused by osteosarcoma resection surgery. In addition, the scaffolds will be assessed for its ability to serve as a local drug delivery platform for doxorubicin for osteosarcoma cases that require adjuvant chemotherapy.

5.2 Materials:

Alginic acid, sodium salt (viscosity of 20.000-40.000 cps) (SA), N,N'-Methylenebisacrylamide (MBIS), tetramethylethylenediamine (TEMED), Acrylamide (AAm), Tetraethyl orthosilicate (TEOS), Ammonium persulfate (APS) was obtained from Sigma Aldrich (Darmstadt, Germany).
Ferric chloride hexahydrate ($FeCl_3$), Calcium Nitrate was obtained from ACE pharmaceuticals. The water used in this study was Mille-Q water from a Millipore Water Purification System (Merck Chemicals GmbH, Darmstadt, Germany). Calcium Nitrate Tetrahydrate, Ammonium dihydrogen phosphate and Sodium hydroxide was obtained from ACE Pharmaceuticals. PEG (Mw = 6000)

Dulbecco's Modified Eagle Medium (DMEM) was obtained from PAN biotech and Foetal Bovine Serum (FBS) and Penicillin-Streptomycin was obtained from Sigma Aldrich (USA), MTT Cell Proliferation Kit I was used (Roche, Basel, Switzerland).

5.3 Methods:

5.3.1 Fabrication of APDL scaffolds:

APDL scaffolds were synthesised according to a modified method reported by (Wang, Lou and Qiu, 2019). Briefly, a two-step method was followed. Alginate was dissolved to form a 6% solution. Thereafter, Acrylamide monomer (1200 mg) was added to 10 mL of 6% alginate solution. 3 mg of MBIS was then added to the solution. This solution was subsequently put in an ice-bath. Following this, 1mL of APS solution 26 mg/mL was added to the solution, followed by 5 µL of TEMED.

The solution was mixed in ice bath for 15 min to ensure homogeneity then transferred to the moulds. The solution was then frozen at -80 °C then lyophilised. Subsequently the scaffolds were immersed in 0,3M $FeCl_3$ cross linker solution overnight (Li *et al.*, 2017; Wang, Lou and Qiu, 2019). The scaffolds were then thoroughly washed to remove any residual crosslinker then frozen at -80 °C and lyophilised again.

5.3.2 Fabrication of BGAPDL scaffolds

Bioglass was synthesised according to Mabrouk et al. (Mabrouk *et al.*, 2014). Bioglass was added to the alginate solution under stirring, allowed to mix for 15 min to ensure homogenous dispersion then the above method of scaffold fabrication was followed. 2% wt bioglass was used as per the previous chapter.

5.3.3 Characterisation studies of the implantable scaffolds.

5.3.3.1 Physicochemical properties of the implantable scaffolds.

Fourier Transform Infrared Spectroscopy (FTIR; PerkinElmer Spectrum 100, FT-IR Spectrometer) was used to determine the molecular vibrations that are indicative of chemical changes within the implantable scaffold samples. FTIR was run between 4000-650 cm^{-1}. X-Ray diffraction (XRD) was undertaken using a Rigaku 600 x-ray diffractometer (RIGAKU, Inc., Tokyo, Japan) to assess the types of phases present (crystalline and or amorphous) in the prepared scaffolds. The XRD spectra was collected from 10 ° to 90 °.

5.3.3.2 Thermal properties of the implantable scaffolds

Thermogravimetric analysis (TGA) was undertaken to ascertain the thermal decomposition profile of the scaffolds and bioglass. Samples of weights between 10 and 20 mg were placed

in a ceramic pan under inert conditions (nitrogen gas) in the thermogravimetric analyser (TGA 400, PerkinElmer Inc., MA). Thermograms were obtained between 30 °C and 900 °C.

5.3.3.3 Mechanical analysis of the implantable scaffolds

Mechanical tests were conducted after the implantable scaffolds were immersed in SBF (pH 7.4, 37 °C) for 24 hours to assess the strength of the scaffolds after exposure to SBF. Mechanical analysis was conducted using a Texture Analyzer (TA.XTplus Stable Microsystems, Surrey, UK) equipped with a 50 kg load cell. The method used to conduct the test was adapted from (Cuadros, Erices and Aguilera, 2015).

The compressive strength, matrix resilience and deformation energy were measured using a compression platen with a test speed of 1,2 mm/min, at 80% strain so as to prevent harm to the instrument.

Mechanical strength was conducted in triplicate and data was recorded as a mean ± SD (n=3)

5.3.3.4 Degradation of the implantable scaffolds

Degradation studies of implantable scaffolds were assessed by immersing scaffold in SBF. At days 7, 14, 21 and 28 scaffolds were removed from media dabbed dry and weighed. Scaffolds were then dried in an oven and weighed. The weights of the scaffolds were recorded before immersion and after drying in an oven and the difference in weights was used to calculate degradation as per the equation below.

$$\text{Degradation \%} = \frac{(Wi - Wt)}{Wi} x100 \qquad \text{Equation 5.1}$$

Whereby W_i is the weight before immersion and W_t is the weight at each time point.

5.3.3.5 Swelling analysis of the implantable scaffolds

Swelling studies of implantable scaffolds were assessed by immersing scaffold in SBF. At predetermined time points, scaffolds were removed from media dabbed dry and weighed. The initial dry weights were recorded as W_i and the wet weight of the scaffolds at each time point were recorded as W_t and the difference in weights was used to calculate swelling % as per the equation below.

$$\text{Swelling \%} = \frac{(Wt - Wi)}{Wi} x100 \qquad \text{Equation 5.2}$$

5.3.3.6 Morphology of the implantable scaffolds

Scanning Electron Microscopy (SEM) was utilised to determine the morphology of the samples at each time point using a SIGMA 03-39 field emission scanning electron microscope (Zeiss,

Jena, Germany). Cross-section samples were cut from the middle of the scaffold and sputter coated with 30 nm of carbon and gold palladium subsequently analysed.

5.3.3.7 Porosity of the implantable scaffolds

Porosity of the scaffolds was established by liquid displacement technique adapted from (Mabrouk *et al.*, 2016; Tohamy *et al.*, 2018). Briefly, Scaffolds were immersed in glycerol for 1 hour then centrifuged at 5000 rpm for 15 min to facilitate the liquid filling the scaffolds pores. Porosity (%) was then calculated by the equation below:

$$\mathrm{P}\% = \frac{W_1 - W_3}{W_2 - W_3} x\ 100 \qquad \text{Equation 5.3}$$

Where W_1 was the weight of the scaffolds before immersion, W_2 was the weight of the scaffolds after immersion and W_3 was the weight of the scaffolds after drying.

5.3.3.8 Biomineralisation of the implantable scaffolds

Biomineralization was conducted by immersion of scaffolds in SBF (pH 7.4, 37 °C). SBF was made according to Kokubo et al. (Kokubo and Takadama, 2006). Scaffolds were immersed in SBF for 4 weeks and media was changed every week. Scaffolds were then removed every week, rinsed thoroughly with deionised water and analysed by XRD, SEM and EDS.

5.3.3.9 Doxorubicin Loading and release of the implantable scaffolds

Scaffolds were immersed in doxorubicin solution of 0,5 mg/mL for 24 hours in the dark. The scaffolds were then briefly rinsed to remove any unloaded drug then dried in an oven at 25 °C (Javanbakht and Namazi, 2018). Drug loading was determined by analysing the remaining solution at 490 nm on the Nanophotometer UV/Vis spectrophotometer NP80 (Implen, Munchen, Germany).

To ascertain the release profile, scaffolds were immersed in 5mL PBS at 37 °C. At predetermined time points, 1mL of release media was removed for analysis and immediately replaced with fresh PBS buffer.

Samples were analysed at 490 nm on the Nanophotometer UV/Vis spectrophotometer NP80 (Implen, Munchen, Germany).

Drug loading and release studies were conducted in triplicate and data was recorded as a mean ± SD (n=3)

5.4 Results

5.4.1 Physicochemical Characterisation of the implantable scaffolds:

The FTIR spectra of the PADL and BGAPDL scaffolds had similar peaks present as the ALG-PAAM and BG-ALG-PAAM scaffolds (**Figure 5.1**).

The characteristic peaks of PAAM can be seen: A peak at 2934 cm^{-1} indicated a symmetric stretch of CH_2, Peaks at 1653 cm^{-1} indicates stretching vibrations of C=O group (Kolek *et al.*, 2007). A small peak at 3328 cm^{-1} (due to the presence of -NH group which may be attributed to the crosslinking of PAAM with MBIS (Richhariya *et al.*, 2020).

Crosslinking of scaffolds in $FeCl_3$, can be confirmed by the peaks at between 1580 and 1590 cm^{-1} (Dong *et al.*, 2011). A minute peak at 817 cm^{-1} is indicative metal-O band of Fe (Tirkistani and Hassan, 2012; Demianenko and Minisini, 2016).

A shift in peak from 1090 cm^{-1} (present in the APDL spectrum) to 1080 cm^{-1} in the BGAPDL spectrum is indicative of an Si-OC bond forming, confirming the presence of bioglass within BGAPDL (Ahn *et al.*, 2020).

The XRD spectra (**Figure 5.2**) of APDL and BGAPDL were like the spectra of ALG-PAAM scaffold as well as BG-ALG-PAAM hydrogels- no noticeable crystalline peaks and were completely amorphous while displaying a broad amorphous peak at around 22 ° (Bahrami, Akbari and Eftekhari-Sis, 2019).

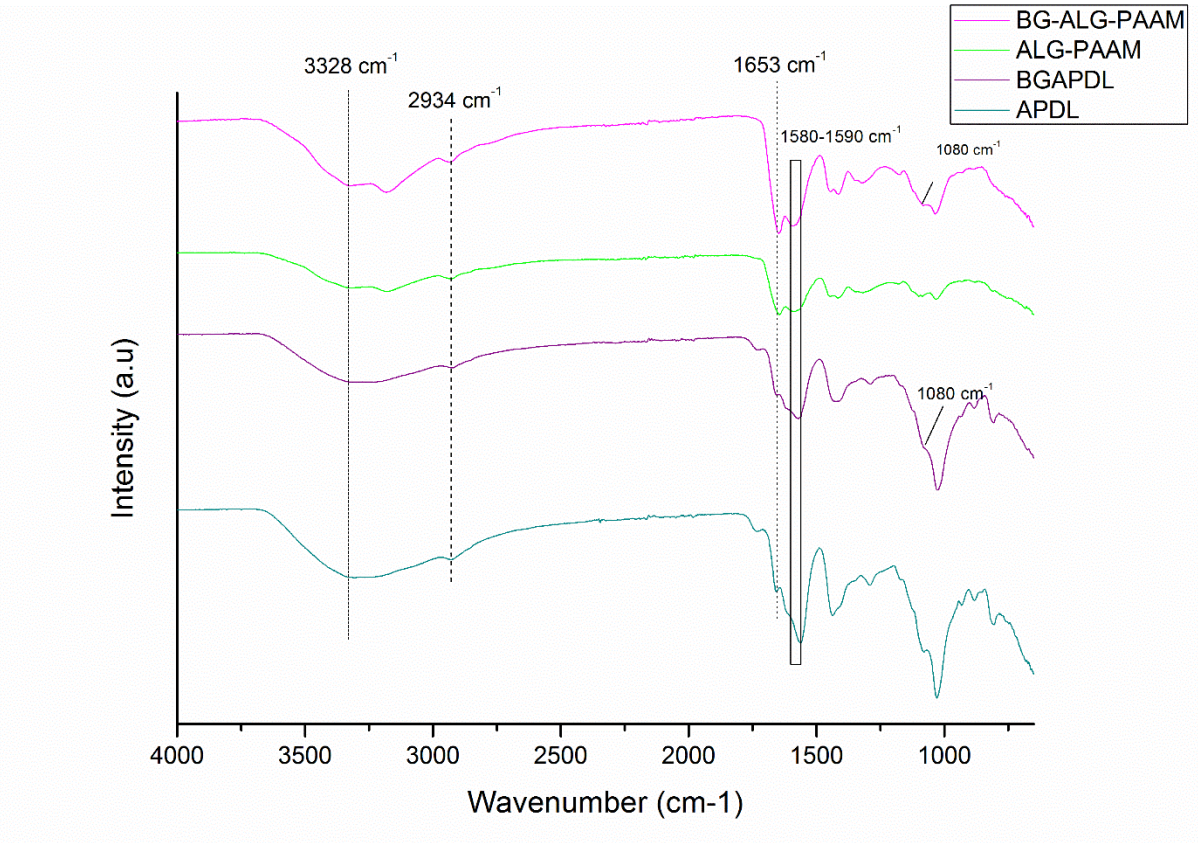


Figure 5.1: FTIR spectra of APDL, BGAPDL, ALG-PAAM and BG-ALG-PAAM. The lines running through the spectra indicate the common bonds found throughout all four spectra.

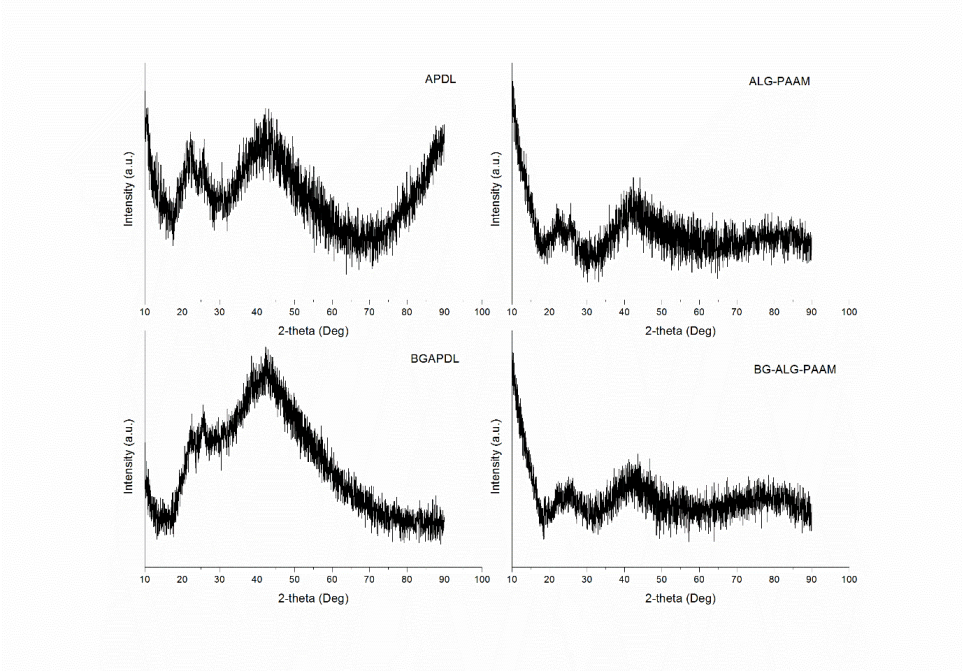


Figure 5.2: XRD spectra of APDL, BGAPDL, ALG-PAAM and BG-ALG-PAAM. The spectra of all four samples indicate a lack of crystalline peaks proving the amorphous nature of the scaffolds.

5.4.2 Thermal Analysis of the implantable scaffolds

Thermograms of, ALG-PAAM and BG-ALG-PAAM (**Figure 5.3**) displayed weight loss in the temperature range of 240–350 °C and can be related to decomposition of ALG-PAAM (Bahrami, Akbari and Eftekhari-Sis, 2019). Derivatives of these thermograms placed the exact degradation temperature at 262,67 °C and 264,5 °C for ALG-PAAM and BG-ALG-PAAM respectively. Although, it can be noted that ALG-PAAM and BG-ALG-PAAM displayed less steeper loss of weight and this can be attributed towards the increased stability of a double network hydrogel that was formed after immersion in $FeCl_3$.

Thermograms of APDL and BGAPDL scaffolds (**Figure 5.3**) displayed a similar weight loss profile. Derivative thermograms (**Figure 5.4**) of APDL and BGAPDL both showed degradation at 261 °C which is below the degradation temperature of ALG-PAAM and BG-ALGPAAM hydrogels. This may be attributed to a weakened structure due to double lyophilisation.

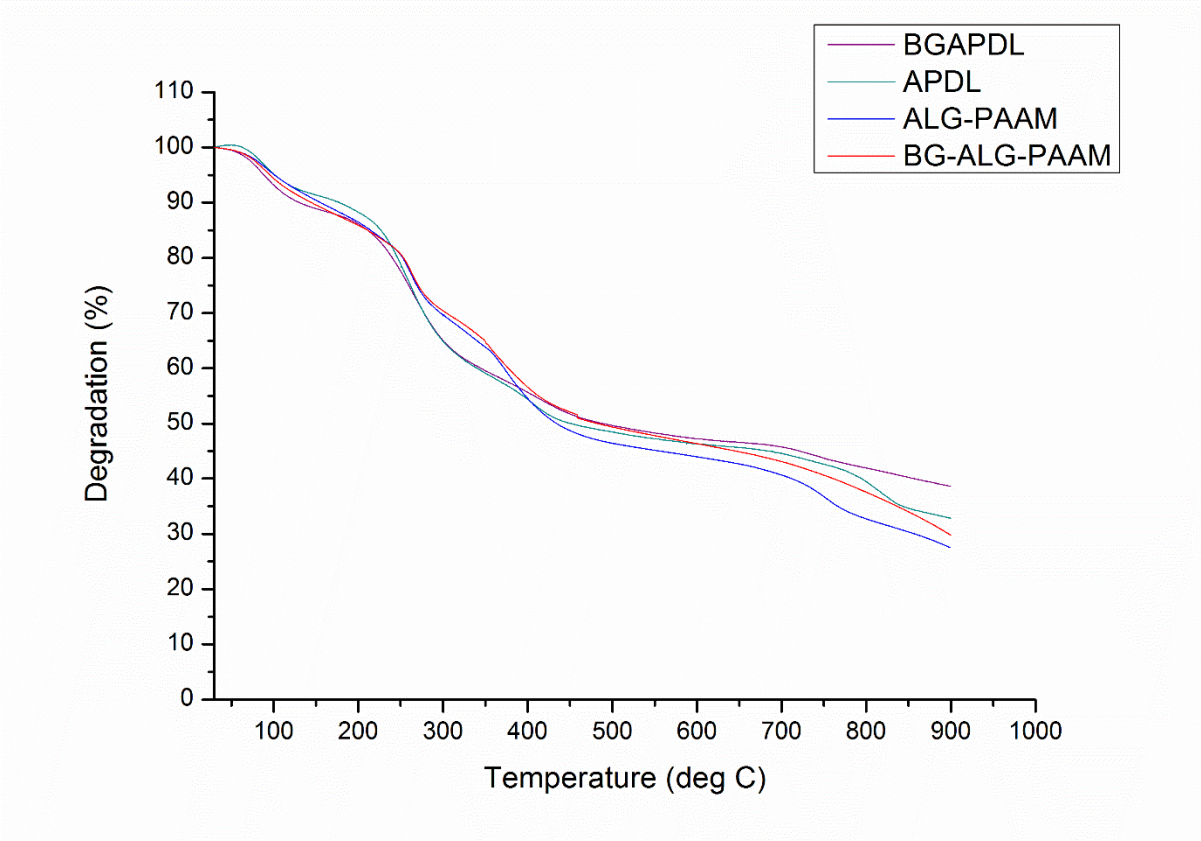


Figure 5.3: TGA thermograms of APDL, BGAPDL, ALG-PAAM and BG-ALG-PAAM. APDL and BGAPDL displayed a slightly greater degradation. This can be attributed towards a weakened structure due to double lyophilisation.

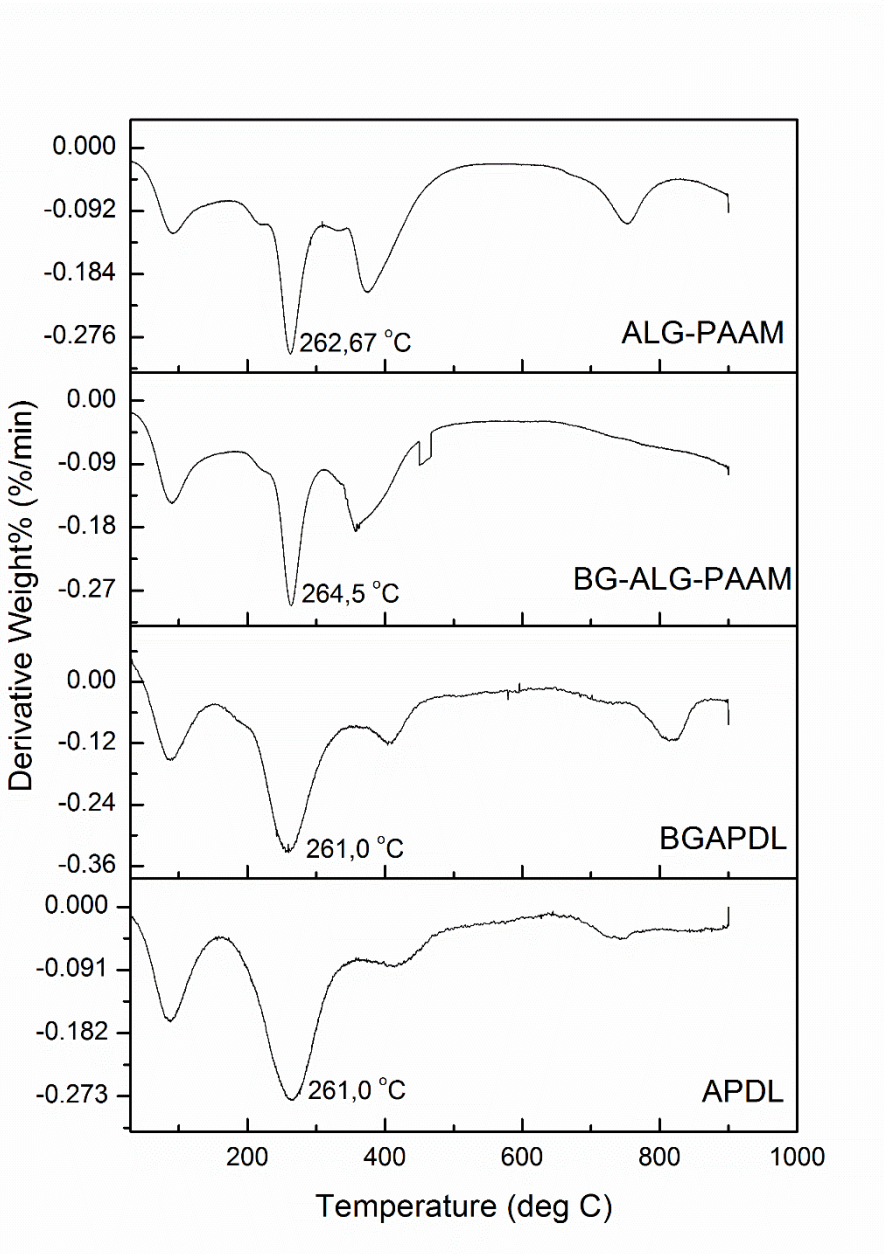


Figure 5.4: Derivatives of TGA thermograms for APDL, BGAPDL, ALG-PAAM and BG-ALG-PAAM. Derivative thermograms indicate that APDL and BGAPDL degrade at a lower temperature compared to ALG-PAAM and BG-ALG-PAAM.

5.4.3 Mechanical Strength of the implantable scaffolds:

The mechanical properties of the scaffold can be seen in **Figure 5.5**. APDL scaffolds displayed a maximum compressive strength of 0,3504 MPa ± 0,03827 whereas BGAPDL scaffolds displayed a maximum compressive strength of 0,5337 MPa ± 0,02815. Matric resilience was calculated to be 0,06248% ± 0,01237 for APDL while BGAPDL scaffolds had a matrix resilience of 0,07193% ± 0,0006115. Matrix hardness of the scaffolds proved to be 11,0137 N/mm ± 1,2735 and 15,21233 N/mm ± 1,5435 while deformation energy was calculated to be

53,2053 N.mm ± 7,3021 and 81,62 N.mm ± 10,407 for APDL and BGAPDL scaffolds respectively.

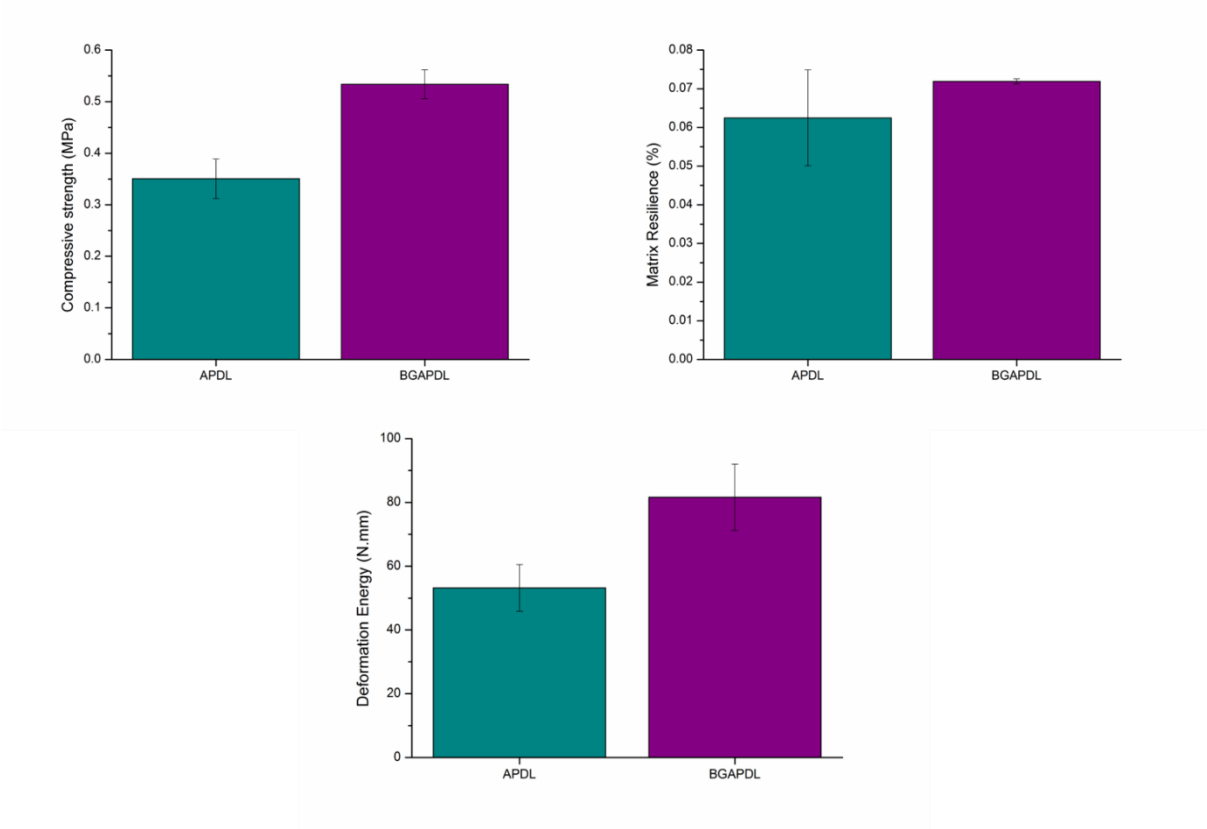


Figure 5.5: Compressive strength, matrix resilience and deformation energy of APDL scaffolds and BGAPDL scaffolds presented as bar graphs. BGAPDL scaffolds have a higher compressive strength, matrix resilience and deformation energy than APDL scaffolds. The experiment was conducted in triplicate and data points were recorded as a mean ± SD (n=3).

5.4.4 Degradation of the implantable scaffolds:

At one week, APDL scaffolds displayed a degradation of 4,413263% ± 0,558323, while at 2 weeks, degradation was at 8,713068% ± 1,213139. At 3 weeks, APDL scaffolds displayed a degradation of 13,3902936% ± 1,181094675 and at 4 weeks a degradation of 14,64758729% ± 0,666321066 was observed. BG scaffolds displayed a slightly greater degradation rate of 5,695919% ± 3,062771 and 9,986261% ± 2,27937 at one and 2 weeks respectively while at 3 weeks degradation was observed at 15,54043642% ± 4,33061972 and at 4 weeks degradation was observed at 16,68260875% ± 4,441622485.

At 5 weeks, degradation was noted at 16,1781% ± 2.0055 for APDL scaffolds while degradation for BGAPDL scaffolds was noted at 19,1106% ± 4,7471. At 8 weeks, degradation only increased to 21,0244% ± 0,2,4814 and 27,6881% ± 3,8892 for APDL and BGAPDL scaffolds respectively (**Figure 5.6**).

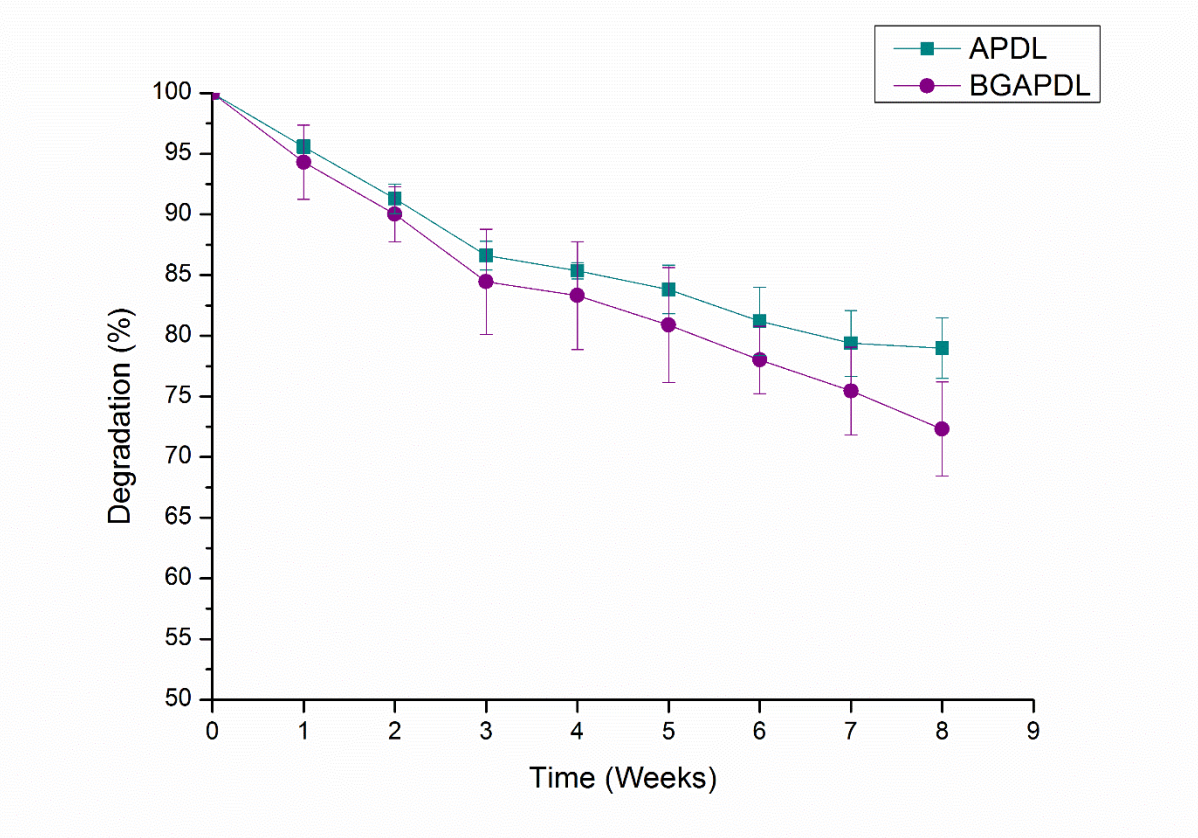


Figure 5.6: Degradation profile of APDL and BGAPDL scaffolds over 8 weeks. BGAPDL scaffolds had a higher degradation than APDL scaffolds. The experiment was conducted in triplicate and data points were recorded as a mean ± SD (n=3).

5.4.5 **Swelling of the implantable scaffolds**:

BGAPDL scaffolds displayed a decreased swelling capability as compared to the APDL scaffolds (**Figure 5.7**). At 24 hours BGAPDL scaffolds displayed swelling of 934,9783% ± 267,2474356 while at 72 hours, swelling was noted to be at 1403,911811% ± 343,273236. At 7 days (144 hours), swelling was noted at 1469,586452% ± 274,333517. APDL scaffolds displayed a swelling of 1316,742566% ± 126,3412632, 1655,45483% ± 163,8713149 and 1756,867581% ± 153,4192123 at 24 hours, 72 hours and 7 days respectively.

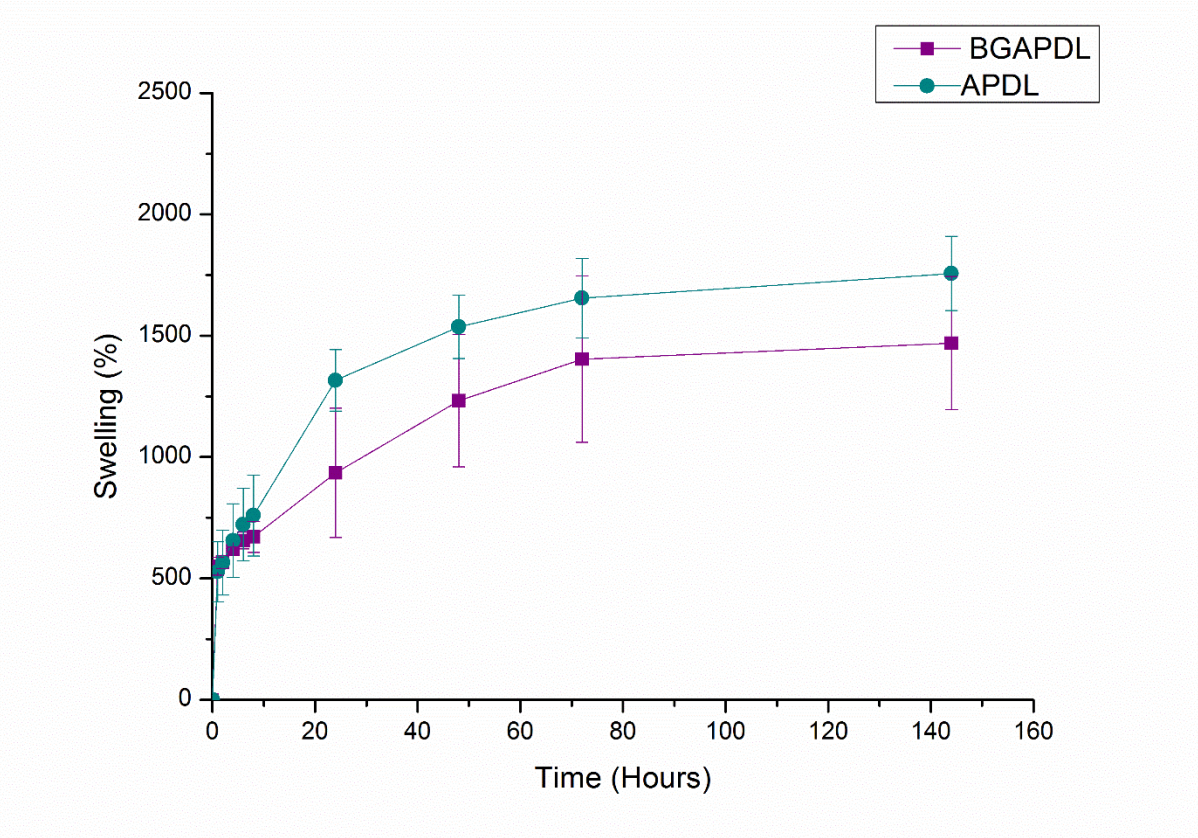


Figure 5.7: Swelling of APDL and BGAPDL scaffolds in SBF. APDL had a greater swelling capacity than BGAPDL scaffolds. The experiment was conducted in triplicate and data points were recorded as a mean ± SD (n=3).

5.4.6 Morphology of the implantable scaffolds

SEM imaging revealed that APDL scaffolds (**Figure 5.8**) and BG APDL scaffolds displayed a variety of pores sizes. While Pore sizes greater and less than 100 ɥm can be seen in both scaffolds, smaller pores are present in BGAPDL scaffolds (**Figure 5.9**).

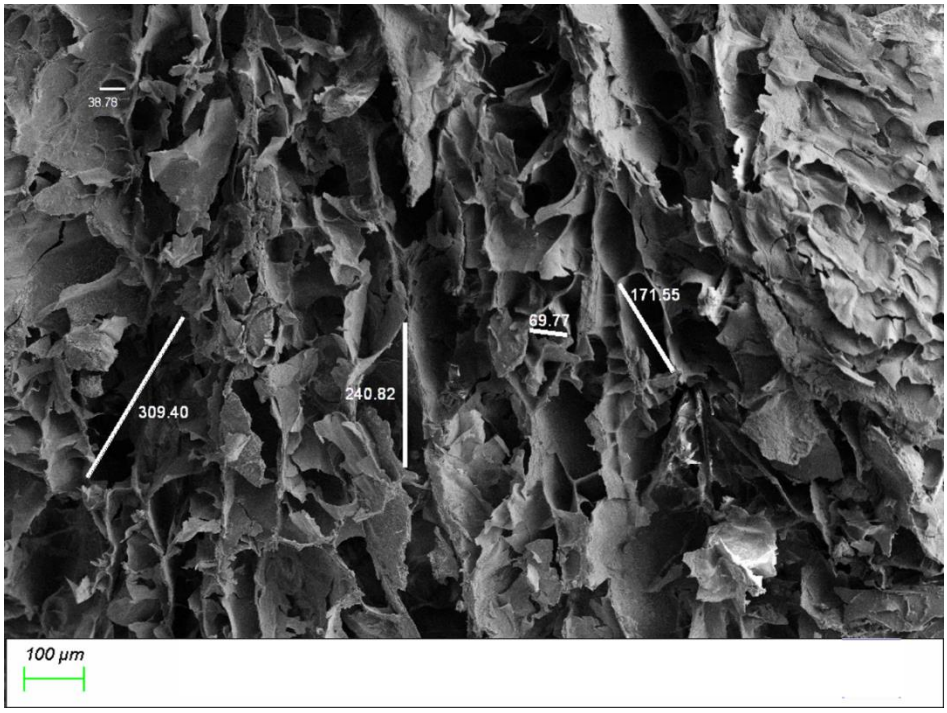


Figure 5.8: Cross-section of APDL scaffold under SEM. A variety of pore sizes can be observed.

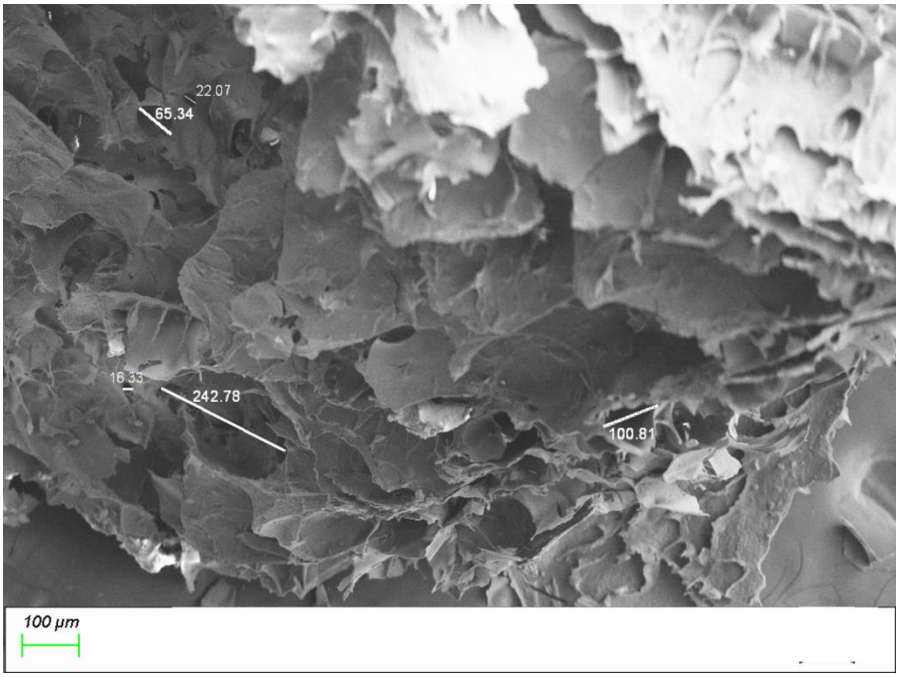


Figure 5.9: Cross-section of BGAPDL scaffold under SEM. Smaller pores can be seen in this image.

5.4.7 Porosity of the implantable scaffolds

Liquid Displacement technique revealed the porosity of APDL scaffolds to be 53,385% ± 20,30445 and BGAPDL at 52,941% ± 17,527.

5.4.8 Biomineralisation of the implantable scaffolds

The initial XRD spectra of APDL and BGAPDL scaffolds both displayed an amorphous profile while peaks with a maximum at around 32 ° could be identified in the XRD spectra (**Figure 5.10 C,D**) of APDL and BGAPDL scaffolds after immersion in SBF. This can be attributed to the 211 plane of hydroxyapatite. (Peter *et al.*, 2009; Mabrouk *et al.*, 2014). These peaks could be seen throughout the immersion timepoints.

FTIR spectra obtained from the scaffold samples at various time points (**Figure 5.10 A,B**) indicated that the initial peak present at 1022 cm^{-1} on the spectra before immersion in SBF broadened in the spectra after immersion in SBF. This can be attributed to the overlap of PO_3 with wavelengths between 1020- 1100 cm^{-1} (Destainville *et al.*, 2003)) that was formed due to the precipitation of Hap.

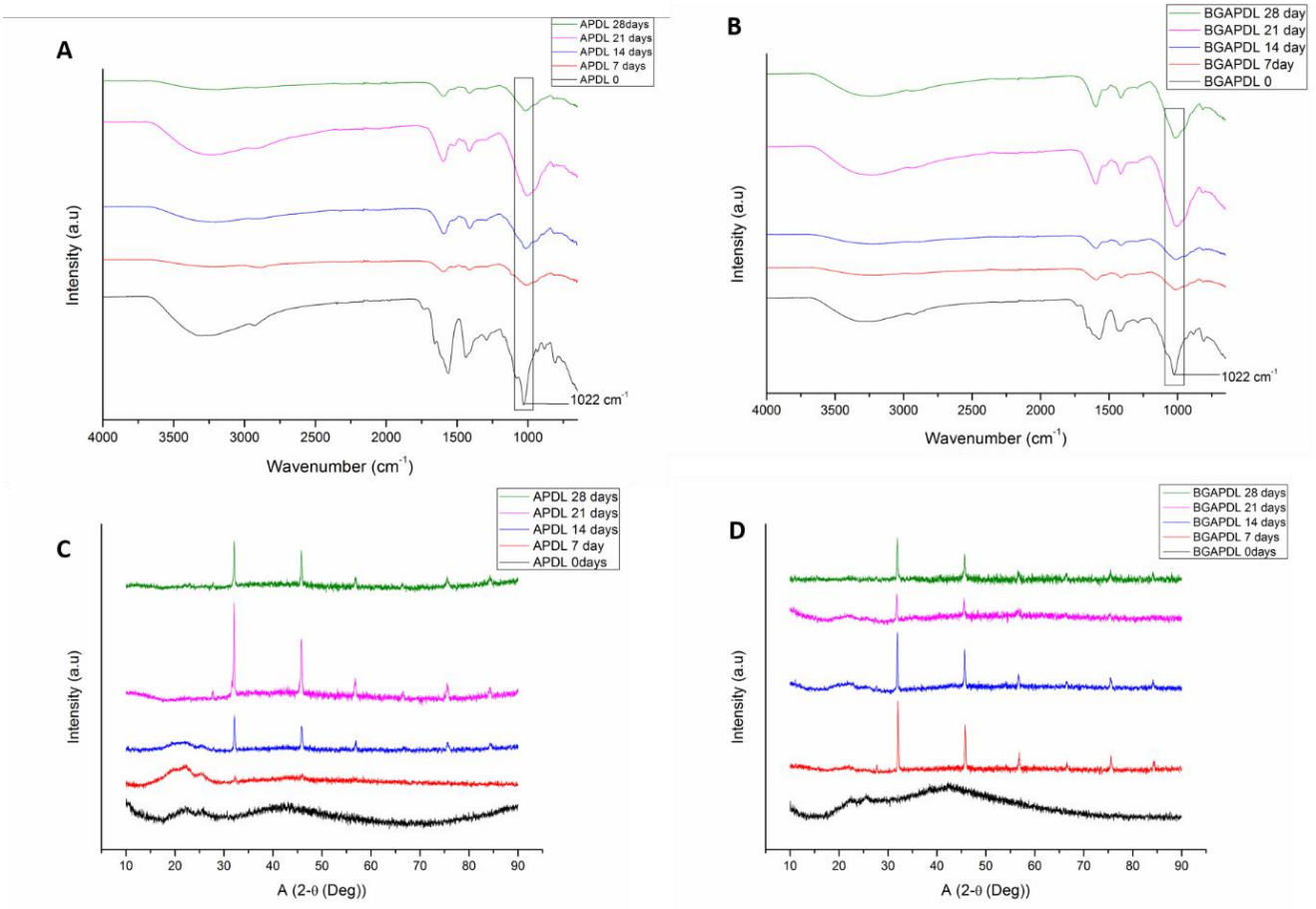


Figure 5.10: FTIR and XRD Spectra of APDL and BGAPDL scaffolds displaying biomineralisation at various time points. A- FTIR spectra of APDL scaffolds. B- FTIR spectra

of BGAPDL scaffolds. C- XRD spectra of APDL scaffolds. D- XRD spectra of APDL scaffolds. FTIR spectra displayed a broad peak between 1020- 1100 cm^{-1} and this could be indicative of PO_3. XRD spectra displayed an initially amorphous profile, however, after exposure to SBF, crystalline peaks could be seen indicating hydroxyapatite formation.

EDX of APDL and BGAPDL scaffolds further confirmed the data obtained from the FTIR and XRD spectra.

EDX of APDL scaffolds before immersion in SBF displayed the presence only of Fe and Cl which can be attributed to the crosslinker used to form these scaffolds (**Figure 5.11 A**). EDX of BGAPDL before immersion in SBF indicated the presence of Ca, Si as well as Fe and Cl. The presence of these ions can be explained due to the presence of bioglass in the scaffolds (**Figure 5.11 B**).

EDX spectra for APDL and BG APDL after immersion in SBF for 4 weeks both display Ca and P after immersion in SBF which can be attributed to the formation of Hydroxyapatite on the surface of the scaffolds. The presence of Fe and Cl can be attributed to the crosslinker used in formation of the scaffolds (**Figure 5.11 C,D**). SEM images display the formation of hydroxyapatite for both implantable scaffolds (**Figure 5.12**).

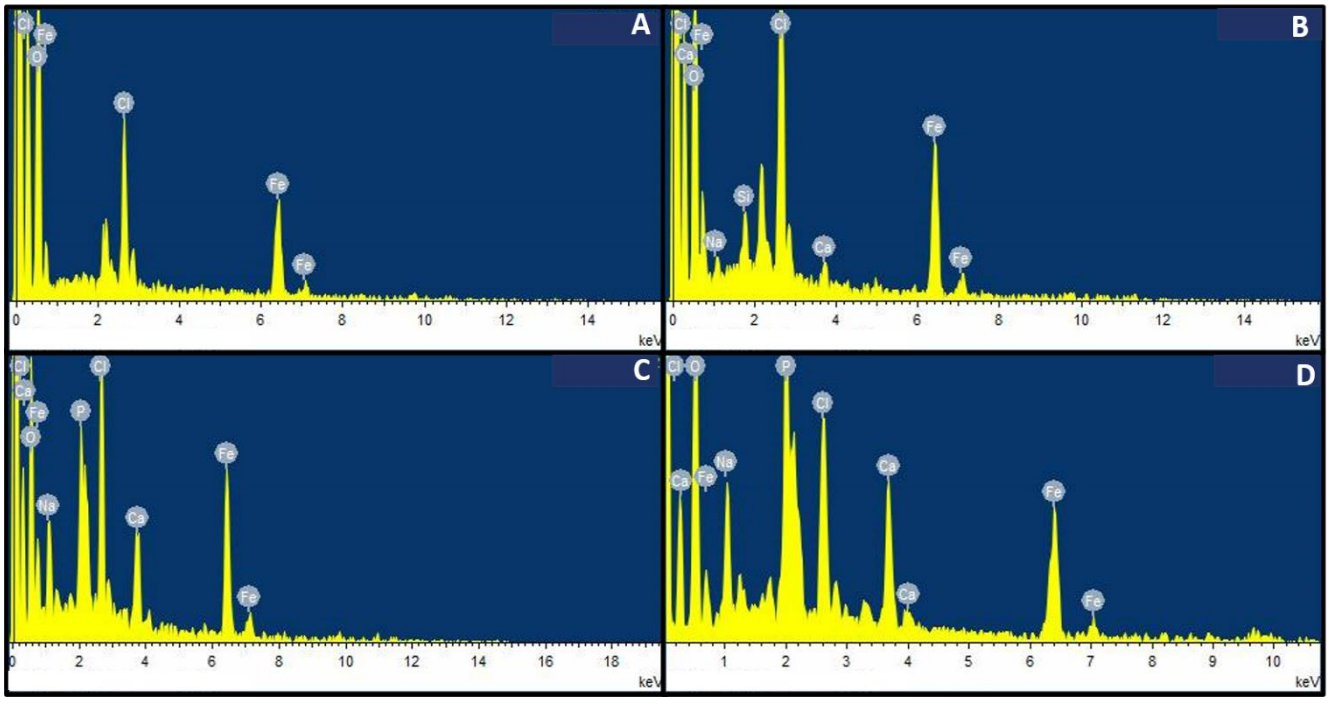


Figure 5.11: EDX spectra of APDL and BGAPDL scaffolds before and after immersion in SBF. A- APDL scaffolds before immersion in SBF. B- BGAPDL scaffolds before immersion in SBF. C- APDL scaffolds after immersion in SBF. D- BGAPDL scaffolds after immersion in SBF. The

EDX spectra display the presence of Ca and P for both APDL and BGAPDL scaffolds after immersion in SBF.

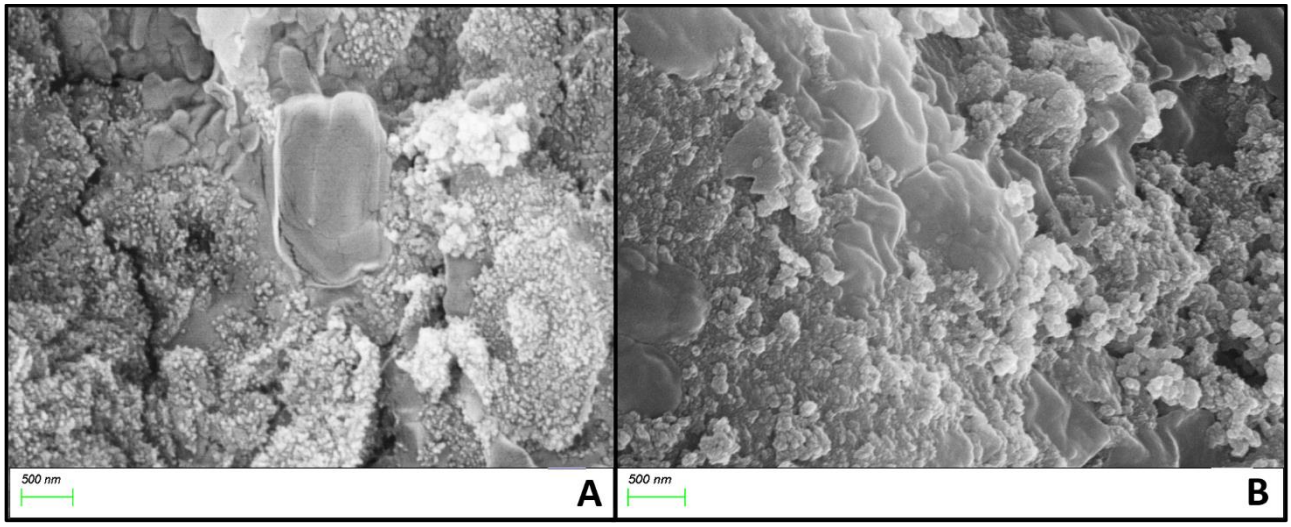


Figure 5.12: Hydroxyapatite formation on APDL and BGAPDL scaffolds as seen at 500 nm. A- Hydroxyapatite crystals on the surface of APDL scaffolds that underwent exposure to SBF. B- Hydroxyapatite crystals on the surface of BGAPDL scaffolds that underwent exposure to SBF.

5.4.9 Doxorubicin loading and release of the implantable scaffolds

APDL scaffolds displayed a slightly greater loading at 72,12333486% ± 3,138215192, while BGAPDL scaffolds displayed a loading of 70,51724333% ± 0,891430571 (**Figure 5.13**).

At 24 hours, the Doxorubicin release profiles from the scaffolds displayed a release of 4,336790008% ± 0,245373171 and 4,046479747% ± 0,300735036 for APDL and BGAPDL scaffolds respectively while at 72 hours the release was observed at 6,286231505% ± 0,897379713 and 7,983525364% ± 3,285465684 respectively. At 3 weeks the release for APDL and BGAPDL scaffolds were observed at 13,74353519% ± 5,774371713 and 11,8818264% ± 4,386478843 respectively while at 4 weeks the release was observed at the release was observed at 15.55561953% ± 6.071702934 and 14.03228573% ± 4.040160304 respectively.

At 5 weeks, drug release was noted at 16,8052% ± 6,2978 and 15,47903% ± 4,0564 for APDL and BGAPDL scaffolds respectively. At 8 weeks, drug release was measured at 18,885% ± 6,4312 and 17,8838% ± 2,95817 for APDL and BGAPDL scaffolds respectively (**Figure 5.14**).

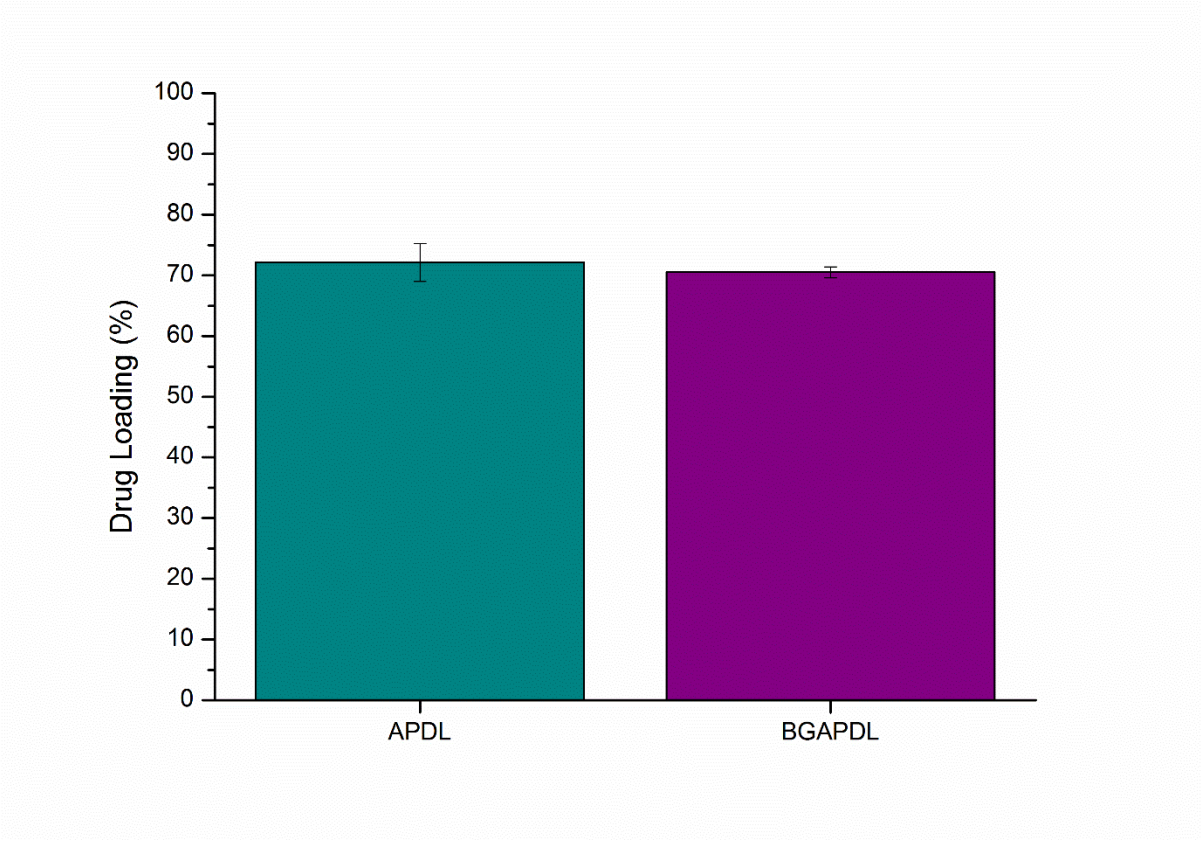


Figure 5.13: The doxorubicin loading profile of APDL and BGAPDL scaffolds. APDL scaffolds displayed a slightly higher loading capacity. The experiment was conducted in triplicate and data points were recorded as a mean ± SD (n=3).

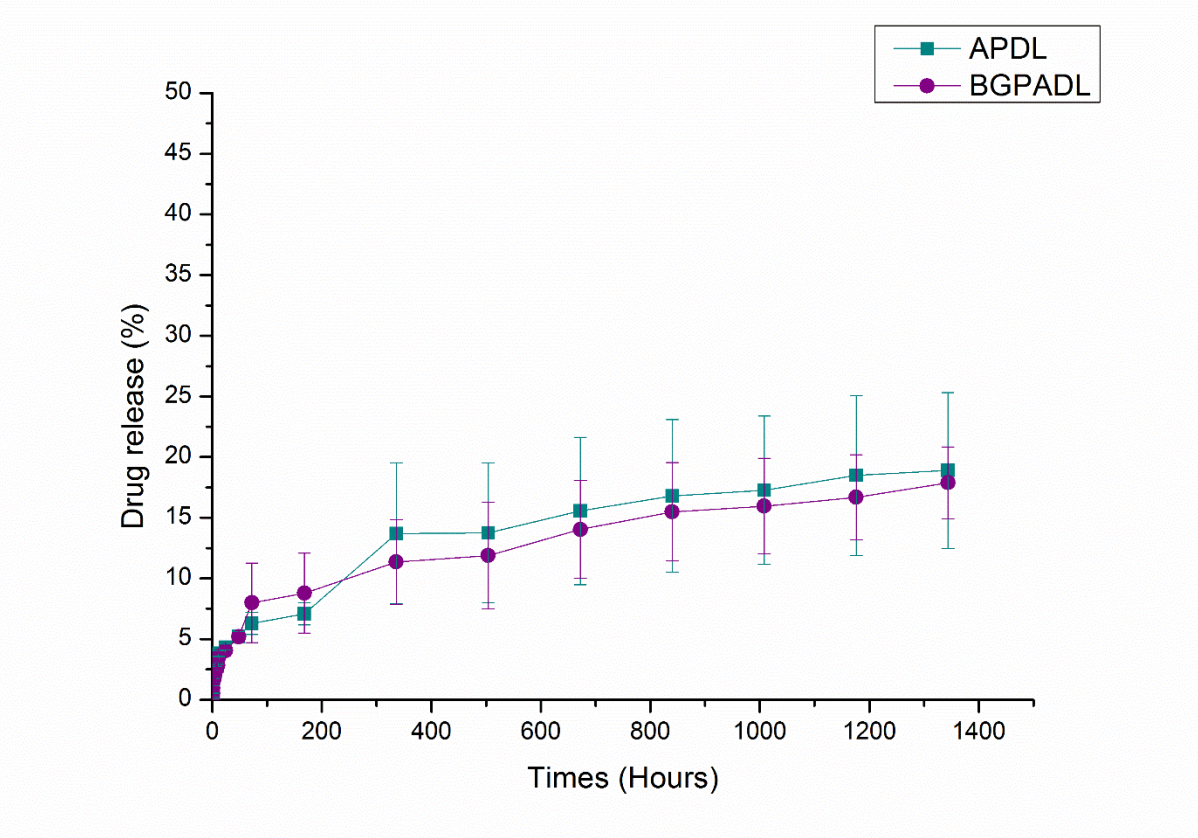


Figure 5.14: The doxorubicin release profiles of APDL and BGAPDL scaffolds. At 8 weeks, drug release was measured at 18,885% ± 6,4312 and 17,8838% ± 2,95817 for APDL and BGAPDL scaffolds respectively. The experiment was conducted in triplicate and data points were recorded as a mean ± SD (n=3).

5.5 Discussion:

In this paper, APDL and BGAPDL scaffolds were synthesised to improve on the porosity of the implant researched in the previous chapter. Physicochemical analysis showed the successful synthesis while thermal characterisation. SEM displayed that the scaffolds had various interconnected pores from the beginning. According to the diamond concept, there are five general therapeutic targets that bone regeneration platforms should aim for; growth factors (osteoinduction), vascularization (angiogenesis), mechanical properties, osteogenesis (synthesis of new bone) and osteoconduction. Scaffolds should possess at least three of these five properties (Giannoudis, Einhorn and Marsh, 2007; Giannoudis *et al.*, 2008; Jahan and Tabrizian, 2016). By incorporating bioglass (which is osteoconductive and osteoproductive (stimulates growth of new bone) (Rainer *et al.*, 2008)) into the scaffold, already two of these criteria were met.

5.5.1 Mechanical Strength of the implantable scaffolds:

Human cortical bone has a compressive strength of between 90 and 230 MPa and the compressive strength of cancellous bone lies between 2 and 45 MPa (Hannink and Arts, 2011). The mechanical properties of a scaffold for application in bone regeneration should be almost the same as the mechanical properties of the surrounding bone and it should maintain the same mechanical properties after implantation (Prasadh and Wong, 2018).

While BGAPDL scaffolds displayed a higher mechanical strength than when compared to APDL scaffolds, both scaffolds did not match the strength of human bone. After 24 hours of immersion in SBF, APDL scaffolds displayed a lower mechanical strength of 0,3504 MPa ± 0,03827 whereas BG scaffolds displayed a higher maximum compressive strength of 0,5337 MPa ± 0,02815. Matrix resilience values indicated that BGAPDL can absorb less impacting force as BGAPDL scaffolds had a higher matrix resilience (0,07193% ± 0,0006115) than APDL scaffolds (0,06248% ± 0,01237) (Indermun *et al.*, 2014). Deformation energy is the energy absorbed that causes deformation to the hydrogel (Mabrouk *et al.*, 2016). It can be noted that BG-ALG-PAAM scaffolds required more energy to be deformed than ALG-PAAM scaffolds. This data supports the premise that bioglass imparted better mechanical strength to the scaffold. However, if the implant is not of appropriate strength, it can still be used for bone regeneration but needs to be fixed with plates, screws, wires or pins (Prasadh and Wong, 2018). The weak mechanical properties exhibited by the implantable scaffolds may be attributed to the double lyophilisation that occurred during scaffold synthesis.

5.5.2 Swelling of the implantable scaffolds:

The good swelling ability and expansion of the scaffold implant is advantageous as it is important for the scaffold to absorb body fluid and for the uptake of cell nutrients (Li *et al.*, 2011; Azhar, Olad and Salehi, 2014) and promotes contact between implant and host tissue which decreases shear forces at implant-bone interface and thus improves bone healing (Podporska-Carroll, Ip and Gogolewski, 2014). At 7 days, BGAPDL scaffolds displayed a swelling of at 1469,586452% ± 274,333517, while APDL scaffolds displayed a greater swelling of 1756,867581% ± 153,4192123. The decreased swelling could be attributed to the presence of bioglass in the BGAPDL scaffold implants.

5.5.3 Biomineralisation of the implantable scaffolds:

Biomineralisation studies confirmed that hydroxyapatite was formed on surfaces of both scaffolds. SEM and EDS also confirmed the presence of Calcium and Phosphorous. However, it cannot be proven that one scaffold had an advantage over the other in terms of biomineralisaton capacity.

5.5.4 Degradation of the implantable scaffolds

At the end of 8 weeks, APDL scaffolds were at 78,977% ± 2,481 of their initial weight while BGAPDL scaffolds weighed 72,311% ± 3,889 of their original weight. From previous research into bioglass composite scaffolds it can be noted that bioglass containing composites do degrade faster than the scaffolds without bioglass. (Maquet *et al.*, 2003; Ryszkowska *et al.*, 2010). This can be attributed to the loss of bioglass particles from the composite into the degradation media (Maquet *et al.*, 2003). This indicated a slow degradation rate for both scaffolds which proves that it will remain in the bone for a while. This is advantageous as bone may take several months to completely heal (Mayo Clininc, 2022) if the biology of fracture repair is followed for critical defect healing (Cameron *et al.*, 2012). A low degradation rate may prove to be advantageous for cell attachment and differentiation (Mabrouk *et al.*, 2014).

5.5.5 Morphology and Porosity of the implantable scaffolds:

Pore size of 100 µm to 500 µm is optimal when considering scaffolds for bone regeneration (Yu *et al.*, 2010) as the size of osteoblasts are 50-80 µm. SEM imaging for both APDL and BGAPDL both displayed pore sizes of greater than 100 µm. This is advantageous as it will facilitate the migration and proliferation of osteoblasts into the scaffold's interior. APDL scaffolds displayed a slightly higher porosity of 53,385% ± 20,30445 while BGAPDL at 52,941% ± 17,527- porosity. Cross sections of the scaffold show that a variety or pore sies are present at scaffold formation.

5.5.6 Drug Loading and Drug Release of the implantable scaffolds:

The slightly decreased drug loading of BG-ALG-PAAM at could be attributed to its slightly lower swelling capacity.

According to the Union for International Cancer Control's 2014 Review of the WHO's cancer medicines on the list of Essential medicines (Union for International Cancer Control, 2014), the standard chemotherapy regimens for osteosarcoma include a 6 cycle MAP or 12 cycle OS99 These chemotherapy regimens include the delivery of doxorubicin by intravenous infusion after surgery. The OS99 Chemotherapeutic regimen for osteosarcoma details the administration of doxorubicin, carboplatin and ifosfamide. Chemotherapy is provided to the patient for 21 weeks after surgery for this regimen. The 6 cycle MAP regimen details the administration of doxorubicin, cisplatin and methotrexate. Chemotherapy is provided to the patient for 17 weeks after surgery for this regimen (Union for International Cancer Control, 2014).

The sustained release shown by both APDL (18,885% ± 6,4312 at 8 weeks) and BGAPDL scaffolds (17,8838 % ± 2,95817 at 8 weeks) may be advantageous as it has the potential to

suit both regimens' duration as it displays a sustained release profile with <19 % of DOX released over 8 weeks. These regimens advise that chemotherapy be administered to the patient for 21 or 17 weeks after surgery. As stated in the previous chapter, a disadvantage to the sustained release of this nature could be that bone growth may not be viable until complete release of doxorubicin has been achieved as the presence of Doxorubicin within the scaffold may kill new bone as is grows onto the scaffold.

5.6 Concluding Remarks

Results of this chapter indicate that there are no significant differences between APDL and BGAPDL scaffolds. Only 2 criteria of the diamond concept are met with BGAPDL scaffolds due to the inherent osteoconductive and osteoproductive nature of bioglass. Lyophilisng the scaffold twice facilitated the presence of pores from the formation of the scaffold. While the sustained DOX release may suit standard treatment regimen times, it can be said that bone will not grow until DOX is released entirely from the scaffold. More research is needed to better the scaffolds so that it may meet at least 3 of the 5 criteria of the Diamond concept.

5.7 References

Abbasi, N. *et al.* (2020) 'Porous scaffolds for bone regeneration', *Journal of Science: Advanced Materials and Devices*. Elsevier Ltd, 5(1), pp. 1–9. doi: 10.1016/j.jsamd.2020.01.007.

Ahn, J. H. *et al.* (2020) 'The effect of mesoporous bioactive glass nanoparticles/graphene oxide composites on the differentiation and mineralization of human dental pulp stem cells', *Nanomaterials*, 10(4), pp. 1–18. doi: 10.3390/nano10040620.

Azhar, F. F., Olad, A. and Salehi, R. (2014) 'Fabrication and characterization of chitosan-gelatin/nanohydroxyapatite- polyaniline composite with potential application in tissue engineering scaffolds', *Designed Monomers and Polymers*. Taylor & Francis, 17(7), pp. 654–667. doi: 10.1080/15685551.2014.907621.

Bahrami, Z., Akbari, A. and Eftekhari-Sis, B. (2019) 'Double network hydrogel of sodium alginate/polyacrylamide cross-linked with POSS: Swelling, dye removal and mechanical properties', *International Journal of Biological Macromolecules*. Elsevier B.V., 129, pp. 187–197. doi: 10.1016/j.ijbiomac.2019.02.046.

Cameron, J. A. *et al.* (2012) 'Employing the Biology of Successful Fracture Repair to Heal Critical Size Bone Defects', *Current Topics in Microbiology and Immunology*, 367, pp. 113–132. doi: 10.1007/82_2012_291.

Cuadros, T. R., Erices, A. A. and Aguilera, J. M. (2015) 'Porous matrix of calcium alginate/gelatin with enhanced properties as scaffold for cell culture', *Journal of the Mechanical Behavior of Biomedical Materials*, 46, pp. 331–342. doi: 10.1016/j.jmbbm.2014.08.026.

Demianenko, P. and Minisini, B. (2016) 'Stiff IPN Hydrogels of Poly(Acrylamide) and Alginate: Influence of the Crosslinking Ion's Valence on Hydrogel's Final Properties', *Journal of Chemical Engineering & Process Technology*, 07(04). doi: 10.4172/2157-7048.1000304.

Destainville, A. *et al.* (2003) 'Synthesis, characterization and thermal behavior of apatitic tricalcium phosphate', *Materials Chemistry and Physics*, 80(1), pp. 269–277. doi: 10.1016/S0254-0584(02)00466-2.

Dong, Y. *et al.* (2011) 'Preparation and catalytic activity of Fe alginate gel beads for oxidative degradation of azo dyes under visible light irradiation', *Catalysis Today*. Elsevier B.V., 175(1), pp. 346–355. doi: 10.1016/j.cattod.2011.03.035.

Giannoudis, P. V. *et al.* (2008) 'The diamond concept - open questions', *Injury*, 39(SUPPL.2),

p. S5. doi: 10.1016/S0020-1383(08)70010-X.

Giannoudis, P. V., Einhorn, T. A. and Marsh, D. (2007) 'Fracture healing: The diamond concept', *Injury*, 38(S4), pp. S3–S6. doi: 10.1016/s0020-1383(08)70003-2.

Hannink, G. and Arts, J. J. C. (2011) 'Bioresorbability, porosity and mechanical strength of bone substitutes: What is optimal for bone regeneration?', *Injury*. Elsevier Ltd, 42(SUPPL. 2), pp. S22–S25. doi: 10.1016/j.injury.2011.06.008.

Hassanajili, S. *et al.* (2019) 'Preparation and characterization of PLA/PCL/HA composite scaffolds using indirect 3D printing for bone tissue engineering', *Materials Science and Engineering C*. Elsevier, 104(March), p. 109960. doi: 10.1016/j.msec.2019.109960.

Howard, D. *et al.* (2008) 'Tissue engineering: Strategies, stem cells and scaffolds', *Journal of Anatomy*, 213(1), pp. 66–72. doi: 10.1111/j.1469-7580.2008.00878.x.

Indermun, S. *et al.* (2014) 'An interfacially plasticized electro-responsive hydrogel for transdermal electro-activated and modulated (TEAM) drug delivery', *International Journal of Pharmaceutics*. Elsevier B.V., 462(1–2), pp. 52–65. doi: 10.1016/j.ijpharm.2013.11.014.

Jahan, K. and Tabrizian, M. (2016) 'Composite biopolymers for bone regeneration enhancement in bony defects', *Biomaterials Science*. Royal Society of Chemistry, 4(1), pp. 25–39. doi: 10.1039/c5bm00163c.

Javanbakht, S. and Namazi, H. (2018) 'Doxorubicin loaded carboxymethyl cellulose/graphene quantum dot nanocomposite hydrogel films as a potential anticancer drug delivery system', *Materials Science and Engineering C*. Elsevier, 87(August 2017), pp. 50–59. doi: 10.1016/j.msec.2018.02.010.

Kokubo, T. and Takadama, H. (2006) 'How useful is SBF in predicting in vivo bone bioactivity?', *Biomaterials*, 27(15), pp. 2907–2915. doi: 10.1016/j.biomaterials.2006.01.017.

Kolek, E. *et al.* (2007) 'Confirmation of polymerisation effects of sodium chloride and its additives on acrylamide by infrared spectrometry', *Journal of Food and Nutrition Research*, 46(1), pp. 39–44.

Li, G. *et al.* (2017) 'Mechanical strengthened alginate/polyacrylamide hydrogel crosslinked by barium and ferric dual ions', *Journal of Materials Science*. Springer US, 52(14), pp. 8538–8545. doi: 10.1007/s10853-017-1066-x.

Li, J. *et al.* (2011) 'Biomimetic multicomponent polysaccharide/nano-hydroxyapatite composites for bone tissue engineering', *Carbohydrate Polymers*. Elsevier Ltd., 85(4), pp. 885–894. doi: 10.1016/j.carbpol.2011.04.015.

Mabrouk, M. *et al.* (2014) ‘Effect of ciprofloxacin incorporation in PVA and PVA bioactive glass composite scaffolds’, *Ceramics International*. Elsevier, 40(3), pp. 4833–4845. doi: 10.1016/j.ceramint.2013.09.033.

Mabrouk, M. *et al.* (2016) ‘The influence of lyophilized EmuGel silica microspheres on the physicomechanical properties, in vitro bioactivity and biodegradation of a novel ciprofloxacin-loaded PCL/PAA scaffold’, *Polymers*, 8(6). doi: 10.3390/polym8060232.

Maquet, V. *et al.* (2003) ‘Preparation, characterization, and in vitro degradation of bioresorbable and bioactive composites based on Bioglass®-filled polylactide foams’, *Journal of Biomedical Materials Research - Part A*, 66(2), pp. 335–346. doi: 10.1002/jbm.a.10587.

Mayo Clininc (2022) *Broken leg*. Available at: https://www.mayoclinic.org/diseases-conditions/broken-leg/diagnosis-treatment/drc-20370416 (Accessed: 30 June 2022).

Peter, M. *et al.* (2009) ‘Development of novel α-chitin/nanobioactive glass ceramic composite scaffolds for tissue engineering applications’, *Carbohydrate Polymers*. Elsevier Ltd, 78(4), pp. 926–931. doi: 10.1016/j.carbpol.2009.07.016.

Podporska-Carroll, J., Ip, J. W. Y. and Gogolewski, S. (2014) ‘Biodegradable poly(ester urethane) urea scaffolds for tissue engineering: Interaction with osteoblast-like MG-63 cells’, *Acta Biomaterialia*. Acta Materialia Inc., 10(6), pp. 2781–2791. doi: 10.1016/j.actbio.2014.02.016.

Prasadh, S. and Wong, R. C. W. (2018) ‘Unraveling the mechanical strength of biomaterials used as a bone scaffold in oral and maxillofacial defects’, *Oral Science International*. Japanese Stomatological Society, 15(2), pp. 48–55. doi: 10.1016/S1348-8643(18)30005-3.

Rainer, A. *et al.* (2008) ‘Fabrication of bioactive glass-ceramic foams mimicking human bone portions for regenerative medicine’, *Acta Biomaterialia*, 4(2), pp. 362–369. doi: 10.1016/j.actbio.2007.08.007.

Richhariya, G. *et al.* (2020) ‘Development of self-healing cement slurry through the incorporation of dual-encapsulated polyacrylamide for the prevention ofwater ingress in oil well’, *Materials*, 13(13), pp. 1–22. doi: 10.3390/ma13132921.

Ryszkowska, J. L. *et al.* (2010) ‘Biodegradable polyurethane composite scaffolds containing Bioglass® for bone tissue engineering’, *Composites Science and Technology*, 70(13), pp. 1894–1908. doi: 10.1016/j.compscitech.2010.05.011.

Sachlos, E. *et al.* (2006) ‘Collagen Scaffolds Reinforced with Biomimetic Composite Nano-Sized Carbonate-Substituted Hydroxyapatite Crystals and Shaped by Rapid Prototyping to

Contain Internal Microchannels', *Tissue Engineering*, 12(9).

Tirkistani, F. A. A. and Hassan, R. M. (2012) 'Kinetics and mechanism of non-isothermal decomposition of some cross-linked metal-alginate complexes especially trivalent metal - alginate complexes', *Oriental Journal of Chemistry*, 28(2), pp. 913–920. doi: 10.13005/ojc/280235.

Tohamy, K. M. *et al.* (2018) 'Novel alginate/hydroxyethyl cellulose/hydroxyapatite composite scaffold for bone regeneration: In vitro cell viability and proliferation of human mesenchymal stem cells', *International Journal of Biological Macromolecules*. Elsevier B.V., 112, pp. 448–460. doi: 10.1016/j.ijbiomac.2018.01.181.

Union for International Cancer Control (2014) 'Osteosarcoma: 2014 Review of Cancer Medicines on the WHO List of Essential Medicines', (3), pp. 1–10. Available at: http://www.who.int/selection_medicines/committees/expert/20/applications/Osteosarcoma.pdf?ua=1.

Wang, J., Lou, L. and Qiu, J. (2019) 'Super-tough hydrogels using ionically crosslinked networks', *Journal of Applied Polymer Science*, 136(44), pp. 1–9. doi: 10.1002/app.48182.

Yu, N. Y. C. *et al.* (2010) 'Biodegradable poly(α-hydroxy acid) polymer scaffolds for bone tissue engineering', *Journal of Biomedical Materials Research - Part B Applied Biomaterials*, 93(1), pp. 285–295. doi: 10.1002/jbm.b.31588.

CHAPTER.6. : CONCLUSIONS, RECOMMENDATIONS AND FUTURE PROSPECTS

6.1 Conclusions

The development of improved treatments and new treatment modalities for osteosarcoma requires a great deal of innovative research. Currently, while some osteosarcomas require chemotherapeutic interventions (like higher grade osteosarcomas), other osteosarcomas (low grade osteosarcomas) just require surgical interventions and thus only require an for bone regeneration) (Tiwari, 2012).

In this study, two double network hydrogel implants were synthesised and characterised for application in osteosarcoma; one with bioglass and the other without bioglass. The hydrogel implants were synthesised using alginate and polyacrylamide. The hydrogel implants displayed brilliant moulding capabilities. Mechanical analysis of the hydrogel implants conducted over 4 weeks displayed that both hydrogel implants decreased drastically in strength over time, however, BG-ALG-PAAM hydrogel implants had better mechanical properties than ALG-PAAM hydrogel implants. Cell viability studies conducted with MG-63 cells indicate that both hydrogel implants had cell viabilities of over 85% and thus according to ISO standards are non-cytotoxic. However, cell attachment studies visually displayed that BG-ALG-PAAM hydrogels had greater clusters of MG-63 cells compared to ALG-PAAM hydrogels.

The formation of scaffold implants was also researched. The same polymers that were used to synthesise ALG-PAAM and BG-ALG-PAAM hydrogel implants were used to synthesise APDL and BGAPDL scaffolds. The lack of pores present in ALG-PAAM and BG-ALG-PAAM hydrogel implants, prompted the use of lyophilisation to form the implantable scaffolds. However, despite having porosity from formation, only 2 criteria of the diamond concept were met with BGAPDL scaffolds (due the inherent osteoconductive and osteoproductive nature of bioglass).

Drug release studies have shown that the hydrogel implants have similar release profiles with ~ 20% of drug released at 8 weeks. This has the potential to suit the WHO regimen of chemotherapy that provides chemotherapy for osteosarcoma in cycles for 17 weeks after surgery, however, during this time, no bone growth may be expected due to the presence of DOX within the scaffold. APDL and BGAPDL scaffold implants displayed drug release profiles of <19% at 8 weeks despite having pores from formation and having a slightly greater degradation rate than the hydrogel implants.

Therefore, it can be concluded that while both ALG-PAAM and BG-ALG-PAAM hydrogels displayed potential for bone regeneration, the BG-ALG-PAAM hydrogels displayed a better promise in bone regeneration than the ALG-PAAM hydrogels. It can also be concluded that more research is required to better APDL and BGAPDL scaffolds so that it may meet at least 3 of the 5 criteria of the Diamond concept. With this in mind, the implications of this study in terms of clinical importance of BG-ALG-PAAM are as follows:

The moulding capabilities of BG-ALG-PAAM hydrogel implants show that this technology possess the potential to be used in a clinical setting to mould the hydrogel to a patient's defect caused by post-surgical resection of osteosarcoma. The bone regeneration capabilities that the BG-ALG-PAAM hydrogel implants displayed, prove that this implantable scaffold has the potential to facilitate bone regeneration thus negating the need for routine specialist appointments to assess prosthetic suitability and adjustments. In osteosarcoma cases whereby patients do not require chemotherapy, BG-ALG-PAAM hydrogel implants have the potential to be used without the incorporation of doxorubicin. The drug loading and release profile of BG-ALG-PAAM hydrogel implants display the potential of negating the need for patients to visit the clinic for adjuvant chemotherapy.

6.2 Future prospects

As stated in chapter 2, indirect 3D printing approaches are needed to overcome the draw backs of limited 3D technology available. Some have demonstrated the possibility of this by using lyophilisation to allow the scaffold to take the shape of the mould (Sachlos *et al.*, 2006; Hassanajili *et al.*, 2019). Chapter 3 highlighted the potential of the scaffold's inherent ability to mould to any shape (without the need of techniques such as lyophilisation) while chapter 4 of this dissertation displayed the full capabilities of the scaffold take on the shape of any mould as well its drug release and mechanical abilities. In chapter 5 lyophilisation was used to form the scaffold implants and therefore imparts a moulding capability. With this ability in mind, the following future prospects may be followed:

Currently, imaging methods such as MRI which has facilitated in-depth details of the tumour to be determined such as the extent of the tumour in the bone marrow cavity and the tumour's relation to its surrounding structures (Bielack *et al.*, 2016). This may enable researchers to determine the dimensions of the mould required to shape the scaffold. The mould can then be designed using CAD then 3D printed. However, as technology evolves the use of scanning applications could allow medical teams to fabricate scaffolds of exact dimensions by directly translating tumour imaging to a CAD design. However, this technology is still in its early phases and is limited and thus is a future prospective.

While BG-ALG-PAAM hydrogel implants did display compressive strength equal that could suit cancellous bone initially, its strength decreased drastically over four weeks. As healing could take several months, the decrease in strength is a limitation of this system. Therefore, more innovative research is required to impart greater strength to the hydrogel implant or to allow the scaffold to inherently maintain strength for a longer period of time without the aid of fixative devices.

This study showcased the potential use of the BG-ALG-PAAM hydrogel implant as a localised drug delivery system to deliver doxorubicin at the resection site to mitigate the risk of residual osteosarcoma cells. The use of localised chemotherapy negates the need of using established dosages that are administered IV. Therefore, animal studies are proposed as a future prospect to determine therapeutic window of released drug.

While the BG-ALG-PAAM hydrogel implants have displayed a sustained release profile that could be suited to the standard regimens, further optimisation studies should be conducted to facilitate the release of a greater amount of doxorubicin within a shorter amount of time. Further optimisation studies to facilitate faster drug release could include coating the surface of the implants with doxorubicin instead of loading the entire implant with it. Another method of optimising drug release could be to load doxorubicin into nano-carriers and adhere these drug-loaded nano carriers onto the surface of the implants (Li *et al.*, 2019). If doxorubicin, releases faster, the scaffold will be free of chemotherapeutic drug faster. This could facilitate bone to start growing sooner onto the scaffold. Therefore, with this in mind, animal studies are proposed as a future prospect to be conducted to establish the amount of time required for localised therapy to be effective.

BG-ALG-PAAM hydrogel implants meet the required three of the five criteria of the diamond concept. Cytocompatibility studies and *in vitro* biomineralization studies indicated its potential for bone regeneration. To assess whether this can be translated to living organisms, a pilot animal study is also recommended as a future prospective to assess the biocompatibility and bone regeneration abilities of BG-ALG-PAAM hydrogels *in vivo*.

6.3 References

Bielack, S. S. *et al.* (2016) 'Advances in the management of osteosarcoma', *F1000Research*, 5(0), pp. 1–10. doi: 10.12688/f1000research.9465.1.

Hassanajili, S. *et al.* (2019) 'Preparation and characterization of PLA/PCL/HA composite scaffolds using indirect 3D printing for bone tissue engineering', *Materials Science and Engineering C*. Elsevier, 104, p. 109960. doi: 10.1016/j.msec.2019.109960.

Li, Yan *et al.* (2019) 'A hybrid 3D-printed aspirin-laden liposome composite scaffold for bone tissue engineering', *Journal of Materials Chemistry B*. Royal Society of Chemistry, 7(4), pp. 619–629. doi: 10.1039/C8TB02756K.

Sachlos, E. *et al.* (2006) 'Collagen Scaffolds Reinforced with Biomimetic Composite Nano-Sized Carbonate-Substituted Hydroxyapatite Crystals and Shaped by Rapid Prototyping to Contain Internal Microchannels', *Tissue Engineering*, 12(9). doi:10.1089/ten.2006.12.2479

Tiwari, A. (2012) 'Current concepts in surgical treatment of osteosarcoma', *Journal of Clinical Orthopaedics and Trauma*. Elsevier, 3(1), pp. 4–9. doi: 10.1016/j.jcot.2012.04.004.

Appendix A: International Published Review Paper



frontiers in Materials

REVIEW
published: 01 July 2021
doi: 10.3389/fmats.2021.668834

The Application of 3D-Printing and Nanotechnology for the Targeted Treatment of Osteosarcoma

*Ayesha Suleman[1], Pierre P. D. Kondiah[1], Mostafa Mabrouk[2] and Yahya E. Choonara[1]**

[1]Wits Advanced Drug Delivery Platform Research Unit, Department of Pharmacy and Pharmacology, School of Therapeutic Science, Faculty of Health Sciences, University of the Witwatersrand, Johannesburg, South Africa, [2]Refractories, Ceramics and Building Materials Department, National Research Centre, Giza, Egypt

Osteosarcoma is a malignant bone neoplasm prevalent in adolescents. Current therapies include chemotherapy and surgery. Surgical resection of osteosarcoma induces a large bone defect which may be overcome by employing scaffolds for bone tissue engineering. This review details the polymers and bioceramics that may be used to fabricate 3D printed scaffolds for bone regeneration and the nanotechnology strategies that may be incorporated into such scaffolds. Natural polymers discussed include chitosan, alginate, collagen, gelatin, and silk fibroin. Synthetic polymers discussed include polycaprolactone, polyurethane, poly(lactic)acid and poly(vinyl) alcohol. Bioceramics that are utilized in bone regeneration such as calcium phosphate, calcium silicate and bioglass are elaborated on. Furthermore, comparison data between different types of 3D printed scaffolds for bone regeneration are presented. A discussion on Photo-responsive and magneto-responsive 3D printed scaffolds that have been fabricated for bone regeneration is included. Research concerning drug-loaded scaffolds as well as the incorporation of nanocarriers into scaffolds for bone regeneration is provided. Chemotherapy utilized in osteosarcoma therapy has severe adverse effects due to being non-selective between healthy cells and tumor cells. A possible way to overcome this is to utilize nanotechnology. Therefore, research detailing other types of nanocarriers that have the potential to be incorporated into 3D printed scaffolds for localized adjuvant therapy is presented.

Keywords: 3D printing, osteosarcoma, nanotechnology, bone regeneration, polymeric platforms

OPEN ACCESS

Edited by:
Jinguang Hu,
University of Calgary, Canada

Reviewed by:
Antonio Greco,
University of Salento, Italy
Hitendra Kumar,
University of British Columbia Okanagan, Canada

****Correspondence:***
Yahya E. Choonara
Yahya.Choonara@wits.ac.za

Specialty section:
This article was submitted to Polymeric and Composite Materials, a section of the journal Frontiers in Materials

Received: *17 February 2021*
Accepted: *22 June 2021*
Published: *01 July 2021*

Citation:
Suleman A, Kondiah PPD, Mabrouk M and Choonara YE (2021) The Application of 3D-Printing and

INTRODUCTION

Osteosarcoma is a malignant neoplasm of which there is osteoid formation by tumor cells (Heck and Toy, 2017). According to the American Cancer Society, osteosarcoma is prevalent in patients between the ages of 10 and 30. Those diagnosed with osteosarcoma over the age of 60, consist of 10% of the population afflicted (The American Cancer Society, 2020). Osteosarcoma may arise from certain predisposing factors such as Paget's disease, exposure to radiation, chemotherapy, genetics as well as foreign bodies inserted into bone such as orthopedic implants. The majority of osteosarcomas

Appendix B: Research output: Oral presentation: BRICS Summit 2021: 04 November 2021

Ayesha Suleman, Pierre Kondiah and Yahya E Choonara. BRICS Summit 2021: 04 November 2021. Oral presentation

